/
Article / Book Information

( )	
Title(English)	Novel Kinematic Pairs Composed of Elastically Constrained Two Curved Surfaces
( )	
Author(English)	Naoto Kimura
( )	: ( ), : , : 11594 , :2020 9 25 , : , : , , , ,
Citation(English)	Degree:Doctor (Engineering), Conferring organization: Tokyo Institute of Technology, Report number: 11594 , Conferred date:2020/9/25, Degree Type:Course doctor, Examiner:,,,,
( )	
Type(English)	Doctoral Thesis

Doctoral Dissertation

July, 2020

Novel Kinematic Pairs Composed of Elastically Constrained Two Curved Surfaces
(弾性拘束された２曲面からなる新しい対偶)

Naoto KIMURA (木村 直人)

Department of Mechanical Engineering
School of Engineering
Tokyo Institute of Technology

Supervisor
Professor Nobuyuki IWATSUKI
Department of Mechanical Engineering
School of Engineering
Tokyo Institute of Technology

Contents

List of Figures

List of Tables

Nomenclature

Main symbols are shown as follows. The detailed definition of each symbol is described in each chapter.

A	A mathematical set which represents a range of motion
b	Width
$\boldsymbol{c}$	An endpoint position vector of an elastic element
$\boldsymbol{d}$	A relative position vector between two points
$\boldsymbol{f}$	A force vector / A numerical vector composed of magnitudes of forces
f	A component of a force vector/ Magnitude of a force
$\boldsymbol{e}$	A basis of a local coordinate system
E	Young's modulus
F	An objective function for an optimization
$\boldsymbol{G}$	A matrix including wrench screws
h	Thickness
$\boldsymbol{I}$	Identity matrix
$\boldsymbol{j}$	Position vector of a joint in a linkage
k	Spring constant
$\boldsymbol{K}$	A stiffness matrix
l, L	Length
$\boldsymbol{n}$	A normal vector
N	A number
$\boldsymbol{p}$	A position vector on a trajectory
r, R	A radius
$\boldsymbol{R}$	A rotation matrix
$\boldsymbol{s}$	A position vector on a surface
$\mathbb{S}^r$	A wrench screw
Σ	A local Cartesian coordinate system
TI	A transmission index
t, u	A parameter for a translation motion
U	Potential energy of elastic elements
$\boldsymbol{v}$	A direction vector/ A tangent vector
w	A weight parameter in multi-objective optimization
$\mathbb{W}$	A wrench
x, y, z	Components on a coordinate system

δ	A gap
κ	A curvature
λ	An arc-length parameter
μ	The coefficient of static friction/ The ratio between tangent force and normal force
$\boldsymbol{\tau}$	A torque vector
τ	A component of a torque vector/ Magnitude of a torque
θ, ψ, ϕ	Angles
$\boldsymbol{\omega}$	A angular velocity vector
$\hat{\boldsymbol{a}}$	An unit vector of a vector $\boldsymbol{a}$
$|\boldsymbol{a}|$	The 2-norm of a vector $\boldsymbol{a}$
$\boldsymbol{A}^{\#}$	The pseudo inverse matrix of a matrix $\boldsymbol{A}$
$[\boldsymbol{a}\times]$	The matrix representing the cross product operation of $\boldsymbol{a}$
$\dot{a}$	The first-order derivative of a with one variable
$\mathrm{mean}(x)$	The mean value of x
$\mathrm{max}(x)$	The maximum value of x
$\mathrm{min}(x)$	The minimum value of x

.

Chapter 1

Introduction

1.1 Background and objective

Linkage mechanisms are used in many mechanical systems in order to generate the specified motion such as robotic mechanisms or to transmit motion and power to different mechanical systems such as steering mechanisms for automobiles. In general, they are synthesized with lower pairs, such as a revolute pair, a prismatic pair, a spherical pair, and so on. These kinematic pairs have surface contact between two links. However, the geometrical limitation of surface contact is severe because curvatures of the contact surfaces in the relative-motion direction must be constant to keep in surface contact. Thus, shapes of such contact surfaces are limited and only six types of simple relative motions (1-axial rotation, linear motion, helical motion, cylindrical motion, 3-axial rotation, and planar motion) are allowed between the links. This means that motion of a linkage is synthesized with a combination of simple relative motions among links. This fact causes the following problems in mechanism synthesis.

(a) It is difficult to synthesize a linkage with 1 degree of freedom (DOF) to generate the specified motions completely because the mechanism does not have enough design parameters such as link length or arrangement of lower pairs.

(b) A linkage with multiple-DOF becomes a complex mechanism with many kinematic pairs and links.

The problem (a) indicates that it is difficult to make detailed output motions with only simple relative motions between the links. Thus, such kinds of linkages have been generally synthesized to generate the specified motion approximately with such as precision-point methods [1]-[16] or optimal-synthesis methods [17]-[33] so far. The problem (b) indicates that DOF of lower pairs is limited up to three and that a large number of kinematic pairs are required to synthesize a linkage with multiple-DOF. Especially, linkages which need redundant DOF tend to have complex structures. For example, in robotic field, underactuated (flexible) robotic-mechanisms have been developed by many researchers [34]-[66] for human safety, for passive adaptability to the environment, and so on. Since these mechanisms need not only actuation DOF but also passive DOF, they need a lot of DOF and their structures tend to have complex.

In order to reduce the geometrical limitation of contact surfaces, the use of higher pairs, where two links are in contact at some points or a line, is a good choice. Since the geometrical limitation of higher pairs is not severe, many kinds of kinematic pairs can be
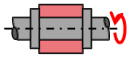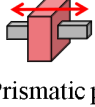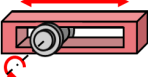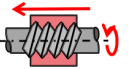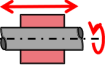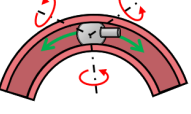
	Lower pair (surface contact)	Higher (point/ line / curve contact)
Closed pair	Revolute pair Prismatic pair Helical pair Cylindrical pair Spherical pair	Cylinder-groove pair Sphere-pipe pair
Unclosed pair	Plane pair	➢ Cam pair ➢ Rolling contact pair　etc…

Fig.1.1　Classification of kinematic pairs based on contact state, type of motion and constraint state

achieved and their relative motion between the links can be specified in detail. Fig.1.1 shows the types of kinematic pairs. Kinematic pairs, which are defined as a joint connecting two links while allows relative motion between them, are classified according to contact state (lower or higher pair), type of motion (rotate, linear, etc...) and constraint state (closed or unclosed) in the literature on the theory of mechanism [67] [68]. Note that the closed state means the state where two links are sufficiently constrained geometrically, and the unclosed state means the state where two links are not sufficiently constrained geometrically. In order to keep in contact between the links with the unclosed kinematic pair, external forces such as gravitational force and spring force are required. Although the use of the closed higher pairs are a good choice for practical applications, it is considered that there are few kinematic pairs such as a cylinder-groove pair (1-axial rotation and 1-axial translations) and a sphere-pipe pair (3-axial rotations and 1-axial translation) because the closed state is a severe geometrical limitation of contact surfaces between the links. However, since the geometrical constraint of the unclosed higher pairs is relatively loose, they can allow wide variety of complex relative motion. As unclosed higher pairs, cams have been used. Cams are used to transform a rotation to a translation with the specified timing or used as motion guidance passing through a complex planar trajectory. Non-circular gears also have been used. They are kinds of rolling contact pairs, which allows the two rotations to be synchronized at the specified relative velocity. By synthesizing 1-DOF mechanisms with them, the exact generation of the specified motion has been achieved [69]-[79]. However, the exact generation of only planar motions have been achieved so far. Although spatial cams have been proposed as a higher pair to transform motions spatially, they have been used only to transform a driving rotation to the specified translational reciprocation of which fixed axis do not intersect to the driving rotation axis or to transform a driving rotation to the specified rotational reciprocation of which fixed axis does not intersect to the driving rotation axis [80] [81]. In other words, there was no spatial cam mechanism which can generate the specified complex spatial trajectory. The
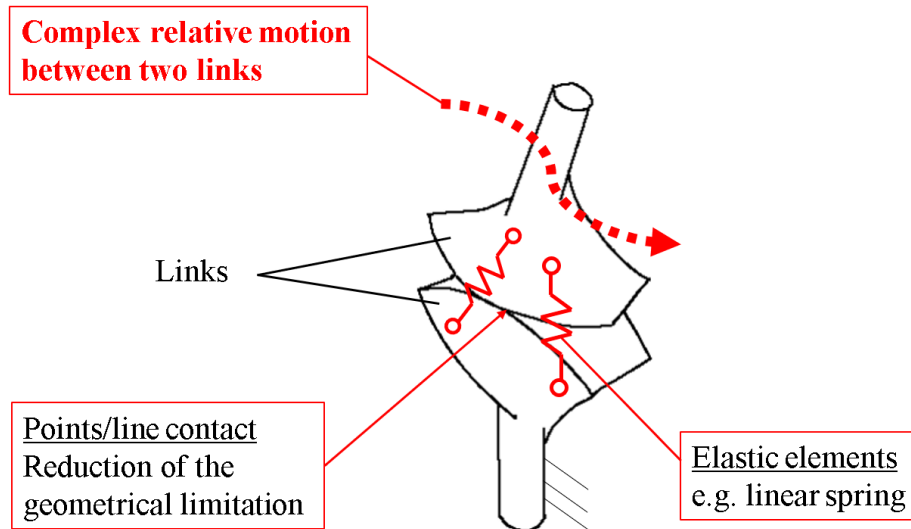
Fig.1.2   The proposed structure of the elastically closed pairs

reason is considered to be because not only theory to generate the specified spatial motion is difficult but also methods to manufacture higher pairing elements with complex curved surfaces generating complex relative spatial motions had not been developed. However, recently, manufacturing a mechanical part with a complex shape has been becoming easy because multi-spindle CNC (Computerized Numerical Control) machining technology and additive manufacturing technology have been developed. Therefore, such complex pairing elements can be manufactured technically. Developing such new mechanical elements to generate complex relative spatial motions is very important especially to extend the synthesis of spatial mechanisms and their applications.

In this dissertation, novel practical kinematic pairs which allow complex relative spatial motion between the links are developed in order to extend the synthesis of spatial mechanisms. Fig.1.2 shows the schematic diagram of the proposed structure. The joint in the figure is an unclosed higher pair of which two curved surfaces with complex shapes contact at points or a line with each other. For practical use of unclosed higher pairs, external forces to the keep in contact between the links are required. Thus, the two links are constrained with some elastic elements. Since it can keep in contact between the links by itself, it can be used as a closed pair in mechanism synthesis. Therefore, joint mechanisms with this structure are called "elastically closed pairs" and they are treated as kinds of kinematic pairs in the following discussion. A similar idea to regard a joint mechanism composed of several mechanical elements as a kinematic pair in mechanism synthesis has been proposed by Huesing et al [82] and it is called "Complex joint". This kind of idea is also seen in the conventional mechanism synthesis. For example, a rotary motor is regarded as an active revolute pair and a universal joint is regarded as a kinematic pair allowing 2-axial rotations in mechanism synthesis. This means that by developing a joint mechanism composed of multiple elements to have a specific kinematic constraint in advance, the only relative motion between its main two links can be considered in mechanism synthesis without considering the detailed structure of the joint. This idea is important for efficient mechanism synthesis because the number of available kinematic
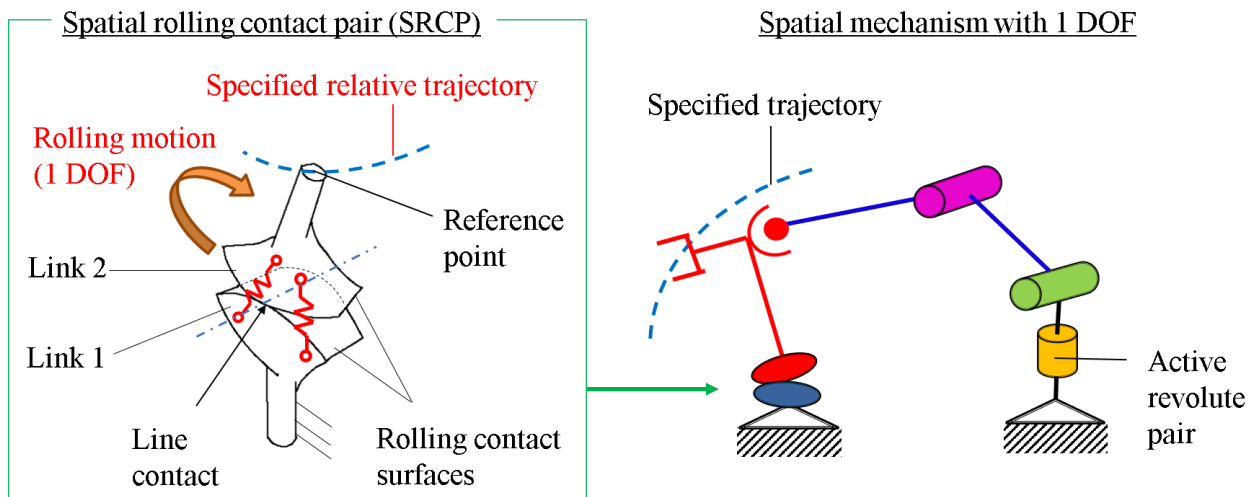
Fig.1.3   Conceptual diagram of the spatial rolling contact pair (SRCP)

pairs can be increased and important parts of the mechanism only have to be focused on in mechanism synthesis. Therefore, in this dissertation, novel practical joint mechanisms with such a structure are developed as "kinematic pairs" based on this idea, and they are applied to the synthesis of spatial mechanisms. Mechanisms with elastically closed pairs are called "ECP-linkages".

The elastically closed pairs have four features. Firstly, they can allow the specified complex relative spatial motions which cannot be generated by the geometrically closed kinematic pairs because of their kinematic limitations. Especially, a kinematic pair generating relative spatial rolling motion is useful to improve the mechanical performances of a mechanism because of its low friction between the links. Secondly, it can have multiple DOF between the links. If the two links are in contact at a single point, it can have 5 DOF. This is effective to reduce the number of links in a mechanism. Thirdly, they have elasticity between the links because of their elastic constraints. If this elasticity is used effectively, flexible mechanism can be synthesized easily. Fourthly, if the elastic elements move like flexible actuators, they can drive the links actively. This means that the pairs can be treated as active kinematic pairs in mechanism synthesis. Based on these features, this research focuses on the following three contents.

(1) Development of "the spatial rolling contact pair", which can generate the specified trajectory while the relative rolling motion between the links
(2) Development of "the flexibly constrained pair", which can have both motion guidance and flexibility between the links
(3) Development of "the elastically closed active pairs", which is driven by active elastic elements, including the active spatial rolling contact pair and the active flexibly constrained pair

The "Spatial Rolling Contact Pair" (SRCP) shown in Fig.1.3 is a 1-DOF kinematic pair of which two links in contact at a line roll relatively. When the link 2 rolls on the link 1 as shown in Fig.1.3, a reference point fixed on the link 2 generates a spatial trajectory. By
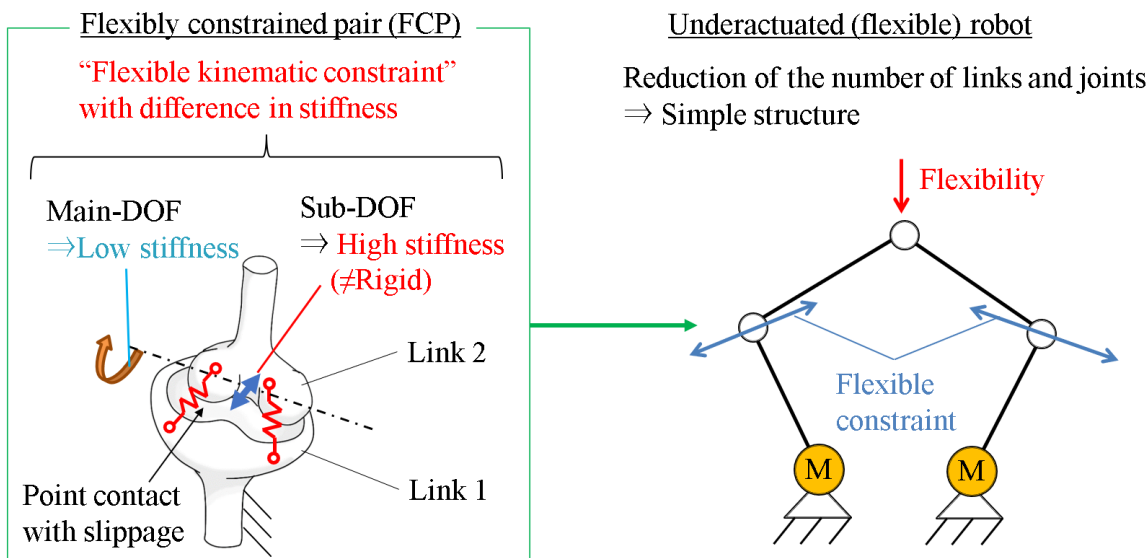
Fig.1.4   Conceptual diagram of the flexibly constrained pair (FCP)

designing the profile of the contact surfaces, the reference point can generate the specified trajectory completely. Thus, by introducing the designed SRCP into a spatial mechanism as shown in the figure, the mechanism can also generate the specified trajectory completely. Therefore, the use of the SRCP for synthesis of 1-DOF mechanism can solve the problem (a) described above. In this dissertation, a design method of the rolling contact surfaces to generate the specified relative trajectory between the links and an effective constraint method to keep ideal rolling contact between the links are proposed. In addition, a spatial ECP-linkage with 1 DOF which can generate the specified spatial trajectory is synthesized by using the SRCP, and it is prototyped with the use of additive manufacturing. Then, its performances are examined.

   The "Flexibly Constrained Pair" (FCP), which has flexibility between the links with the use of its elastic elements, is shown in Fig.1.4. The FCP, where two links are in contact at some points with slippage, allow multiple-DOF at most 5-DOF. Besides, it has stiffness in each direction of its DOF because of the elastic forces of the elastic element and reaction forces at each contact point between the links. By dividing directions of the relative motion between the links into the main-directions and the sub-directions, and by specifying stiffness in the sub-directions higher than in the main directions, a weak kinematic constraint with the difference of the stiffness can be achieved. Because of this constraint, this kinematic pair can move in main-directions under small external loads, but it can move in the sub-directions under large external loads. This means that the kinematic constraint can be changed according to the mechanical condition. This kinematic constraint is named "flexible kinematic constraint". Since the FCP has both motion guidance and flexibility because of this constraint, a mechanism of flexible robot can be synthesized with simple structure by using the FCP as shown in Fig.1.4. Therefore, an extreme case of the problem (b) described above can be solved with the FCP. In this dissertation, a design method of the FCP to specify the specified flexible constraint between the links is proposed. In addition, a simple flexible robotic mechanism

Active spatial rolling contact pair (ASRCP)

Active rolling motion

Specified trajectory

Active flexibly constrained pair (AFCP)

Main-DOF (Active)

Sub-DOF (Passive)

Active elastic elements
e.g. reeled elastic wires, flexible actuators
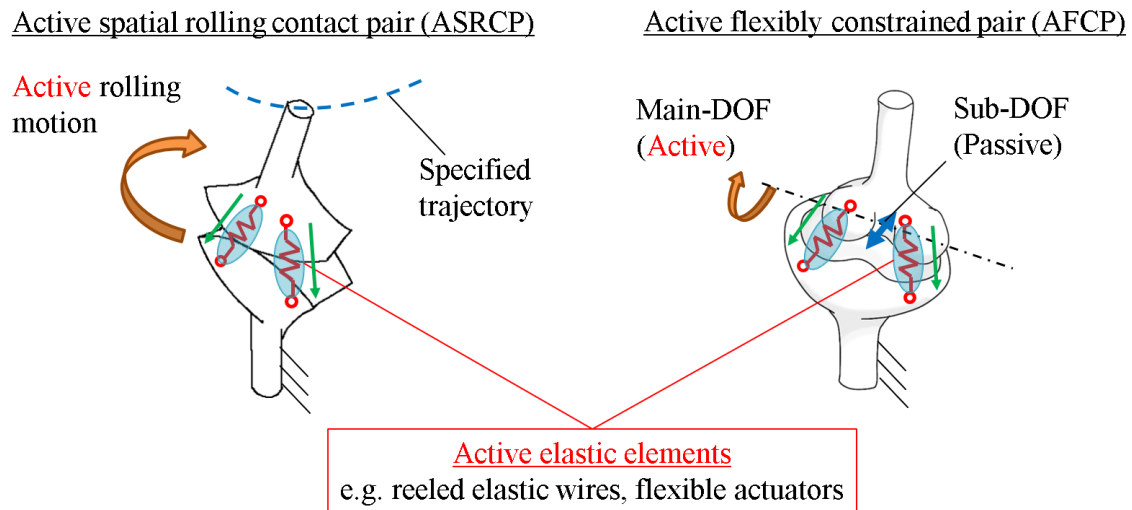
Fig.1.5   Conceptual diagram of elastically closed active pairs including the active spatial rolling contact pair (ASRCP) and the active flexibly constrained pair (AFCP)

(an underactuated ECP-linkage) is synthesized by using the FCP, and it is prototyped with the use of additive manufacturing. Then, its performances are examined.

The conceptual diagram of "elastically closed active pair" including the "Active Spatial Rolling Contact Pair" (ASRCP) and the "Active Flexibly Constrained Pair" (AFCP) is shown in Fig.1.5. In both ASRCP and AFCP, linear elastic elements are replaced by active elastic elements such as reeled elastic wires, flexible linear actuators, and so on. Since a serial mechanism with these active kinematic pairs can be synthesized, a further simplification of mechanisms with the SRCP or the FCP can be achieved. In order to obtain the ASRCP and the AFCP with high mechanical performances, a design method of them with good actuation transmission is proposed. Besides, a motion control method of them with keeping contact between the links is also proposed. Then, several examples of them are designed and prototyped with the use of additive manufacturing, and their performances are examined.

1.2   Related researches

Three topics of related researches are introduced in this section. The first topic is about synthesis of mechanisms with 1 DOF, which is related to the research on the spatial rolling contact pair. The second topic is about underactuated (flexible) robot mechanisms, which is related to the research on the flexibly constrained pair. The third topic is the design of the wire-driven joint mechanism, which is related to the research on elastically closed active pairs. Based on a review of these topics, novelty and contribution of the proposed approaches are discussed.

1.2.1 Synthesis of mechanisms with 1 DOF

Linkage mechanisms with 1 DOF are traditionally used for industrial machines, toys, walking robots, and so on, because of their simple structures driven with a single actuator. They are classified to function-generating linkages and path-generating linkages. Function-generating linkages are linkages to generate the specified relationship between input and output of translational or angular displacement. Path-generating linkages are linkages to generate the specified trajectory of a coupler point. Path-generating linkages are sometimes synthesized to generate both the specified coupler curve and the specified orientation of the coupler link. This is called rigid-body guidance. In order to synthesize them to generate the specified motions approximately, many methods have been proposed so far. Traditionally, precision-point methods have been researched for this purpose. These are methods to synthesize a linkage with 1 DOF to pass through some designated points precisely. These designated points are called precision points. In these methods, precision points are substituted into non-linear equations on the geometrical relationship of the linkage, and they are solved for mechanical parameters of the linkage. Freudenstein synthesized a function-generating planar 4-bar linkage with three precision points [1]. Wamper et al. synthesized a path-generating planar 4-bar linkage with 9 precision points [2]. Note that the number of precision points are limited depending on the number of mechanical parameters. Thus, several researchers have proposed to synthesize other mechanisms with a larger number of mechanical parameters than the planar 4-bar linkage. McLarnan synthesized function-generating planar 6-bar linkages with from 6 to 9 precision points [3]. Roth and Freudenstein synthesized a path-generating geared 5-bar linkage with 9 precision points [4]. Besides, spatial linkages are also synthesized to increase the number of mechanical parameters. Denavit and Hartenberg extended Freudensten's equations for function-generating spatial linkages and synthesized an RRRR spherical linkage with 3 precision points, an RSSR 4-bar linkage with 6 precision points and an RCCC 4-bar linkages with 3 precision points [5]. Ogawa et al. synthesized a function-generating RCSR 4-bar linkage with 3 precision points [6] and a function-generating RSSR linkage with 8 precision points [7]. Although these algebraic approaches to solve closed-loop equations can obtain mechanical parameters directly, the non-linear equations tend to be complex and the order to pass through precision points cannot be designated basically. Hence, approaches where positions of kinematic pairs are derived based on the position of the instantaneous center between each two adjacent precision points have been proposed. These approaches are mainly used for path-generating or rigid-body guidance. In these approaches, non-linear equations for synthesis are built for each serial kinematic chains in a closed-loop. Willson proposed an analytical method to synthesize planar and spherical linkages with revolute pairs [8]. Suh and Radcliffe extended the Willson's method with homogeneous transformation matrices [9] and applied this method for a spherical linkage [10]. Suh derived synthesis equations of RR chain, RS chain and RR chain to synthesize various spatial linkages [11]. Kim and Hamid proposed a method to derive synthesis equations for a serial kinematic chain with three revolute pairs and synthesized a planar 6-bar linkage with the proposed method [12]. Synthesis equations can be derived not only with homogeneous matrices but also with the other representations. Sandor proposed a representation with quaternion-operators [13]. Tsai and Roth proposed the representation

with geometric relationships of screws of kinematic pairs for dyads (a serial chain with two kinematic pairs) with revolute pairs, prismatic pairs, cylindrical pairs, spherical pairs and screw pairs [14]. Sandor et al. proposed a systematic approach to derive synthesis equations represented with screws [15]. Perez proposed the representation with dual quaternion and derived an equation to synthesize an RPRP closed-loop linkage [16].

As mentioned above, the number of designated points is limited in precision-point methods. In order to overcome this limitation, optimal-synthesis methods have been proposed. Although the output motion does not always pass the designated points precisely, a lot of output points can be designated in optimal synthesis methods. The simplest approaches are to minimize errors between the actual output motion and the specified motion of a linkage. In order to minimize this objective function, many approaches have been proposed. Han performed the optimization by numerically solving the equation that the first-derivative of the objective function is zero [17]. Lewis and Gyory applied damped least square method to minimize the objective function [18]. Fox and Willmert used a Gradient-based method with inequality constraints on dimensions, Grashof conditions, and so on [19]. Nechi proposed a combination method with a relaxation method and a gradient method [20]. Paradis and Willmert proposed the "Gauss constrained method" to improve the convergence of the optimization [21]. Ananthasuresh and Kramar synthesized an RCSR spatial 4-bar linkage with a gradient-based optimization [22]. Zhang et al. applied interior-point methods to mechanism synthesis [23]. Sancibrian simplified to derive the gradient of the objective function by expressing the kinematic equation of a planar linkage with a complex function, and optimized it with a gradient method [24]. Although gradient methods are simple and useful for optimization, optimized results with them tend to fall into the local minima. Thus, methods of metaheuristics have been applied to synthesize a linkage. Krishnamurty and Turcic used a pattern search method [25], Cabrera et al. used a genetic algorithm (GA) [26], Shiacolas used the differential evolution [27], and Lin used a combination method with a genetic algorithm and the differential evolution [28] to synthesize planar linkages. Laribi et al. used a kind of GA to the synthesis of spatial linkages [29]. As the objective function, not only structural errors on the output motion but also different criteria have been proposed to synthesize a linkage effectively. Sarkisyan et al. proposed a method to find a circle point and an instantaneous center of a planar linkage which are close to them of the specified output motion with the least-squares method [30]. Ullah and Kota [32] and Kim et al. [33] proposed methods that minimize structural errors in the shape of the output and the specified trajectories at first and then adjust the size and orientation of the output trajectory to the specified one by expansion and rotation of the linkage. Zhou and Cheung proposed a method where inverse kinematics is solved for a linkage of which a stationary point is assumed not to be fixed and find the dimensions to minimize the motion of the stationary point [31].

As described above, 1-DOF linkage with only lower pairs can not completely generate the specified trajectory. In order to achieve exact path generation, methods to introduce kinds of higher pairs into parts of a link mechanism has been proposed. These are close to the proposed concept in this dissertation. Singh and Kohli introduced a cam and a linear follower into a path-generating mechanism [69]. Ye and Smith used a cam and an oscillating roller follower in a path-generating mechanism [70]. Mundo et al. proposed to optimize dimensions of a cam-link mechanism to obtain the cam of which pressure angle, size and acceleration are small [71]. Gatti and Mundo achieved exact rigid-body guidance

with a 6-bar mechanism which has two sets of a cam and linear roller follower [72]. Soong and Chang achieved exact-function generation with a cam-link mechanism [73]. Shao et al. proposed a method to synthesize a path-generating cam-link mechanism considering the time series of tracking path [74]. Soong developed a simple planar-path generator with a cam and planetary gear [75]. Zhao et al. proposed a method to obtain a smooth cam profile by using a point close to the circle point of the mechanism for the position of the follower [76]. Zhang et al. achieved exact path generation without changes in posture by using a cam and a double-parallelogram linkage to develop an efficient parking system [77]. Besides, some methods to use non-circular gears have been proposed. A pair of non-circular gears is a kind of rolling contact pair. Mckinley et al. achieved exact rigid-body guidance with 6-bar mechanism geared by two pairs of non-circular gears [78]. Mundo et al. proposed a method to minimize non-circularity of pitch curves of non-circular gears in a path-generating mechanism geared by non-circular gears [79].

In conclusion, exact path generation of spatial linkages has not been achieved so far. Although a spatial cam is sometimes used in a spatial mechanism to generate specified reciprocating motion of its follower [80] [81], it has not been used for exact path generation so far. However, by using the spatial rolling contact pair, the exact spatial-path generation can be achieved.

1.2.2 Mechanisms for flexible robots

In order to reduce external loads applied when a robot comes into contact with people or the other external environment, or in order to increase adaptability to an uncertain external environment, methods to introduce flexibility in some parts of the robot have been proposed. A classification of this research is shown in Table 1.1. The active compliance approach can achieve compliance of a robot virtually by controlling its actuators. Thus, this approach achieve flexibility with a simple hardware. Since this approach can control compliance actively, it is possible to use different compliance according to the task. Salisbury [83] and Hogan [84] proposed a method to control output compliance of a serial manipulator. Tsuji et al. proposed a method to control both output compliance and joint compliance of a redundant serial manipulator [85]. Although these methods can achieve flexibility with a simple hardware, it is difficult to respond to a sudden change of external forces, such as a dynamic collision between a robot and the environment, without sophisticated control systems. Therefore, this approach is possible to be expensive in such applications. Besides, since this approach has to control both the posture and compliance of a robot, the control method is complicated.

Table 1.1   Classification of flexible robot mechanisms

Active compliance	Impedance control of actuators	
Passive compliance	Use of variable stiffness joint	Antagonistic-drive
		Separation-drive
	Use of invariable stiffness joint	for small deformation
		for large deformation

(a) Antagonistic drive   (b) Separation drive
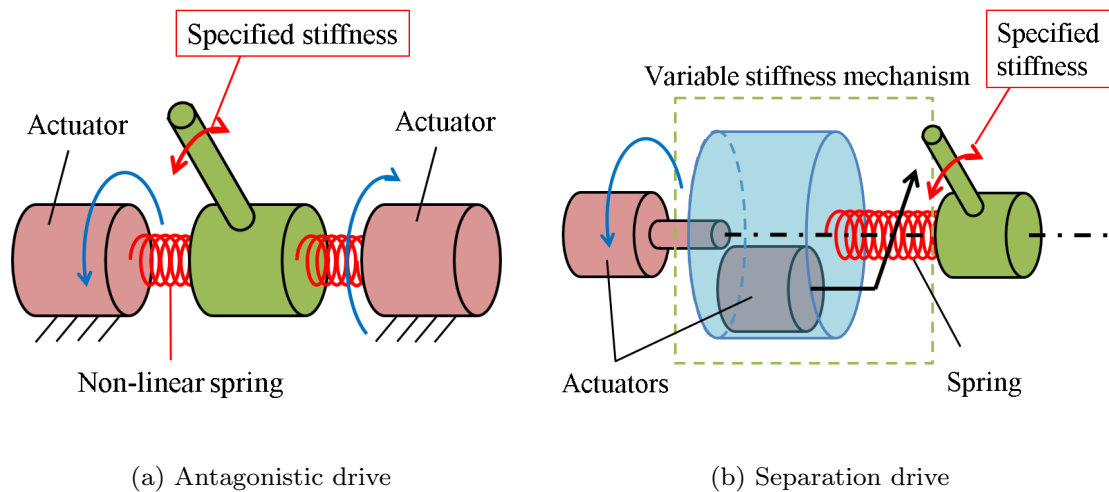
Fig.1.6   Classification of previous variable stiffness joints

As another approach, the passive compliance approach, where compliance of a mechanism is achieved with some elastic elements used in its joint, has been proposed. In order to achieve passive compliance effectively, a lot of flexible joint mechanisms have been proposed so far. Variable stiffness joints shown in Table 1.1 can adjust their passive stiffness with the additional actuators according to the task. They can be further classified into two types. One type is the antagonistic drive shown in Fig.1.6 (a), where some non-linear springs are antagonized by multiple actuators to control both joint displacement and stiffness. This type has variations according to how to achieve non-linear springs. Hyodo and Kobayashi achieved a non-linear stiffness in the tensile direction of the wire by pushing linear springs in the direction orthogonal to the wire [34]. Tonietti et al. used the same idea in the belt-driven pulley system [35]. Migliore et al. [36] and Friedi et al. [37] used cam mechanisms, Matsuda and Murata used non-circular gears [38], and WANG et al. [39] and Schiavi et al. [40] used linkage mechanisms to achieve non-linear springs by changing the displacement of linear springs. As the other approaches, Palli et al. proposed to design rotational non-linear spring with a compliant link mechanism [41], and Koganezawa proposed a method to achieve non-linear rotational stiffness by changing the radius of a torsion coil spring wrapped around a guide [42]. Besides, methods to use nonlinear material properties have been proposed. English achieved a non-linear spring by designing the shape of the flexure in a rolamite mechanism [43]. Nakamura used non-linear stiffness characteristics of a fluid-driven rubber actuators [44]. Another type is the separation drive shown in Fig.1.6 (b), where one actuator is used to control displacement and another actuators is used to adjust joint stiffness. This type has variation according to principles to adjust rotation stiffness with an additional actuator. Morita and Sugano [45], Kim and Song [46], and Groothuis et al. [47] proposed methods to adjust rotation stiffness by changing the moment arms on which spring forces act. Wolf and Hirzinger [48] and Wolf et al. [49] adjusted stiffness by changing preload which applies springs in their cam-spring based rotational spring. Ahmed and Kalaykov proposed to adjust stiffness by changing characteristics of MR fluid [50]. Kajikawa and Abe used a method to change

share stiffness of rubber cushion by compressing them [51].

Note that variable stiffness joints have the disadvantage that they tend to be heavy and to have complex structures because of the additional actuators. If a lot of variable stiffness joints are used in a robot to have multi-directional flexibility, the whole mechanism of the robot naturally becomes heavyweight. In order to reduce the weight of a flexible robot, it is considered that the use of invariable stiffness joints shown in Table 1.1 is a good choice. Pratt and Williamson proposed a series elastic actuator (SEA), where a torsion spring is attached serially to the rotation output of a motor [52]. Lee et al. proposed a linear SEA, where a linear spring made of a compliant mechanism is attached serially to the output of a linear motor [53]. Okada and Nakamura developed a 3-DOF flexible joint with a parallel linkage composed of flexible links [54]. Grebenstein et al. achieved a flexible joint by constraining an unclosed cylindrical pair with elastic cables [55]. Lessard et al. [56] and Jung et al. [57] achieved flexible joint with multi-directional flexibility with tensegrity. Note that flexibility and motion accuracy are generally trade-off. Thus, these are not suitable for applications which require large deformation, such as shock absorption, because of the need to sacrifice motion accuracy for flexibility. In order to balance both flexibility and motion accuracy, methods to use non-linear stiffness characteristics have been proposed. Park and Song developed a rotational softening spring mechanism with a slider-crank mechanism pushed by a linear spring to apply into a human safe robot [58]. A robot with softening spring characteristics has high stiffness during the normal task and has small stiffness when a large external force is applied to the mechanism. Therefore, these characteristics can work like kinds of force (torque)-limiters [59]-[63]. Besides, Okada and Kino developed a rotational hardening spring using singularity of a linkage [64], and Okada and Takeishi developed a hardening spring with elastically constrained linkages [65]. They applied them for shock absorption during the landing of legged robots. In the landing of a legged robot, legs with hardening spring characteristics reduce velocity in the low stiffness part at first and finally support the body of the robot in the high stiffness part. Therefore, these characteristics are suitable for this application. Kuo and Deshpande developed a small rotational hardening spring mechanism with rubber and pulley to apply a robotic finger for manipulation tasks [66]. In this case, fingers with hardening spring characteristics adapt an object with the low stiffness part and grasp it with the high stiffness part. Therefore, the use of these characteristics is a good choice for this application.

In conclusion, almost all of flexible joints have flexibility just in a single direction, such as around the rotation axis. Thus, when multi-directional flexibility is required such as for human safety, a robotic mechanism has to be synthesized with many of them. In this case, the mechanism tends to have a complex structure and a large weight. Although some joints have multi-directional flexibility by using elastic links or elastic wires [54]-[57], it is not possible to specify the detailed stiffness characteristics in the directions of passive displacement. However, the flexibly constrained pairs, which proposed in this dissertation, have multi-directional flexibility and the specified stiffness characteristics in the directions of passive deformation. Therefore, they can achieve simplification and high performance of flexible robot mechanisms.

1.2.3 Design of wire-driven joint mechanisms

Wire-driven joint mechanisms are traditionally used to reduce the weight of a manipulator, to imitate musculoskeletal motions of a biological body, and so on. From the perspective of driving methods, they are classified to the pulley-drive and the direct-drive as shown in Fig.1.7. Pulley-drive shown in Fig.1.7 (a) is the method where a wire tension is transmitted to a revolute pair via a pulley. This type can achieve high force transmission although the applicable joint is limited to the revolute pair. Direct-drive shown in Fig.1.7 (b) is the method where wire tension is transmitted to a joint from the attachment point of the wire. This type can be used in any type of kinematic pairs.

Pulley-drive is mainly used in applications of robotic arms and hands. One purpose is developing lightweight and low inertia robots. Hirose and Ma developed a serial manipulator with a coupled pulley drive system to reduce the weight of moving links and distribute torques of motors [86]. Kim developed a lightweight dual-arm robot with pulley-drive systems [87]. Another purpose is developing flexible manipulators. The flexible manipulators can be classified to two types. One type is the antagonistic-drive type described in section 1.2.2 [34] [43] [44]. This type achieves flexibility with the elasticity of reeled-wires at each joint. Another type is the underactuated-drive type, where a serial manipulator with multiple joints is driven with fewer wires than its DOF. This type achieves flexibility with passive DOF of the whole mechanism. For example, Hirose and Umetani developed the "soft gripper" with two fingers each of which is a multi-joint serial mechanism driven with a single reeled-wire [88]. This finger has shape adaptability to the gripped object. Ozawa et al. proposed a general design method to arrange wires to achieve mechanisms with shape adaptability and designed a compact robotic finger [89].

Direct-drive is used in a wide variety of applications because applicable joints are not limited. This can be further classified based on arrangement methods of wires. The sim-

(a) Pulley-drive   (b) Direct-drive
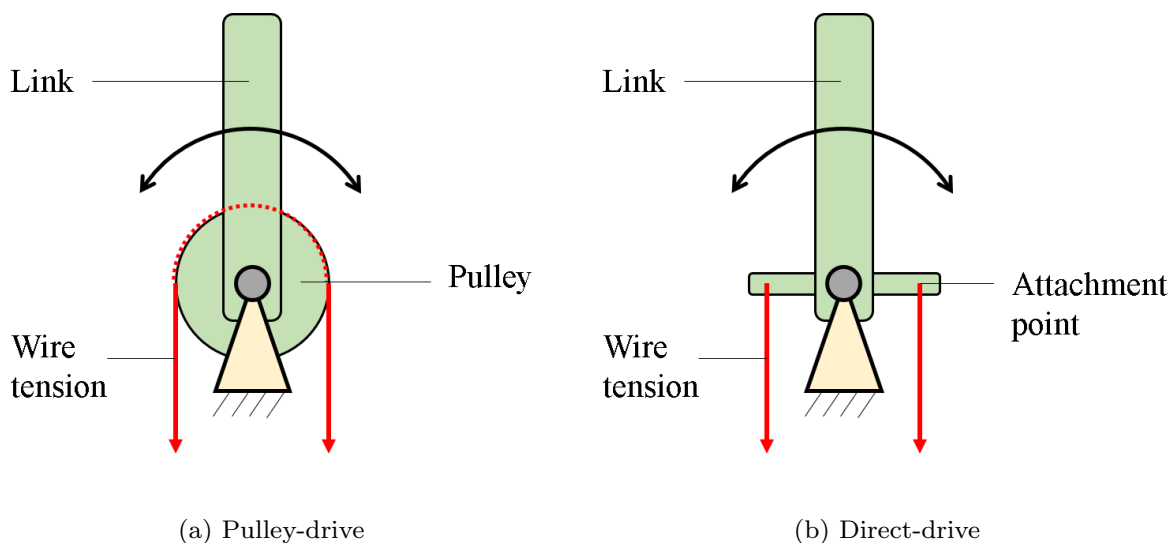
Fig.1.7   Classification of wire-driven joints based on driving methods

plest arrangement is parallel-arrangement, where all wires are simply arranged in parallel with each other. In the literature of developing serial manipulators for medical instruments, various types of joints were driven by this arrangement. Zhang et al. [90], Dong et al. [91] and Li et al. [92] developed manipulators with wire-driven elastic joints. Ji et al. developed manipulators with wire-driven spherical joints [93]. Nai et al. [94], Suh et al. [95] [96], and Jelinek et al. [97] developed manipulators with wire-driven planar rolling contact joints. However, although this arrangement is easy to apply to a wide variety of joints, the workspace of each joint tends to be limited. Thus, wire-arrangement methods to maximize the workspace with numerical optimizations have been proposed. Takeda et al. proposed a method to arrange wires (pneumatic rubber muscle) between two links of a joint with multiple DOF to maximize the force-transmission of the mechanism [98] [99]. Lim et al. proposed a method to arrange wires between two links of a universal joint to maximize the volume of the joint workspace [100]. Agrawal et al., proposed a method to arrange wires in an upper arm exoskeleton, which have a spherical joint at the shoulder and a rovolute joint at the elbow, to minimize the number of output points where wire tensions are negative [101]. Bryson et al. proposed a method to arrange wires to a serial manipulator to generate the specified motion by minimizing wire tensions subjecting to the condition of positive wire tensions [102]. As another wire arrangement method, methods to mimic the musculoskeletal structure have been proposed. Asano et al. drove joints which mimic the human knee joint by mimicking the human tendon arrangements [103] [104]. Kurumaya et al. developed a lower-limb robot which mimics the human musculoskeletal structure with thin McKibben artificial muscles [105]. Russel et al. arranged wires to the joint which mimics the human knee joint so as to generate a similar motion to the actual human knee joint [106]. Assuming that tendon arrangements of creatures are optimized in nature, it is a reasonable way to drive biomimetic joints.

As described above, direct-drive can be applied to a wide variety of joints, and optimal wire arrangement is especially useful to design wire-driven joints with high performances. However, methods to optimally arrange wires to the unclosed higher pairs have not been proposed so far. In order to drive them, not only arranging wires to generate its complex relative motion but also keeping contact between the links is required. Therefore, a method to optimally arrange active elastic elements between the links of the unclosed kinematic pairs is proposed to obtain the ASRCP and the AFCP with high performances.

1.3   Structure of the dissertation

This dissertation is composed of six chapters as shown in Fig.1.8. The abstracts of from chapter 2 to chapter 6 are as follows.

Chapter 2: The Spatial Rolling Contact Pair

The spatial rolling contact pair (SRCP), which can generate the specified relative trajectory between two links, is developed to achieve the exact spatial-path generation. Firstly, a method to specify the relative rolling motion between two links is proposed. Next, the method to derive rolling contact surfaces between the links to generate the specified rolling motion is proposed. In addition, a hybrid elastic constraint composed of flexible bands and linear springs and its design method are proposed. The flexible bands are arranged on the rolling contact surfaces to suppress slippage between the links.

	Generation of a complex relative motion	Use of multiple DOF and elasticity between two links
Passive pair	Chapter 2: The Spatial Rolling Contact Pair	Chapter 4: The Flexibly Constrained Pair
Active pair	Chapter 3: The Active Spatial Rolling Contact Pair	Chapter 5: The Active Flexibly Constrained Pair
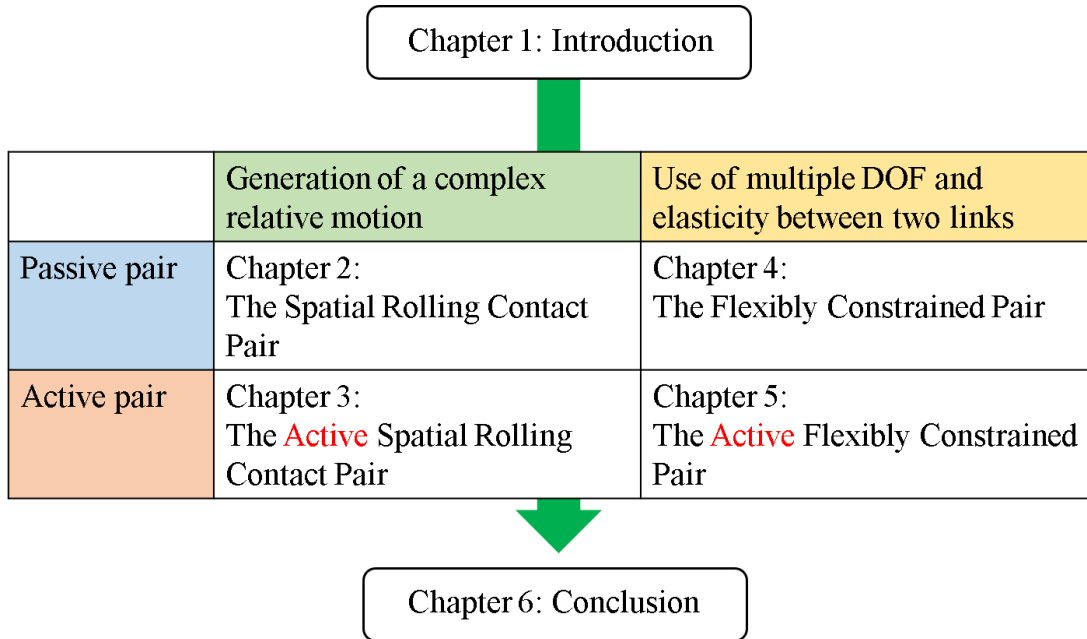
Fig.1.8   Structure of the dissertation

The linear springs are optimally arranged between the links to suppress separation and keep line contact between the links. As examples, spatial ECP-linkages with 1 DOF to generate the specified linear trajectory and the specified spatial trajectory are synthesized by using the SRCPs, and they are prototyped. Finally, performances of the designed elastic constraints and the possibility of the exact spatial-path generation with the SRCP are investigated by experiments of force measurement and motion capture.

Chapter 3: The Active Spatial Rolling Contact Pair

The active spatial rolling contact pair, which is driven by active elastic elements such as flexible linear actuators, is developed as an elastically closed active pair. Firstly, a design method to optimally arrange active elastic elements between the links based on a transmission index is proposed. Here, a method to use more than the minimum number of active elastic elements required to constitute force-closure state is described to design the ASRCP with sufficient motion range. Besides, a control method of the ASRCP to generate the ideal rolling motion is proposed, where actuation forces of active elastic elements to get high stability between the links are calculated with the use of the actuation redundancy. For examples, the ASRCP driven with reeled-wires and the ASRCP driven with fluid-driven artificial muscles are designed and prototyped. Then, they are controlled with the proposed method, and their performances are investigated through motion capture experiments.

Chapter 4: The Flexibly Constrained Pair

The flexibly constrained pair (FCP), which has flexible kinematic constraints due to the difference in stiffness, is developed. Firstly, a method to specify the relative motion between the links is proposed, where DOF between the links is divided into main-DOF

and sub-DOF and the main relative motion is specified. Next, a design method of the flexible constraint to achieve the specified difference in stiffness is proposed, where linear springs are optimally arranged to reduce stiffness in main-DOF and the specified stiffness are implemented in sub-DOF by designing the contact surfaces between the links. As examples, the FCP with 1-axial main rotation and the FCP with 3-axial main rotations and 1-axial main translation along the specified trajectory are designed and prototyped. Then, it is confirmed that they have the specified flexible constraints by some experiments. In addition, a simple flexible robotic mechanism (an underactuated ECP-linkage) is synthesized by using the FCPs, and it is fabricated. Finally, its performances are investigated by analysis of the output flexibility and by experiments of force measurement and motion capture.

Chapter 5: The Active Flexibly Constrained Pair

The active flexibly constrained pair (AFCP), which is driven by active elastic elements, is developed as an elastically closed active pair. This is an underactuated active kinematic pair antagonistically driven with one more active elastic element than the number of its main-DOF. As the active elastic elements for the AFCP, reeled elastic wires with linear elasticity are used to simplify its design and control. In order to design it, a method to optimally arrange reeled elastic wires between the links of such an underactuated joint based on a transmission index is described. Besides, a method to specify the stiffness required to perform the task in main-DOF (actuation DOF) and the stiffness to have both flexibility and motion accuracy in sub-DOF (passive DOF) is proposed. In addition, a method to analyze the kinetostatic motion between the links is proposed to evaluate the motion accuracy. As examples, the AFCP with 1-axial main rotation and the AFCP with 1-axial translation along the specified trajectory are designed and analyzed. Finally, they are prototyped, and their performances are examined by experiments.

Chapter 6: Conclusion

The achievements of this research are summarized. Then, future challenges of this research and prospects for new mechanical systems with the proposed kinematic pairs are described.

Chapter 2

The Spatial Rolling Contact Pair

2.1   Chapter introduction

Linkage mechanisms with 1 DOF are widely used in industries because of their simple structure and reliability. However, those linkages composed of only lower pairs cannot completely generate the specified output motion. This is because the output motion of a linkage is a combination of finite simple relative motions between two links which are allowed by lower pairs. Therefore, methods for kinematic synthesis to generate the approximate output motion have been proposed [1]-[33]. Methods to introduce a kind of higher pairs including cam pairs into mechanisms with 1 DOF have been proposed to generate exact output motions [69]-[79]. However, exact spatial-path generation has not been achieved with these methods. Although a spatial cam is sometimes used in a spatial mechanism to generate specified reciprocating motion of its follower [80], it is not used for exact path generation so far.

In this chapter, the "spatial rolling contact pair" (SRCP), which can generate the specified spatial trajectory between two links, is proposed to achieve exact spatial-path
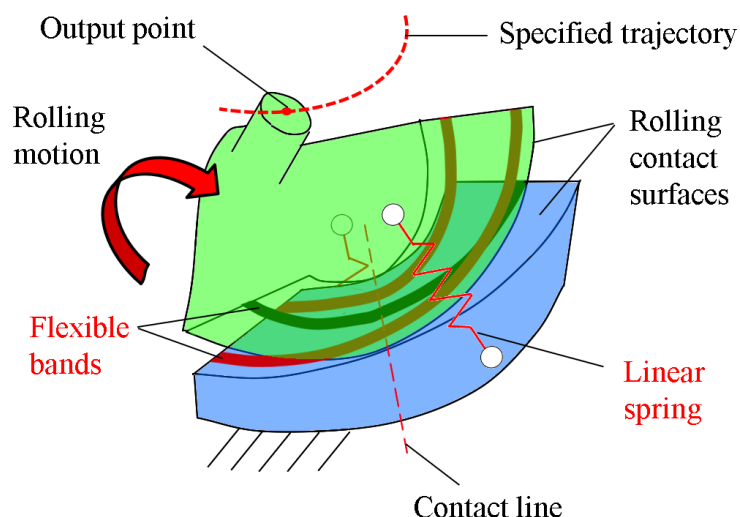
Fig.2.1   Structure of the spatial rolling contact pair (SRCP)

generation. The proposed structure of the SRCP is shown in Fig.2.1. When two links in contact at a line roll relatively, the output point on one of the two links passes through the specified spatial trajectory relative to another link. In order to generate the ideal relative rolling motion, the SRCP has a hybrid elastic constraint composed of flexible bands and linear springs between the links. The flexible bands are attached to suppress slippage between the links, and linear springs are arranged to suppress separation between the links. By using the SRCP, a spatial mechanism which can completely generate the specified spatial trajectory can be synthesized. This mechanism is expected to be used in some industrial applications such as a pick and place machine, in medical applications such as an exoskeleton for the human knee joint, and so on. In addition, since the SRCP has higher energy efficiency because of low friction between the links, it is expected to increase the mechanical performances of such machines.

This chapter describes the following three contributions to achieve the SRCP.

(1) Proposal and validation of a design method of rolling contact surfaces to generate the specified spatial trajectory
(2) Proposal and validation of a design method of the elastic constraint to keep ideal relative rolling motion between the links
(3) Prototyping and examination of spatial mechanisms with 1 DOF to generate the specified trajectory

In section 2.2, a design method of the rolling contact surfaces is proposed. In section 2.3, it is confirmed that the flexible bands can be applied to the rolling contact surfaces designed in section 2.2 by a mathematical approach, and their design method is described. In section 2.4, the method to arrange linear springs optimally to maximize the stability of the relative rolling motion between the links is proposed. In section 2.5, design examples of spatial-path generators with the SRCP are shown. Finally, in section 2.6, the validity of the proposed design method is confirmed through experiments with fabricated prototypes of the mechanisms designed in section 2.5.

2.2 Rolling contact surfaces

In this section, a design method of the rolling contact surfaces to generate the specified trajectory is proposed. At first, the relative rolling motion between the links is specified. Next, the rolling contact surfaces to generate the specified rolling motion is mathematically derived.

2.2.1 Specification of the relative rolling motion

When two links in contact at a line roll relatively in space, the relative velocity on the contact line is always zero. Thus, the contact line corresponds to the instantaneous screw axis of the relative motion, and the component of the relative velocity in the direction parallel to the contact line is zero. Therefore, when a trajectory ${}^1\boldsymbol{p}(t)$ is specified with a parameter t ($t_0 \leqq t \leqq t_1$) as shown in Fig.2.2, the following kinematic condition holds.

$$ {}^1\dot{\boldsymbol{p}}(t) \cdot {}^1\boldsymbol{\omega}(t) = 0, \tag{2.1} $$
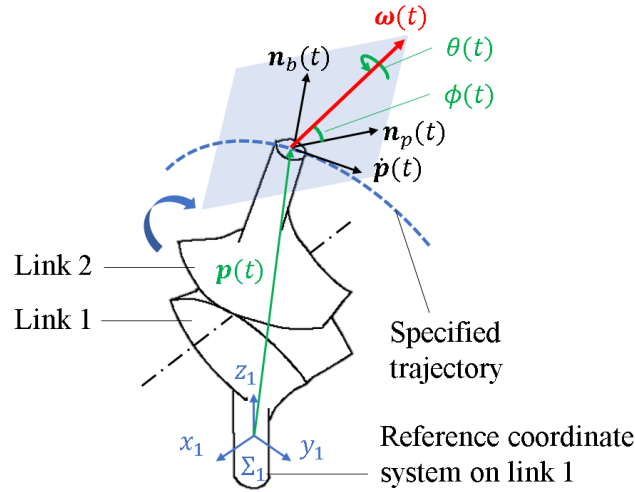
Fig.2.2   Specification of the relative rolling motion between the links to generate the specified trajectory

where $^1\boldsymbol{\omega}(t)$ is the angular velocity of the relative rolling motion and superscript 1 denotes that this parameter is on the reference coordinate system Σ_1, which is fixed on the link 1. When $^1\boldsymbol{\omega}(t)$ is specified to place on the plane spanned by the principal normal vector $^1\boldsymbol{n}_p(t)$ and the bi-normal vector $^1\boldsymbol{n}_b(t)$ of $^1\boldsymbol{p}(t)$ as shown in Fig.2.2, it satisfies Eq.(2.1). Thus, $^1\boldsymbol{\omega}(t)$ is specified with the following equation.

$$^1\boldsymbol{\omega}(t) = \dot{\theta}(t)[\cos\phi(t)\,^1\boldsymbol{n}_p(t) + \sin\phi(t)\,^1\boldsymbol{n}_b(t)], \tag{2.2}$$

where $\theta(t)$ is an angle around $^1\boldsymbol{\omega}(t)$ and $\phi(t)$ is an angle between $^1\boldsymbol{n}_p(t)$ and $^1\boldsymbol{\omega}(t)$. $^1\boldsymbol{n}_p(t)$ and $^1\boldsymbol{n}_b(t)$ can be calculated as follows.

$$^1\boldsymbol{n}_b(t) = \frac{^1\dot{\boldsymbol{p}}(t) \times \,^1\ddot{\boldsymbol{p}}(t)}{|^1\dot{\boldsymbol{p}}(t) \times \,^1\ddot{\boldsymbol{p}}(t)|}, \quad ^1\boldsymbol{n}_p(t) = \frac{^1\boldsymbol{n}_b(t) \times \,^1\dot{\boldsymbol{p}}(t)}{|^1\boldsymbol{n}_b(t) \times \,^1\dot{\boldsymbol{p}}(t)|} \tag{2.3}$$

Let Σ_2 be the reference coordinate system attached on the link 2. The rotation matrix $\boldsymbol{R}_{1,2}$, which represents the posture of link 2 on Σ_1, can be calculated by solving the following differential equation.

$$\dot{\boldsymbol{R}}_{1,2}(t) = [^1\boldsymbol{\omega}(t)\times]\boldsymbol{R}_{1,2}(t) \tag{2.4}$$

where $[^1\boldsymbol{\omega}(t)\times]$ is the matrix representing the vector product of $^1\boldsymbol{\omega}(t)$.

2.2.2   Design of rolling contact surfaces

Since a contact line of the two links in the SRCP corresponds to the instantaneous screw axis, the ruled surface generated by the axis, which is moved by changing parameter t, corresponds to the rolling contact surface. Based on this idea, rolling contact surfaces to generate the specified rolling motion is calculated. Fig.2.3 shows the schematic diagram
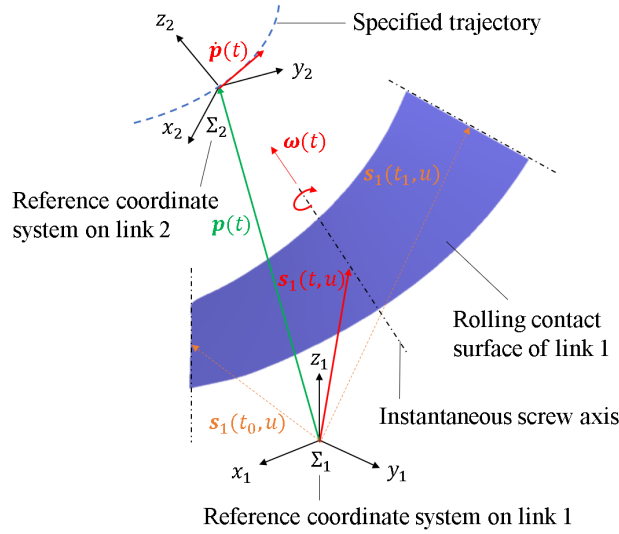
Fig.2.3   Calculation of the rolling contact surface to generate the specified rolling motion

for the calculation of the rolling contact surface. Since the velocity $^1\dot{\boldsymbol{p}}(t)$ is generated by only rotation around the instantaneous screw axis $^1\boldsymbol{s}_1$, the following equation holds.

$$[^1\boldsymbol{\omega}(t)\times][^1\boldsymbol{p}(t) - {}^1\boldsymbol{s}_1(t)] = {}^1\dot{\boldsymbol{p}}(t) \tag{2.5}$$

Therefore, the instantaneous screw axis $^1\boldsymbol{s}_1(t)$ can be represented as the following equation.

$$^1\boldsymbol{s}_1(t) = {}^1\boldsymbol{p}(t) - [^1\boldsymbol{\omega}(t)\times]^{\#}{}^1\dot{\boldsymbol{p}}(t) + u{}^1\hat{\boldsymbol{\omega}}(t), \tag{2.6}$$

where $[^1\boldsymbol{\omega}(t)\times]^{\#}$ is the pseudo inverse matrix of $[^1\boldsymbol{\omega}(t)\times]$, $^1\hat{\boldsymbol{\omega}}(t)$ is the unit directional vector of $^1\boldsymbol{\omega}(t)$, and u is an arbitrary real number. As described above, $^1\boldsymbol{s}_1(t, u)$ is the rolling contact surface of the link 1. On the other hand, the rolling contact surface of the link 2, $^2\boldsymbol{s}_2(t, u)$, can be represented as the following equation because the instantaneous screw axes of the two links coincide with each other at each value of t.

$$^2\boldsymbol{s}_2(t, u) = \boldsymbol{R}_{1,2}^T(t)[^1\boldsymbol{s}_1(t, u) - {}^1\boldsymbol{p}(t)] \tag{2.7}$$

Note that width of the rolling contact surfaces (actual length of the instantaneous screw axis) can be specified with the range of the parameter u: $u_0 \leqq u \leqq u_1$.

2.3   Constraint with flexible bands

In order to suppress slippage between two links of the SRCP, constraint with flexible bands is introduced between the links. This constraint method has been proposed in the context of rolling contact joints, whose purpose is to develop joint mechanisms with high energy efficiency. Kuntz (1995) described that the flexible bands can be used to keep connection two circular-shaped rolling contact surfaces [107], and some researchers have developed planar rolling contact joint with flexible bands [108] [109] [110] [111]. In terms
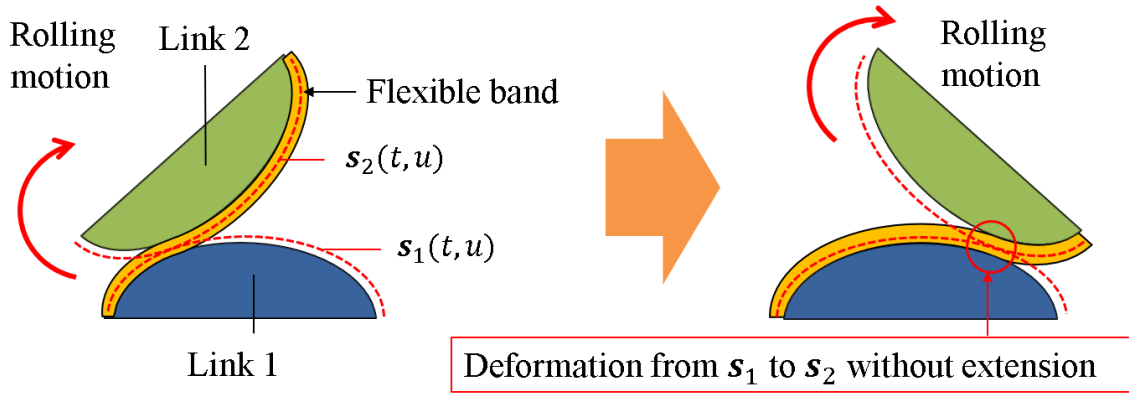
Fig.2.4   Deformation of a flexible band during the rolling motion

of spatial rolling contact joints, flexible bands have been applied to developable rolling contact surfaces, such as cylindrical surfaces, conical surfaces and tangent surfaces [112]. However, it has not been revealed that flexible bands can be applied to any other profiles of the rolling contact surfaces. Therefore, it is confirmed that the flexible bands can be applied to the proposed SRCP with a mathematical approach. Besides, a design method of flexible bands of which total bending moment always becomes zero around the contact line between the links is described.

2.3.1   Application of flexible bands to the SRCP

In order to confirm that the flexible bands fitting the rolling contact surface of the link 1 can be deformed to the surface of the link 2 without extension or contraction as shown in Fig.2.4, it should be confirmed that infinitesimal lengths on $^1\boldsymbol{s}_1(t,u)$ and $^2\boldsymbol{s}_2(t,u)$ are the same value at all of the values for (t,u). Note that thickness of the flexible band is assumed to be negligibly thin. An infinitesimal length on $^i\boldsymbol{s}_i(t,u)$ $(i=1,2)$ can be calculated as the following equation.

$$
\begin{aligned}
|d\ ^i\boldsymbol{s}_i(t,u)|^2 &= |\partial_t\ ^i\boldsymbol{s}_i(t,u)dt + \partial_u\ ^i\boldsymbol{s}_i(t,u)du|^2 \\
&= (\partial_t{}^i\boldsymbol{s}_i(t,u))^2(dt)^2 + 2\partial_t{}^i\boldsymbol{s}_i(t,u)\cdot\partial_u{}^i\boldsymbol{s}_i(t,u)dtdu + (\partial_u{}^i\boldsymbol{s}_i(t,u))^2(du)^2 \\
&\equiv A_{i,a}(dt)^2 + 2A_{i,b}dtdu + A_{i,c}(du)^2
\end{aligned}
\tag{2.8}
$$

, where ∂_t and ∂_u represents partial derivatives for t and u, respectively. By using Eq.(2.4), (2.6) and (2.7), $A_{2,a}$, $A_{2,b}$ and $A_{2,c}$ are transformed as follows. Note that $\boldsymbol{I}$ denotes an identity matrix.

$$
\begin{aligned}
&A_{2,a} \\
&= \partial_t{}^2\boldsymbol{s}_2(t,u)\cdot\partial_t{}^2\boldsymbol{s}_2(t,u) \\
&= [\partial_t\boldsymbol{R}_{1,2}^T(^1\boldsymbol{s}_1 - {}^1\boldsymbol{p}) + \boldsymbol{R}_{1,2}^T(\partial_t{}^1\boldsymbol{s}_1 - \partial_t{}^1\boldsymbol{p})]^T[\partial_t\boldsymbol{R}_{1,2}^T(^1\boldsymbol{s}_1 - {}^1\boldsymbol{p}) + \boldsymbol{R}_{1,2}^T(\partial_t{}^1\boldsymbol{s}_1 - \partial_t{}^1\boldsymbol{p})] \\
&\quad (\because \text{Eq.}(2.7)) \\
&= (^1\boldsymbol{s}_1^T - {}^1\boldsymbol{p}^T)\partial_t\boldsymbol{R}_{1,2}\partial_t\boldsymbol{R}_{1,2}^T(^1\boldsymbol{s}_1 - {}^1\boldsymbol{p}) + 2(\partial_t{}^1\boldsymbol{s}^T - \partial_t{}^1\boldsymbol{p}^T)\boldsymbol{R}_{1,2}\partial_t\boldsymbol{R}_{1,2}^T(^1\boldsymbol{s}_1 - {}^1\boldsymbol{p})
\end{aligned}
$$

$$+(\partial_t{}^1\boldsymbol{s}_1^T - \partial_t{}^1\boldsymbol{p}^T)\boldsymbol{R}_{1,2}\boldsymbol{R}_{1,2}^T(\partial_t{}^1\boldsymbol{s}_1 - \partial_t{}^1\boldsymbol{p})$$

$$= ({}^1\boldsymbol{s}_1^T - {}^1\boldsymbol{p}^T)[{}^1\boldsymbol{\omega}\times][{}^1\boldsymbol{\omega}\times]^T({}^1\boldsymbol{s}_1 - {}^1\boldsymbol{p}) + 2(\partial_t{}^1\boldsymbol{s}_1^T - \partial_t{}^1\boldsymbol{p}^T)[{}^1\boldsymbol{\omega}\times]^T({}^1\boldsymbol{s}_1 - {}^1\boldsymbol{p})$$

$$\quad +(\partial_t{}^1\boldsymbol{s}_1^T - \partial_t{}^1\boldsymbol{p}^T)(\partial_t{}^1\boldsymbol{s}_1 - \partial_t{}^1\boldsymbol{p}) \quad (\because \boldsymbol{R}_{1,2}\boldsymbol{R}_{1,2}^T = \boldsymbol{I},\ \text{Eq.}(2.4))$$

$$= [-\partial_t{}^1\boldsymbol{p}^T([{}^1\boldsymbol{\omega}\times]^{\#})^T + u{}^1\hat{\boldsymbol{\omega}}^T][{}^1\boldsymbol{\omega}\times][{}^1\boldsymbol{\omega}\times]^T(-[{}^1\boldsymbol{\omega}\times]^{\#}\partial_t{}^1\boldsymbol{p} + u{}^1\hat{\boldsymbol{\omega}})$$

$$\quad +2(\partial_t{}^1\boldsymbol{s}_1^T - \partial_t{}^1\boldsymbol{p}^T)[{}^1\boldsymbol{\omega}\times]^T(-[{}^1\boldsymbol{\omega}\times]^{\#}\partial_t{}^1\boldsymbol{p} + u{}^1\hat{\boldsymbol{\omega}})$$

$$\quad +(\partial_t{}^1\boldsymbol{s}_1^T - \partial_t{}^1\boldsymbol{p}^T)(\partial_t{}^1\boldsymbol{s}_1 - \partial_t{}^1\boldsymbol{p}) \quad (\because \text{Eq.}(2.6))$$

$$= [\partial_t{}^1\boldsymbol{p}^T([{}^1\boldsymbol{\omega}\times][{}^1\boldsymbol{\omega}\times]^{\#})^T - u([{}^1\boldsymbol{\omega}\times]{}^1\hat{\boldsymbol{\omega}})^T]([{}^1\boldsymbol{\omega}\times][{}^1\boldsymbol{\omega}\times]^{\#}\partial_t{}^1\boldsymbol{p} - u[{}^1\boldsymbol{\omega}\times]{}^1\hat{\boldsymbol{\omega}})$$

$$\quad +2(\partial_t{}^1\boldsymbol{s}_1^T - \partial_t{}^1\boldsymbol{p}^T)([{}^1\boldsymbol{\omega}\times][{}^1\boldsymbol{\omega}\times]^{\#}\partial_t{}^1\boldsymbol{p} - u[{}^1\boldsymbol{\omega}\times]{}^1\hat{\boldsymbol{\omega}})$$

$$\quad +(\partial_t{}^1\boldsymbol{s}_1^T - \partial_t{}^1\boldsymbol{p}^T)(\partial_t{}^1\boldsymbol{s}_1 - \partial_t{}^1\boldsymbol{p}) \quad (\because [{}^1\boldsymbol{\omega}\times]^T = -[{}^1\boldsymbol{\omega}\times])$$

$$= \partial_t{}^1\boldsymbol{p}^T\partial_t{}^1\boldsymbol{p} + 2(\partial_t{}^1\boldsymbol{s}_1^T - \partial_t{}^1\boldsymbol{p}^T)\partial_t{}^1\boldsymbol{p} + (\partial_t{}^1\boldsymbol{s}_1^T - \partial_t{}^1\boldsymbol{p}^T)(\partial_t{}^1\boldsymbol{s}_1 - \partial_t{}^1\boldsymbol{p})$$

$$\quad (\because [{}^1\boldsymbol{\omega}\times][{}^1\boldsymbol{\omega}\times]^{\#} = \boldsymbol{I},\ [{}^1\boldsymbol{\omega}\times]{}^1\hat{\boldsymbol{\omega}} = \boldsymbol{0})$$

$$= \partial_t{}^1\boldsymbol{s}_1^T\partial_t{}^1\boldsymbol{s}_1 = A_{1,a}, \tag{2.9}$$

$$A_{2,b}$$

$$= \partial_t{}^2\boldsymbol{s}_2(t,u)\cdot\partial_u{}^2\boldsymbol{s}_2(t,u)$$

$$= [({}^1\boldsymbol{s}_1^T - {}^1\boldsymbol{p}^T)\partial_t\boldsymbol{R}_{1,2} + (\partial_t{}^1\boldsymbol{s}_1^T - \partial_t{}^1\boldsymbol{p}^T)\boldsymbol{R}_{1,2}](\boldsymbol{R}_{1,2}^T\partial_u{}^1\boldsymbol{s}_1) \quad (\because \text{Eq.}(2.7))$$

$$= ({}^1\boldsymbol{s}_1^T - {}^1\boldsymbol{p}^T)\partial_t\boldsymbol{R}_{1,2}\boldsymbol{R}_{1,2}^T\partial_u{}^1\boldsymbol{s}_1 + (\partial_t{}^1\boldsymbol{s}_1^T - \partial_t{}^1\boldsymbol{p}^T)\partial_u{}^1\boldsymbol{s}_1 \quad (\because \boldsymbol{R}_{1,2}\boldsymbol{R}_{1,2}^T = \boldsymbol{I})$$

$$= [-\partial_t{}^1\boldsymbol{p}^T([{}^1\boldsymbol{\omega}\times]^{\#})^T + u{}^1\hat{\boldsymbol{\omega}}][{}^1\boldsymbol{\omega}\times]\partial_u{}^1\boldsymbol{s}_1 + (\partial_t{}^1\boldsymbol{s}_1^T - \partial_t{}^1\boldsymbol{p}^T)\partial_u{}^1\boldsymbol{s}_1 \quad (\because \text{Eq.}(2.6))$$

$$= \partial_t{}^1\boldsymbol{s}_1^T\partial_u{}^1\boldsymbol{s}_1 = A_{1,b} \quad (\because [{}^1\boldsymbol{\omega}\times][{}^1\boldsymbol{\omega}\times]^{\#} = \boldsymbol{I},\ [{}^1\boldsymbol{\omega}\times]{}^1\hat{\boldsymbol{\omega}} = \boldsymbol{0}) \tag{2.10}$$

$$A_{2,c}$$

$$= \partial_u{}^2\boldsymbol{s}_2(t,u)\cdot\partial_u{}^2\boldsymbol{s}_2(t,u)$$

$$= \partial_u{}^1\boldsymbol{s}_1^T\boldsymbol{R}_{1,2}\boldsymbol{R}_{1,2}^T\partial_u{}^1\boldsymbol{s}_1 \quad (\because \text{Eq.}(2.7))$$

$$= \partial_u{}^1\boldsymbol{s}_1^T\partial_u{}^1\boldsymbol{s}_1 = A_{1,c} \quad (\because \boldsymbol{R}_{1,2}\boldsymbol{R}_{1,2}^T = \boldsymbol{I}) \tag{2.11}$$

Thus, $|d\,{}^1\boldsymbol{s}_1| = |d\,{}^2\boldsymbol{s}_2|$ holds for all values of (t,u), that is, a thin flexible band fitting the rolling contact surface on the link 1 can be deformed to the surface on the link 2 without extension or contraction. Therefore, constraint with flexible bands are applicable to the proposed SRCP, even if it has non-developable rolling contact surfaces.

2.3.2 Design of flexible bands

Statics model of flexible bands attached to developable rolling contact surfaces has been proposed by Nelson and Herder [112]. They have proposed the concept to design the flexible bands which can generate zero torque around the contact line in their rolling contact joint based on their statics model. This idea is applied to the proposed SRCP. In this method, widths of flexible bands are calculated so that flexible bands generate zero bending moment around the contact line. The schematic diagram for designing flexible bands is shown in Fig.2.5. Here, it is assumed that the neutral surfaces of flexible bands
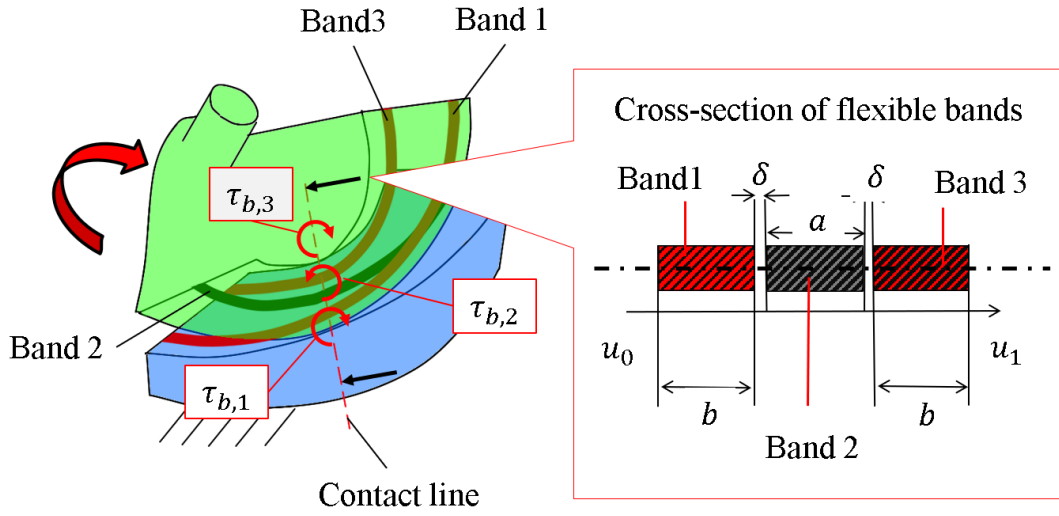
Fig.2.5   Schematic diagram for designing flexible bands based on statics

in the natural shape are on the rolling contact surface of the link 1 and they deform to fit the surface of the link 2. In addition, the thickness of flexible bands h is assumed as constant for (t, u). When the total bending moment around the contact line is always zero, the following statics equation holds for all values of t.

$$\tau_{b,2}(t) - \tau_{b,1}(t) - \tau_{b,3}(t) = 0, \tag{2.12}$$

where $\tau_{b,i}$ is bending moment of the i-th flexible band about the contact line. On the cross-section of the flexible bands through contact line, it is assumed that widths of the band 1 and the band 3 are same value b, and gap between adjacent flexible bands is the same value δ. Then, b is represented as the following equation with width of the band 2, a.

$$b = \frac{(u_1 - u_0) - a}{2} - \delta, \tag{2.13}$$

where u_0 and u_1 are minimum and maximum values of u specified in section 2.2. Then, $\tau_{b,1}$, $\tau_{b,2}$ and $\tau_{b,3}$ can be calculated as follows.

$$\tau_{b,1}(a,t) = \frac{Eh^3}{12} \int_{u_0}^{u_0+b(a)} [\kappa_{n,2}(t, u) - \kappa_{n,1}(t, u)] du, \tag{2.14}$$

$$\tau_{b,2}(a,t) = \frac{Eh^3}{12} \int_{u_0+b(a)+\delta}^{u_1-b(a)-\delta} [\kappa_{n,2}(t, u) - \kappa_{n,1}(t, u)] du, \tag{2.15}$$

$$\tau_{b,3}(a,t) = \frac{Eh^3}{12} \int_{u_1-b(a)}^{u_1} [\kappa_{n,2}(t, u) - \kappa_{n,1}(t, u)] du, \tag{2.16}$$

where E is Young's modulus of the bands. $\kappa_{n,2}(t, u)$ is normal curvature of the deformed shape, $\boldsymbol{s}_2(t, u)$, in the tangential direction, $\partial_t \boldsymbol{s}_2$. $\kappa_{n,1}(t, u)$ is normal curvature of the

natural shape, $\boldsymbol{s}_1(t,u)$, in the tangent direction, $\partial_t \boldsymbol{s}_1$. In general, normal curvature of a surface $\boldsymbol{s}_i(t,u)$ at a point (t,u) in the tangential direction $\boldsymbol{v}_i = \alpha \partial_t \boldsymbol{s}_i + \beta \partial_u \boldsymbol{s}_i$ can be calculated with the following equation [113].

$$\kappa_{n,i} = \frac{(\partial_{tt}{}^i\boldsymbol{s}_i^{T\,i}\hat{\boldsymbol{n}}_i)\alpha^2 + 2(\partial_{tu}{}^i\boldsymbol{s}_i^{T\,i}\hat{\boldsymbol{n}}_i)\alpha\beta + (\partial_{uu}{}^i\boldsymbol{s}_i^{T\,i}\hat{\boldsymbol{n}}_i)\beta^2}{(\partial_t{}^i\boldsymbol{s}_i^T)(\partial_t{}^i\boldsymbol{s}_i)\alpha^2 + 2(\partial_t{}^i\boldsymbol{s}_i^T)(\partial_u{}^i\boldsymbol{s}_i)\alpha\beta + (\partial_u{}^i\boldsymbol{s}_i^T)(\partial_u{}^i\boldsymbol{s}_i)\beta^2}, \tag{2.17}$$

where ${}^i\hat{\boldsymbol{n}}_i$ is the unit normal vector of ${}^i\boldsymbol{s}_i$. In this case, since $\alpha = 1$ and $\beta = 0$, $\kappa_{n,i}$ can be calculated as follows.

$$\kappa_{n,i} = \frac{\partial_{tt}{}^i\boldsymbol{s}_i}{|\partial_t{}^i\boldsymbol{s}_i|^2} \cdot \frac{\partial_t{}^i\boldsymbol{s}_i \times \partial_u{}^i\boldsymbol{s}_i}{|\partial_t{}^i\boldsymbol{s}_i \times \partial_u{}^i\boldsymbol{s}_i|} \tag{2.18}$$

By solving the simultaneous equations in Eqs.(2.12)-(2.18) for a, each width of the flexible band can be calculated.

2.4   Constraint with linear elastic elements

If two rolling contact surfaces have convex shapes, even just constraint with flexible bands is enough. However, if one of the two surfaces has a concave shape, the only constraint with flexible bands is not enough because separation between the links may occur as shown in Fig.2.6. In order to suppress the separation, constraint with linear springs is introduced as shown in Fig.2.1. In addition, the linear springs are optimally arranged so that their elastic forces effectively apply to the contact line to generate the ideal rolling motion.
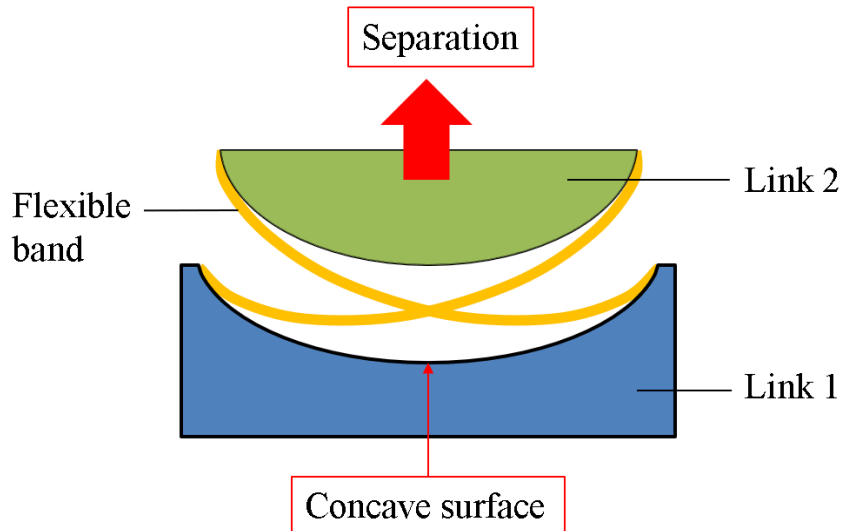
Fig.2.6   Separation between two links of the SRCP when a link has a concave rolling contact surface

External Force

Link 2

z_q

y_q

Σ_q

Q

x_q

Link 1

Contact line

Surface on link 1
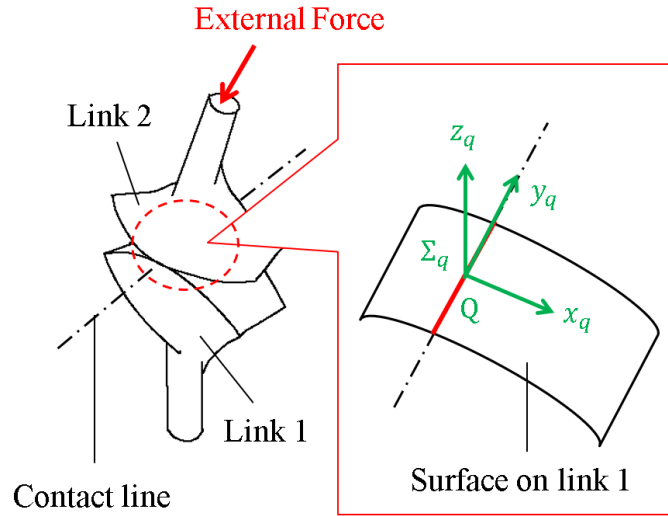
Fig.2.7   Local frame Σ_q defined on the rolling contact surface of the SRCP

2.4.1   Formulation of the optimal design

In order to evaluate performances of the rolling motion, two criteria are proposed. One of the criteria evaluates whether both slippage and separation between the two links in the SRCP occur. Another criterion evaluates whether the two links can keep in contact at a line between the links. These criteria are implemented into the objective function for the optimal arrangement of linear springs.

Fig.2.7 shows the reference coordinate system Σ_q, whose origin Q is at the center position of the contact line ($u_c = \frac{u_0+u_1}{2}$) between the links, and coordinate-axes coincide to the contact line and the normal line at point Q. On Σ_q, let sum of external forces including elastic forces of linear springs be represented as $[{}^q\boldsymbol{f}_{e,q}^T \ {}^q\boldsymbol{\tau}_{e,q}^T]^T = [f_{q,x} \ f_{q,y} \ f_{q,z} \ \tau_{q,x} \ \tau_{q,y} \ \tau_{q,z}]^T$. Then, the criterion of slippage and separation is represented as the following equation.

$$\mu_q = -\frac{\sqrt{f_{q,x}^2 + f_{q,y}^2}}{f_{q,z}} \tag{2.19}$$

Let the coefficient of static friction between the two rolling contact surfaces be μ_0. If $0 \leqq \mu_q \leqq \mu_s$, the two links do not slip relatively. Note that the slippage between the links can be suppressed by the flexible bands. However, a large value of μ_q leads to the large stress in the flexible bands. Thus, this criterion has to be minimized in order to suppress extra load applied to the flexible bands.

Even just using this criterion is not enough because unintentional relative rolling (rotation) between the two links occurs on an edge of the contact segment between the links. This means that the two links cannot keep in contact at a line. In order to evaluate the unintentional relative rolling, zero moment point (ZMP) between the links has been proposed as another criterion. ZMP [114] is generally used to evaluate the stability of walking robots. This is applied to evaluate the stability of rolling motion between two
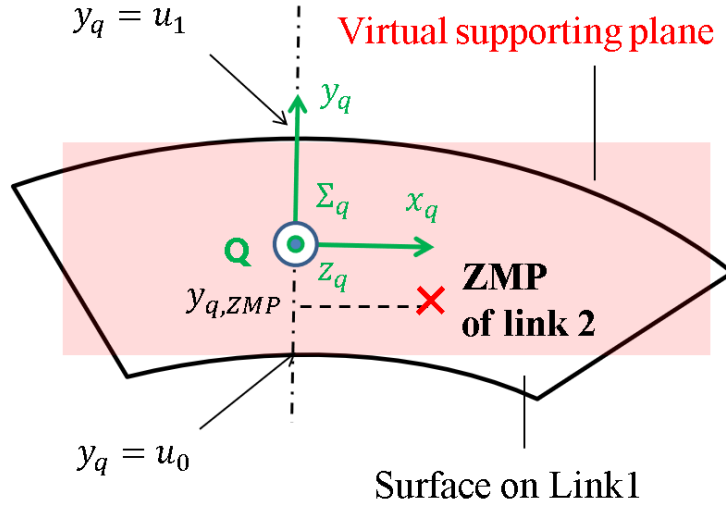
Fig.2.8 Zero moment point (ZMP) on the virtual supporting plane defined between two links of the SRCP

links of the SRCP. Fig.2.8 shows the schematic diagram on ZMP between the links. The virtual supporting plane for ZMP is defined on $x_q - y_q$ plane on Σ_q, where width of this plane is limited with $u_0 \leqq u \leqq u_1$. If ZMP of the link 2 is on this plane, the link 2 can roll about the contact line. In contrast, if the ZMP is out of this plane, the link 2 rolls (rotates) on a point at $y_q = u_0$ or $y_q = u_1$ on the contact line. The y_q component of ZMP on Σ_q can be calculated with the following equation [115].

$$y_{q,ZMP} = \frac{{}^q\boldsymbol{e}_{q,y}^T({}^q\boldsymbol{e}_{q,z} \times {}^q\boldsymbol{\tau}_{e,q})}{{}^q\boldsymbol{e}_{q,z}^T \, {}^q\boldsymbol{f}_{e,q}}, \qquad (2.20)$$

where ${}^q\boldsymbol{e}_{q,y}$ and ${}^q\boldsymbol{e}_{q,z}$ are unit vectors $[0\ 1\ 0]^T$, $[0\ 0\ 1]^T$ on Σ_q, respectively. If $u_0 \leqq y_{q,ZMP} \leqq u_1$ holds, the unintentional relative rolling does not occur. Therefore, $|u_c - y_{q,ZMP}|$ has to be minimized in order to suppress the unintentional rolling.

Eqs.(2.19) and (2.20) show that the criteria μ_q and $y_{q,ZMP}$ become small when $f_{q,z}$ is large. This means that the magnitude of the elastic forces by linear springs increase if the criteria are minimized. If the magnitude of the elastic forces becomes large, $\tau_{q,y}$, which can be resistance torque on the specified rolling motion, also becomes large. Therefore, the mean potential energy U_p of linear springs also has to be minimized in this optimization. Let the position where endpoint of the i-th spring is attached on the link 1 be ${}^1\boldsymbol{c}_{1,i}$ on Σ_1 and the position of the other side attached on the link 2 be ${}^2\boldsymbol{c}_{2,i}$ on Σ_2 as shown in Fig.2.9. Then, mean potential energy U_p of all linear springs can be calculated with the following equations.

$$^1\boldsymbol{d}_{s,i}(t) = [\boldsymbol{R}_{1,2}(t)^2\boldsymbol{c}_{2,i} + {}^1\boldsymbol{p}(t)] - {}^1\boldsymbol{c}_{1,i}, \qquad (2.21)$$

$$U_p(t) = \frac{1}{N_s}\sum_{i=1}^{N_s}[\frac{k_i}{2}(|^1\boldsymbol{d}_{s,i}(t)| - l_{0,i})^2 + f_{s,0,i}(|^1\boldsymbol{d}_{s,i}(t)| - l_{0,i})], \qquad (2.22)$$
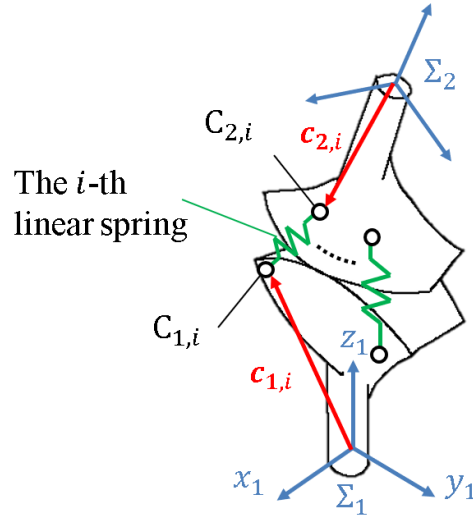
Fig.2.9   Linear springs arranged between two links of the SRCP

where N_s is the number of linear springs, k_i is the spring constant, $l_{0,i}$ is natural length of springs. In these equations, initial tension of springs $f_{s,0,i}$ is included because actual extension coil springs have initial tension to tighten their coil.

Let the design parameters be endpoint positions of linear springs $\boldsymbol{c} = [{}^1\boldsymbol{c}_{1,1}^T, ..., {}^1\boldsymbol{c}_{1,N_a}^T,$ ${}^2\boldsymbol{c}_{2,1}^T, ..., {}^2\boldsymbol{c}_{2,N_a}^T]^T$. Then, the objective function can be formulated as

$$F(\boldsymbol{c}) = \max\{w_1 F_1(\boldsymbol{c}), \ w_2 F_2(\boldsymbol{c}), \ w_3 F_3(\boldsymbol{c})\}, \tag{2.23}$$

where w_1, w_2 and w_3 are weight parameters, and where $F_1(\boldsymbol{c})$, $F_2(\boldsymbol{c})$ and $F_3(\boldsymbol{c})$ are represented as follows by using Eqs.(2.19)-(2.22).

$$F_1(\boldsymbol{c}) = \frac{1}{t_1 - t_0} \int_{t_0}^{t_1} \mu_q(t, \boldsymbol{c})^2 dt \tag{2.24}$$

$$F_2(\boldsymbol{c}) = \frac{1}{t_1 - t_0} \int_{t_0}^{t_1} [u_c - y_{q,ZMP}(t, \boldsymbol{c})]^2 dt \tag{2.25}$$

$$F_3(\boldsymbol{c}) = \frac{1}{t_1 - t_0} \int_{t_0}^{t_1} U_p(t, \boldsymbol{c}) dt \tag{2.26}$$

Eq,(2.23) is minimized for $\boldsymbol{c}$ subjecting to the following constraint conditions.

$${}^j\boldsymbol{c}_{j,i,min} \leqq {}^j\boldsymbol{c}_{j,i} \leqq {}^j\boldsymbol{c}_{j,i,max} \quad ({}^j\boldsymbol{c}_{j,i,min}, {}^j\boldsymbol{c}_{j,i,max} : \text{Size limitation}), \tag{2.27}$$

$$\frac{1}{t_1 - t_0} \int_{t_0}^{t_1} f_{q,z}(t, \boldsymbol{c}) dt \geqq f_{q,z,req} \quad (f_{q,z,req} : \text{Required contact force}), \tag{2.28}$$

$$l_{0,i} \leqq |{}^1\boldsymbol{d}_{s,i}(t, \boldsymbol{c})| \leqq l_{max,i} \quad (\leqq l_{max,i} : \text{Maximum length of linear springs}), \tag{2.29}$$

where $j = 1, 2$ and $i = 1, ..., N_s$. Eq.(2.27) represents a design space with a rectangular parallelepiped shape on Σ_j, where ${}^j\boldsymbol{c}_{j,i,min}$ and ${}^j\boldsymbol{c}_{j,i,max}$ are its diagonal positions. However, it is not useful specify the design space with this representation because the shape
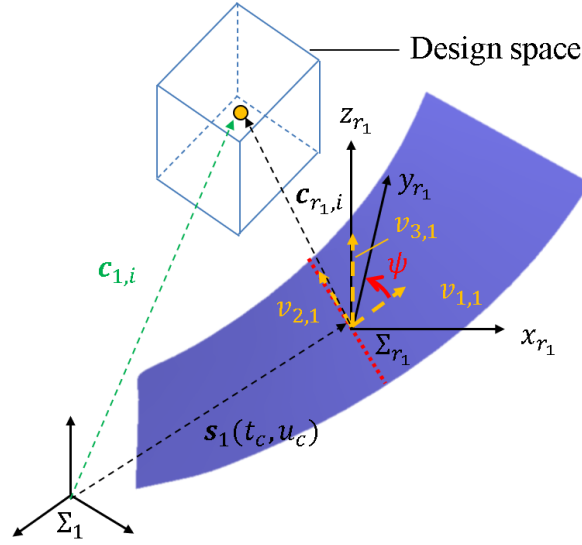
Fig.2.10   Design space of endpoints of linear springs

of each rolling contact surface is possible to be complex. Therefore, the design space is specified according to the rolling contact surfaces. Fig.2.10 shows local coordinate system, Σ_{r_j}, whose origin is ${}^j\boldsymbol{s}_j(t_c, u_c)$ $(j = 1, 2)$ and basis are as follows.

$$
{}^j\boldsymbol{e}_{r_j,x} = \frac{-{}^j\boldsymbol{v}_{1,j}\sin\psi + {}^j\boldsymbol{v}_{2,j}\cos\psi}{|-{}^j\boldsymbol{v}_{1,j}\sin\psi + {}^j\boldsymbol{v}_{2,j}\cos\psi|}, \tag{2.30}
$$

$$
{}^j\boldsymbol{e}_{r_j,y} = \frac{{}^j\boldsymbol{v}_{1,j}\cos\psi + {}^j\boldsymbol{v}_{2,j}\sin\psi}{|{}^j\boldsymbol{v}_{1,j}\cos\psi + {}^j\boldsymbol{v}_{2,j}\sin\psi|}, \tag{2.31}
$$

$$
{}^j\boldsymbol{e}_{r_j,z} = \frac{{}^j\boldsymbol{v}_{3,j}}{|{}^j\boldsymbol{v}_{3,j}|}, \tag{2.32}
$$

where

$$
{}^j\boldsymbol{v}_{2,j} = \partial_u {}^j\boldsymbol{s}_j(t_c, u_c), \quad {}^j\boldsymbol{v}_{3,j} = \partial_t {}^j\boldsymbol{s}_j(t_c, u_c) \times {}^j\boldsymbol{v}_{2,j}, \quad {}^j\boldsymbol{v}_{j,1} = {}^j\boldsymbol{v}_{2,j} \times {}^j\boldsymbol{v}_{3,j}. \tag{2.33}
$$

Let ${}^j\boldsymbol{c}_{j,i}$ on Σ_{r_j} be ${}^{r_j}\boldsymbol{c}_{r_j,i}$. Then, the limitation can be represented as follows;

$$
\begin{aligned}
&{}^j\boldsymbol{c}_{j,i} \quad ({}^j\boldsymbol{c}_{j,i,min} \leqq {}^j\boldsymbol{c}_{j,i} \leqq {}^j\boldsymbol{c}_{j,i,max}) \\
&\Leftrightarrow {}^j\boldsymbol{c}_{j,i} = [{}^j\boldsymbol{e}_{r_j,x} \; {}^j\boldsymbol{e}_{r_j,y} \; {}^j\boldsymbol{e}_{r_j,z}]^{r_j}\boldsymbol{c}_{r_j,i} + {}^j\boldsymbol{s}_j(t_c, u_c) \\
&({}^{r_j}\boldsymbol{c}_{r_j,i,min} \leqq {}^{r_j}\boldsymbol{c}_{r_j,i} \leqq {}^{r_j}\boldsymbol{c}_{r_j,i,max}),
\end{aligned} \tag{2.34}
$$

These limitations (design space) also have a rectangular parallelepiped shape as shown in Fig.2.10.

2.4.2   A solution for the optimization

The formulated optimization problem can be solved with various techniques. However, the computational complexity should be low in order to design the SRCP quickly. There-

fore, a technique to solve the problem with low computational complexity is introduced.

The objective function of Eq.(2.23) is the discontinuous function. Thus, the gradient method cannot be used to solve the optimization problem. However, using gradient based methods is desirable because metaheuristic optimization methods lead to long calculation time to obtain the solution. Therefore, the problem to minimize Eq.(2.23) is transformed into the following problem with a slack variable ϵ.

$$\text{minimize } \epsilon, \tag{2.35}$$

$$\text{subject to } F_1(\boldsymbol{c}'),\ F_2(\boldsymbol{c}'),\ F_3(\boldsymbol{c}') \leqq \epsilon,\ \boldsymbol{c}'_{min} \leqq \boldsymbol{c}' \leqq \boldsymbol{c}'_{max} \tag{2.36}$$

where $\boldsymbol{c}' = [{}^1\boldsymbol{c}_{1,1}^T...{}^1\boldsymbol{c}_{1,N_s}^T...{}^2\boldsymbol{c}_{2,1}^T...{}^2\boldsymbol{c}_{2,N_s}^T\ \epsilon]^T$. Since the objective function of Eq.(2.35) is the continuous function, gradient methods can be solved to solve the problem. Note that gradient methods lead to a local minimum. Thus, the original objective function $g(\boldsymbol{c}')$ is calculated for some randomly generated values of $\boldsymbol{c}'$ in the design space, and the minimum value of them is selected as an initial value of the optimization.

In addition, since some integrals have to be calculated in Eqs.(2.24)-(2.26), the calculation in each step in the optimization is complex. Therefore, Gauss-Legendre quadrature [117] is used. This method can calculate integrals accurately with a small number of sampling points. Thus, the calculation complexity can be reduced.

The constraint about spring length in Eq.(2.29) includes the variable t. Thus, the number of constraints tends to be large depending on the sampling of t. Therefore, the constraint in Eq.(2.29) is included in the objective function by replacing k in Eq.(2.22) with the following variable $k_i'(t)$.

$$k_i'(t) = k_i + \alpha[\max\{0, l_{0,i} - |{}^1\boldsymbol{d}_{s,i}(t)|\}^{2\beta} + \max\{0, |{}^1\boldsymbol{d}_{s,i}(t)| - l_{max,i}\}^{2\beta}], \tag{2.37}$$

where α is a large positive real value and β is a natural number. Since the objective function is calculated with a small sampling points of t, the calculation complexity can be reduced.

2.5   Design examples

By using the proposed design method of the SRCP, two examples of spatial-path generators with the SRCP were designed. The first examples is an open-loop 2-bar mechanism with the single SRCP to generate a planar trajectory. The second example is a closed-loop 4-bar mechanism with the single SRCP to generate a spatial trajectory. In this section, the procedure and the result of each design are described.

2.5.1   Example 1: An open-loop 2-bar mechanism with the SRCP to generate a linear trajectory

For a simple example, an open-loop mechanism which has two links connected with the single SRCP was designed. The specified trajectory was the linear trajectory represented as the following equation.

$$^1\boldsymbol{p}(t) = \begin{bmatrix} 100t - 50 & 0 & 100 \end{bmatrix}^T \quad (0 \leqq t \leqq 1), \tag{2.38}$$
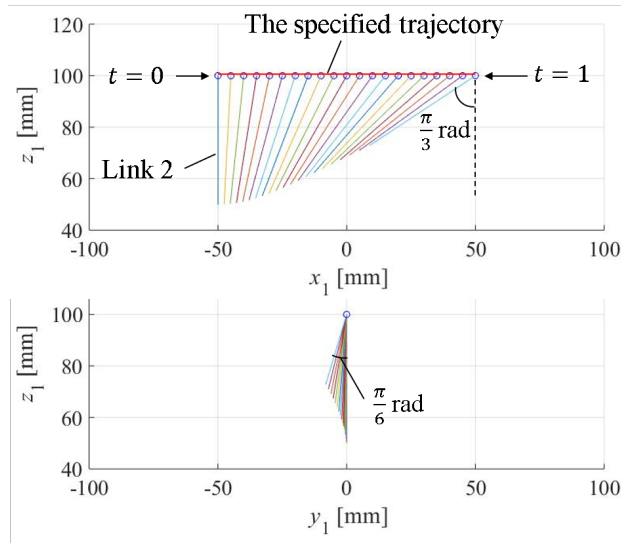
Fig.2.11   The specified rolling motion along the linear trajectory on Σ_1

(a) $\boldsymbol{s}_1(t,u)$ on Σ_1

(b) $\boldsymbol{s}_2(t,u)$ on Σ_2
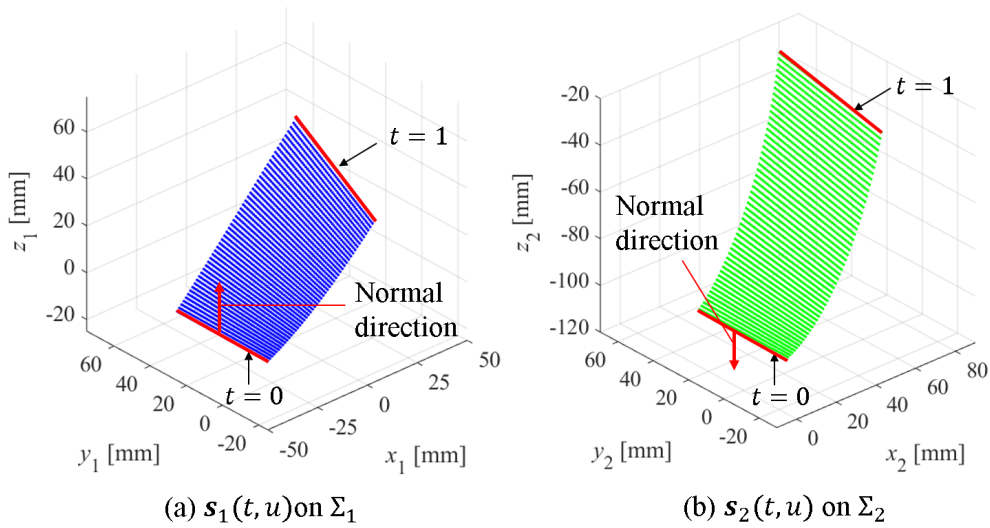
Fig.2.12   The designed rolling contact surfaces of the SRCP in example 1

where the unit is mm. Parameters of the angular velocity in Eq.(2.2) were specified as $\theta(t) = \frac{\pi t}{3}$ [rad], $\phi(t) = \frac{\pi t}{6}$ [rad]. The specified rolling motion of the link 2 on Σ_1 is shown in Fig.2.11. The posture angle changed by $\frac{\pi}{3}$ rad in the parallel direction to the rolling motion because of the specified $\theta(t)$ and by $\frac{\pi}{6}$ rad in the vertical direction to the rolling motion because of the specified $\phi(t)$. Note that the vector $^1\boldsymbol{n}_b(t)$ was specified as $^1\boldsymbol{n}_b(t) = [0\ 0\ 1]^T$ because the vector $^1\boldsymbol{n}_b(t)$ cannot be calculated with the linear trajectory. Rolling contact surfaces to generate the specified rolling motion were calculated with Eqs.(2.6) and (2.7), where the range of u was specified as $-25 \leqq u \leqq 25$ [mm]. The calculated surfaces are shown in Fig.2.12. The surface on the link 1 on Σ_1 is shown in the figure (a) and the surface on the link 2 on Σ_2 is shown in the figure (b). The two surfaces are in contact on
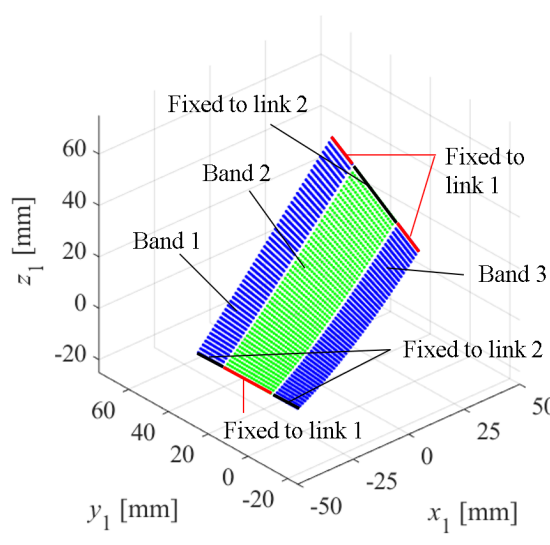
Fig.2.13   The designed flexible bands of the SRCP in example 1 in the natural state

Table 2.1   Parameters for the optimal arrangement of linear springs in example 1

$k_1 = k_2 = 0.028$ N/mm	$\psi = -\frac{\pi}{3}$ rad
$l_{0,1} = l_{0,2} = 35.1$ mm	$[-40 \ 40 \ -40] \leqq {}^{r_1}\boldsymbol{c}_{r_1,1}^T \leqq [40 \ 70 \ -10]$
$l_{max,1} = l_{max,2} = 124.1$ mm	$[-40 \ -65 \ -40] \leqq {}^{r_1}\boldsymbol{c}_{r_1,2}^T \leqq [40 \ -35 \ -10]$
$f_{s,0,1} = f_{s,0,2} = 0.412$ N	$[-40 \ 40 \ 25] \leqq {}^{r_2}\boldsymbol{c}_{r_2,1}^T \leqq [40 \ 70 \ 60]$
$(w_1, w_2, w_3) = (1, 1, 1)$	$[-40 \ -70 \ 25] \leqq {}^{r_2}\boldsymbol{c}_{r_2,2}^T \leqq [40 \ -40 \ 60]$
$f_{q,z,req} = 2$ N	(Unit: mm)

each contact line at each point represented with t.

Next, the flexible bands were designed with the method described in section 2.3. The gap between adjacent bands was specified as $\delta = 2$ mm. Note that the thickness of bands h and Young's modulus E do not have to be specified in this process because they are deleted in the statics equation of Eq.(2.12). The width of flexible bands at each point t was calculated by solving Eq.(2.12) with the bisection method at each point t. Since the calculated width at each point t was always $b = 11.51$ mm, $a = 22.97$ mm ($b : a \simeq 1 : 2$), the result is intuitively valid. The natural shape of the flexible bands was assumed to adjust to the rolling contact surface of the link 1 shown in Fig.2.12 (a). Then, intermediate surfaces of flexible bands in the natural state were obtained as shown in Fig.2.13.

Finally, linear springs were optimally arranged between the two links with the method described in section 2.4. According to the idea of the "force closure," which is considered in the context of parallel wire-driven mechanisms and so on, at least seven independent translation forces are required to constrain an object in space [116]. In the SRCP, it can be considered that there are two normal forces and three tangential forces on the contact line between the links. Thus, the links are constrained with two linear springs.
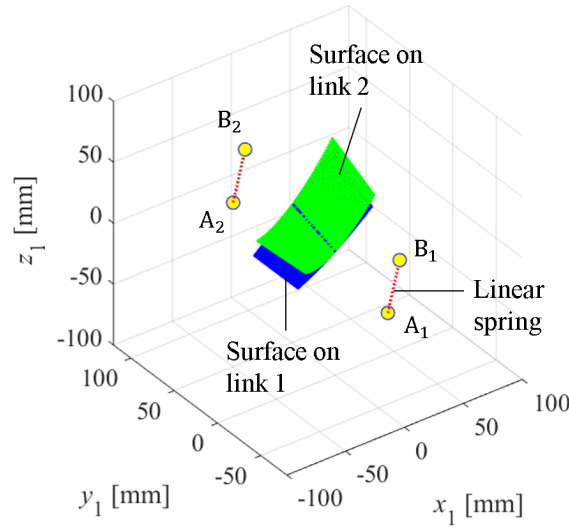
Fig.2.14   The designed SRCP with optimally arranged linear springs in example 1

(a) μ_q (b) $y_{q,ZMP}$
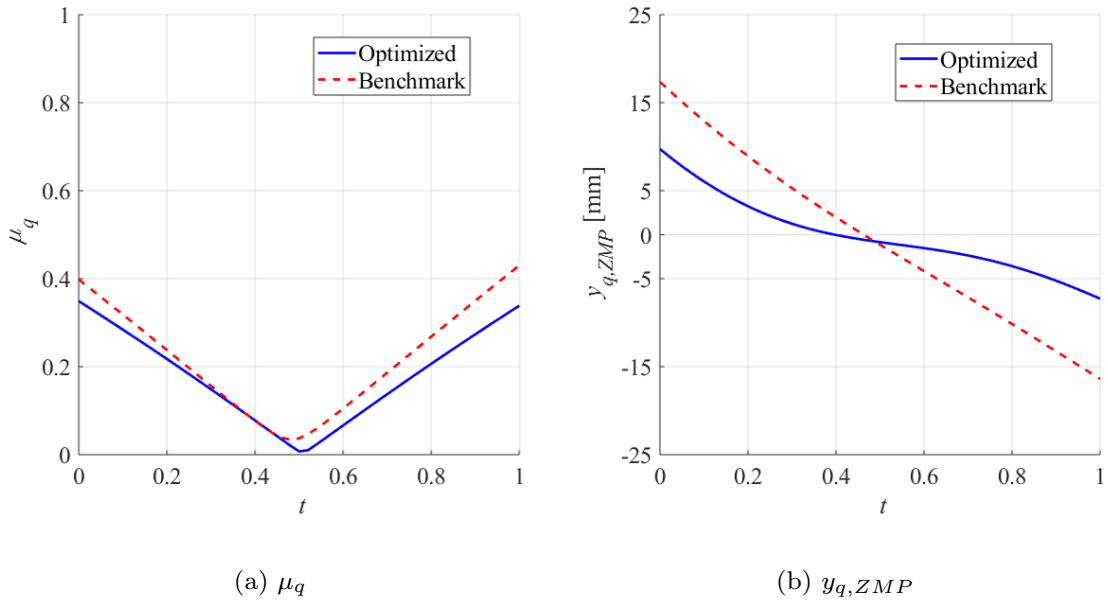
Fig.2.15   Evaluation criteria in the motion simulation of example 1

Design parameters for the optimization are listed in Table 2.1. In this optimization, it was assumed that no external forces except for elastic forces of the linear springs are applied between the links. The optimization problem was solved with the interior-point method [118]. As a result of the optimization, endpoints of the springs became ${}^1\boldsymbol{c}_{1,1} = [18.6 \quad -35.7 \quad -37.1]^T$ [mm] and ${}^1\boldsymbol{c}_{1,2} = [-16.4 \quad 95.5 \quad 2.84]^T$ [mm] on Σ_1, and ${}^2\boldsymbol{c}_{2,1} = [55.4 \quad -51.7 \quad 67.0]^T$ [mm] and ${}^2\boldsymbol{c}_{2,2} = [15.8 \quad 81.3 \quad -51.1]^T$ [mm] on Σ_2. Fig.2.14 shows the SRCP with the optimal arrangement of the linear springs when $t = 0.5$.
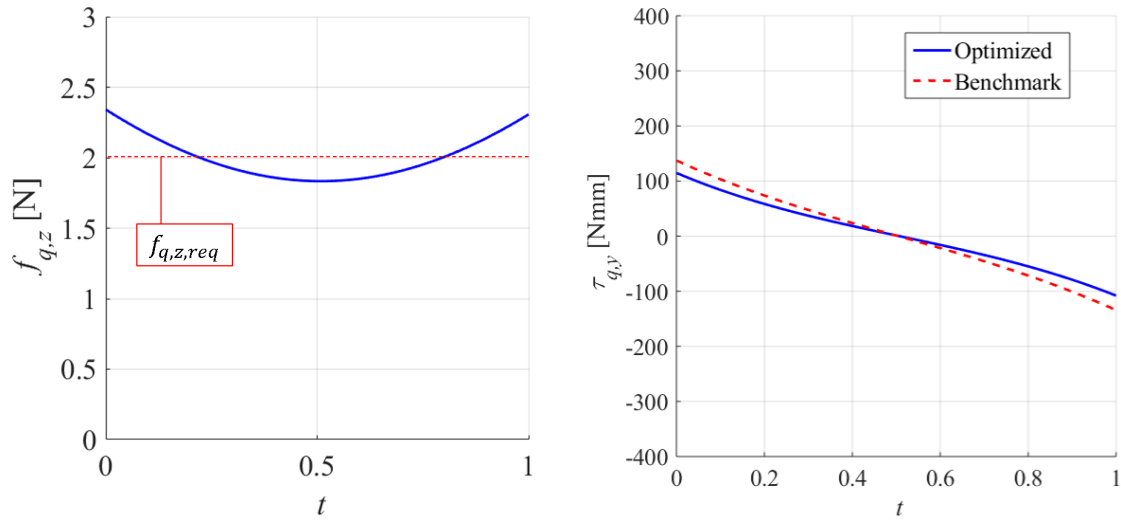
(a) The normal reaction force between the links

(b) Torque around the contact line generated by linear springs

Fig.2.16   Forces acting between the links in the motion simulation of example 1

The motion of the mechanism was simulated to confirm the performances. Fig.2.15 shows the evaluation criteria during the simulation. The figure (a) shows μ_q, and the figure (b) shows $y_{q,ZMP}$ during the relative rolling motion between the links. The benchmarks plotted in the figures (a) and (b) are the results when endpoints of the springs are assumed to be placed at the center point in the specified design space. Since μ_q is always small value, it is considered that the extra load applied to the flexible bands was always small. Since $y_{q,ZMP}$ is always in $-25 \leqq y_{q,ZMP} \leqq 25$ [mm], it is considered that the ZMP was always on the virtual supporting plane. In addition, they were better than their benchmarks. Besides, forces acting between the links are shown in Fig.2.16. The normal reaction force between the links shown in the figure (a) is always about the specified value. Therefore, the two links were able to keep ideal relative rolling contact in the simulation. In addition, torque about the contact line $\tau_{q,y}$ shown in Fig.2.16 (b) was smaller than the benchmark even though increasing stability between the links and reducing $\tau_{q,y}$ are in the trade-off relationship. Therefore, the better arrangement of the springs was able to be found with the proposed design method.

2.5.2   Example 2: A closed-loop 4-bar mechanism with the SRCP to generate a spatial trajectory

A spatial mechanism with 1 DOF shown in Fig.2.17 was synthesized as an example of a spatial-path generator. The mechanism is composed of a universal joint, a revolute pair, a spherical pair, and one SRCP. This mechanism can be regarded as a spatial 4-bar mechanism if the universal joint is not regarded as R-R kinematic chain but a kind of
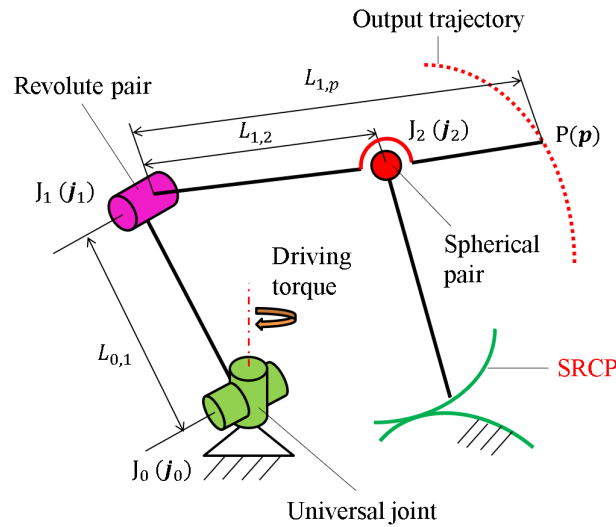
Fig.2.17   A spatial 4-bar mechanism with 1 DOF which can completely generate the specified trajectory because of the SRCP
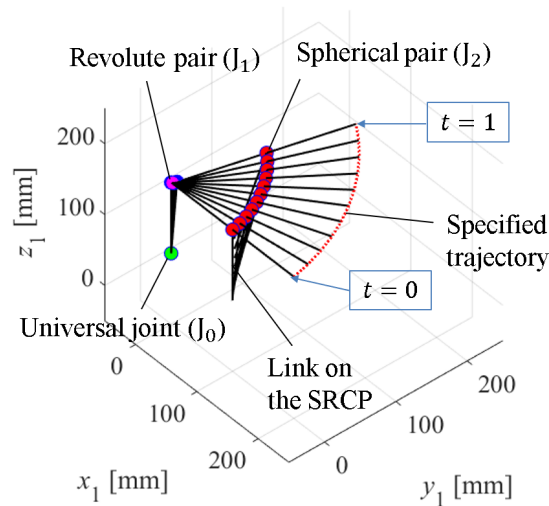
Fig.2.18   The specified motion of the mechanism in example 2

kinematic pair. One of the two revolute pairs in the universal joint is driven with an actuator such as a motor. The output trajectory of the mechanism was specified as the following equation.

$$
{}^{1}\boldsymbol{p}(t) = \begin{bmatrix} 200\cos\frac{\pi t}{3} & 200\sin\frac{\pi t}{3} & 50t+150 \end{bmatrix}^{T} \quad (0 \leqq t \leqq 1) \tag{2.39}
$$

Then, the position of the universal joint ${}^{1}\boldsymbol{j}_{0}$ and link length $L_{0,1}$ and $L_{1,p}$ shown in Fig.2.17 were specified so that the specified trajectory is included in the maximum workspace of the open-loop linkage, which has the universal joint, the revolute pair and the spherical
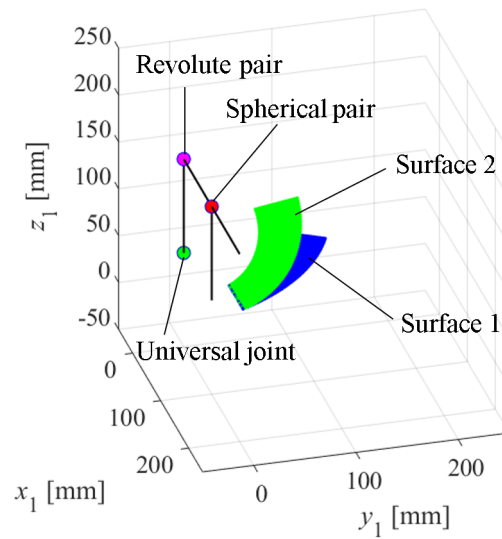
Fig.2.19   The designed rolling contact surfaces in example 2
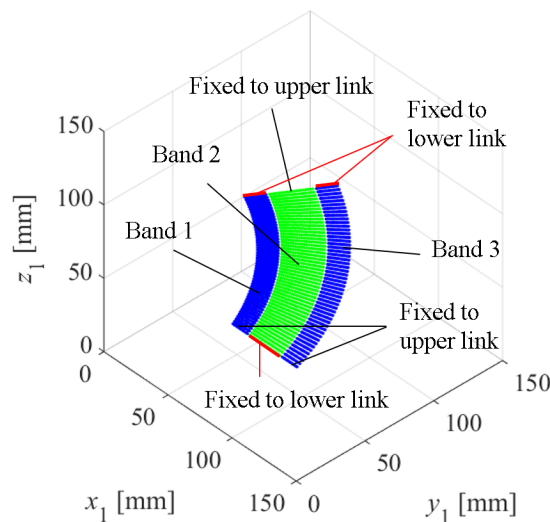
Fig.2.20   The designed flexible bands of the SRCP in example 2 in the natural state

pair. Its maximum workspace has a simple shape because it is the sphere whose center is laid on J_0 and radius is $L_{0,1} + L_{1,p}$. Therefore, these parameters were easily to be specified as $^1\boldsymbol{j}_0 = [0 \; 0 \; 50]^T$ [mm], $L_{0,1} = 100$ mm and $L_{1,p} = 200$ mm. As shown here, some kinematic constraints of kinematic chains can be represented as inequality constraints by using the SRCP. Therefore, procedure of mechanism synthesis can be simplified with the SRCP.

Next, the SRCP was designed to generate the trajectory $^1\boldsymbol{j}_2(t)$. The trajectory $^1\boldsymbol{j}_2(t)$ was calculated by specifying the length $L_{1,2}$ as 100 mm. Parameters of the angular velocity were specified as $\theta(t) = \frac{\pi t}{3}$ rad, and $\phi = 0$ rad so that the links did not interfere with each other. Then, the specified motion of the mechanism became as shown in Fig.2.18.
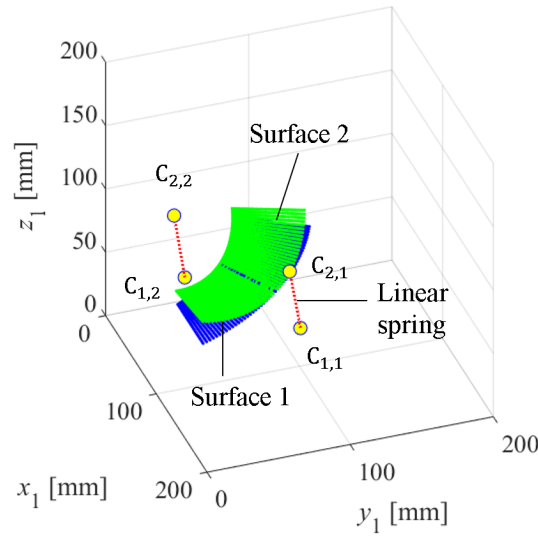
Fig.2.21 The designed SRCP with optimally arranged linear springs in example 2

Table 2.2 Parameters for the optimal arrangement of linear springs in example 2

$k_1 = k_2 = 0.028$ N/mm	$\psi = -\frac{5\pi}{12}$ rad
$l_{0,1} = l_{0,2} = 35.1$ mm	$[-30\ 40\ -40] \leqq {}^{r_1}\boldsymbol{c}_{r_1,1}^T \leqq [30\ 70\ -10]$
$l_{max,1} = l_{max,2} = 124.1$ mm	$[-30\ -70\ -40] \leqq {}^{r_1}\boldsymbol{c}_{r_1,2}^T \leqq [30\ -40\ -10]$
$f_{s,0,1} = f_{s,0,2} = 0.412$ N	$[-30\ 40\ 25] \leqq {}^{r_2}\boldsymbol{c}_{r_2,1}^T \leqq [30\ 70\ 55]$
$(w_1, w_2, w_3) = (1, 1, 1)$	$[-30\ -70\ 25] \leqq {}^{r_2}\boldsymbol{c}_{r_2,2}^T \leqq [30\ -40\ 55]$
$f_{q,z,req} = 2$ N	(Unit: mm)

Rolling contact surfaces were designed to generate the specified rolling motion in the same way as example 1. The designed rolling contact surfaces are shown in Fig.2.19, where the range of u is $-25 \leqq u \leqq 25$ [mm] and the posture is at $t = 0$. The surface 1 is on the fixed link and the surface 2 is on the link with the spherical pair. In order to keep ideal rolling motion between the two links, elastic constraints were designed. Fig.2.20 shows designed flexible bands, where each gap between adjacent bands is 2 mm and the natural shape adjusts the surface 1. Fig.2.21 shows the posture of the SRCP at $t = 0.5$ and the optimally arranged linear springs, where parameters shown in Table 2.2 were used. In the optimal arrangement of springs, it was assumed that no external forces except for elastic forces of the linear springs are applied between the links of the SRCP, and the optimization problem was solved with the interior-point method. The optimized positions were ${}^{1}\boldsymbol{c}_{1,1} = [110.4\ \ 97.0\ \ 37.1]^T$ [mm], ${}^{1}\boldsymbol{c}_{1,2} = [19.9\ \ 48.3\ \ 31.9]^T$ [mm] on Σ_1 and ${}^{2}\boldsymbol{c}_{2,1} = [19.0\ \ 70.3\ \ -51.0]^T$ [mm], ${}^{2}\boldsymbol{c}_{2,2} = [-71.7\ \ 24.2\ \ -64.9]^T$ [mm] on Σ_2.

The motion was simulated to confirm the performance. Fig.2.22 shows the evaluation criteria during the simulation. The figure (a) shows that μ_q was always small positive value during the motion. The figure (b) shows that $y_{q,ZMP}$ was always on the virtual supporting plane. In addition, they were better values than its benchmark, which was calculated with

(a) μ_q (b) $y_{q,ZMP}$
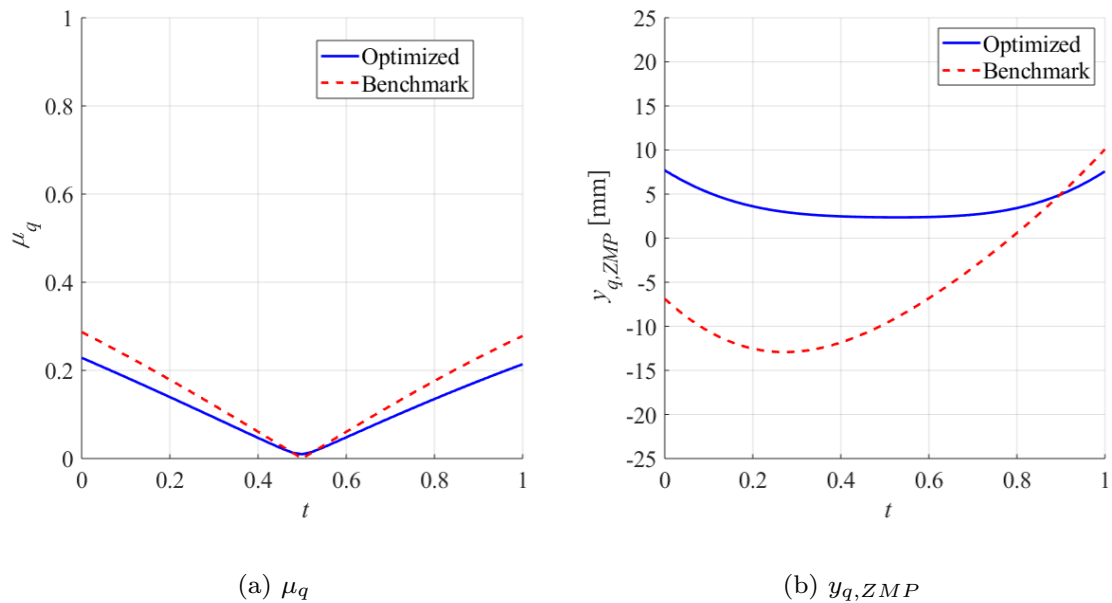
Fig.2.22   Evaluation criteria in the motion simulation of example 2

(a) The normal reaction force between the links

(b) Torque around the contact line generated by linear springs
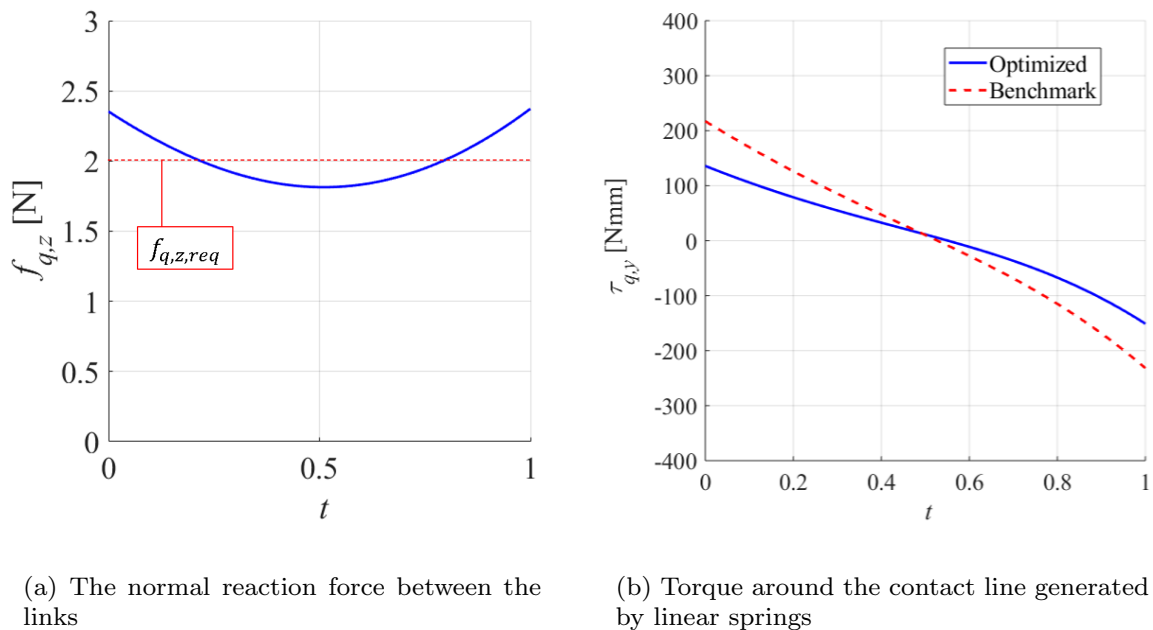
Fig.2.23   Forces acting between the links in the motion simulation of example 2

the center position in the specified design space as the endpoints of the springs. Fig.2.23 shows force acting between the two links of the SRCP during the simulation. The figure (a) shows that the normal reaction force $f_{q,z}$ was always about the specified value. Therefore, the SRCP in the mechanism was able to generate the ideal rolling motion in the simulation.

$\tau_{q,y}$ shown in Fig.2.23 (b) are smaller than its benchmark. Therefore, a better arrangement of springs was also obtained with the proposed method in this example.

2.6 Prototyping and evaluation

In order to confirm the validity of the proposed design method, some evaluation experiments were performed with prototypes of the SRCP-link mechanisms designed in section 2.5.

2.6.1 Measurement of torque about the contact line

Rotation torque about the contact line between the links of a fabricated SRCP was measured to confirm that the design method of the flexible bands to achieve zero torque about the contact line is valid.

The 2-bar mechanism with the SRCP, which was designed as example 1 in section 2.5.1, was fabricated as a prototype. Each of the rolling contact surfaces shown in Fig.2.12 was offset by 0.3 mm to make space to attach the flexible bands because the thickness of flexible bands was specified as 0.6 mm. Solid models of the links were made by using the offset surface. Solid models of the flexible bands were made by giving thickness to the intermediate surfaces shown in Fig.2.13. Linear springs were not attached so as to measure the torque generated by only flexible bands. The 3D-CAD model was fabricated with 3D-printers. Fig.2.24 shows the fabricated prototype. The links were fabricated by the fused deposition modeling (FDM). The flexible bands were fabricated by the material jetting method.

Measuring torque between the two links is difficult because the rotation axis between the links drifts. Thus, the force at the output point in the direction along the specified linear trajectory was measured instead of the torque. Fig.2.25 shows the experimental setup.
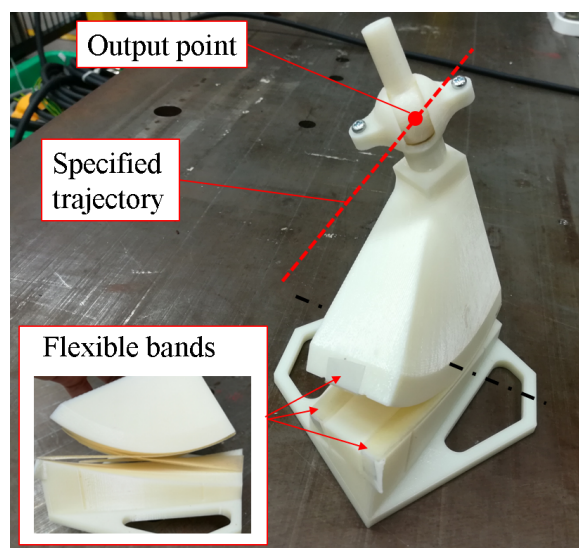
Fig.2.24   A prototype of the SRCP-link mechanism designed in example 1
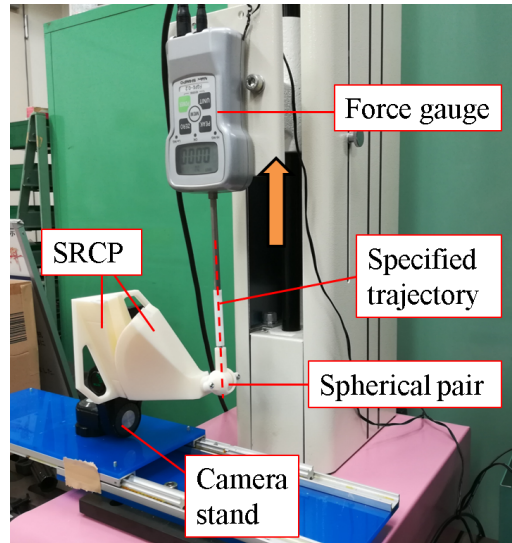
Fig.2.25   An experimental setup to measure the output force of the prototype

The prototype was attached to a force gauge stand. The output point was connected to the force gauge through a spherical pair so that the spherical pair gives contact force between the links during the rolling motion. The force at the output point was measured by pulling the force gauge along the specified linear trajectory.

The measured force-displacement relationship is shown in Fig.2.26, where the offset force generated by gravity was removed by tare of the force gauge. The measured torque was always small. The mean value of the force was 2.87×10^{-4} N and the standard deviation was 2.39×10^{-3} N. Thus, the output force was assumed as zero. It means that the torque about the contact line is negligible. Note that the error in the result was caused by the friction in the spherical pair. Therefore, the design method of the flexible bands is valid.

2.6.2   Motion capture of the output motion

Output motion of a spatial mechanism with the SRCP was measured with a motion capture system to confirm the validity of the design method of the rolling contact surfaces and elastic constraints.

As the prototype, the spatial 4-bar mechanism with the SRCP designed in example 2 was fabricated. Fig.2.27 shows the fabricated mechanism. The SRCP was fabricated by the same procedure as described in section 2.6.1, where the thickness of the flexible bands was specified as 0.6 mm. The linear springs were attached to the two links through spherical joints. The active revolute pair in the universal joint was driven by a DC motor.

In the experiment, the input angle was controlled so that the output point reciprocates three times in the range of motion. The generated output trajectories were measured with OptiTrack V120:Duo (a motion capture system).

The measured trajectories are shown in Fig.2.28. It is shown that each measured trajectory agrees well with the specified one. Although the mean position error between the measured and specified trajectories was 0.739 mm, it is considered that the error
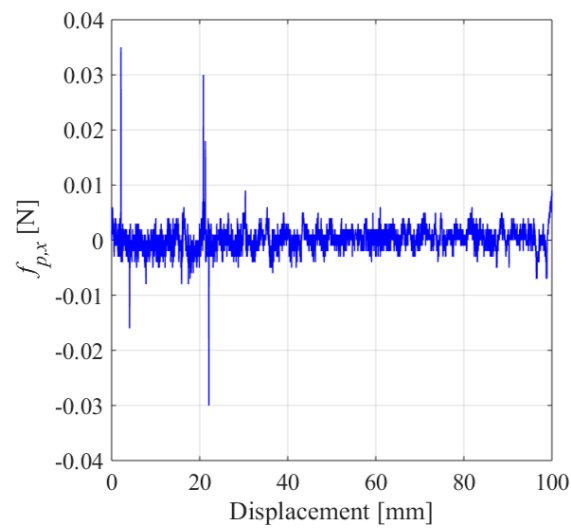
Fig.2.26   The measured output force of the prototype

was caused by the fabrication error of the mechanism and the calibration error in the motion capture experiment. Thus, this result shows that calculation of the rolling contact surfaces were correct and the two links of the SRCP generated ideal rolling motion due to the designed elastic constraints. Therefore, the validity of the design methods of the rolling contact surfaces and elastic constraints was able to be confirmed.
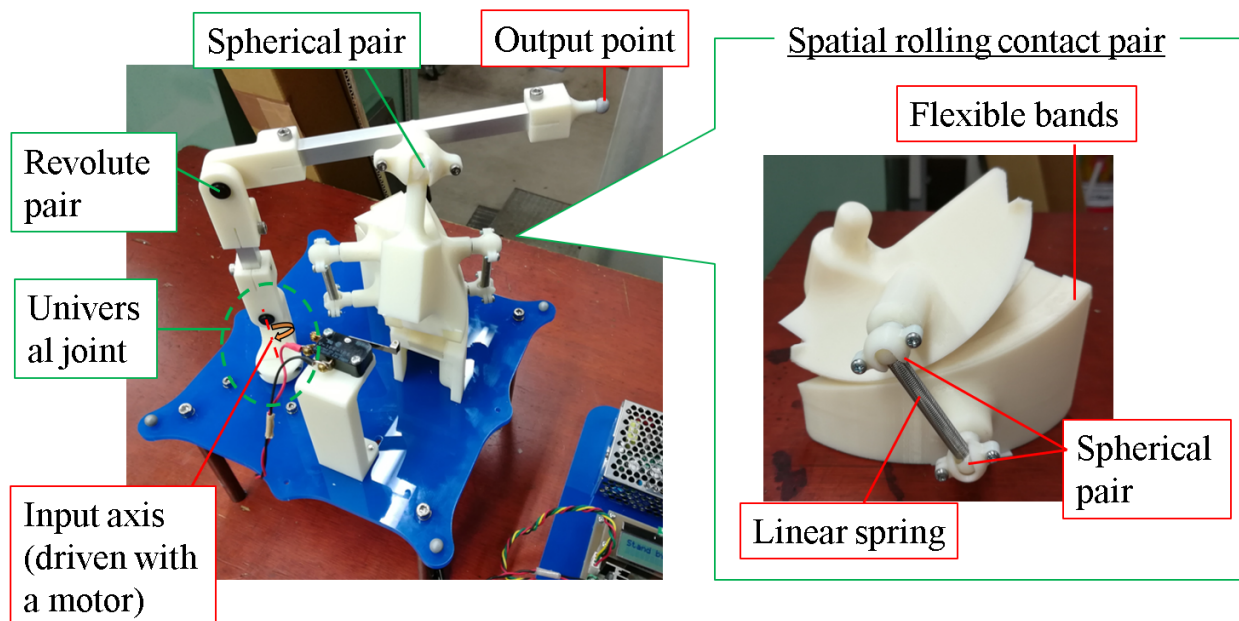
Fig.2.27   A prototype of the spatial 4-bar mechanism designed in example 2
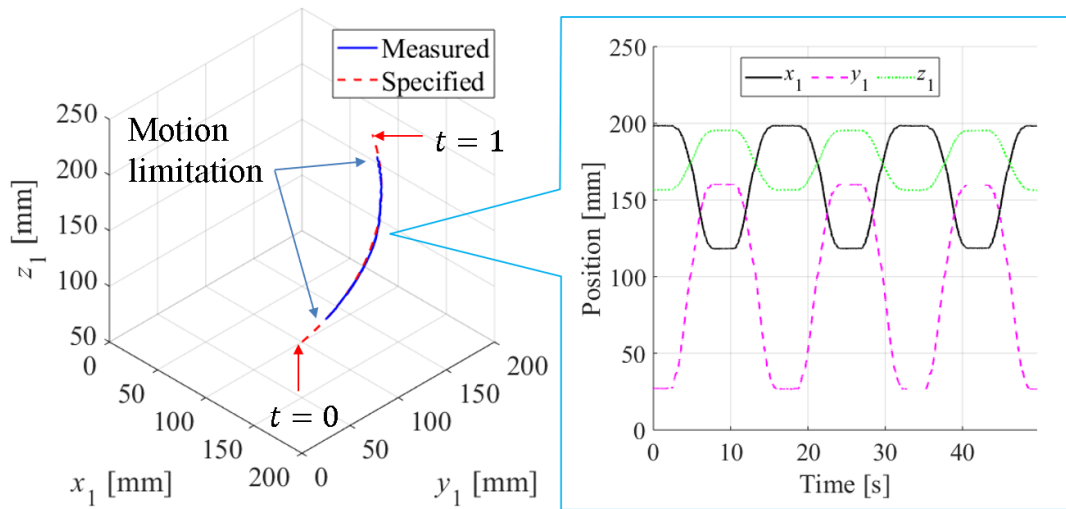
Fig.2.28　The measured output trajectories generated by the fabricated spatial 4-bar mechanism with the SRCP

2.7 Discussion

The scope of application of the SRCP designed with the proposed methods is discussed for future developments of its applications. Although the SRCP can be designed to generate the specified trajectory, trajectories which can be specified have some limitations. If a complex trajectory whose curvature changes frequently is specified, profiles of rolling contact surfaces between the links may be complicated. In this case, the designed SRCP cannot generate the specified trajectory because structural interference between the two surfaces may occur at a part different from its contact line. In addition, the SRCP cannot generate a periodic closed-loop trajectory because of the structural limitation of the flexible bands. Therefore, the SRCP is preferable to be used for any applications where an open-loop trajectory with small curvature change is required to be generated.

Although the SRCP can support tangential loads between its links with the proposed elastic constraint, allowable loads are not so large. Therefore, the SRCP is preferable to be used for any applications where the directions of external forces are known or where tangential loads between the links are not so large.

An example of applications to satisfy the scope is an automatic transfer machine which repeats to pick and place a specific object along the specified open-loop trajectory to avoid obstacles.

2.8 Chapter summary

The spatial rolling contact pair (SRCP) to generate the specified relative trajectory between two links was developed to achieve exact spatial-path generation. This is the kinematic pair with 1 DOF where a link rolls on another link with keeping in contact at

a line and passing through the specified trajectory. In order to generate the ideal relative rolling motion between the links, the SRCP has a hybrid elastic constraint with flexible bands and linear springs between the links. By using the SRCP in a spatial mechanism with 1 DOF, the mechanism can completely generate the specified trajectory. In this chapter, a design method of the SRCP was proposed, and some examples were designed and examined by experiments. The obtained results in this chapter are summarized bellow.

(1) A design method of rolling contact surfaces between the links to generate the specified trajectory was proposed, where the rolling motion is specified to satisfy the kinematic condition of rolling motion and rolling contact surfaces are derived as ruled surfaces of the instantaneous screw axis of the specified rolling motion.

(2) In order to suppress slippage between the links, the elastic constraint with flexible bands were applied. It was confirmed that this constraint can be applied to any profiles of rolling contact surfaces designed with the proposed method by a mathematical approach. Then, a design method of the flexible bands is proposed, where their dimensions are derived so that they generate zero torque about the contact line between the links.

(3) In order to suppress separation between the links during the rolling motion, linear springs were optimally arranged between the links. For this optimization to generate the ideal relative rolling motion between the links, two evaluation criteria were proposed. One of the criteria is the ratio of normal reaction force and tangent reaction force between the links, and another is zero moment point (ZMP) defined between the links.

(4) By using the SRCP, a spatial-path generators to generate a linear trajectory and a spatial trajectory were designed. Especially, it was revealed that procedure to synthesis a spatial-path generator can be simplified by using the SRCP.

(5) The designed examples were fabricated, and their torque about the contact line between the links and the output motion were measured by experiments. As a result, it was confirmed that the proposed design methods are valid and exact spatial-path generation can be achieved with the SRCP.

Chapter 3

The Active Spatial Rolling Contact Pair

3.1   Chapter introduction

The spatial rolling contact pair (SRCP) proposed in chapter 2 can generate the specified spatial trajectory between two links. However, since the SRCP is a passive kinematic pair, it must be used in a closed-loop mechanism with multiple kinematic pairs. Thus, structure of the spatial-path generator cannot be simplified enough. However, if linear springs of the SRCP are replaced by "active" elastic elements such as flexible actuators as shown in Fig.3.1 and if the SRCP is driven actively with the actuators, the SRCP can move actively with a simpler structure. Besides, if this structure can be compactly modularized and treated as a kinematic pair, the use of the SRCP in mechanism synthesis can be simplified in the same way that a motor is treated as an active revolute pair. Therefore, in this chapter, the active spatial rolling contact pair (ASRCP), which is composed of two links actively constrained with active elastic elements, is developed.

This chapter describes the following three contributions to achieve the ASRCP.

(1) Proposal and validation of a method to optimally arrange active elastic elements
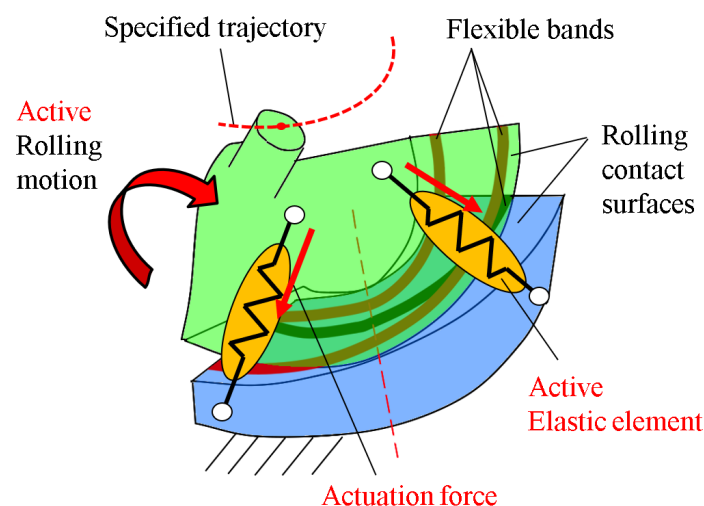
Fig.3.1   The proposed structure of the active spacial rolling contact pair (ASRCP)

between the links to maximize the actuation-force transmission
(2) Proposal and validation of a method to antagonistically drive the SRCP with keeping in the ideal rolling contact between the links with the use of actuation redundancy
(3) Prototyping and examination of the ASRCPs to generate the specified trajectory actively

In section 3.2, a design method of the ASRCP, where active elastic elements are optimally arranged between the links so as to maximize the driving force transmission, is proposed to achieve a large motion range. In section 3.3, a control method to drive the ASRCP while keeping ideal rolling contact between the links is proposed. In section 3.4, an example of the ASRCP is designed, and numerical simulation of control is performed. In section 3.5, the ASRCP driven with reeled elastic wires and the ASRCP driven with artificial muscles (flexible pneumatic actuators) are prototyped, and their performances are examined by motion capture experiments.

3.2   Design Method

In this section, a design method of the ASRCP based on force transmission is proposed. Firstly, a transmission index for parallel wire-driven mechanisms, $\mathrm{TI_w}$, proposed by Takeda et.al. [98] is introduced. Next, a criterion to evaluate the force transmission of a parallel wire-driven mechanism with the redundant number of wires is proposed based on the idea of $\mathrm{TI_w}$. Then, a method to optimally arrange active elastic elements between the links of the SRCP to maximize the transmission index is proposed.

3.2.1   Transmission index for parallel wire-driven mechanisms

In previous research on parallel wire-driven mechanisms, it was revealed that at least seven wires (uni-directional translation forces) are required to constrain an object in the
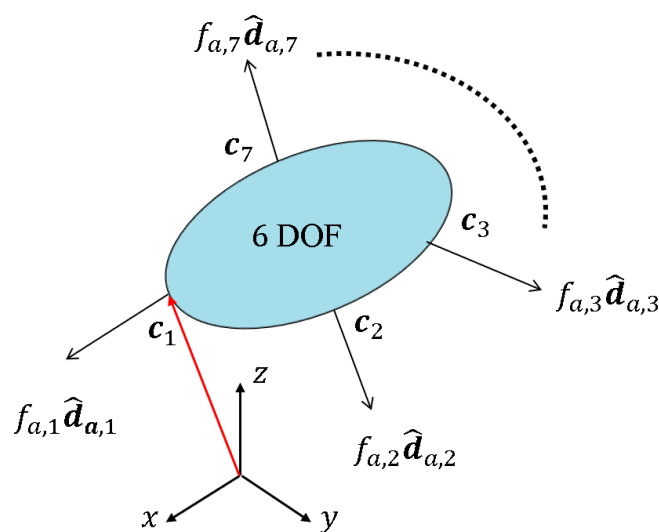
Fig.3.2   A parallel wire-driven mechanism with the least number of wires
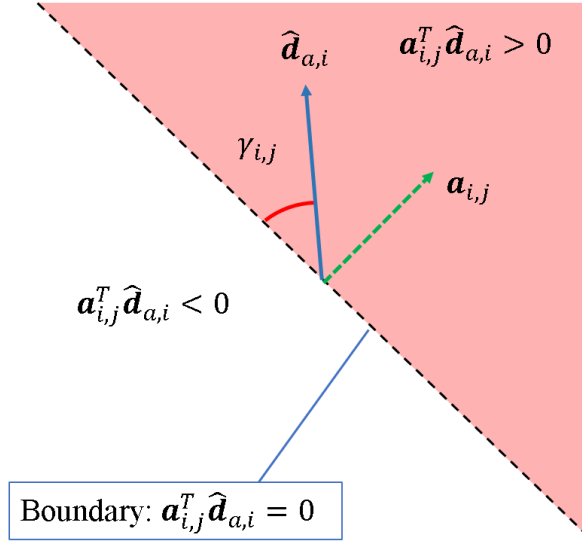
Fig.3.3   Schematic diagram of the transmission index, $\mathrm{TI_w}$, for parallel wire-driven mechanisms

3-dimensional space as shown in Fig.3.2 [116]. In order to evaluate the force transmission of a wire-driven mechanism with the least number of wires, the transmission index, $\mathrm{TI_w}$, has been proposed by Takeda et al. [98]. This index is useful for design because the force transmission can be evaluated with only kinematic conditions. In the following, its definition and calculation method are described.

The statics equation of the mechanism shown in Fig.3.2 is represented as the following equation.

$$\sum_{k=1}^{7} f_{a,i} \mathbb{S}_{a,i}^{r} = \sum_{k=1}^{7} f_{a,i} \begin{bmatrix} \hat{\boldsymbol{d}}_{a,i} \\ \boldsymbol{c}_i \times \hat{\boldsymbol{d}}_{a,i} \end{bmatrix} = \boldsymbol{0}, \tag{3.1}$$

where $f_{a,i}$ is the magnitude of the i-th wire tension, $\hat{\boldsymbol{d}}_{a,i}$ is the unit directional vector of the i-th wire tension and $\boldsymbol{c}_i$ is the point where the i-th wire tension is applying on the object. Focusing on the i-th wire tension, the other wire tensions to balance it can be represented as the following equation.

$$\boldsymbol{f}_{a,-i} = -\boldsymbol{G}_{a,-i}^{-1}(f_{a,i}\mathbb{S}_{a,i}^{r}) = -f_{a,i} \begin{bmatrix} \boldsymbol{I}_{3\times 3} \\ [\boldsymbol{c}_i \times] \end{bmatrix} \hat{\boldsymbol{d}}_{a,i} = f_{a,i} \begin{bmatrix} \boldsymbol{a}_{i,1}^{T} \\ \vdots \\ \boldsymbol{a}_{i,6}^{T} \end{bmatrix} \hat{\boldsymbol{d}}_{a,i}, \tag{3.2}$$

where $\boldsymbol{f}_{a,-i} = [f_{a,1}...f_{a,i-1} \; f_{a,i+1}...f_{a,7}]^T$ and $\boldsymbol{G}_{a,-i} = [\mathbb{S}_{a,1}...\mathbb{S}_{a,i-1} \; \mathbb{S}_{a,i+1}...\mathbb{S}_{a,7}]$. Note that magnitudes of all tensions must be positive values to make a force closure state. Thus, $\boldsymbol{a}_{i,j}^{T}\hat{\boldsymbol{d}}_{a,i} > 0 \; (j = 1, 2, ..., 6)$ must be satisfied when $f_{a,i}$ is positive. Fig.3.3 shows the schematic diagram of this inequality. The boundary of this condition, $\boldsymbol{a}_{i,j}^{T}\hat{\boldsymbol{d}}_{a,i} = 0$, represents a plane in a spatial mechanism. When $\hat{\boldsymbol{d}}_{a,i}$ is in the area of $\boldsymbol{a}_{i,j}^{T}\hat{\boldsymbol{d}}_{a,i} > 0$, the condition $\boldsymbol{a}_{i,j}^{T}\hat{\boldsymbol{d}}_{a,i} > 0$ is satisfied. As shown in the figure, whether $\hat{\boldsymbol{d}}_{a,i}$ is in the area of

$\boldsymbol{a}_{i,j}^T \hat{\boldsymbol{d}}_{a,i} > 0$ or not depends on the angle $\gamma_{i,j}$ between $\hat{\boldsymbol{d}}_{a,i}$ and the boundary. This means that it just depends on the kinematic configuration of the mechanism. In order to make it robust against external force and to transmit the i-th wire tension to the other wires efficiently, $\hat{\boldsymbol{d}}_{a,i}$ should lay far from the boundary $\boldsymbol{a}_{i,j}^T \hat{\boldsymbol{d}}_{a,i} = \boldsymbol{0}$. In other words, $\sin\gamma_{i,j}$ should be large. This value can be calculated as

$$\sin\gamma_{i,j} = \frac{\boldsymbol{a}_{i,j}^T \hat{\boldsymbol{d}}_{a,i}}{|\boldsymbol{a}_{i,j}|}. \tag{3.3}$$

The performance of the parallel wire-driven mechanism can be evaluated with the minimum value of $\sin\gamma_{i,j}$ for all boundaries $j = 1, 2, ..., 6$ and all wires $i = 1, 2, ..., 7$. Therefore, the transmission index $\mathrm{TI_w}$ is defined as

$$\mathrm{TI_w} = \min_{i=1,...,7}[\rho_i \min_{j=1,...,6}(\sin\gamma_{i,j})], \tag{3.4}$$

where ρ_i is a value defined as follows.

$$\rho_i = \begin{cases} 1 \ (\sin\gamma_{i,j} > \boldsymbol{0}) \\ 0 \ (\sin\gamma_{i,j} \leqq \boldsymbol{0}) \end{cases} \tag{3.5}$$

Note that $\mathrm{TI_w}$ cannot be calculated when $\mathrm{rank}(\boldsymbol{G}_{a,-i}) < 6$. In this case, $\mathrm{TI_w}$ is set to zero. The posture of the mechanism in the case of $\mathrm{TI_w} = 0$ is called singular configuration, and the area satisfying $\mathrm{TI_w} > 0$ is called the workspace.

3.2.2   Evaluation in the case of the redundant number of wires

If a parallel wide-driven mechanism cannot be designed to have sufficient workspace, increasing the number of wires is an effective solution to expand the workspace. When the number of wires N_w is more than 7, the matrix $\boldsymbol{G}_{a,-i}$ in Eq.(3.2) is not a regular matrix. Thus, Eq.(3.2) can be rewritten as the following equation.

$$\boldsymbol{f}_{a,-i} = -\boldsymbol{G}_{a,-i}^{\#}(f_{a,i}\mathbb{S}_{a,i}^r) + \boldsymbol{b}_i = \begin{bmatrix} f_{a,i}\boldsymbol{a}_{i,1}^T\hat{\boldsymbol{d}}_{a,i} + b_1 \\ \vdots \\ f_{a,i}\boldsymbol{a}_{i,N_w-1}^T\hat{\boldsymbol{d}}_{a,i} + b_{N_w-1} \end{bmatrix}, \tag{3.6}$$

where $\boldsymbol{G}_{a,-i}^{\#}$ is pseudo-inverse matrix of $\boldsymbol{G}_{a,-i}$ and $\boldsymbol{b}_i = [b_1...b_{N_w-1}]^T$ is a null space of $\boldsymbol{G}_{a,-i}$. Fig.3.4 shows the schematic diagram of this inequality. In this case, since the boundary is offset from $\boldsymbol{a}_{i,1}^T\hat{\boldsymbol{d}}_{a,i} = 0$ by $\frac{1}{f_{a,i}}b_j$, conditions to satisfy $\boldsymbol{f}_{a,-i} > \boldsymbol{0}$ depend not only on the direction of $\hat{\boldsymbol{d}}_{a,i}$ but also on the value of $f_{a,i}$. Thus, the force-closure state can hold even when the calculated value of $\mathrm{TI_w}$ is zero. This means that the workspace cannot be evaluated correctly with $\mathrm{TI_w}$. In order to solve this problem, alternative expression of the transmission index is proposed as

$$\mathrm{TI_{rw}} = \mathrm{mean}_{i=1,...,N_w}[\rho_i \min_{j=1,...,N_w-1}(\sin\gamma_{i,j})], \tag{3.7}$$
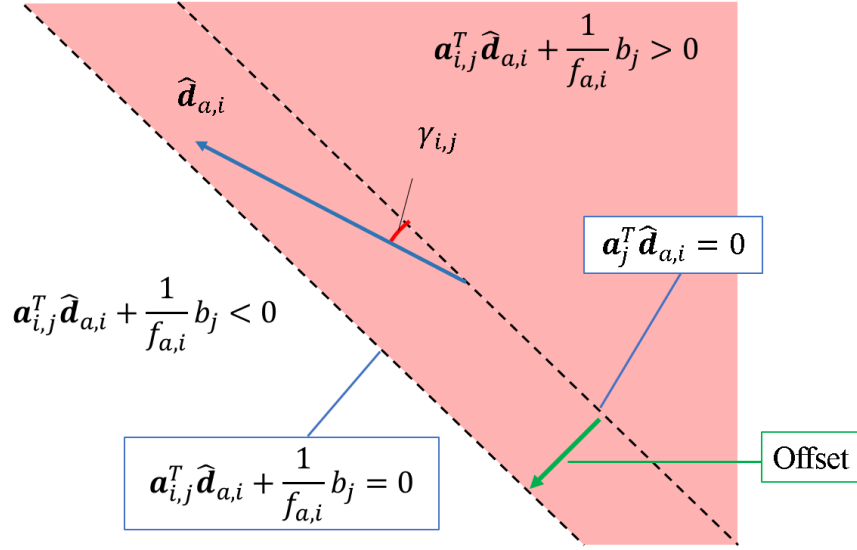
Fig.3.4 Schematic diagram of the transmission index for parallel wire-driven mechanisms with the redundant number of wires

where $\text{mean}(x)$ represents the mean value of x. Since $\sin\gamma_{i,j}$ means whether the i-th wire can generate a positive tension in the j-th wire, $\min_{j=1,\dots,N_w-1}(\sin\gamma_{i,j}) > 0$ means that the i-th wire can make all wire tensions positive values. Since each wire tension is the summation of tensions exerted by all the other wires, if at least one wire satisfy $\min_{j=1,\dots,N_w-1}(\sin\gamma_{i,j}) > 0$, all wire tensions can be made positive values just by increasing the tension of that wire. In this case, the mechanism with more than seven wires can be the force-closure state at least seven wires. Since TI_{rw} can evaluate such a situation, it is considered that this index can evaluate the workspace of the mechanism with the redundant number of wires correctly. Therefore, TI_{rw} is used to evaluate the force transmission in this chapter.

3.2.3   Optimal design method of the ASRCP

The optimization problem where active elastic elements are arranged between the links of the SRCP so as to maximize TI_w is formulated. When the two links of the SRCP keep in line contact, it can be assumed that five independent translation forces are acting at edges of the contact segment between the links. Fig.3.5 shows forces acting on a link of the ASRCP. $f_{c,1}{}^1\hat{\boldsymbol{d}}_{c,1}$, $f_{c,2}{}^1\hat{\boldsymbol{d}}_{c,2}$ and $f_{c,3}{}^1\hat{\boldsymbol{d}}_{c,3}$ are frictional forces. $f_{c,4}{}^1\hat{\boldsymbol{d}}_{c,4}$ and $f_{c,5}{}^1\hat{\boldsymbol{d}}_{c,5}$ are normal reaction forces. Their direction vectors can be obtained by using the position vector of the rolling contact surface $\boldsymbol{s}_1(t,u)$ derived in section 2.2.2 as follows.

$$^1\hat{\boldsymbol{d}}_{c,1} = \frac{\partial_t{}^1\boldsymbol{s}_1(t,u_0)}{|\partial_t{}^1\boldsymbol{s}_1(t,u_0)|}, \quad ^1\hat{\boldsymbol{d}}_{c,2} = \frac{\partial_t{}^1\boldsymbol{s}_1(t,u_1)}{|\partial_t{}^1\boldsymbol{s}_1(t,u_1)|}, \quad ^1\hat{\boldsymbol{d}}_{c,3} = \frac{\partial_u{}^1\boldsymbol{s}_1(t,u)}{|\partial_u{}^1\boldsymbol{s}_1(t,u)|}$$

$$^1\hat{\boldsymbol{d}}_{c,4} = {}^1\hat{\boldsymbol{d}}_{c,1} \times {}^1\hat{\boldsymbol{d}}_{c,3}, \quad ^1\hat{\boldsymbol{d}}_{c,5} = {}^1\hat{\boldsymbol{d}}_{c,2} \times {}^1\hat{\boldsymbol{d}}_{c,3} \tag{3.8}$$
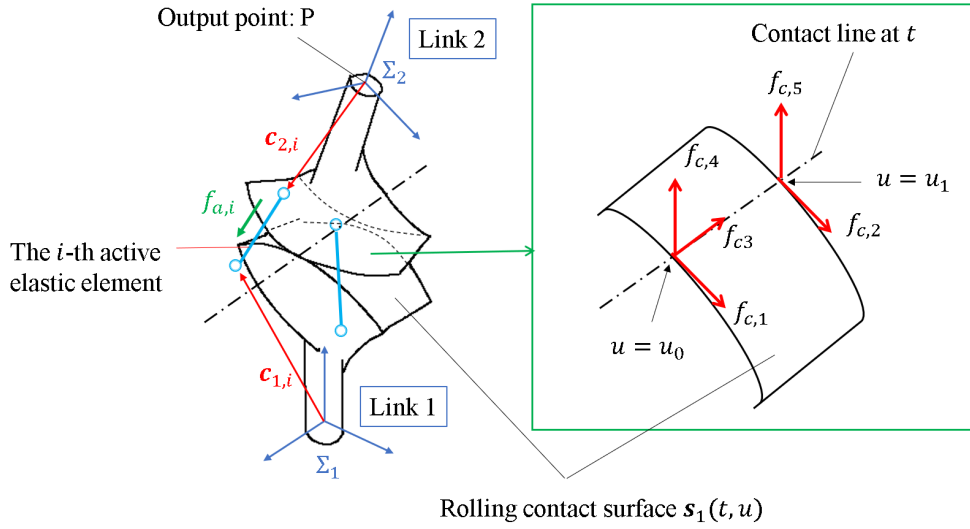
Fig.3.5   Constrained forces acting between the links of the ASRCP

Thus, their wrench screws can be obtained as follows.

$$
{}^1\mathbb{S}_{c,1}^r = \begin{bmatrix} {}^1\hat{\boldsymbol{d}}_{c,1} \\ {}^1\boldsymbol{s}_1(t,u_0) \times {}^1\hat{\boldsymbol{d}}_{c,1} \end{bmatrix}, \quad
{}^1\mathbb{S}_{c,2}^r = \begin{bmatrix} {}^1\hat{\boldsymbol{d}}_{c,2} \\ {}^1\boldsymbol{s}_1(t,u_1) \times {}^1\hat{\boldsymbol{d}}_{c,2} \end{bmatrix}, \quad
{}^1\mathbb{S}_{c,3}^r = \begin{bmatrix} {}^1\hat{\boldsymbol{d}}_{c,3} \\ {}^1\boldsymbol{s}_1(t,u_0) \times {}^1\hat{\boldsymbol{d}}_{c,3} \end{bmatrix}
$$

$$
{}^1\mathbb{S}_{c,4}^r = \begin{bmatrix} {}^1\hat{\boldsymbol{d}}_{c,4} \\ {}^1\boldsymbol{s}_1(t,u_0) \times {}^1\hat{\boldsymbol{d}}_{c,4} \end{bmatrix}, \quad
{}^1\mathbb{S}_{c,5}^r = \begin{bmatrix} {}^1\hat{\boldsymbol{d}}_{c,5} \\ {}^1\boldsymbol{s}_1(t,u_1) \times {}^1\hat{\boldsymbol{d}}_{c,5} \end{bmatrix} \tag{3.9}
$$

Since at least seven translation forces are required to constrain between the links, at least two active elastic elements have to be arranged between the links. Thus, the number of active elastic elements N_a has to be satisfy $N_a \geqq 2$. Let the endpoint position of the i-th active elastic element attached on the link 1 and link2 be ${}^1\boldsymbol{c}_{1,i}$ (on Σ_1) and ${}^2\boldsymbol{c}_{2,i}$ (on Σ_2), respectively as shown in Fig.3.5. Then, the wrench screws of the j-th actuation forces is obtained as follows.

$$
{}^1\boldsymbol{c}_{2,i} = \boldsymbol{R}_{1,2}(t)\,{}^2\boldsymbol{c}_{2,i} + {}^1\boldsymbol{p}(t) \tag{3.10}
$$

$$
{}^1\boldsymbol{d}_{a,i} = {}^1\boldsymbol{c}_{1,i} - {}^1\boldsymbol{c}_{2,i}, \tag{3.11}
$$

$$
{}^1\mathbb{S}_{a,i}^r = \begin{bmatrix} {}^1\hat{\boldsymbol{d}}_{a,i} \\ {}^1\boldsymbol{c}_{2,i} \times {}^1\hat{\boldsymbol{d}}_{a,i} \end{bmatrix} \quad (i = 1, ..., N_a), \tag{3.12}
$$

where ${}^1\boldsymbol{p}(t)$ is the specified trajectory and $\boldsymbol{R}_{1,2}(t)$ is the rotation matrix from Σ_1 to Σ_2 described in section 2.2.1. Focusing on the i-th actuation force, the other forces to balance it can be represented as follows like Eq.(3.6).

$$
\boldsymbol{f}_{a,-i} = -\boldsymbol{G}_{a,-i}^{\#}(f_{a,i}\mathbb{S}_{a,i}^r) + \boldsymbol{b}_i = \begin{bmatrix} f_{a,i}\boldsymbol{a}_1^{T}\,{}^1\hat{\boldsymbol{d}}_{a,i} + b_1 \\ \vdots \\ f_{a,i}\boldsymbol{a}_{N_a+4}^{T}\,{}^1\hat{\boldsymbol{d}}_{a,i} + b_{N_a+1} \end{bmatrix}, \tag{3.13}
$$

where $\boldsymbol{f}_{a,-i} = [...f_{a,i-1}\ f_{a,i+1}...f_{c,1}...f_{c,5}]^T$ and $\boldsymbol{G}_{a,-1} = [...{}^1\mathbb{S}_{a,i-1}^r \ {}^1\mathbb{S}_{a,i+1}^r...]$. In the AS-RCP, actuation forces $f_{a,1}, ..., f_{a,N_a}$ and normal reaction forces $f_{c,4}$, $f_{c,5}$ must be positive

although frictional forces $f_{c,1}$, $f_{c,2}$, $f_{c,3}$ allow negative values. Therefore, the evaluation criterion of the i-th actuation force ($\sin\gamma_{i,j}$) is considered just in terms of $j = 1, ..., N_a - 1$ (on the other actuation forces) and $j = N_a + 3, N_a + 4$ (on the normal reaction forces), and $\mathrm{TI_{rw}}$ is calculated with them.

In this optimal design, the design parameters are endpoint positions of active elastic elements $\boldsymbol{c} = [^1\boldsymbol{c}_{1,1}^T, ..., ^1\boldsymbol{c}_{1,N_a}^T, {}^2\boldsymbol{c}_{2,1}^T, ..., ^2\boldsymbol{c}_{2,N_a}^T]^T$. Then, the objective function based on $\mathrm{TI_{rw}}$ is formulated as follows.

$$F_a(\boldsymbol{c}) = \frac{1}{t_1 - t_0} \int_{t_0}^{t_1} \mathrm{mean}(\sin\gamma_{i,j}) dt, \tag{3.14}$$

This is maximized subject to the following size limitation.

$$^j\boldsymbol{c}_{j,i,min} \leqq {}^j\boldsymbol{c}_{j,i} \leqq {}^j\boldsymbol{c}_{j,i,max} \quad (i = 1, ..., N_a, \ j = 1, 2) \tag{3.15}$$

As described in section 2.4.1, this size limitation represents a design space with a rectangular parallelepiped shape, and it can be redefined with $^{r_j}\boldsymbol{c}_{r_j,i}$ on Σ_{r_j} for ease of use.

Note that maximizing $\mathrm{TI_{rw}}$ and maximizing $F_a(\boldsymbol{c})$ are equivalent problems. Although $\mathrm{TI_{rw}}$ is a discontinuous function for $\boldsymbol{c}$, the objective function $F_a(\boldsymbol{c})$ is a continuous function. Therefore, gradient-based optimization methods can be applied to reduce calculation time.

In order to simplify the structure of the ASRCP, it is desirable that the small number of active elastic elements are used. Therefore, initially, two active elastic elements are arranged between the links optimally, and the workspace of the ASRCP is then evaluated with $\mathrm{TI_{rw}}$. If a sufficient workspace is then not available, the number of active elastic elements is increased by one, and the optimal arrangement of them and workspace evaluation are performed again. When a sufficient workspace is obtained, the design procedure is finished.

3.3   Control Method

In order to control the ASRCP, a method to calculate actuation forces generated by active elastic elements is proposed. The statics equation on a link of the ASRCP is represented as the following equation.

$$\boldsymbol{G}_a\boldsymbol{f}_a = \boldsymbol{0}, \tag{3.16}$$

where $\boldsymbol{G}_a = [^1\mathbb{S}_{a,1}...^1\mathbb{S}_{a,N_a} \ ^1\mathbb{S}_{c,1}...^1\mathbb{S}_{c,5}]$ and $\boldsymbol{f}_a = [f_{a,1}...f_{a,N_a} \ f_{c,1}...f_{c,5}]^T$. Since $\boldsymbol{G}_a$ is not a regular matrix, there are countless solutions for $\boldsymbol{f}_a$. Therefore, the magnitudes of cable tensions $\boldsymbol{f}_a$ are calculated with an optimization problem to maximize the stability of the rolling contact between the links. In section 2.4.1, two criteria μ_q and $y_{q,ZMP}$ to evaluate the stability of the rolling contact in the SRCP have been proposed. μ_q is a criterion to evaluate whether slippage and separation between the links occur or not. $y_{q,ZMP}$ is a criterion to evaluate whether the two links can keep in line contact or not. In order to generate the ideal rolling motion between the links, these criteria have to be small values. Therefore, actuation forces are calculated to minimize them. Let the design

parameters in this optimization is represented as $\boldsymbol{f}_d = [f_{a,1}...f_{a,N_a}]$ Then, the objective function is formulated as follows.

$$F_d(\boldsymbol{f}_d) = \max\{w_1\mu_q^2, \ w_2(u_c - y_{q,ZMP})^2, \ w_3|\boldsymbol{f}_d|\}, \tag{3.17}$$

where w_1, w_2, w_3 are weight variables and u_c is the center value of the range of u. This function is minimized subject to the following constraint conditions for each value of the motion parameter t.

$$\boldsymbol{G}_a\boldsymbol{f}_a = \boldsymbol{0}, \tag{3.18}$$
$$f_{q,z} > f_{q,z,req}, \tag{3.19}$$

where $f_{q,z}$ is the normal reaction force at the middle point of the contact segment between the links, and $f_{q,z,req}$ is the required normal reaction force. This optimization problem can be solved with a gradient-based numerical optimization method by using the same technique described in section 2.4.2.

3.4   Design and simulation

An example of the ASRCP was designed with the proposed design method and simulation to control it was performed with the proposed control method.

3.4.1   Design example

As an example, the relative rolling motion between the links of the SRCP was specified as the following output trajectory ${}^1\boldsymbol{p}(t)$ and angular velocity ${}^1\boldsymbol{\omega}(t)$.

$$
{}^1\boldsymbol{p}(t) = \begin{bmatrix} 60\cos\frac{\pi t}{2} & 60\sin\frac{\pi t}{2} & 40t + 40 \end{bmatrix}^T \quad (0 \leqq t \leqq 1) \ \ [\text{mm}], \tag{3.20}
$$
$$
{}^1\boldsymbol{\omega}(t) = \frac{\pi}{2}{}^1\boldsymbol{n}_p(t) \ \ [\text{rad/s}], \tag{3.21}
$$

where ${}^1\boldsymbol{n}_p(t)$ is the principal normal vector of ${}^1\boldsymbol{p}(t)$. Then, the rolling contact surfaces to generate the specified motion were derived with the design method described in section 2.2, where the width of the rolling contact surfaces were specified with $-25 \leqq u \leqq 25$ [mm]. Then, flexible bands to suppress slippage between the links were designed with the method described in section 2.3, where the gap δ between each two adjacent flexible bands was 2 mm.

At first, two active elastic elements were tried to arrange between the links of the designed SRCP. The constraint conditions were as follows.

$$
\begin{aligned}
[-70 \ -180 \ -60]^T &\leqq {}^{r_1}\boldsymbol{c}_{r_1,1} \leqq [70 \ -120 \ -10]^T, \\
[100 \ -70 \ -60]^T &\leqq {}^{r_1}\boldsymbol{c}_{r_1,2} \leqq [160 \ 70 \ -10]^T \ \ (\text{on } \Sigma_{r_1}), \\
[-50 \ -120 \ 60]^T &\leqq {}^{r_2}\boldsymbol{c}_{r_2,1} \leqq [50 \ -70 \ 100]^T, \\
[30 \ -50 \ 60]^T &\leqq {}^{r_2}\boldsymbol{c}_{r_2,2} \leqq [80 \ 50 \ 100]^T \ \ (\text{on } \Sigma_{r_2}) \ [\text{mm}],
\end{aligned}
$$

where Σ_{r_1} and Σ_{r_2} are defined with $\psi = \pi/12$ rad as described in section 2.4.1. For the optimal design, many candidates of the initial design value were generated in the specified
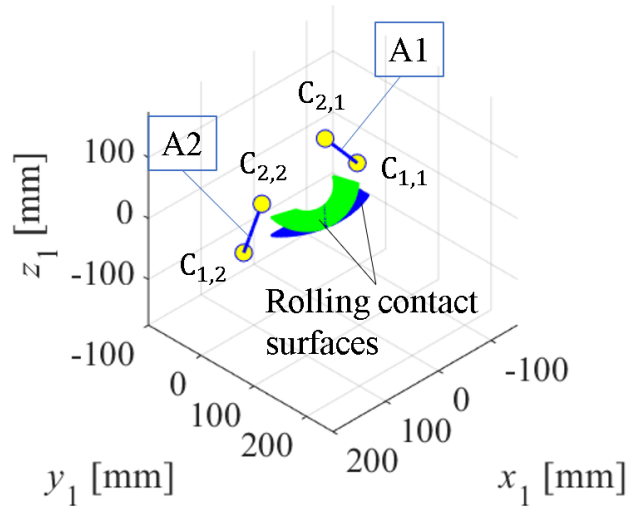
Fig.3.6   An example of the ASRCP with two active elastic elements
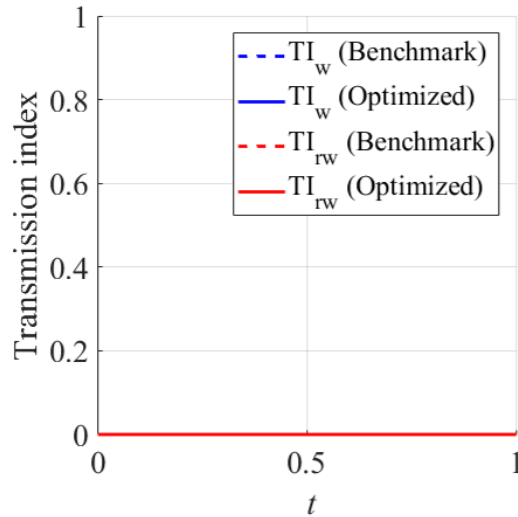
Fig.3.7   Transmission index of the example with two active elastic elements

design space, and the value to maximize $\mathrm{TI_{rw}}$ in among the candidates was chosen as the initial value. The optimization was performed with the interior-point method [118]. The result is shown in Fig.3.6, where the ASRCP has the posture at $t = 0.5$. The calculated endpoint of active elastic elements were $^1c_{1,1} = [-83.21 \; 12.91 \; 5.912]^T$ [mm], $^1c_{1,2} = [108.3 \; -10.87 \; -57.58]^T$ [mm], $^2c_{2,1} = [-75.22 \; -44.81 \; -4.517]^T$ [mm] and $^2c_{2,2} = [44.72 \; 4.695 \; -53.35]^T$ [mm]. $\mathrm{TI_{rw}}$ of the designed ASRCP was calculated during $0 \leqq t \leqq 1$ to confirm the workspace. Then, $\mathrm{TI_w}$ was also calculated to be compared with $\mathrm{TI_{rw}}$. Fig.3.7 shows the results, where benchmarks were calculated with midpoints in the specified design space as the endpoints of the active elastic elements. In the figure, $\mathrm{TI_w}$ and $\mathrm{TI_{rw}}$ are always zero both before and after the optimization. Therefore, the ASRCP with sufficient workspace was not able to be designed.
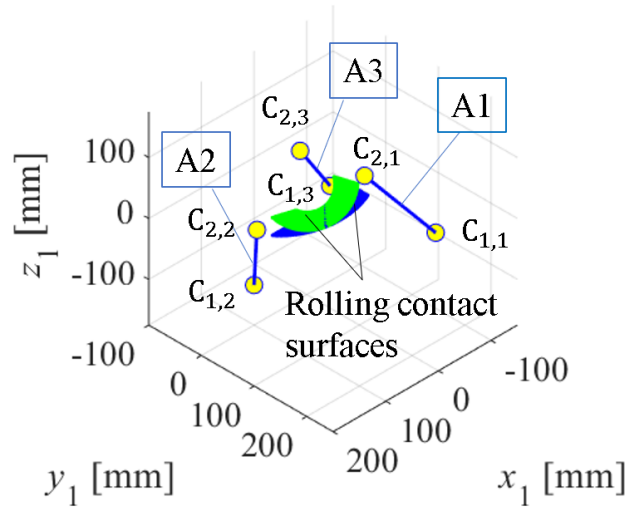
Fig.3.8   An example of the ASRCP with three active elastic elements
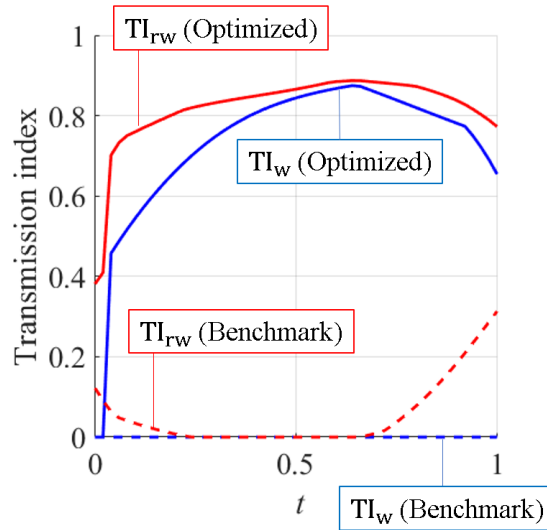
Fig.3.9   Transmission index of the example with three active elastic elements

In order to obtain sufficient workspace, three active elastic elements were then arranged between the links. The constraint conditions defined on the same Σ_{r_1} and Σ_{r_2} were as follows,

$$[-70\ 120\ -60]^T \leqq {}^{r_1}\boldsymbol{c}_{r_1,1} \leqq [70\ 180\ -10]^T$$
$$[-70\ -180\ -60]^T \leqq {}^{r_1}\boldsymbol{c}_{r_1,2} \leqq [70\ -120\ -10]^T$$
$$[100\ -70\ -60]^T \leqq {}^{r_1}\boldsymbol{c}_{r_1,3} \leqq [160\ 70\ -10]^T \quad (\text{on } \Sigma_{r_1})$$
$$[-50\ 70\ 60]^T \leqq {}^{r_2}\boldsymbol{c}_{r_2,1} \leqq [50\ 120\ 100]^T$$
$$[-50\ -120\ 60]^T \leqq {}^{r_2}\boldsymbol{c}_{r_2,2} \leqq [50\ -70\ 100]^T$$
$$[30\ -50\ 60]^T \leqq {}^{r_2}\boldsymbol{c}_{r_2,3} \leqq [80\ 50\ 100]^T \quad (\text{on } \Sigma_{r_2})\ [\text{mm}]$$

The optimization was performed in the same way to when two active elastic elements were used. The result is shown in Fig.3.8, where the ASRCP has the posture at $t = 0.5$. The calculated endpoint of active elastic elements were ${}^1\boldsymbol{c}_{1,1} = [-51.17\ 193.7\ -2.069]^T$ [mm], ${}^1\boldsymbol{c}_{1,2} = [160.9\ 60.90\ -48.43]^T$ [mm], ${}^1\boldsymbol{c}_{1,3} = [-87.83\ -43.30\ -62.08]^T$ [mm], ${}^2\boldsymbol{c}_{2,1} = [-19.53\ 38.69\ 75.95]^T$ [mm], ${}^2\boldsymbol{c}_{2,2} = [89.12\ 39.22\ -43.81]^T$ [mm] and ${}^2\boldsymbol{c}_{2,3} = [-50.50\ -45.27\ -32.74]^T$ [mm]. $\mathrm{TI_w}$ and $\mathrm{TI_{rw}}$ during $0 \leqq t \leqq 1$ are shown in Fig.3.9. The results shows that both $\mathrm{TI_w}$ and $\mathrm{TI_{rw}}$ after the optimization became better values than their benchmarks. Although $\mathrm{TI_w}$ is zero at $t = 0$, $\mathrm{TI_{rw}}$ is not zero at $t = 0$. Here, it is possible to satisfy the force-closure state because of its redundancy. Thus, it is considered that this ASRCP is possible to move in $0 \leqq t \leqq 1$. Thus, the ASRCP with the sufficient workspace was able to be designed.

3.4.2   Control simulation

Actuation forces which have to be generated by the active elastic elements were calculated to control the designed ASRCP with three active elastic elements. The required normal reaction force was specified as $f_{q,z,req} = 3$ N, and weight values of the multiple-optimizations were specified as $w_1 = 1 \times 10^{-1}$, $w_2 = 1 \times 10^{-3}$ and $w_3 = 1$. The calculated actuation forces during $0 \leqq t \leqq 1$ are shown in Fig.3.10, where the i-th active elastic element is described as A_i.

The sum of translation forces between the links during $0 \leq t \leq 1$ is shown in Fig.3.11. Although $\mathrm{TI_w}$ was not zero at $t = 0$ in Fig.3.9, actuation forces were able to be calculated at the point as shown in Fig.3.10. In addition, the force-closure state was satisfied as shown in Fig.3.11. Therefore, the workspace was able to be evaluated correctly with $\mathrm{TI_{rw}}$.

By using the calculated actuation forces, the ASRCP was driven in a simulation. $y_{q,ZMP}$ during the rolling motion is shown in Fig.3.12. This figure shows that the AS-
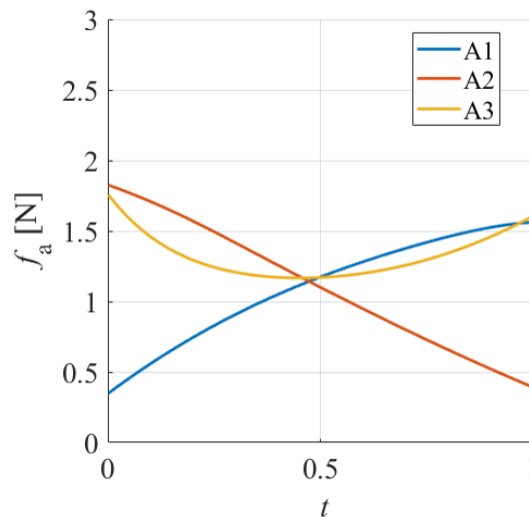
Fig.3.10   Actuation forces generated by three active elastic elements to control the designed ASRCP
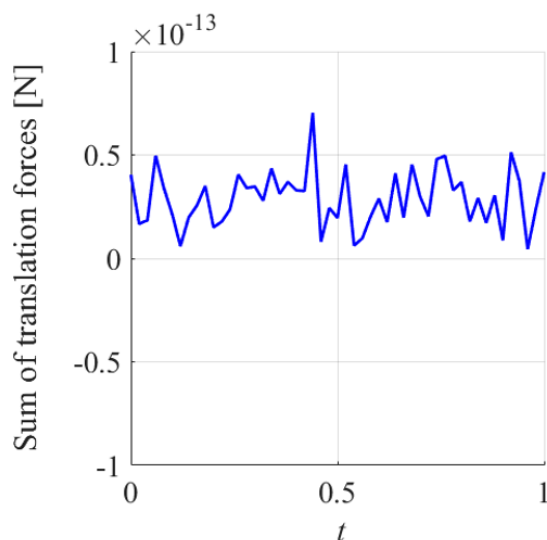
Fig.3.11   Sum of the translation forces between the links of the ASRCP during the rolling motion
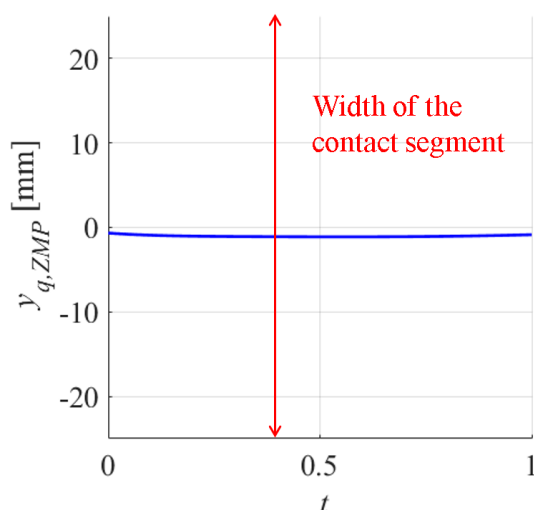
Fig.3.12   Zero moment point between the links of the ASRCP during the rolling motion

RCP was always in a very stable state because $y_{q,ZMP}$ was always near the midpoint of the contact segment. In addition, the normal reaction force at the midpoint of the contact segment, $f_{q,z}$, is shown in Fig.3.13. This figure shows that the normal reaction force was always kept constant to the specified value. Therefore, the ASRCP was able to generate the ideal rolling motion. These results are considered due to the actuation redundancy of the designed ASRCP. Therefore, the ASRCP is considered to generate the relative rolling motion between the links more stably than a spatial-path generator with the passive SRCP.
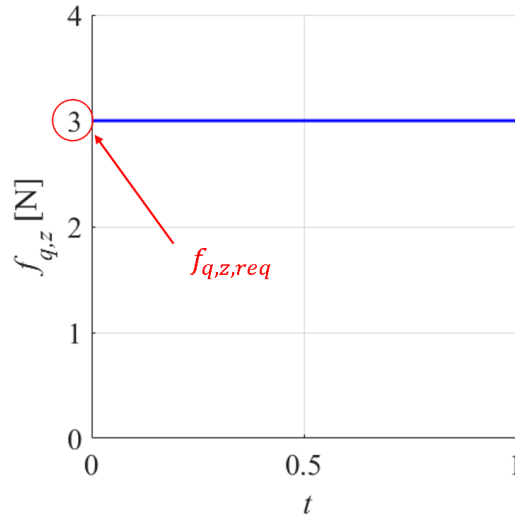
Fig.3.13   The normal reaction force between the links of the ASRCP during the rolling motion

3.5   Prototyping and evaluation

In this section, the ASRCPs with some types of active elastic elements are prototyped, and their performances are evaluated by motion-capture experiments.

3.5.1   The ASRCP driven with reeled elastic wires

The ASRCP designed in section 3.4 was prototyped with reeled elastic wires. The fabricated ASRCP is shown in Fig.3.14. The two links of the SRCP were fabricated with the FDM by a 3D-printer. The flexible bands between the links were fabricated with the material-jetting method by another 3D-printer. Note that the thickness of the fabricated flexible bands is 0.6 mm and the gap between adjacent bands is 2 mm. Each wire is composed of serially connected the UHPE (Ultra High Molecular Weight Polyethylene) cable and a linear spring. The wires can be reeled by pulleys driven with geared DC motors via cable guides. Each cable guide for A_i is placed at the position corresponding to ${}^1\boldsymbol{c}_{1,i}$.

The actuation forces calculated in section 3.4 can be generated just by position feedback control of the pulleys in the fabricated reeled-wire system. Fig.3.15 shows the schematic diagram of the reeled-wire system. Let k_s and k_c be the spring constants of the linear spring and the cable, respectively. Then, the spring constant of the elastic wire is as follows.

$$k_w = (\frac{1}{k_c} + \frac{1}{k_s})^{-1} \tag{3.22}$$

The tension of the i-th wire can be generated by controlling displacements of wires as shown in the following equation.

$$f_{a,i}(t) = k_w(r_p \Delta \theta_i) - k_w \Delta l_w(t), \tag{3.23}$$
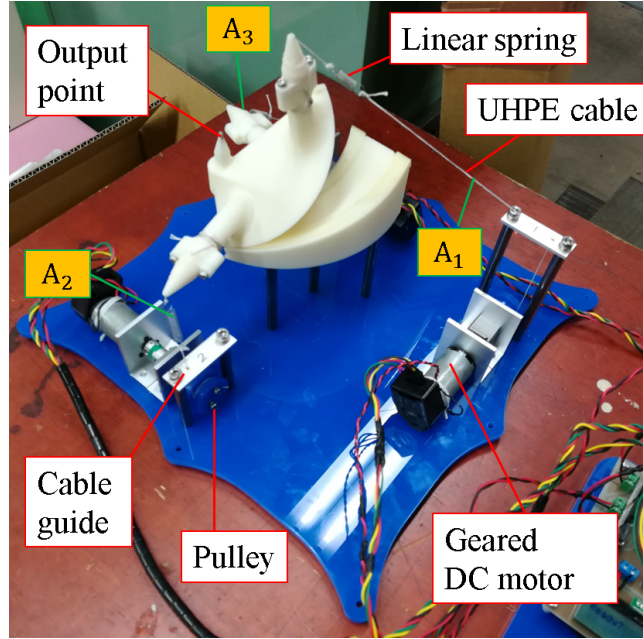
Fig.3.14   The fabricated ASRCP driven with three reeled elastic wires.
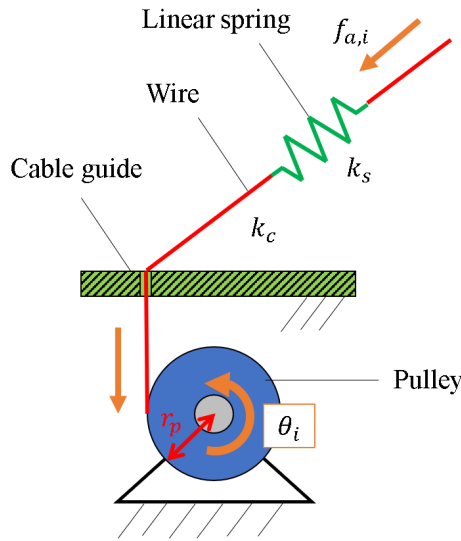
Fig.3.15   Schematic diagram of the reeled elastic-wire drive system

where r_p is the radius of the pulley, $\Delta\theta_i$ is the angular displacement of the i-th pulley, and Δl_w is the kinematic displacement of the i-th wire. Therefore, $\Delta\theta_i$ can be calculated with the following equation.

$$\Delta\theta_i(t) = \frac{\Delta l_w(t)}{r_p} + \frac{f_{a,i}(t)}{r_p k_w} \tag{3.24}$$

Note that it is possible that the cable has non-linear stiffness characteristics. However, if k_c is much larger than k_s, $k_w \simeq k_s$ holds. Therefore, stiffness characteristics of the wire can be assumed as linear characteristics of the linear spring.
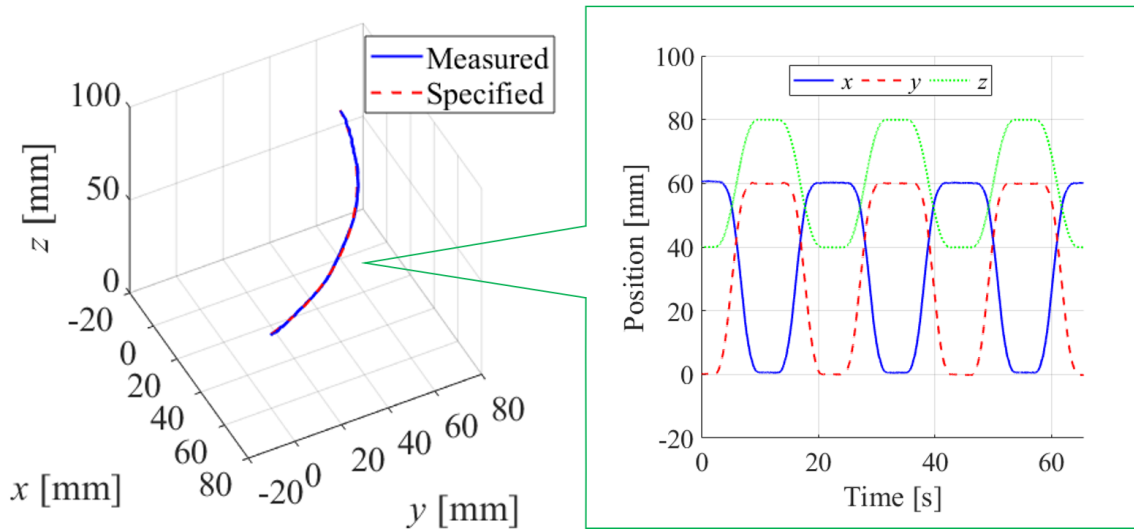
Fig.3.16 The measured output trajectories generated by the fabricated ASRCP with the reeled elastic-wire drive system

The fabricated ASRCP was controlled with the proposed method, and the output trajectories were measured with the motion capture system (OptiTrack V120:Duo). In this experiment, the output point reciprocated three times in the workspace. The measured trajectories are shown in Fig.3.16. This result shows that the measured trajectories agree well with the specified trajectory. The mean error between the measured and the specified trajectories was 0.341 mm. It is considered that this error was caused by fabrication errors. Therefore, it was confirmed that the proposed design method and control method of the ASRCP are valid. In addition, this error is smaller than the error in the experiment in section 2.6. The reasons are considered as follows.

- The number of parts, especially joints, of the fabricated ASRCP is smaller than the closed-loop SRCP-link mechanism fabricated in section 2.6.
- The stability of the rolling motion is better than the passive SRCP because of the redundant actuation with the active elastic elements.

Therefore, the ASRCP is useful to generate the specified trajectory accurately.

3.5.2 The ASRCP driven with artificial muscles

In order to achieve a compact and lightweight structure of the ASRCP, the ASRCP with artificial muscles (flexible pneumatic actuators) was designed and fabricated. As artificial muscles, many types of flexible pneumatic actuators have been proposed. For example, there are fluid-driven pneumatic actuators [119] such as Mckiben actuator, shape memory alloy actuators [120] [121], dielectric elastomer actuators [122] and so on. In order to drive the SRCP with a compact structure, both a large contraction ratio and sufficient output force are required. Recently, Li et al. proposed the fluid-driven origami-inspired artificial muscle (FOAM) [123]. It is expected to have both a large contraction ratio up to about 90% and sufficient output force. Thus, it is suitable to drive the SRCP. Therefore, the
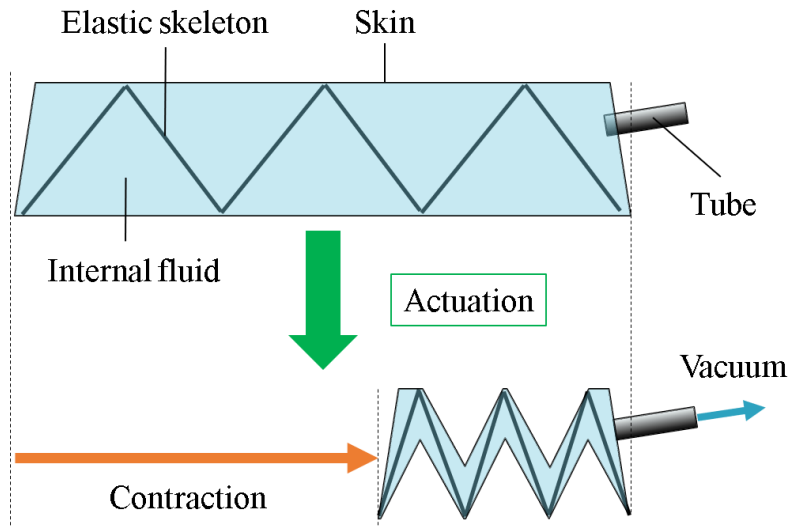
Fig.3.17 Operation principle of the fluid-driven origami inspired artificial muscle (FOAM) proposed by Li et al.[123]
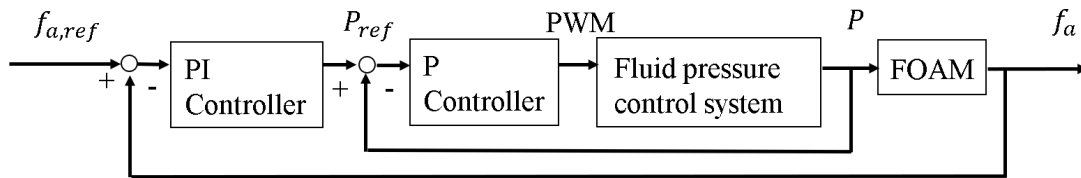
Fig.3.18 Block diagram of the output-force control of the FOAM

ASRCP with the FOAMs was designed and fabricated.

Fig.3.17 shows operation principle of the pneumatic FOAM. It has an elastic skeleton with zigzag shape, and it is covered by a thin skin. In the skin, fluid such as air is filled. When internal fluid is vacuumed from the skin and the pressure in the skin becomes lower than the outside, the FOAM contracts because the elastic skeleton is deformed by the tension generated on the skin. In order to control the output force of the FOAM, force-feedback control was used. Fig.3.18 shows the block diagram. It is a cascade control with force feedback control (PI control) in the major loop and fluid-pressure feedback control (P control) in the minor loop. Since the error of the fluid-pressure do not affect the output force because of the minor loop, the FOAM can be controlled with robustness against disturbances. Fig.3.19 shows a detailed control system in the case when air is used as the internal fluid of the FOAM. The air-pressure control system has two proportional control valves with 2 ports at inflow side from the atmosphere and at outflow side to the vacuum pump. The current input to the valves is controlled by PWM control. When pulse with a duty ratio ν is input to one side of the valves and pulse with the duty ratio $(1 - \nu)$ is input to another side, the same function of a proportional valve with 3 ports can be achieved. Therefore, this system can achieve a 3-ports valve system with low cost parts.

The ASRCP with pneumatic FOAMs was designed. The specified rolling motion of
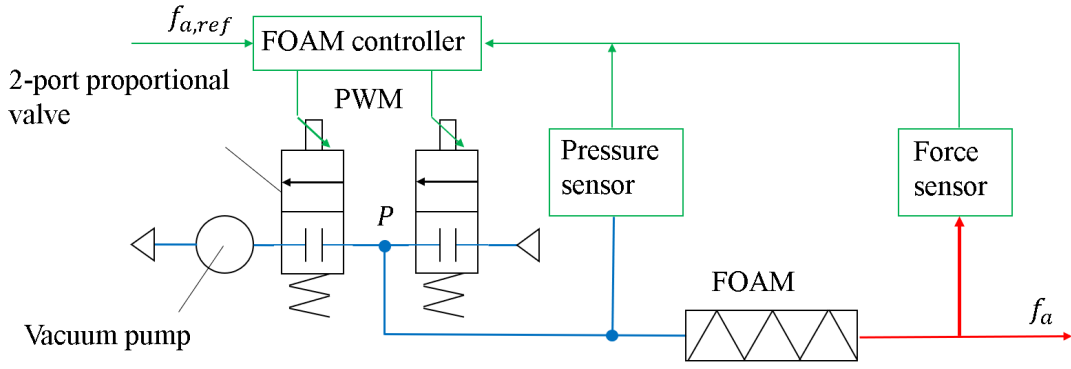
Fig.3.19   The detailed system to control the output force of the FOAM

SRCP is as follows.

$$^1\boldsymbol{p}(t) = \begin{bmatrix} 60\cos\frac{\pi t}{3} & 60\sin\frac{\pi t}{3} & 40t+40 \end{bmatrix}^T \quad (0 \leqq t \leqq 1) \ [\text{mm}] \tag{3.25}$$

$$^1\boldsymbol{\omega}(t) = \frac{\pi}{3}{}^1\boldsymbol{n}_p(t) \ [\text{rad/s}] \tag{3.26}$$

The rolling contact surfaces with width of 50 mm was derived with the parameter $25 \leqq u \leqq 25$ [mm]. Between the two surfaces, flexible bands with thickness of 0.6 mm were attached. Arrangement of the FOAMs were optimized subjecting to the following conditions.

$$[-100\ 70\ -120]^T \leqq {}^{r_1}\boldsymbol{c}_{r_1,1} \leqq [70\ 120\ -70]^T,$$
$$[-100\ -120\ -100]^T \leqq {}^{r_1}\boldsymbol{c}_{r_1,2} \leqq [70\ -70\ -50]^T,$$
$$[70\ -70\ -100]^T \leqq {}^{r_1}\boldsymbol{c}_{r_1,3} \leqq [120\ 80\ -50]^T \quad (\text{on } \Sigma_{r_1}),$$
$$[-50\ 60\ 50]^T \leqq {}^{r_2}\boldsymbol{c}_{r_2,1} \leqq [50\ 110\ 100]^T,$$
$$[-50\ -110\ 50]^T \leqq {}^{r_2}\boldsymbol{c}_{r_2,2} \leqq [50\ -60\ 100]^T,$$
$$[30\ -50\ 50]^T \leqq {}^{r_2}\boldsymbol{c}_{r_2,3} \leqq [80\ 50\ 100]^T \quad (\text{on } \Sigma_{r_2}) \ [\text{mm}],$$

where Σ_{r_1} and Σ_{r_2} were specified with $\psi = \frac{\pi}{6}$ rad. Then, the optimized endpoint positions of FOAMs became $^1\boldsymbol{c}_{1,1} = [-27.47\ 228.8\ 0.7181]^T$ [mm], $^1\boldsymbol{c}_{1,2} = [141.2\ 78.83\ -85.07]^T$ [mm], $^1\boldsymbol{c}_{1,3} = [-94.84\ 22.02\ -68.42]^T$ [mm], $^2\boldsymbol{c}_{2,1} = [-21.75\ 51.42\ 58.56]^T$ [mm], $^2\boldsymbol{c}_{2,2} = [79.21\ 32.84\ -50.19]^T$ [mm] and $^2\boldsymbol{c}_{2,3} = [-72.81\ -28.85\ -36.65]^T$ [mm]. In order to drive this ASRCP, FOAMs where minimum length is smaller than 87 mm, stroke is larger than 89 mm and the contraction ratio is larger than 44 %, were required. Therefore, the FOAMs to satisfy these requirements were designed. The design method and the procedure are described in appendix B.

   The ASRCP with the FOAMs was prototyped as shown in Fig.3.20. An end of each FOAM A_i is connected to the upper link with 1-axial free rotation and another end is connected to the lower link with 2-axis free rotation. The other rotations at connected points can be absorbed by the flexibility of the FOAM because those rotation angles are small. The detail of the fabricated FOAM was shown in Fig.3.21. The skeleton, of which material is copolyester, was fabricated with FDM by a 3D-printer. The skin was made of thin polyethylene (PE) sheets, of which thickness was 0.06 mm. On an end of the FOAM,
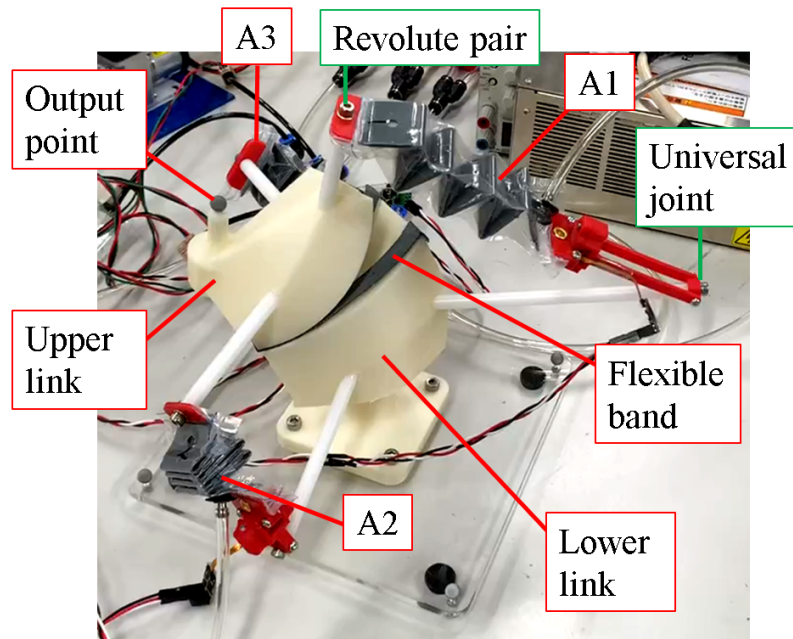
Fig.3.20   The prototype of the ASRCP with FOAMs
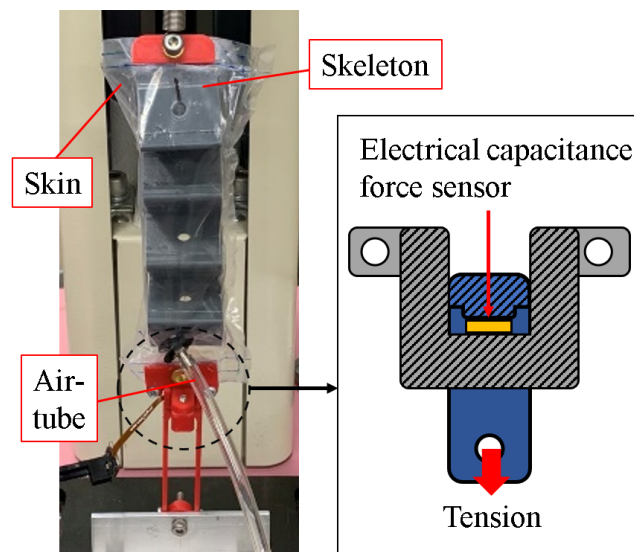
Fig.3.21   The fabricated FOAM with a tension sensor

a tension sensor was attached. This sensor can measure tension by transmitting from the tension of the FOAM to a compressive force to push an electrical capacitance force sensor.

The fabricated ASRCP was controlled with the proposed method, and the output trajectories were measured by the motion capture system. In this experiment, the output point also reciprocated three times. Fig.3.22 shows the measured trajectories. The figure (a) is the top view and the figure (b) is the side view. Although the specified trajectory was generated, there were some errors between the measured and the specified trajectories. The mean error between the specified and the measured trajectories was 2.59 mm. Various factors can be considered as the cause of the errors as follows.

(a) Top view   (b) Side view
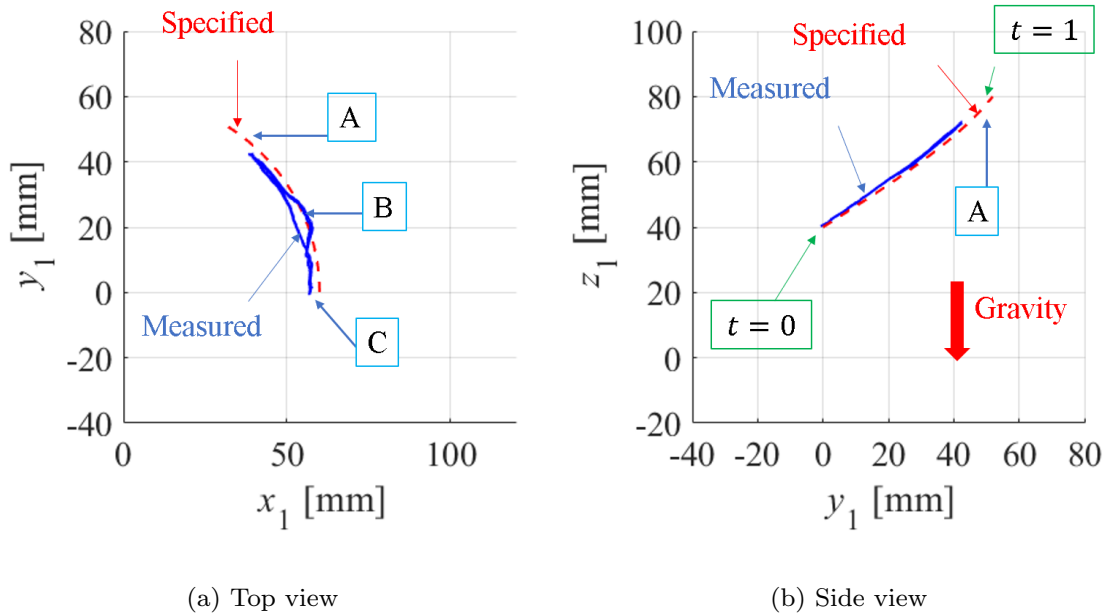
Fig.3.22   The measured output trajectories generated by the fabricated ASRCP with the FOAMs

- At part A shown in Fig.3.22 (a) and (b), the output point was not able to reach the position at $t = 1$. It is considered due to gravity. Since force-feedback control was used to control the FOAMs, the output stiffness of the ASRCP was generated just with kinematic non-linearity in the antagonistic drive system. Thus, the output stiffness of the ASRCP was small. Therefore, the two links were able to roll relatively from the position at $t = 1$ to the position at $t = 0$ easily.
- At part B shown in Fig.3.22 (a), the forward and backward trajectories are different. This is because the tension sensors had hysteresis due to the friction generated in the mechanism to convert pulling motion to pushing motion.
- The steady-sate errors shown at part C shown in Fig.3.22 (a) is considered due to the fabrication error of the ASRCP.

Although the motion was not so accurate, the SRCP was able to be driven with the FOAMs. If the control method of the FOAMs can be improved, it is possible to increase accuracy of the output motion in this system. Therefore, it was confirmed that it is possible to design the ASRCP with a compact structure by using fluid-driven artificial muscles.

3.6   Chapter summary

The active spatial rolling contact pair (ASRCP), which can generate the specified trajectory actively, was developed. In the ASRCP, the SRCP is constrained by several active elastic elements (pneumatic flexible actuators) to keep in contact between the links and to drive the pair actively. In this chapter, a design method and a control method of the

ASRCP were proposed, and some examples were designed and examined by experiments. The obtained results are summarized as follows.

(1) A criterion to evaluate the force transmission of parallel wire-driven mechanisms with the redundant number of the wires was proposed based on the idea of the transmission index proposed by Takeda et al. [98]. Then, a design method of the ASRCP was proposed, where several active elastic elements are arranged between two links of the SRCP optimally so as to maximize the transmission index, which is calculated with both tension of active elastic elements and contact forces between the links of the SRCP.

(2) A method to control the ASRCP with use of its actuation redundancy was proposed, where actuation forces of active elastic elements are optimally calculated to generate the ideal relative rolling motion between the links based on the evaluation criteria on the stability of relative rolling motion between the links proposed in chapter 2.

(3) An example of the ASRCP was designed and simulated. As a result, it was confirmed that it can generate the ideal rolling motion more efficiently than the passive SRCP because of its actuation redundancy.

(4) The ASRCP driven by reeled wire systems was prototyped and examined by a motion-capture experiment. As a result, it was confirmed that the proposed design method and the control method are valid and that it can generate the specified trajectory accurately.

(5) The ASRCP driven by fluid-driven origami-inspired artificial muscles (FOAMs) was prototyped and examined. As a result, it was confirmed that the ASRCP with a compact structure can be achieved by using artificial muscles.

Chapter 4

The Flexibly Constrained Pair

4.1   Chapter introduction

Flexibility is one of the required properties for a robot to reduce the load applying to it when it bumps with a human, or to adapt to an uncertain environment in a manipulation task. Therefore, many methods to introduce flexibility into joints of a robot have been proposed so far [83]-[66]. However, almost all methods provide flexibility in a single direction such as a rotation of a revolute pair. Thus, many flexible joints are required when multi-directional flexibility has to be achieved such as to increase safety for collision. In this case, the whole mechanism of the robot is possible to have a complex structure and heavy weight. Although some flexible joints have multi-directional flexibility [54]-[57], it is difficult to specify their flexibility in detail in their design. Since flexibility and force transmission are in the trade-off relationship, it is required to specify flexibility which is suitable to perform the task.

In order to solve the above problem, the "flexibly constrained pair" (FCP), which has the specified multi-directional flexibility, is proposed. Fig.4.1 shows the structure of the
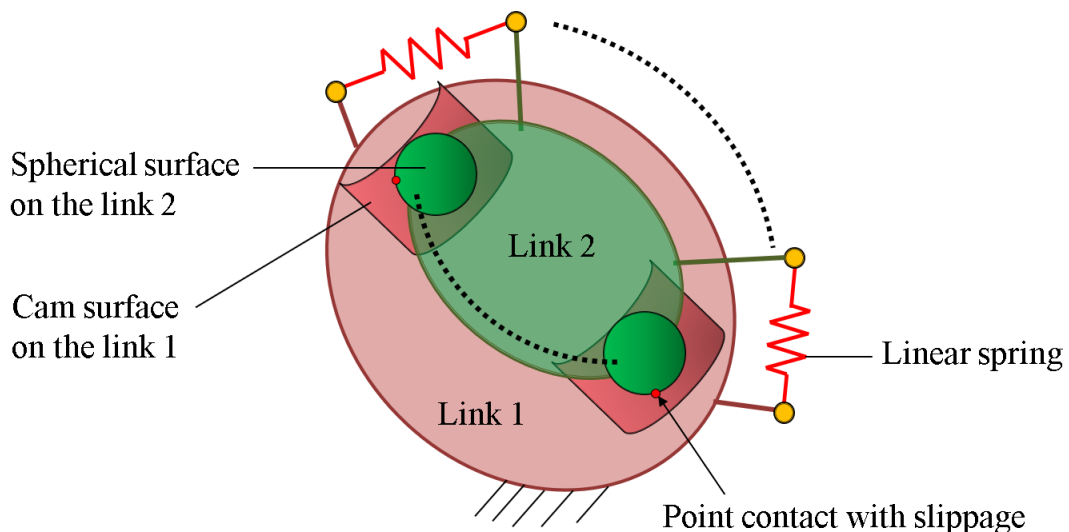
Fig.4.1   Structure of the flexibly constrained pair (FCP)

(a) Relative sub-translation   (b) Relative sub-rotation
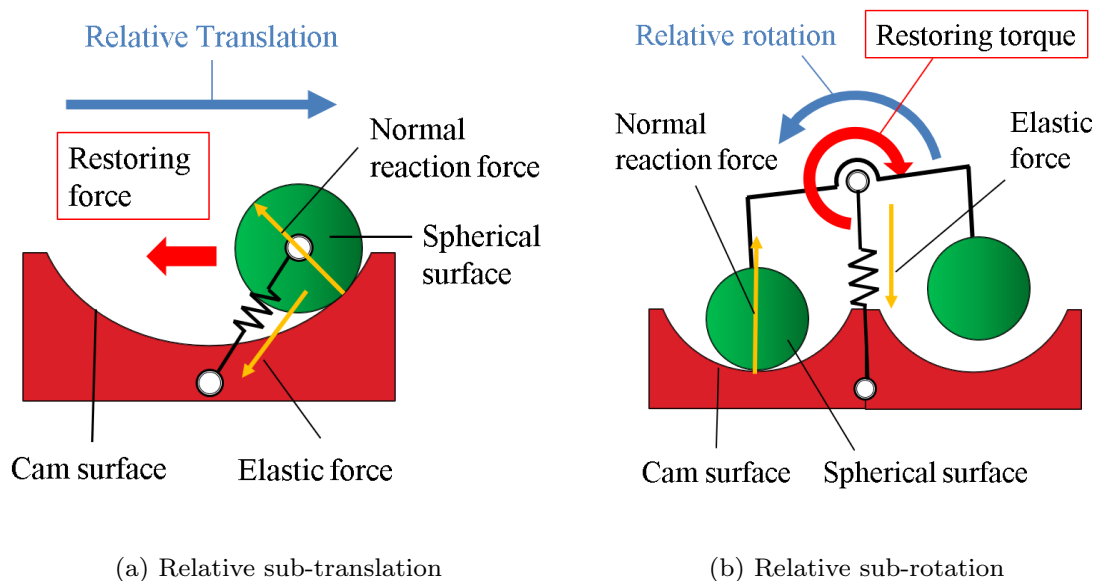
Fig.4.2   Principle of the flexibly kinematic constraint of the FCP

FCP. The FCP has a link with several spherical surfaces and a link with several cam surfaces. The two links are kept in contact by several linear springs so that each spherical surface and cam surface are in contact at a point. When the two links move relatively with slippage in the translation directions, they have stiffness generated by normal reaction forces between the links and elastic forces of the linear springs as shown in Fig.4.2 (a). In the same way, when the two links move relatively in the rotational directions, they have rotational stiffness as shown in Fig.4.2 (b). The stiffness in each direction can be specified by designing the arrangement of the linear springs, the cam profile, and arrangement of the cam and the spherical surfaces. When stiffness in some directions is specified to be higher than in the other directions, a weak kinematic constraint with the difference of the stiffness can be generated. The directions with small stiffness are called main-directions, and the other directions are called sub-directions. Because of this constraint, the two links can move relatively mostly in main-directions under small external loads, but they can also displace relatively in the sub-directions under large external loads. This means that this kinematic constraint can change according to mechanical conditions. Therefore, this kinematic constraint is named "flexible kinematic constraint". Since the FCP has both motion guidance and flexibility because of this constraint, a mechanism of a flexible robot can be synthesized with simple structure by using the FCP.

This chapter describes the following three contributions to achieve the FCP.

(1) Proposal and validation of a design method to achieve a flexible kinematic constraint with the specified difference in stiffness between the links
(2) Proposal and validation of a design method to achieve the specified non-linear stiffness characteristics in sub-directions between the links
(3) Prototyping and examination of a simple robotic mechanism with the FCPs

In section 4.2, a design method of the FCP is described. In section 4.3, several design examples of the FCP are shown. In section 4.4, several examples are prototyped and examined to confirm the validity of the proposed design method. In section 4.5, a simple robotic mechanism with the FCP is synthesized and prototyped, and its performances are investigated through analyses and experiments.

4.2 Design method

A design method for the FCP to have the specified flexible kinematic constraint is described. Firstly, multiple directions allowed between the links is divided into the main-directions and the sub-directions. DOF of the main-directions and the sub-directions are called main-DOF and sub-DOF, respectively. Then, the main relative kinematic motion is specified. Next, linear springs are optimally arranged between the links to reduce stiffness in the main-direction. Then, profiles of the cam surface is derived to have the specified stiffness characteristics in the relative translation directions. Finally, several sets of the designed cam and the spherical surfaces are arranged between the links to constrain relative rotations between the links flexibly.

4.2.1 Motion specification

The relative motion between the links of the FCP is specified. If two links of the FCP keep in contact at least at a single point, the FCP allows two relative translations and three relative rotations. Thus, the FCP can allow 5 DOF. Let parameters on the two translations be t, u, and parameters on three rotations be θ_r, θ_p and θ_y, which are the roll, pitch and yaw angles, respectively. Then, parameters in main-DOF are represented as t_m, u_m, $\theta_{r,m}$, $\theta_{p,m}$ and $\theta_{y,m}$, while parameters in sub-DOF are represented as t_s, u_s, $\theta_{r,s}$, $\theta_{p,s}$ and $\theta_{y,s}$. Firstly, several main-parameters are chosen from the five parameters, and the other main-parameters are then specified as zero. In the same way, several sub-parameters are chosen from the five parameters, and the other sub-parameters are then specified as zero. Note that the choice of sub-parameters must reciprocate to the chosen main-parameters. For example, if t_m and u_m are chosen from main-parameters, $\theta_{r,s}$, $\theta_{p,s}$ and $\theta_{y,s}$ must be chosen from sub-parameters.

Next, the relative main-motion is specified in detail. The reference position (output position) $^1\boldsymbol{p}$ can generate the specified point, curve (line) and surface (plane) as follows.

$$^1\boldsymbol{p}(t_m, u_m) = [x_1(t_m, u_m)\ y_1(t_m, u_m)\ z_1(t_m, u_m)]^T, \tag{4.1}$$

where $x_1(t_m, u_m)$, $y_1(t_m, u_m)$ and $z_1(t_m, u_m)$ are arbitrary functions. If $^1\boldsymbol{p}$ is a curve (line), only t_m is used and u_m is specified to be zero. Besides, ranges of main parameters are specified as follows.

$$A_m = \{(t_m, ...)|\ t_{m,0} \leqq t_m \leqq t_{m,1}, ...\} \tag{4.2}$$

As described above, parameters which have not been chosen are fixed to zero in A_m.

4.2.2 Reduction of stiffness in main-directions

In order to reduce stiffness in main-directions, linear springs are optimally arranged between the links so as to minimize elastic forces applied in main-directions. Fig.4.3 shows the schematic diagram of the FCP. Σ_1 is the reference coordinate system fixed on the link with the cam surface (link1). Σ_2 is the reference coordinate system fixed on the link with the spherical surface (link2), of which origin is normally at $^1\boldsymbol{p}$. Several linear springs are arranged between the two links. The endpoint positions of the i-th linear spring attached on the link 1 and link 2 are represented as $^1\boldsymbol{c}_{1,i}$ on Σ_1 and $^2\boldsymbol{c}_{2,i}$ on Σ_2, respectively. Thus, the elastic force of the i-th linear spring is represented as the following equation.

$$^1\boldsymbol{d}_{s,i} = [\boldsymbol{R}_{1,2}(\theta_{r,m}, \theta_{p,m}, \theta_{y,m})^2\boldsymbol{c}_{2,i} + {}^1\boldsymbol{p}(t_m, u_m)] - {}^1\boldsymbol{c}_{1,i} \tag{4.3}$$

$$^1\boldsymbol{f}_{s,i} = -[k_i(|^1\boldsymbol{d}_{s,i}| - l_{0,i}) + f_{s,0,i}]\frac{^1\boldsymbol{d}_{s,i}}{|^1\boldsymbol{d}_{s,i}|}, \tag{4.4}$$

where $\boldsymbol{R}_{1,2}(\theta_{r,m}, \theta_{p,m}, \theta_{y,m})$ is the rotation matrix from Σ_1 to Σ_2, and where k_i, $l_{0,i}$ and $f_{s,0,i}$ are the spring constant, natural length and the initial tension respectively of the i-th linear spring. Therefore, the sum of the wrench on Σ_2 is calculated with the following equation.

$$^2\mathbb{W}_s(t_m, u_m, \theta_{r,m}, \theta_{p,m}, \theta_{y,m}) = \sum_{i=1}^{N_s}\left[\begin{matrix}\boldsymbol{R}_{1,2}^{T\,1}\boldsymbol{f}_{s,i} \\ ^2\boldsymbol{c}_{2,i} \times (\boldsymbol{R}_{1,2}^{T\,1}\boldsymbol{f}_{s,i})\end{matrix}\right], \tag{4.5}$$

where N_s is the number of linear springs.

In the optimization, the mean value of $|^2\mathbb{W}_s|$ in the specified motion range A_m is minimized subject to the condition where the normal reaction force is larger than the required value. Thus, the normal reaction force between the links is also calculated. Since
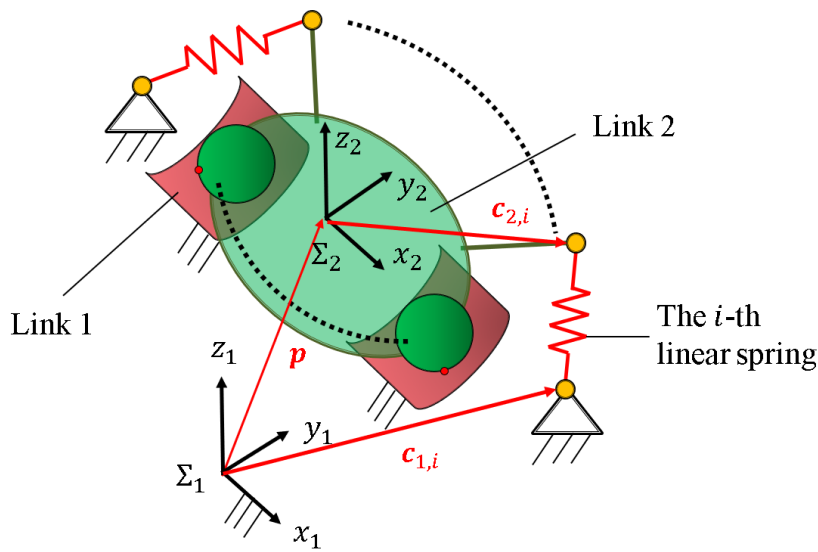
Fig.4.3 Schematic diagram of the FCP for the optimal arrangement of linear springs

the cam profile has not been determined yet in this procedure, the direction of the normal reaction force $^1\hat{\boldsymbol{n}}_p$ between the links is assumed in this process. Based on geometry of the specified reference position $^1\boldsymbol{p}(t_m, u_m)$, $^1\hat{\boldsymbol{n}}_p$ can be determined as follows.

- If $^1\boldsymbol{p}(t_m, u_m)$ is a point, $^1\hat{\boldsymbol{n}}_p$ is an arbitrary direction.
- If $^1\boldsymbol{p}(t_m, u_m)$ is a line, $^1\hat{\boldsymbol{n}}_p$ is an arbitrary direction orthogonal to $^1\dot{\boldsymbol{p}}$.
- If $^1\boldsymbol{p}(t_m, u_m)$ is a curve, $^1\hat{\boldsymbol{n}}_p$ is the unit bi-normal vector of $^1\boldsymbol{p}$.
- If $^1\boldsymbol{p}(t_m, u_m)$ is a surface (plane), $^1\hat{\boldsymbol{n}}_p$ is the normal vector of $^1\boldsymbol{p}$.

Then, the normal reaction force can be calculated as follows.

$$f_n(t_m, u_m, \theta_{r,m}, \theta_{p,m}, \theta_{y,m}) = {}^1\hat{\boldsymbol{n}}_p^T \sum_{i=1}^{N_s} {}^1\boldsymbol{f}_{s,i} \tag{4.6}$$

Therefore, the design parameter $\boldsymbol{c} = [^1\boldsymbol{c}_{1,1}^T, ...^1, \boldsymbol{c}_{1,N_s}^T, {}^2\boldsymbol{c}_{2,1}^T, ..., {}^2\boldsymbol{c}_{2,N_s}^T]$ is calculated by solving the following optimization problem with a numerical optimization method.

$$\text{minimize} \qquad\qquad F(\boldsymbol{c}) = \underset{A_m}{\text{mean}}(|^2\mathbb{W}_s|), \tag{4.7}$$

$$\text{subject to} \qquad\qquad \underset{A_m}{\text{mean}}(|f_n|) \geqq f_{n,req}, \tag{4.8}$$

$$\boldsymbol{c}_{min} \leqq \boldsymbol{c} \leqq \boldsymbol{c}_{max}, \tag{4.9}$$

$$l_{0,i} \leqq |^1\boldsymbol{d}_{s,i}| \leqq l_{max,i} \tag{4.10}$$

where $f_{n,req}$ is the required normal reaction force, and $l_{max,i}$ is the allowable maximum length of the i-th linear spring.

4.2.3   Flexible translation constraint

If the specified $^1\boldsymbol{p}(t_m, u_m)$ is a surface, the cam profile is uniquely derived as an envelope surface of the spherical surface generating main-translations. However, if $\boldsymbol{p}(t_m, u_m)$ is a point or a curve (line), the sub-translations can be specified freely. In these cases, the motion can be specified to have the specified stiffness characteristics in the sub-translation directions by designing the cam profile. In this section, a design method of the cam profile to have the specified stiffness characteristics in sub-translation directions is described.

Since stiffness characteristics in the sub-translation directions are generated by elastic forces of the linear springs and the normal reaction forces between the links, they can be specified as a relationship between the restoring force and the translation displacement. As such kind of relationships, the following two types are proposed.

(a)   Relationship between force and displacement of the center of the sphere
(b)   Relationship between force and displacement of the contact point between the links

When the characteristics (a) are used, designers can intuitively understand the motion when an external force is applied to the FCP. However, the size of the cam surface is possible to be large because the size cannot be controlled in the design process. On the other hand, when the characteristics (b) are used, designers can control the size of the cam surface because the cam surface coincides with the area where the contact point can move. However, the relative displacement between the links is not intuitive for designers.
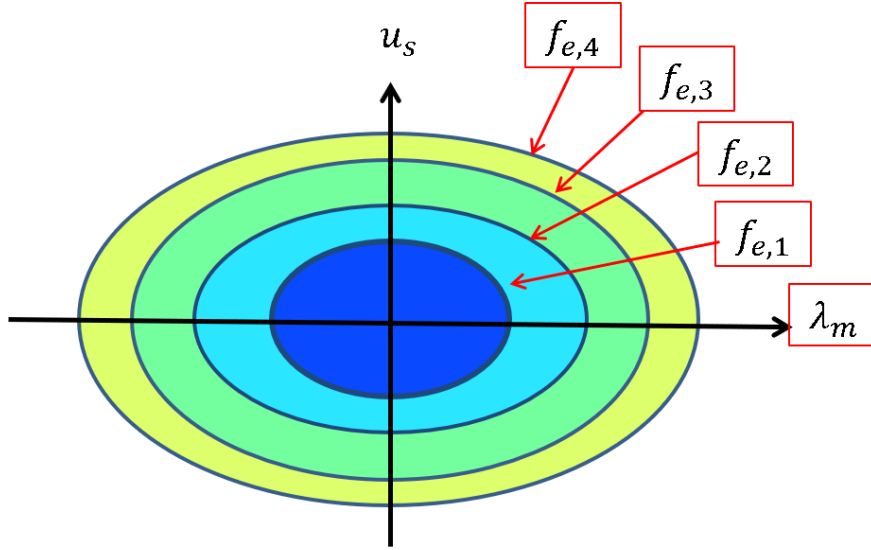
Fig.4.4   Conceptual diagram of the contour map on anisotropy between specified stiffness characteristics in the sub-direction and those in the main-direction

Since the advantage and the disadvantage of the characteristics (a) and (b) are opposite, one of the two characteristics should be chosen by designers according to its application.

If $\boldsymbol{p}(t_m, u_m)$ is a curve (line), it is important to specify the larger stiffness in the sub-direction than in the main-direction. Thus, the stiffness characteristics in the sub-direction is compared with ones in the main-direction in the process that the stiffness characteristics are specified. If the curve (line) is represented as $^1\boldsymbol{p}(t_m, 0)$, the restoring force in the main-direction is calculated with $^1\boldsymbol{f}_{s,i}$ of Eq.(4.4) as follows.

$$f_{s,t}(t_m) = \sum_{i=1}^{N_s} \frac{{}^1\boldsymbol{f}_{s,i}^T(t_m, 0, \theta_{r,m}, \theta_{p,m}, \theta_{y,m})\,{}^1\dot{\boldsymbol{p}}(t_m, 0)}{|{}^1\dot{\boldsymbol{p}}(t_m, 0)|}, \tag{4.11}$$

where $\theta_{r,m}$, $\theta_{p,m}$, $\theta_{y,m}$ can be specified to arbitrary posture angles. In order to obtain the force-displacement characteristics in the main-direction, the parameter t_m is transformed to the following arc-length parameter in the main-direction.

$$\lambda_m = \int_{t_{m,0}}^{t_m} |{}^1\dot{\boldsymbol{p}}(t, 0)| dt \tag{4.12}$$

Let the specified force-displacement characteristics be $f_{d,u}(u_s)$. Then, the following function is plotted in contour map as shown in Fig.4.4.

$$f_e(\lambda_m, u_s) = \sqrt{f_{s,t}(\lambda_m)^2 + f_{d,u}(u_s)^2} \tag{4.13}$$

Eq.(4.13) is displayed as an elliptical shape for a value of f_e. If $f_{d,u}(u_s)$ is specified so that the λ_m axis is its major axis, the stiffness in the sub-direction becomes larger than the stiffness in the main-direction.

The cam profile to generate the specified force-displacement characteristics is derived. Fig.4.5 shows the kinetostatic model of a pair of the cam and the spherical surface constrained with several linear springs, where friction between the two surfaces is neglected.
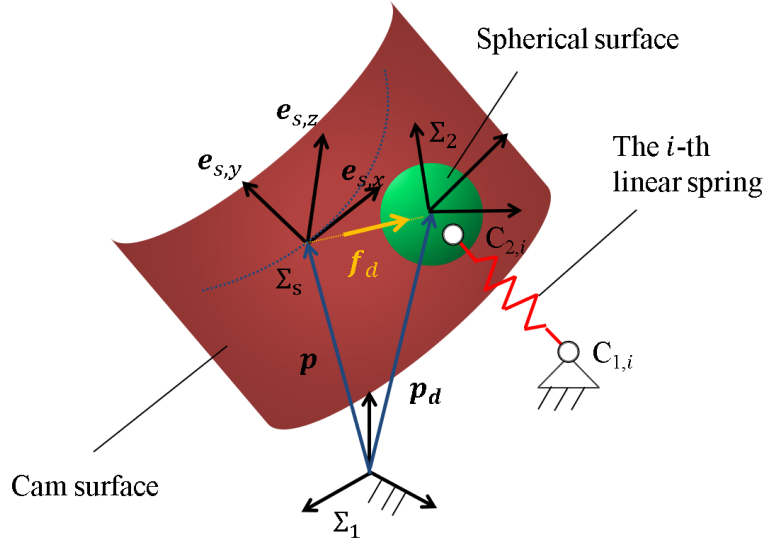
Fig.4.5 Kinetostatic model of the FCP for the cam profile design

In this process, it is assumed that the center of the sphere is initially located at the position $^1\boldsymbol{p}(t_m, u_m)$. In addition to Σ_1 and Σ_2, Σ_s is defined. The origin of Σ_s is located at the position $\boldsymbol{p}(t_m, u_m)$ and one of its bases $^1\boldsymbol{e}_{s,z}$ is corresponding to $^1\hat{\boldsymbol{n}}_p$, which has been specified in section 4.2.2. The other basis $^1\boldsymbol{e}_{s,x}$, $^1\boldsymbol{e}_{s,y}$ are specified based on the geometry of $^1\boldsymbol{p}(t_m, u_m)$ as follows.

- If $^1\boldsymbol{p}(t_m, u_m)$ is a point or a surface, $^1\boldsymbol{e}_{s,x}$ can be specified in an arbitrary direction orthogonal to $^1\boldsymbol{e}_{s,z}$, and $^1\boldsymbol{e}_{s,y}$ is specified orthogonal to $^1\boldsymbol{e}_{s,x}$ and $^1\boldsymbol{e}_{s,z}$.
- If $^1\boldsymbol{p}(t_m, u_m)$ is a curve (line), $^1\boldsymbol{e}_{s,x}$ is specified to be the unit tangent vector of the curve, and $^1\boldsymbol{e}_{s,y}$ is specified orthogonal to $^1\boldsymbol{e}_{s,x}$ and $^1\boldsymbol{e}_{s,z}$.

In the following, the methods to derive cam profile for each of the above force-displacement characteristics (a), (b) are described.

(a) Design based on the center of the sphere

When an external force $^s\boldsymbol{f}_d(t_s, u_s) = [f_{d,t}(t_s)\ f_{d,u}(u_s)\ 0]^T$ (on Σ_s) is applied to the sphere, the center point of the spherical surface displace in the sub-translation direction from $^1\boldsymbol{p}(t_m, u_m)$. Then, the displaced position $^1\boldsymbol{p}_d$ is represented as following equation.

$$^1\boldsymbol{p}_d = {}^1\boldsymbol{p}(t_m, u_m) + \boldsymbol{R}_{1,s}[t_s\ u_s\ g_d]^T, \tag{4.14}$$

where $\boldsymbol{R}_{1,s} = [^1\boldsymbol{e}_{s,x}\ {}^1\boldsymbol{e}_{s,y}\ {}^1\boldsymbol{e}_{s,z}]$. In this case, the relationship between works of the external force and the potential energy of linear springs are as follows.

$$\sum_{i=1}^{N_s}[\frac{k_i}{2}(\Delta l_i^2 - \Delta l_{i,0}^2) + f_{s,0,i}(\Delta l_i - \Delta l_{i,0})] - \int_{u_{s,0}}^{u_s} f_{d,u}(u)du - \int_{t_{s,0}}^{t_s} f_{d,t}(t)dt = 0,$$

$$\tag{4.15}$$

$$\Delta l_i = |^1\boldsymbol{d}_{s,i}| - l_{0,i}, \tag{4.16}$$

$$^1\boldsymbol{d}_{s,i} = [\boldsymbol{R}_{1,2}(\theta_{r,m}, \theta_{p,m}, \theta_{y,m})^2\boldsymbol{c}_{2,i} + {}^1\boldsymbol{p}_d(t_m, u_m, t_s, u_s, g_d)] - {}^1\boldsymbol{c}_{1,1}, \tag{4.17}$$

where $\Delta l_{i,0}$ is Δl_i when $t_s = u_s = 0$. The posture angles $\theta_{r,m}$, $\theta_{p,m}$, $\theta_{y,m}$ are assumed to be arbitrary values. In this case, Eq.(4.15) is the function of t_m, u_m, t_s, u_s and g_d, where two variables of t_m, u_m, t_s, u_s are fixed to zero as described in section 4.2.1. Therefore, each set of (t_m, u_m, t_s, u_s) is substituted in Eq(4.15), and it is solved for g_d numerically. Then, the surface which the center of the sphere passes through, $^1\boldsymbol{p}_d$, can be calculated with Eq.(4.14). Since the cam surface is an envelope surface of this surface, it can be calculated as follows.

$$^1\boldsymbol{s}_c = {}^1\boldsymbol{p}_d + \frac{r_s}{\sqrt{1 + (\frac{\partial g_d}{\partial t})^2 + (\frac{\partial g_d}{\partial u})^2}} \boldsymbol{R}_{1,s} \begin{bmatrix} \frac{\partial g_d}{\partial t} \\ \frac{\partial g_d}{\partial u} \\ -1 \end{bmatrix}, \tag{4.18}$$

where r_s is the radius of the sphere, t is t_s or t_m, and u is u_s or u_m, which are chosen in section 4.2.

Note that since a unique cam profile is derived for the assumed $\theta_{r,m}$, $\theta_{p,m}$, $\theta_{y,m}$, the specified and output force-displacement characteristics have errors when the posture angles change from the specified values. Therefore, a method where posture angles are specified so that the output force-displacement characteristics vary around the specified characteristics is proposed. Let the motion range of only translation motions be represented as $A_{tr} = \{t_m, u_m, t_s, u_s | t_{m,0} \leqq t_m \leqq t_{m,1}, ...\}$. Then, the following function is defined.

$$M(\theta_{r,m}, \theta_{p,m}, \theta_{y,m}) = \underset{A_{tr}}{\mathrm{mean}}(|^1\boldsymbol{f}_s(t_m, u_m, t_s, u_s, \theta_{r,m}, \theta_{p,m}, \theta_{y,m})|) \tag{4.19}$$

$$^1\boldsymbol{f}_s = -\sum_{i=1}^{N_s}(k_i \Delta l_{0,i} + f_{s,0,i})\frac{^1\boldsymbol{d}_{s,i}}{|^1\boldsymbol{d}_{s,i}|} \tag{4.20}$$

This function represents an effect of the elastic forces in the translation directions. Therefore, the posture angles $\theta_{r,m}$, $\theta_{p,m}$, $\theta_{y,m}$ which take median of $M(\theta_{r,m}, \theta_{p,m}, \theta_{y,m})$ in the motion range $A_{rot} = \{\theta_{r,m}, \theta_{p,m}, \theta_{y,m} | \theta_{r,m,0} \leqq \theta_{r,m} \leqq \theta_{r,m,1}, ...\}$ are used for the cam profile design. Such posture angles can be calculated by solving the following non-linear equation numerically.

$$M(\theta_{r,m}, \theta_{p,m}, \theta_{y,m}) - \frac{\max_{A_{rot}}(M) + \min_{A_{rot}}(M)}{2} = 0 \tag{4.21}$$

where $\max_{A_{rot}}(M)$ and $\min_{A_{rot}}(M)$ are calculated with a numerical optimization method in advance.

(b) Design based on the contact point

When an external force $^s\boldsymbol{f}_d(t_s, u_s) = [f_{d,t}(t_s) \; f_{d,u}(u_s) \; 0]^T$ (on Σ_s) is applied to the sphere, the contact point of the spherical surface displace in the sub-translation direction from the initial position. Then, the position $^1\boldsymbol{s}_c$ is represented as following equation.

$$^1\boldsymbol{s}_c = {}^1\boldsymbol{p}(t_m, u_m) + \boldsymbol{R}_{1,s}[t_s \; u_s \; g_c]^T \tag{4.22}$$

In this case, the statics equation in translation directions on Σ_s is represented as follows.

$$^s\boldsymbol{f}_d + \boldsymbol{R}_{1,s}^{T}\,^1\boldsymbol{f}_s + f_{n,c}\,^s\hat{\boldsymbol{n}}_c = \boldsymbol{0}, \tag{4.23}$$

$$^s\hat{\boldsymbol{n}}_c = \frac{1}{\sqrt{1 + (\frac{\partial g_c}{\partial t})^2 + (\frac{\partial g_c}{\partial u})^2}} \begin{bmatrix} -\frac{\partial g_c}{\partial t} \\ -\frac{\partial g_c}{\partial u} \\ 1 \end{bmatrix}, \tag{4.24}$$

$$^1\boldsymbol{f}_s = -\sum_{i=1}^{N_s}[k_i(^1\boldsymbol{d}_{s,i} - l_{0,i}) + f_{s,0,i}]\frac{^1\boldsymbol{d}_{s,i}}{|^1\boldsymbol{d}_{s,i}|}, \tag{4.25}$$

$$^1\boldsymbol{d}_{s,i} = [\boldsymbol{R}_{1,2}(\theta_{r,m}, \theta_{p,m}, \theta_{y,m})^2\boldsymbol{c}_{2,i} + (^1\boldsymbol{s}_c + r_s\boldsymbol{R}_{1,s}\,^s\hat{\boldsymbol{n}}_c)] - {}^1\boldsymbol{c}_{1,i}, \tag{4.26}$$

where $f_{n,c}$ is the magnitude of normal reaction force, g_c is the cam profile on Σ_s, t is t_s or t_m, and u is u_s or u_m. When components of $\boldsymbol{R}_{1,s}^T\,^1\boldsymbol{f}_s$ are represented as $[f_{s,t}\ f_{s,u}\ f_{s,n}]^T$, the statics equation can be rewrite as follows.

$$\begin{cases} f_{s,n}\frac{\partial g_c}{\partial t} + f_{d,t} + f_{s,t} = 0 \\ f_{s,n}\frac{\partial g_c}{\partial u} + f_{d,u} + f_{s,u} = 0 \end{cases} \tag{4.27}$$

When the arbitrary posture angles $\theta_{r,m}$, $\theta_{p,m}$ and $\theta_{y,m}$ and each set of (t_m, u_m, t_s, u_s) are substituted into Eq.4.27, the equation can be solved for g_c. However, it is difficult to solve the partial differential equation numerically because $\frac{\partial g_c}{\partial t}$ and $\frac{\partial g_c}{\partial u}$ are implicitly included in $f_{s,t}$, $f_{s,u}$ and $f_{s,n}$. Thus, this differential equation is solved with the following procedure.

(1) Arbitrary posture angles $\theta_{r,m}$, $\theta_{p,m}$ and $\theta_{y,m}$ are assumed and substituted into Eq.(4.27).
(2) (t_m, u_m, t_s, u_s) is substituted into Eq.(4.27).
(3) Eq.(4.27) is regarded as a non-linear equations for $\frac{\partial g_c}{\partial t}$ and $\frac{\partial g_c}{\partial u}$, and is solved for them with a numerical method such as the Newton-Raphson method.
(4) g_c is updated with the following equations.

$$g_c(t + \nu, u) = g_c(t, u) + \frac{\partial g_c}{\partial t}\nu \tag{4.28}$$

$$g_c(t, u + \nu) = g_c(t, u) + \frac{\partial g_c}{\partial u}\nu \tag{4.29}$$

$$g_c(t + \nu, u + \nu) = g_c(t, u) + \frac{\partial g_c}{\partial t}\nu + \frac{\partial g_c}{\partial u}\nu \tag{4.30}$$

where ν is a step variable.

The above processes (2)-(4) are performed for each value of (t, u). Finally, the cam profile on Σ_1 can be derived with Eq.(4.22).

4.2.4   Flexible rotation constraint

In order to constraint relative rotation between the links flexibly, several pairs of the designed cam and spherical surfaces are arranged between the links. Depending on the

number of posture angles in main-DOF, the pairs of the cams and the spheres are placed in parallel in the same plane as the following patterns.

- If the number of main-posture angles is three, a single cam-sphere pair is arranged so that the center of the sphere is located at $^1\boldsymbol{p}$ as shown in Fig.4.6 (a).
- If the number of main-posture angles is one, two cam-sphere pairs are arranged so that the centers of the two spheres are located on the same rotation axis passing through $^1\boldsymbol{p}$ as shown in Fig.4.6 (b).
- If the number of main-posture angles is zero, three cam-sphere pairs are arranged so that $^1\boldsymbol{p}$ is located inside of a triangle consisting of the centers of three spheres as shown in Fig.4.6 (c).

(a) 3-axial main-rotations   (b) 1-axial main-rotation

(c) No main-rotations
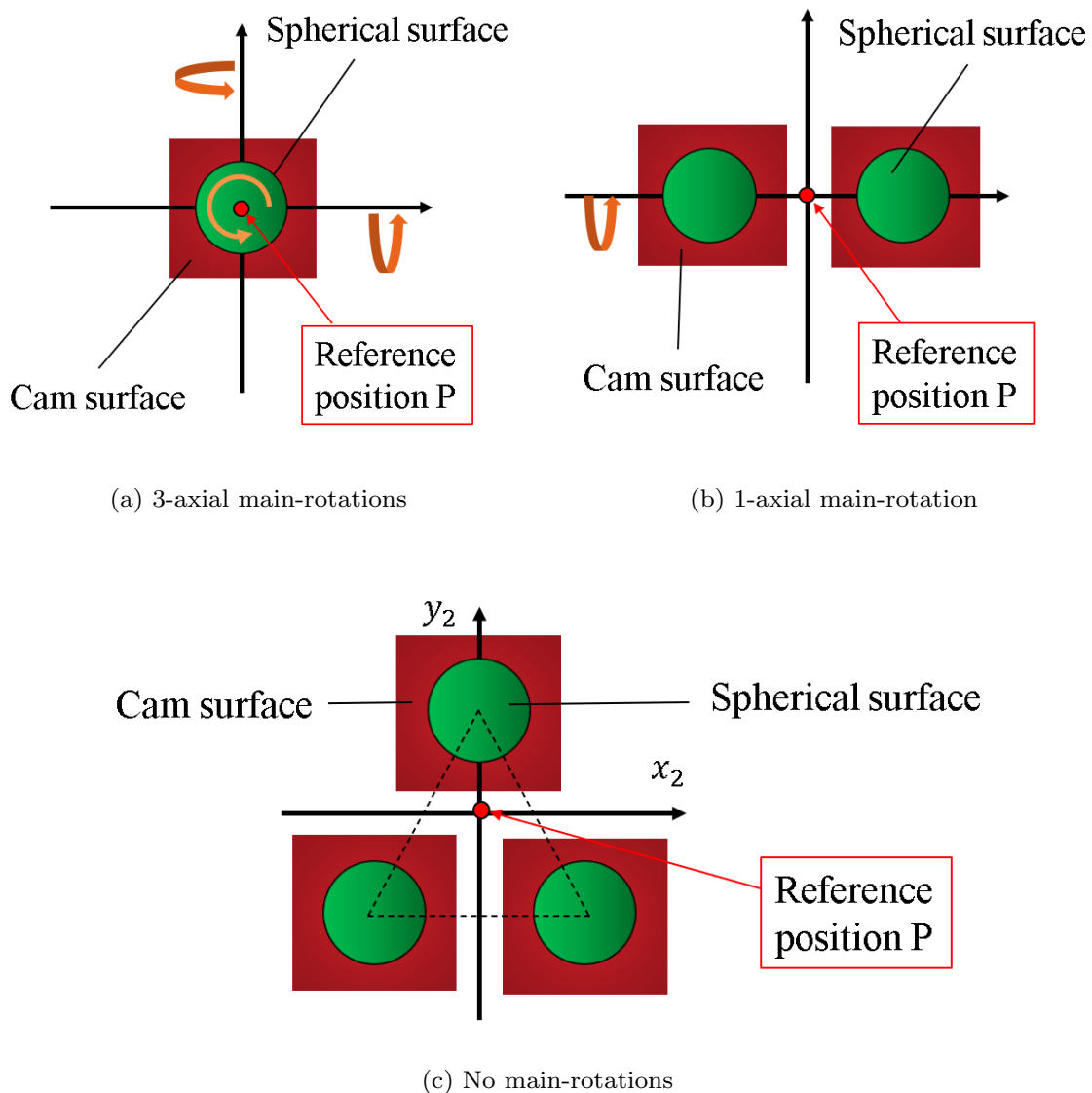
Fig.4.6   Arrangement patterns of the designed cam-sphere pairs

Note that the force-displacement characteristics generated in the sub-translation directions do not change even if several cam-sphere pairs are arranged in parallel between the links. This can be explained as follows.

Let the number of contact point be N_c, magnitude of the i-th normal reaction force be $f_{n,i}$ and direction vector of $f_{n,i}$ be $^1\hat{\boldsymbol{n}}_{c,i}$. Then, the statics equation in translation directions on Σ_1 is represented as following equation.

$$^1\boldsymbol{f}_d + {}^1\boldsymbol{f}_s + \sum_{i=1}^{N_c} f_{n,i} {}^1\hat{\boldsymbol{n}}_{c,i} = \boldsymbol{0} \tag{4.31}$$

When $^1\hat{\boldsymbol{n}}_{c,1} = ... = {}^1\hat{\boldsymbol{n}}_{c,N_c} = {}^1\hat{\boldsymbol{n}}_c$ holds, the statics equation can be rewritten as shown below.

$$^1\boldsymbol{f}_d + {}^1\boldsymbol{f}_s + {}^1\hat{\boldsymbol{n}}_c \sum_{i=1}^{N_c} f_{n,i} = \boldsymbol{0} \tag{4.32}$$

Thus, magnitude of the normal reaction force can be obtained as follows.

$$\sum_{i=1}^{N_c} f_{n,i} = -{}^1\hat{\boldsymbol{n}}_c^T ({}^1\boldsymbol{f}_d + {}^1\boldsymbol{f}_s) \tag{4.33}$$

By substituting Eq.(4.33) into Eq.(4.32), the statics equation can be rewritten as follows.

$$^1\boldsymbol{f}_d + {}^1\boldsymbol{f}_s - [{}^1\hat{\boldsymbol{n}}_c^T ({}^1\boldsymbol{f}_d + {}^1\boldsymbol{f}_s)]{}^1\hat{\boldsymbol{n}}_c = \boldsymbol{0} \tag{4.34}$$

Therefore, the statics equation does not depend on N_c. This means that the force-displacement characteristics generated in the sub-translation do not depend on the number of cam-sphere pairs if the cam-sphere pairs are arranged in parallel.

4.3   Design examples

By using the proposed design method, two types of the FCP were designed. In this section, the procedure and the result of each design are described.

4.3.1   The flexibly constrained revolute pair

As a simple example, the flexibly constrained revolute pair (FCRP), which allows 1-axial rotation in main-DOF, was designed. Fig.4.7 is the schematic diagram of the motion specification. The reference point is fixed at $^1\boldsymbol{p} = [0\ 0\ 33]^T$ [mm], and the rotation around the axis parallel to the x_1-axis of Σ_1 is allowed. Thus, the roll angle $\theta_{r,m}$ was just chosen as parameter of main-DOF, and the other main-parameters were specified to be zero. In contrast, t_s, u_s, $\theta_{p,s}$, $\theta_{y,s}$ were chosen from sub-parameters, and $\theta_{r,s}$ was specified to be zero. The motion range in the main-direction was specified as $A_m = \{\theta_{r,m} | -\frac{\pi}{2} \leqq \theta_{r,m} \leqq \frac{\pi}{2}\}$, where unit of the angle is rad.

Next, two linear springs were optimally arranged to minimize elastic forces in the main-directions. In this case, the optimal solutions are obvious. When an endpoint of a linear
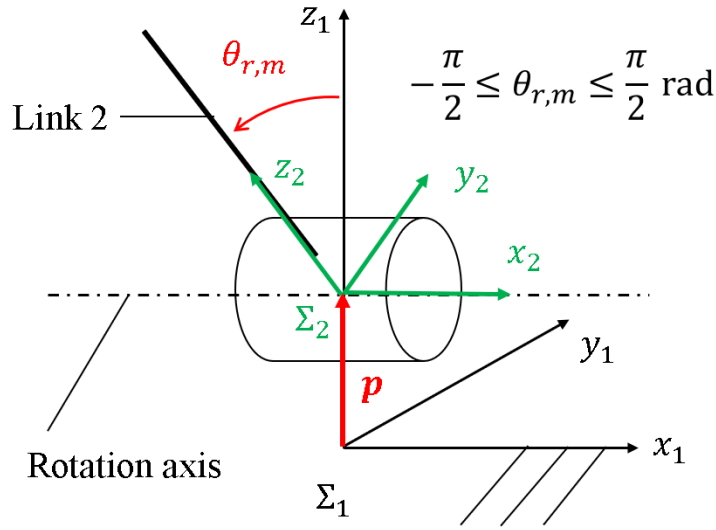
Fig.4.7 Specification of the main-relative motion between the links of the flexibly constrained revolute pair (FCRP)

spring is attached on the rotation axis with free rotations, the restoring torque in the main-direction is always zero. Therefore, endpoints of linear springs were arranged at $^1c_{1,1} = [45\ 0\ 0]^T$ [mm], $^1c_{1,2} = [-45\ 0\ 0]^T$ [mm], $^2c_{2,1} = [45\ 0\ 0]^T$ [mm] and $^2c_{2,2} = [-45\ 0\ 0]^T$ [mm], where the direction of the normal reaction force was assumed to be in the z_1-direction. The characteristics of the linear springs were specified as $k_1 = k_2 = 0.166$ N/mm, $l_{0,1} = l_{0,2} = 20.3$ mm and $f_{s,0,1} = f_{s,0,2} = 1.01$ N, which are specs of a commercial linear spring.

Cam profile is derived to generate the specified force-displacement characteristics. Since the direction of the normal reaction force was in z_1-direction, Σ_s was specified so that $^1e_{s,x}$ directed in the x_1-direction, $^1e_{s,y}$ directed in the y_1-direction and $^1e_{s,z}$ directed in the z_1-direction. Besides, since t_s and u_s were chosen as the sub-parameters, force-displacement characteristics were specified for the two directions orthogonal to $^1e_{s,z}$. In the following, the two different types of force-displacement characteristics are specified as examples.

(a) Design based on the center of the sphere
The specified force-displacement characteristics were as follows.

$$^s\boldsymbol{f}_d(t_s, u_s) = \begin{bmatrix} 3.0\,\mathrm{sgn}(t_s)(e^{0.1|t_s|} - 1) \\ 6.0\,\mathrm{sgn}(u_s)(e^{0.1|u_s|} - 1) \\ 0 \end{bmatrix} \ [\mathrm{N}] \ \ (-10 \leqq t_s,\ u_s \leqq 10) \qquad (4.35)$$

These characteristics are illustrated in Fig.4.8. The figure (a) shows the specified characteristics in the $t_s(x_1)$-direction and (b) shows the characteristics in the $u_s(y_1)$-direction. These characteristics are hardening spring characteristics.

The radius of the spherical surface was specified as $r_s = 13$ mm and the posture angles were assumed as $\theta_{r,m} = 0$ rad. Then, the cam profile was designed. The designed cam surface is shown in Fig.4.9. In order to simplify the design problem, just a part of a cam

(a) t_s-direction   (b) u_s-direction
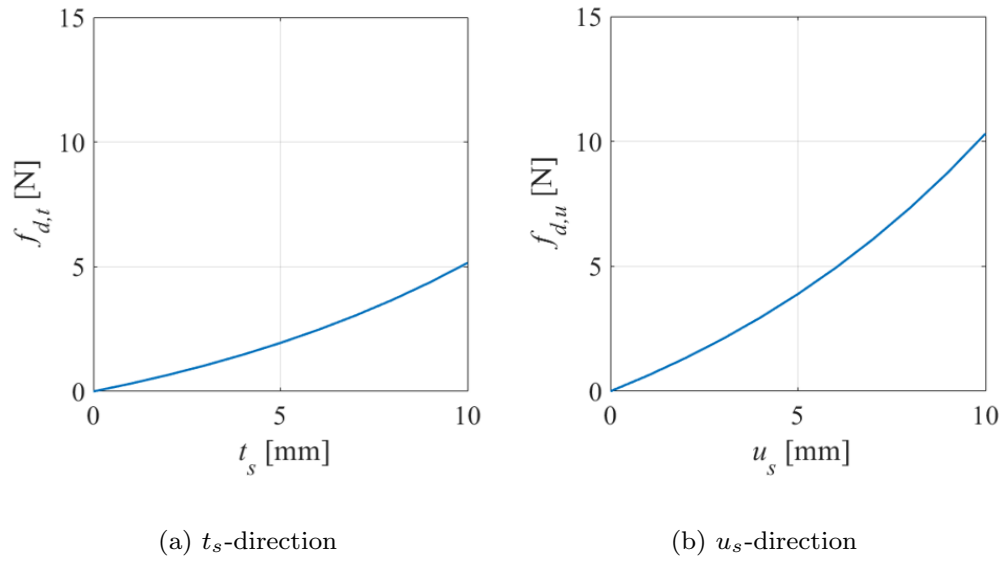
Fig.4.8   The specified force-displacement characteristics based on the center point of the sphere for the FCRP

(a) Calculated surface   (b) Whole cam surface
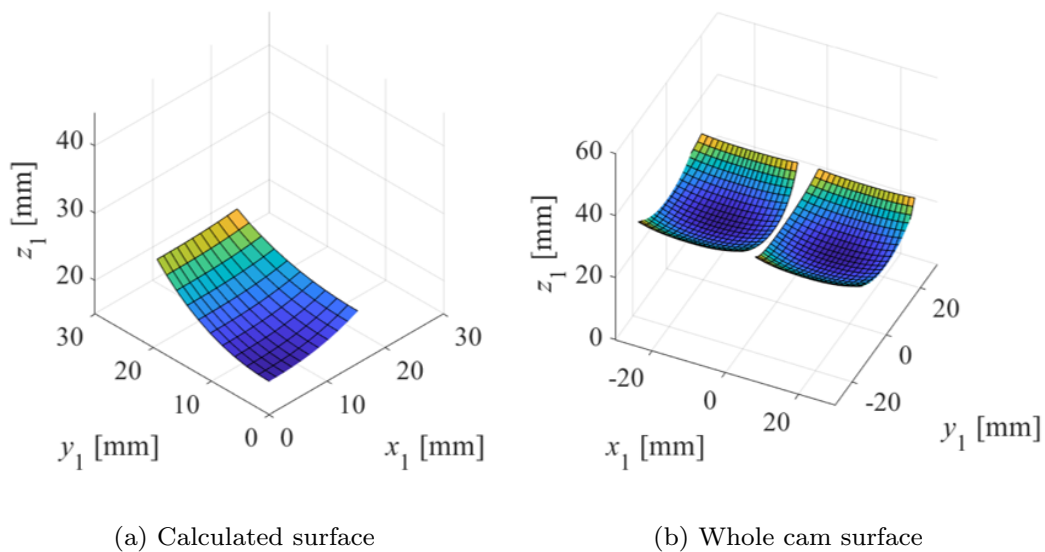
Fig.4.9   The cam surfaces of the FCRP designed with force-displacement characteristics based on the center point of the sphere

surface in $x_1 \geq 0$ and $y_1 \geq 0$ was designed as shown in Fig.4.9 (a). The width of the calculated cam surface was about 15 mm in the x_1-direction and about 20 mm in the y_1-direction. These sizes were bigger than the specified displacement (10 mm).

Two cam surfaces were finally arranged in parallel because 1-axial main-rotation was allowed. One of the two cam surfaces was obtained by placing this surface symmetrically

about $x_1 - z_1$ plane, $y_1 - z_1$ plane and z_1 axis. Then, the two cam surfaces were placed next to each other so that the centers of the spheres were located at $[x_1\ y_1\ z_1]^T = [16\ 0\ 33]^T$, $[-16\ 0\ 33]^T$ [mm] as shown in Fig.4.9 (b).

(b) Design based on the contact point

The specified force-displacement characteristics were as follows.

$$
{}^s\boldsymbol{f}_d(t_s, u_s) = \begin{bmatrix} 1.5\mathrm{sgn}(t_s)(e^{0.1|t_s|} - 1) \\ 2.0\mathrm{sgn}(u_s)(e^{0.1|u_s|} - 1) \\ 0 \end{bmatrix} \quad [\mathrm{N}]\quad (-15 \leqq t_s,\ u_s \leqq 15) \tag{4.36}
$$

These characteristics are shown in Fig.4.10. The figure (a) shows the specified characteristics in the t_s-direction and (b) shows the characteristics in the u_s-direction.

The radius of the spherical surface was specified as $r_s = 13$ mm and the posture angles were assumed as $\theta_{r,m} = 0$ rad. Since the center point of the sphere was located in ${}^1\boldsymbol{p} = [0\ 0\ 33]^T$ [mm], the initial value of g_c was $33 - 13 = 20$ mm. Then, the cam profile was calculated by solving the derivative equation. Fig.4.11 (a) shows the calculated a part of the cam surface in $x_1 \geqq 0$ and $y_1 \geqq 0$. Then, a cam surface was obtained by placing this part symmetrically about $x_1 - z_1$ plane, $y_1 - z_1$ plane and z_1 axis. Finally, two cam surfaces were placed so that the centers of the spheres were located at $[x_1\ y_1\ z_1]^T = [15\ 0\ 33]^T$, $[-15\ 0\ 33]^T$ [mm] as shown in Fig.4.11 (b). The width of the calculated part of the surface shown in Fig.4.11 (a) was 15 mm in both x_1- and y_1-direction. This was the same value as the specified displacement. Therefore, the size of the cam surface was able to be controlled with this method although the relative displacement between the links is not intuitive for designers.

(a) t_s-direction   (b) u_s-direction
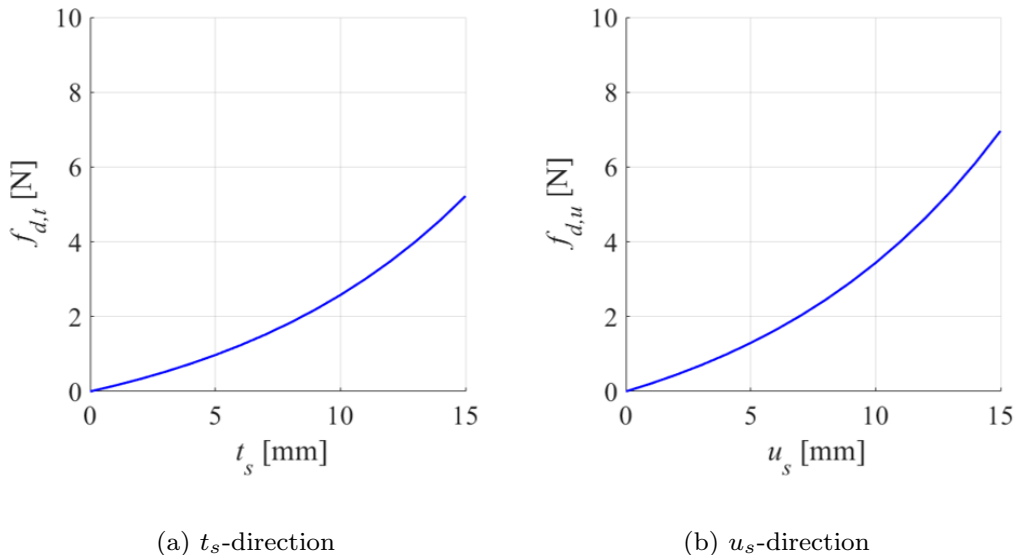
Fig.4.10   The specified force-displacement characteristics based on the contact point between the links for the FCRP

(a) The calculated surface   (b) Whole cam surface
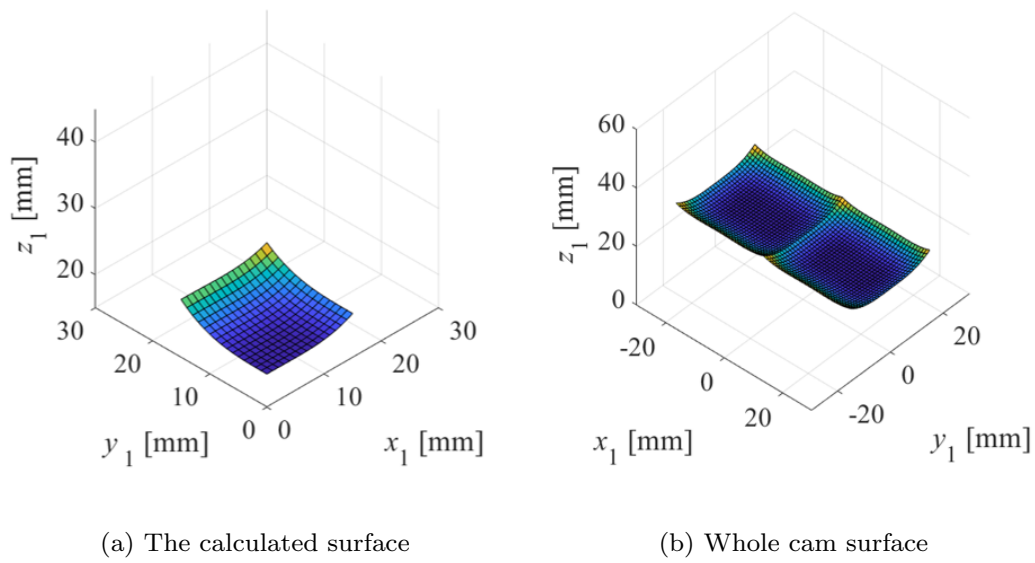
Fig.4.11   The cam surfaces of the FCRP designed with force-displacement charac-
teristics based on the contact point between the links
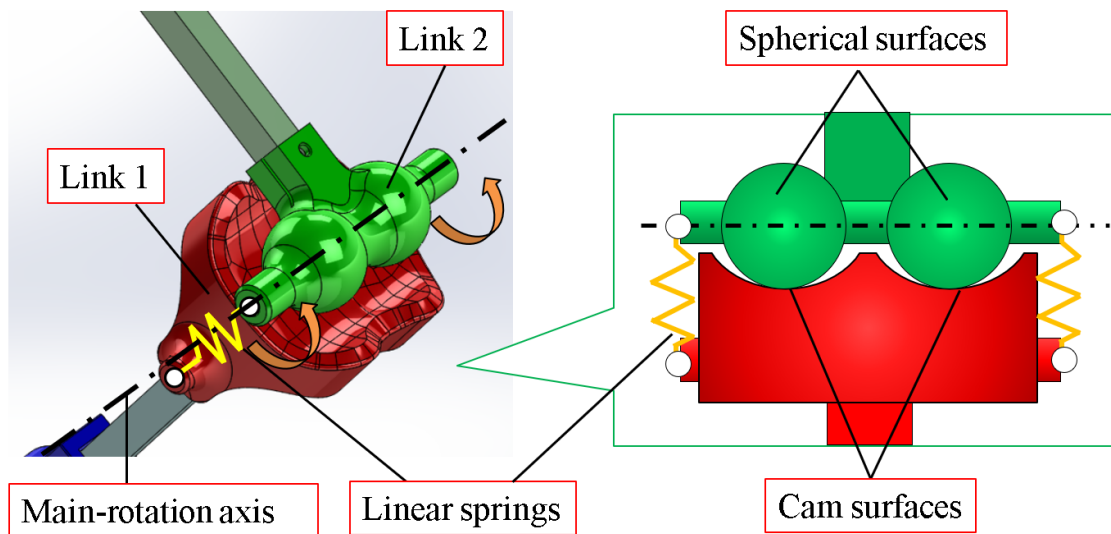
Fig.4.12   The 3D-CAD model of the FCRP

The structure of the FCRP designed in 3D-CAD is shown in Fig.4.12. It has multi-axial flexibility with a simple structure. Besides, it has the specified flexibility to balance between the performance of motion guidance and flexibility between the links. Therefore, the FCRP is useful for the flexible robotic mechanism with a simple structure.

4.3.2 Path-generating flexibly constrained pair

The FCP which allows the translation along the specified trajectory and three axial rotations was designed. Fig.4.13 shows the schematic diagram of the motion specification. In this example, t_m, $\theta_{r,m}$, $\theta_{p,m}$, $\theta_{y,m}$ were chosen as the main-parameters, and u_m was specified to be zero. In contrast, u_s was chosen as the sub-parameters, and the other sub-parameters were specified to be zero. As the main-translation for t_m, the ordinary helix which is represented as the following equation was specified.

$$^1\boldsymbol{p}(t_m) = \begin{bmatrix} 60\cos(\frac{\pi t_m}{2}) \\ 60\sin(\frac{\pi t_m}{2}) \\ 30t_m \end{bmatrix} \quad [\text{mm}] \tag{4.37}$$

The range of the main-relative motion was also specified as $A_m = \{t_m, \theta_{r,m}, \theta_{p,m}, \theta_{y,m} | \, 0.2 \leqq t_m \leqq 0.8, \ -\frac{\pi}{6} \leqq \theta_{r,m}, \theta_{p,m}, \theta_{y,m} \leqq \frac{\pi}{6}\}$.

Next, two linear springs are arranged between the links to minimize elastic forces in the main-directions. The same linear spring used in the examples in section 4.3.1 was chosen for the two springs. Note that the maximum length of this spring was 46.5 mm. The design spaces of endpoints of the springs, which are represented as box-shape areas, were as follows.

$$[70 \ 60 \ -40]^T \leqq {}^1\boldsymbol{c}_{1,1} \leqq [100 \ 100 \ 0]^T, \tag{4.38}$$

$$[-20 \ -20 \ -40]^T \leqq {}^1\boldsymbol{c}_{1,2} \leqq [20 \ 25 \ 0]^T, \tag{4.39}$$

$$[30 \ -20 \ 5]^T \leqq {}^2\boldsymbol{c}_{2,1} \leqq [60 \ 20 \ 20]^T, \tag{4.40}$$

$$[-60 \ -20 \ 5]^T \leqq {}^2\boldsymbol{c}_{2,2} \leqq [-30 \ 20 \ 20]^T, \tag{4.41}$$

where the unit is mm. The required normal reaction force was specified as $f_{n,req} = 5$ N.
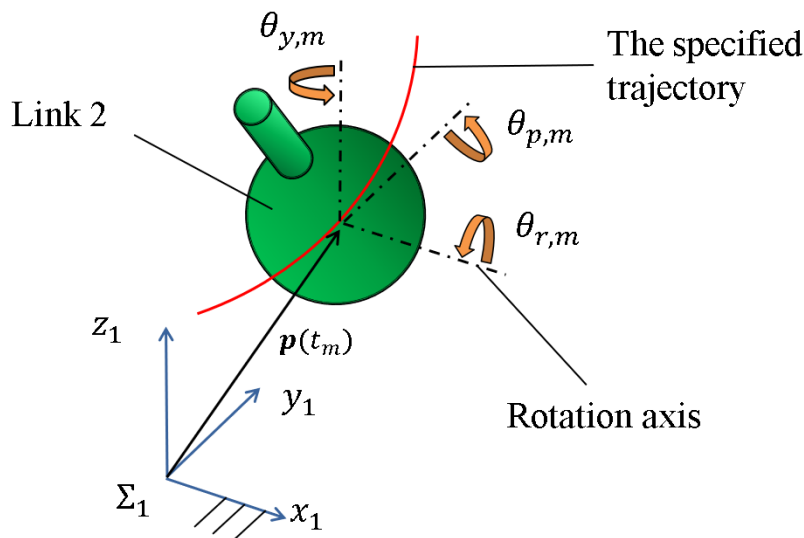
Fig.4.13 Specification of the relative main-motion between the links of the path-generating FCP

(a) Force in the t_m-direction

(b) Torque in the $\theta_{r,m}$-direction

(c) Torque in the $\theta_{p,m}$-direction

(d) Torque in the $\theta_{y,m}$-direction
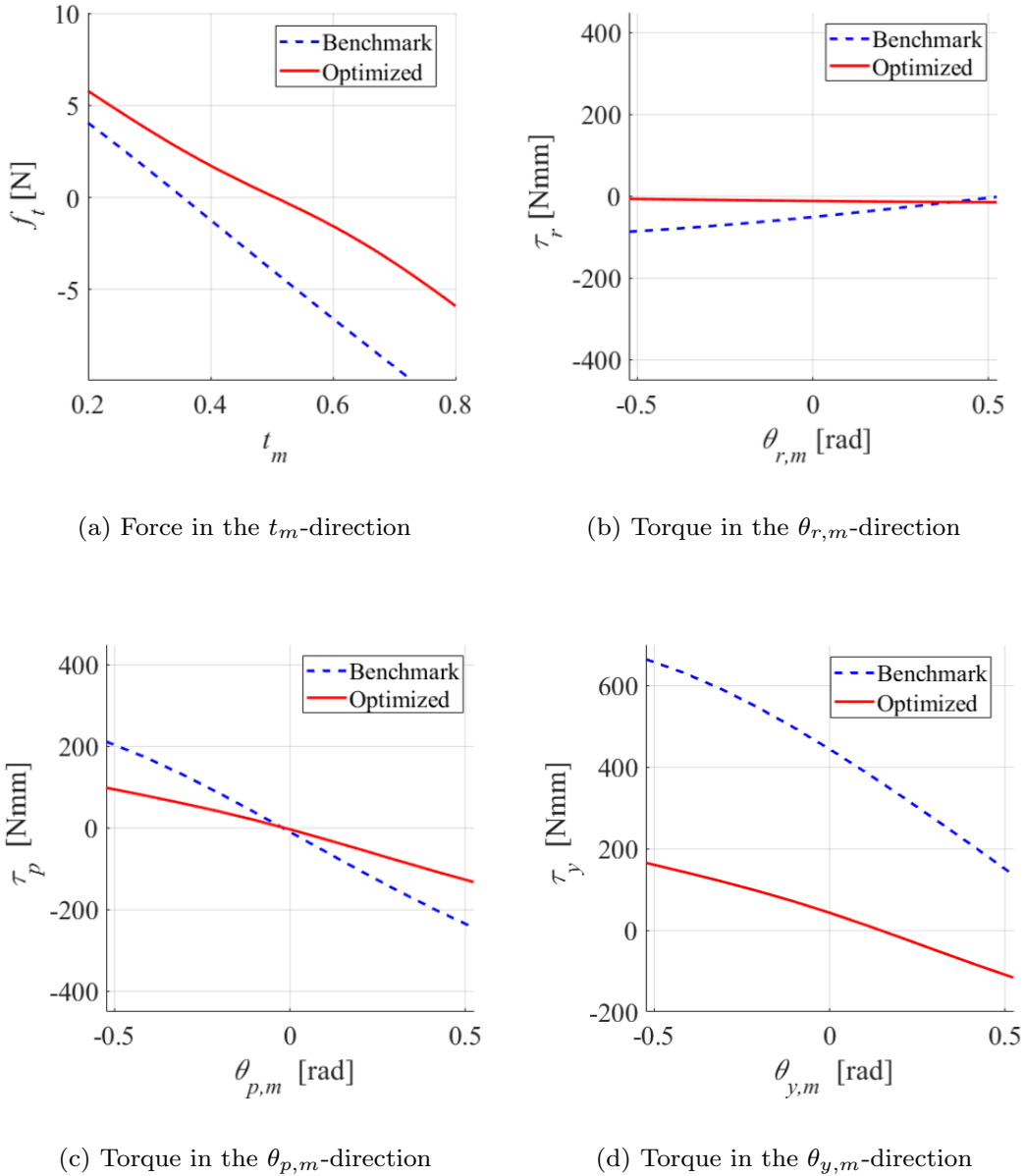
Fig.4.14   Elastic forces in various main-directions of the designed path-generating FCP

Note that the direction of the normal reaction force was assumed to be the direction of the bi-normal vector of the specified trajectory because ^1p was the spatial curve. Many candidates of the initial points for the optimization were randomly generated, and the point to minimize the objective function was selected as the initial position. Then, the optimization was performed with the interior-point method [118]. Note that the Gauss-Legendre quadrature [117] was used to calculate the mean value of elastic forces in order to reduce the calculation time. The result of the calculation became $^1c_{1,1} = [70.0 \ 60.0 \ -6.31]^T$ [mm], $^1c_{1,2} = [-2.39 \ 25.0 \ -2.81]^T$ [mm], $^2c_{2,1} = [30.0 \ 4.66 \ 5.00]^T$ [mm] and $^2c_{2,2} = [-30.0 \ -10.9 \ 5.00]^T$ [mm]. Elastic force (torque) in the main-directions are shown
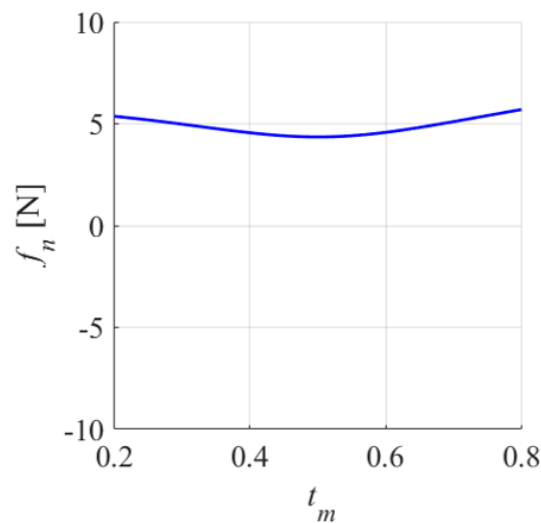
Fig.4.15   Normal reaction force of the designed path-generating FCP
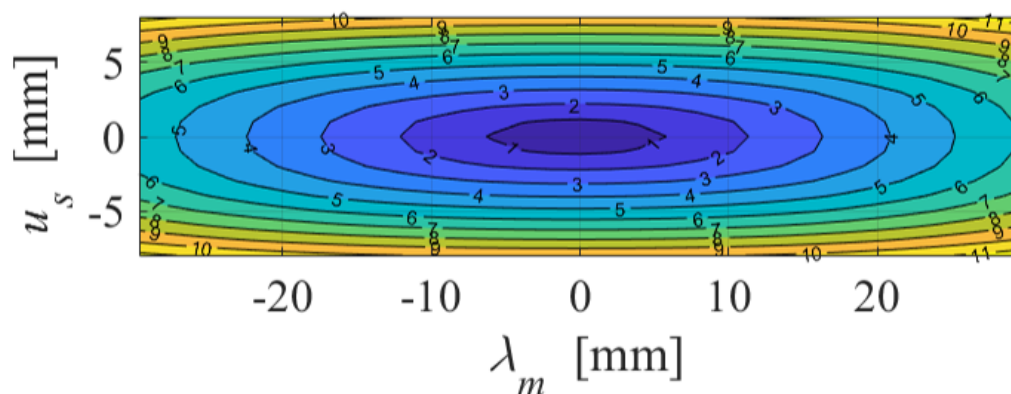
Fig.4.16   Contour map on anisotropy of stiffness in between the main- and the sub-directions of the designed path-generating FCP

in Fig.4.14, where figure (a) shows the restoring tangent force along the specified trajectory when the two links displaced along the specified trajectory. The figures (b)-(d) show restoring rotation torque when $\theta_{r,m}$, $\theta_{p,m}$ and $\theta_{y,m}$ are displaced from $(\theta_{r,m}, \theta_{p,m}, \theta_{y,m}) = (0, 0, 0)$, respectively at $^1\boldsymbol{p}(t_m) = {}^1\boldsymbol{p}(0.5)$. Benchmarks in the figures were calculated with the center positions in the design spaces. These figures show that the normal reaction force was kept in about the specified value and restoring forces and stiffness were reduced in the main-directions. Besides, Fig.4.15 shows the normal reaction force when the two links displaced along the specified trajectory. This figure indicates that the normal reaction force was kept in about the specified value.

Then, the cam profile was designed. In order to make a difference of stiffness between the t_m-direction and the u_s-direction, the following force-displacement characteristics based

(a) Calculated cam surface

(b) Cam surface, spherical surface and end-points of springs
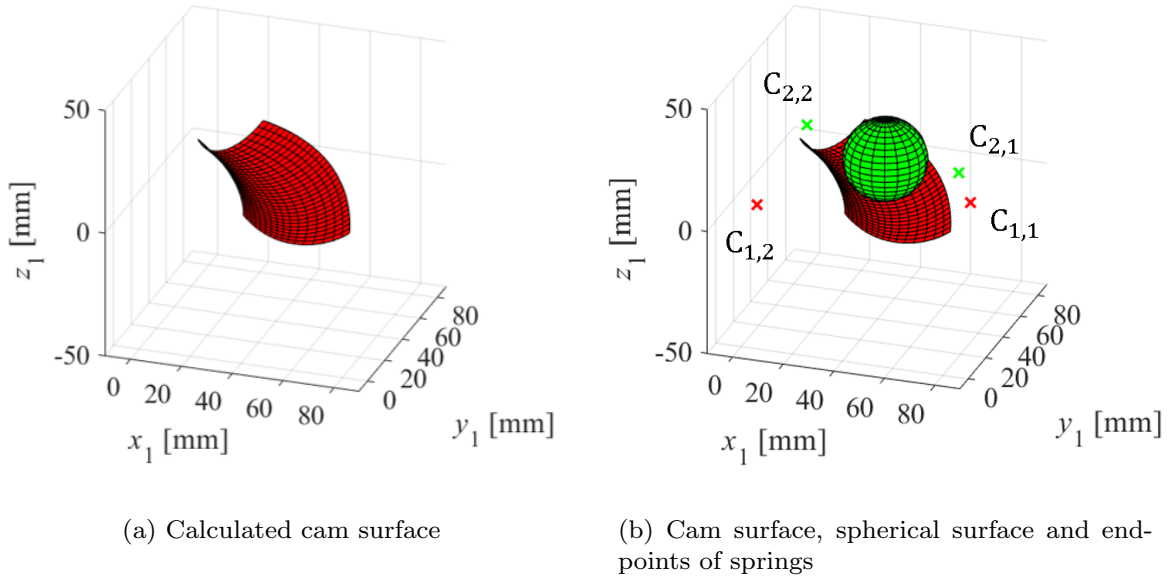
Fig.4.17   The cam surfaces of the designed path-generating FCP
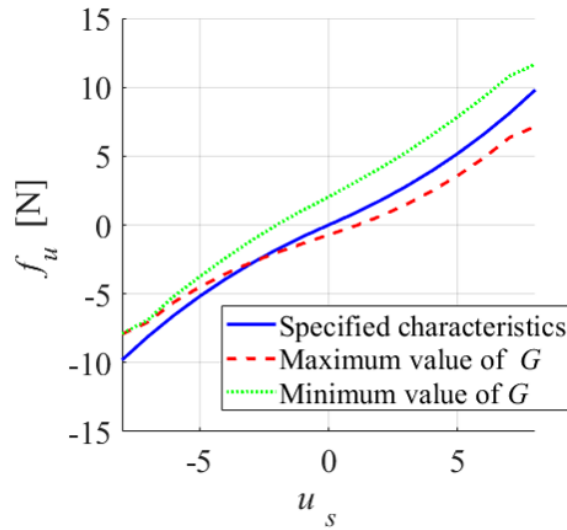
Fig.4.18   Sift of the stiffness characteristics for posture angles in the designed path-generating FCP

on the center of the sphere were specified.

$$f_{d,u}(u_s) = 8.0\mathrm{sgn}(u_s)(e^{0.1|u_s|} - 1) \ \ [\mathrm{N}] \ \ (-8 \leqq u_s \leqq 8 \ [\mathrm{mm}]) \tag{4.42}$$

Fig.4.16 shows the contour map of the force-displacement characteristics in the t_m-direction (displacement: λ_m) and the u_m-direction. Since the major axis of ellipses was in the λ_m-direction, it was considered that the two links is easy to displace in the
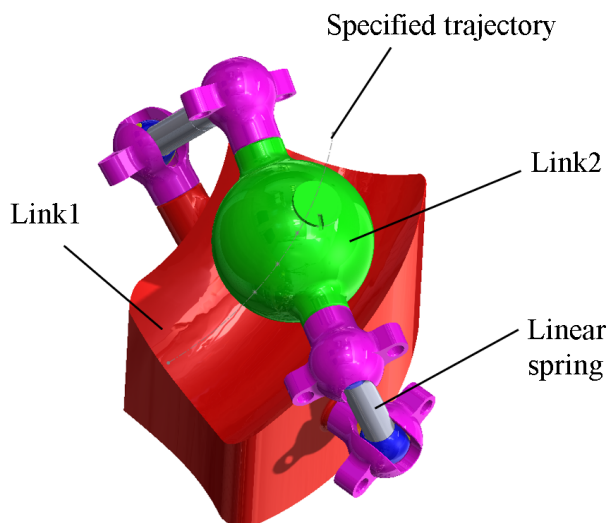
Fig.4.19 The 3D-CAD model of the designed path-generating FCP

t_m-direction, and hard to displace in the u_s-direction. In order to calculate the cam profile, the radius of the sphere was specified as $r_s = 15$ mm. The posture angles were assumed as $(\theta_{r,m}, \theta_{p,m}, \theta_{y,m}) = (0.118, -0.155, -0.298)$ [rad], which were obtained by solving Eq.(4.21). Then, cam profile was calculated. The designed cam surface is shown in Fig.4.17. The figure (a) shows the calculated cam surface, and the figure (b) shows the cam, the sphere and endpoints of springs on Σ_1. Note that since this FCP allows 3-axial main-rotations, one pair of the cam surface and the spherical surfaces was arranged on Σ_1. Fig.4.18 shows the force-displacement characteristics when two links of the designed FCP displace in the u_s-direction from $^1\boldsymbol{p}(t_m) = {}^1\boldsymbol{p}(0.5)$. The red broken line denotes the characteristics when the posture angles were kept in the angles to maximize $M(\theta_{r,m}, \theta_{p,m}, \theta_{y,m})$. The green dotted line denotes the characteristics when the posture angles were kept in the angles to minimize $M(\theta_{r,m}, \theta_{p,m}, \theta_{y,m})$. This result shows that the force-displacement characteristics varies around the specified characteristics as expected in the design.

The structure of the FCP designed in 3D-CAD is shown in Fig.4.19. Therefore, the FCP allowing a complex main-relative motion was able to be designed.

4.4 Prototyping and evaluation

In this section, some prototypes of the FCP are fabricated and examined by experiments to confirm the validity of the design method.

4.4.1 Validity of the cam profile design

Prototypes of the two FCRPs designed in section 4.3.1, were fabricated with 3D-printers. Fig.4.20 shows one of the prototype. The prototype with the force-displacement
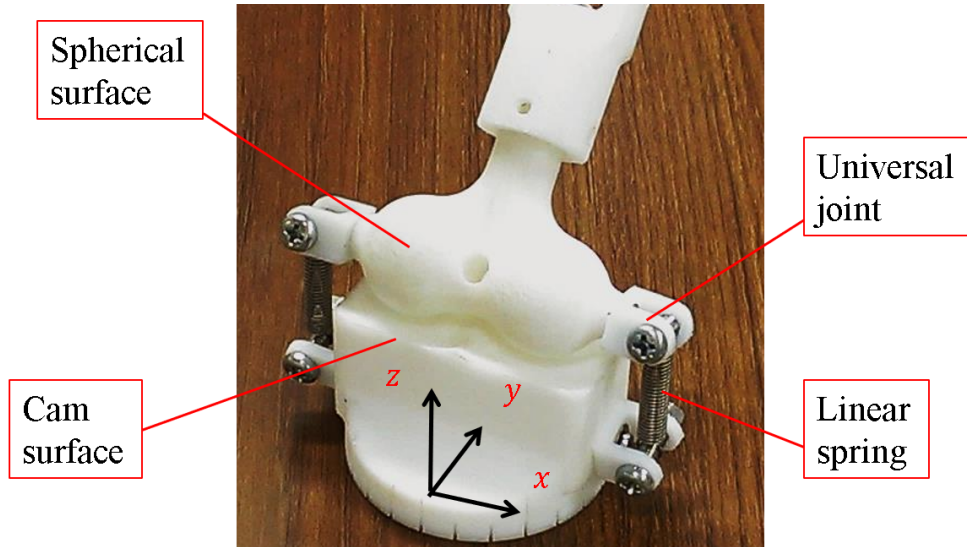
Fig.4.20　Prototype of the FCRP fabricated by a 3D-printer

(a) Overall view　(b) x- direction　(c) y- direction
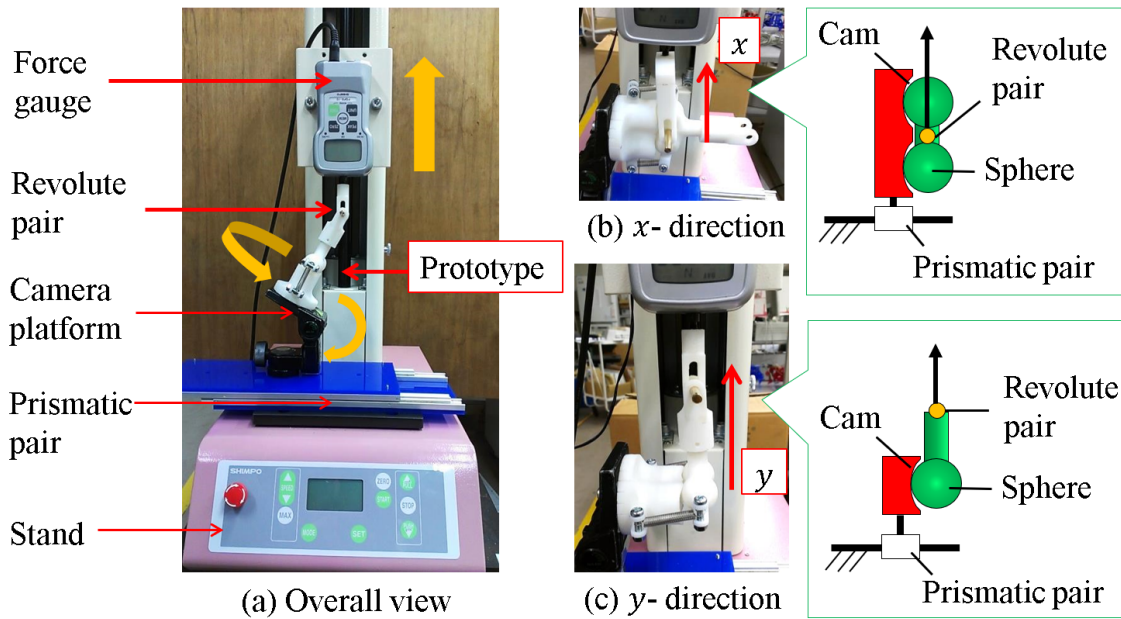
Fig.4.21　Experimental setup to measure force-displacement characteristics between two links of prototypes

characteristics based on the center point of the sphere was fabricated by the fused deposition modeling (FDM). On the other hand, the prototype with the characteristics based on the contact point between the links was fabricated by the material jetting. Although these prototypes have the same structure shown in Fig.4.20, modeling accuracy of the prototype fabricated by the material jetting is better than that of the prototype fabricated by the FDM. By comparing the FCRPs fabricated by the two different methods, it is possible to investigate the effect of modeling accuracy on the experimental results.

　The force-displacement characteristics of the prototypes in the x- and y- directions

(a) x-direction (b) y-direction
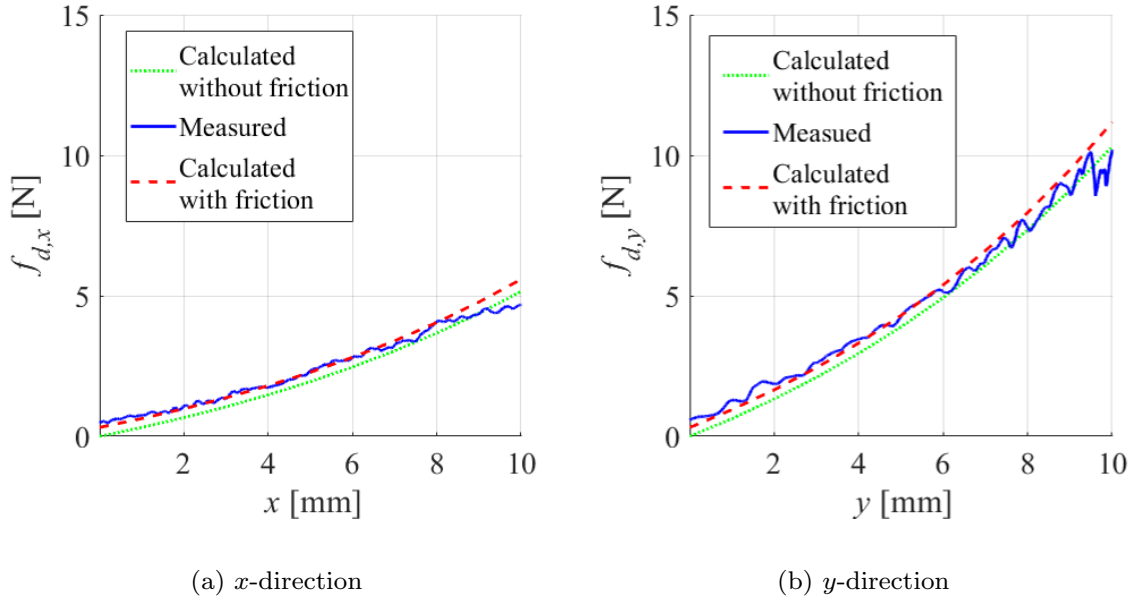
Fig.4.22 Comparison between calculated and measured stiffness characteristics of the prototype designed besed on the center of the sphere

which are shown in Fig.4.20 were measured with a force gauge. Fig.4.21 shows the experimental setup. The force-displacement characteristics in the x- and y-directions were measured by the tensile testing machine composed of the force gauge and a stand for the force gauge. The prototype mounted on a camera platform was attached to the force-gauge stand through prismatic pair to reduce loads orthogonal to the measured direction. In the measurement, the link with the spherical surfaces is connected to the force gauge via a revolute pair as shown in Fig.4.21 (b) and (c) so that the force acts at the midpoint between the two spheres. In order to reduce friction as much as possible, a lubricant is applied between the two links.

Fig.4.22 shows force-displacement characteristics of the prototype designed based on the center of the sphere. Fig.4.22 (a) shows the result of the $x(t_s)$-direction and Fig.4.22 (b) shows the result of the $y(u_s)$-direction. The blue solid line in each figure is the measured characteristics and the green dotted line is the calculated theoretical characteristics. These figures show that the measured characteristics were little different from the calculated characteristics. It is considered that these errors were caused by friction between the two surfaces because the friction was not able to be small enough. Thus, the theoretical characteristics were modified to include the effect of the friction with the following equation.

$$^1\boldsymbol{f}_d = -^1\boldsymbol{f}_s + \frac{^1\boldsymbol{e}_{z,1}^T \, ^1\boldsymbol{f}_s}{^1\boldsymbol{e}_{z,1}^T(^1\hat{\boldsymbol{n}}_c - \mu^1\hat{\boldsymbol{v}})}(^1\hat{\boldsymbol{n}}_c - \mu^1\hat{\boldsymbol{v}}), \qquad (4.43)$$

where μ is the coefficient of static friction, $^1\hat{\boldsymbol{v}}$ is the unit tangent vector of the cam surface in the direction of the motion and $^1\boldsymbol{e}_{z,1}$ is the unit vector in the z_1-direction. μ was

(a) x-direction (b) y-direction
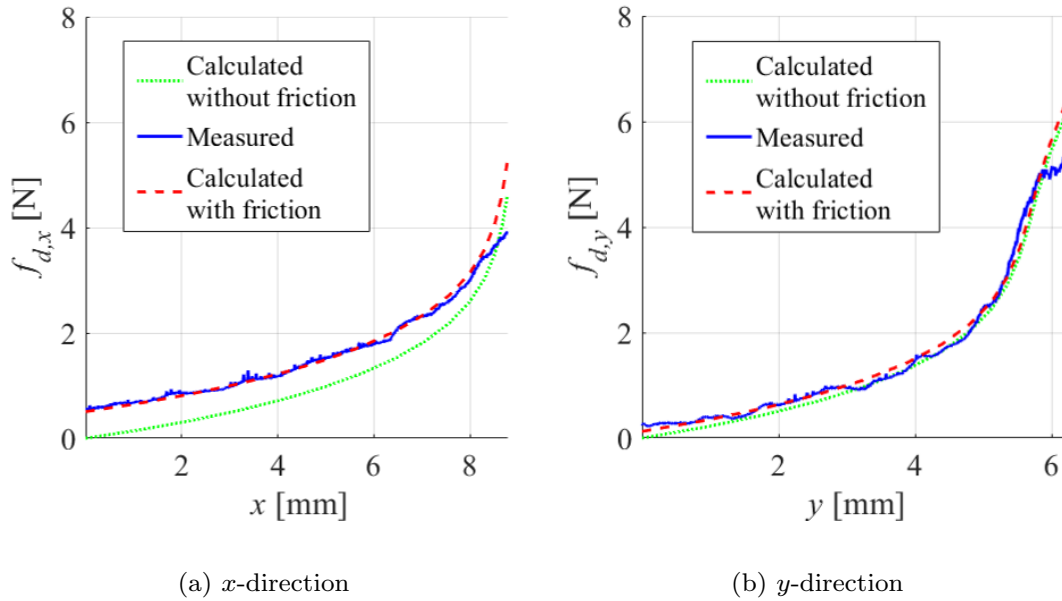
Fig.4.23 Comparison between calculated and measured stiffness characteristics of the prototype designed besed on the contact point between the links

substituted into Eq.(4.43) so that the theoretical characteristics fitted the measured ones because measuring the coefficient of the static friction on the curved surface was difficult. The recalculated theoretical values are shown as the red broken lines in Fig.4.22 (a) and (b). The recalculated characteristics agreed very well with the measured ones. Note that the coefficient of static friction in both results in the x- and y-directions was 0.05. This value can be agreed upon intuitively.

Fig.4.23 shows force-displacement characteristics of the prototype designed based on the contact point between the links. Fig.4.23 (a) shows the result of the $x(t_s)$-direction and (b) shows the result of the $y(u_s)$-direction. The blue solid line in each figure is the measured characteristics, the green dotted line is the calculated theoretical characteristics without the effect of friction. Note that the theoretical characteristics are the characteristics based on the center of the sphere which is modified from the characteristics based on the contact point shown in Fig.4.10 in order to be compared with the measured characteristics. The red broken line is the recalculated theoretical characteristics with the effect of the friction. It agreed very well with the measured characteristics while the theoretical characteristics without the effect of the friction did not agree with the measured characteristics. In this case, the coefficient of the static friction in the x-direction was 0.08 and the coefficient in the y-direction was 0.02. These values can be agreed upon intuitively.

In Fig.4.22 and Fig.4.23, there were large errors between the measured and the calculated values in near the maximum displacement. The reason is considered that contact points between the two links were located at the edge of the cam surface. Since the edge had a corner, the link with spherical surfaces was able to have several postures. Thus, the cause of the error is considered that the link with the spherical surface had a different

posture from the theoretical one. In addition, the ripples shown in Fig.4.23 look less than the ripples shown in Fig.4.22. The reason is considered due to the fabrication accuracy.

The results of the above experiments indicate that the proposed design method of the cam surfaces is valid.

4.4.2   Performance of the flexible constraint of a path-generating FCP

An experiment was performed to confirm that two links of a path-generating FCP can displace in the main-translation direction more easily than in the sub-translation direction by a difference of stiffness. In order to perform the experiment easily, the path-generating FCP which allows translation along a linear trajectory and 3-axial rotations was designed and prototyped. The design parameters are listed in Table 4.1. This FCP was designed with the same procedure of the FCP designed in section 4.3.2. Then, the FCP was fabricated by the FDM with a 3D-printer as shown in Fig.4.24. The experimental setup is shown in Fig.4.25. The FCP is fixed on the workbench. The upper part of the sphere (link 2) and the tip of the force gauge are connected with a UHPE (Ultra High Molecular Weight Polyethylene) cable. The force gauge is attached to the end effector of a serial robot manipulator with 6 DOF. The manipulator can pull the cable with the specified tensile force by controlling the motion of it based on the tensile force measured by the force gauge. The manipulator pulled the cable slowly in the various direction with the tensile force of 2.0 N as shown in Fig.4.26, and the stationary center position of the sphere was then measured with a camera from its vertically upward.

The measured positions were plotted on the theoretical contour map as shown in

Table 4.1   Design parameters of the path-generating FCP for the experiment

Trajectory [mm]	$^1\boldsymbol{p}(t_m) = [0 \ \ 50t_m - 25 \ \ 20]^T$
Range of the main-DOF	$0 \leqq t_m \leqq 1$
	$-\frac{\pi}{6} \leqq \theta_{r,m}, \ \theta_{p,m}, \ \theta_{y,m} \leqq \frac{\pi}{6}$ [rad]
Range of end points of springs [mm]	$[30 \ -30 \ -30]^T \leqq {}^1\boldsymbol{c}_{1,1} \leqq [60 \ 30 \ 0]^T$
	$[-60 \ -30 \ -30]^T \leqq {}^1\boldsymbol{c}_{1,2} \leqq [-30 \ 30 \ 0]^T$
	$[25 \ -20 \ 0]^T \leqq {}^2\boldsymbol{c}_{2,1} \leqq [50 \ 20 \ 15]^T$
	$[-50 \ -20 \ 0]^T \leqq {}^2\boldsymbol{c}_{2,2} \leqq [-25 \ 20 \ 15]^T$
Stiffness characteristics [N]	$f_d(u_s) = 2.0\mathrm{sgn}(u_s)(e^{0.1|u_s|} - 1) \ (-10 \leqq u_s \leqq 10 \ [\mathrm{mm}])$
Characteristics of springs	$k_1 = k_2 = 0.166$ N/mm
	$l_{0,1} = l_{0,2} = 20.3$ mm
	$l_{max,1} = l_{max,2} = 46.5$ mm
	$f_{s,0,1} = f_{s,0,2} = 1.01$ N
Radius of the sphere [mm]	$r_s = 15$
Reference value of the normal force [N]	$f_{n,req} = 5$
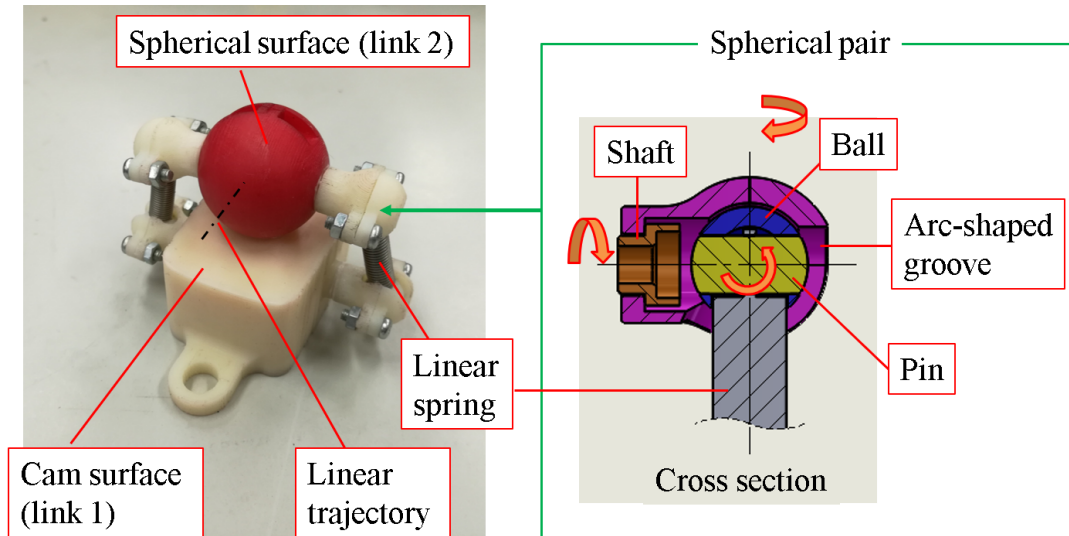
Fig.4.24   Prototype of the FCP which allows translation along a linear trajectory and 3-axial rotations
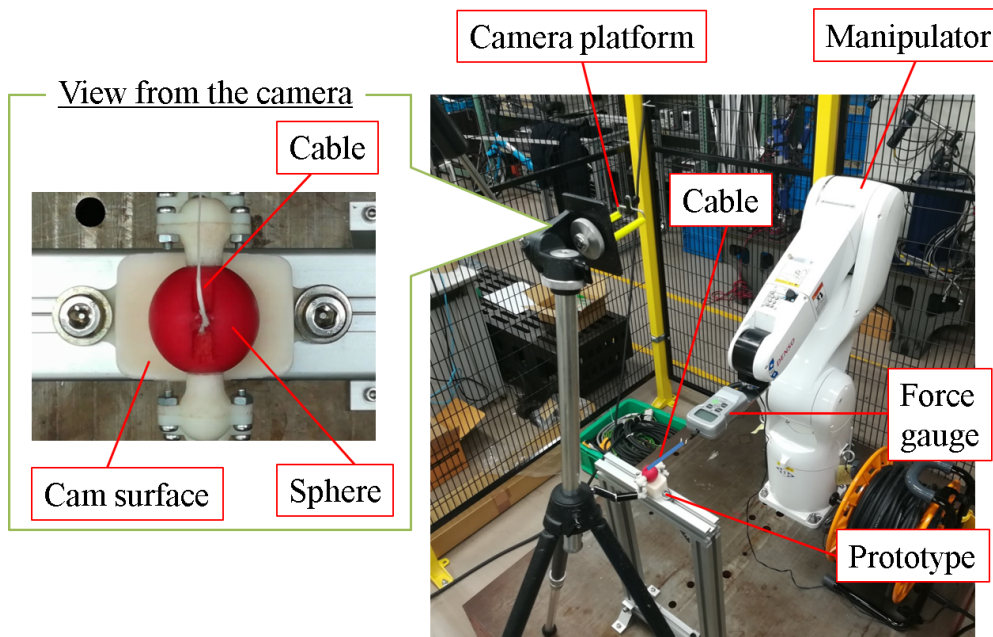
Fig.4.25   Experimental setup for evaluation of the effect of the anisotropic stiffness of the fabricated path-generating FCP

Fig.4.27. It is shown that the sphere was able to displace in the main-translation direction (the λ_m-direction) more easily than in the sub-translation direction (the u_s-direction) as shown in the theoretical contour map. The measured positions were close to the theoretical contour of 2.0 N. Although some errors were shown in the result, their reasons can be explained physically. The position of 0° displaced in the $\lambda_m > 0$ direction more largely than the theory. This reason is considered that the sphere displaced largely with rolling in the pulling direction, and then it was not able to return the theoretical position by
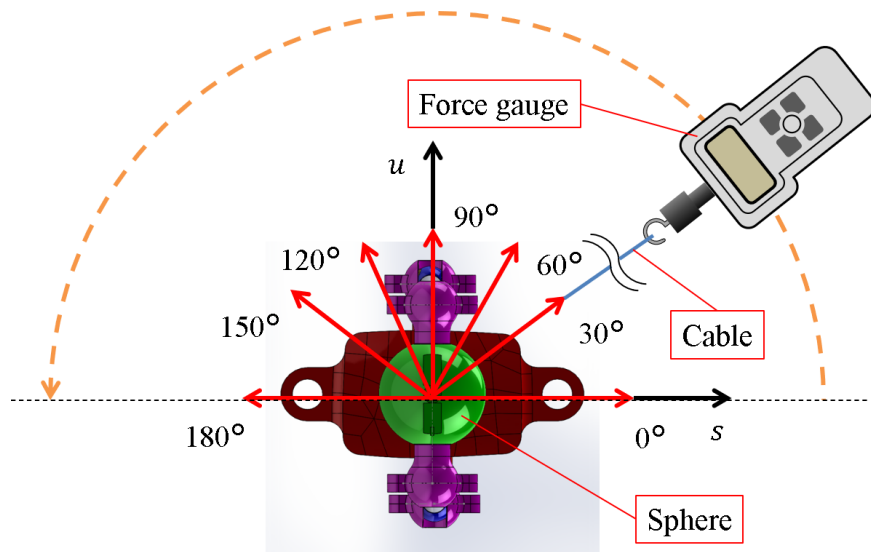
Fig.4.26   Operation of the serial robotic manipulator in the experiment
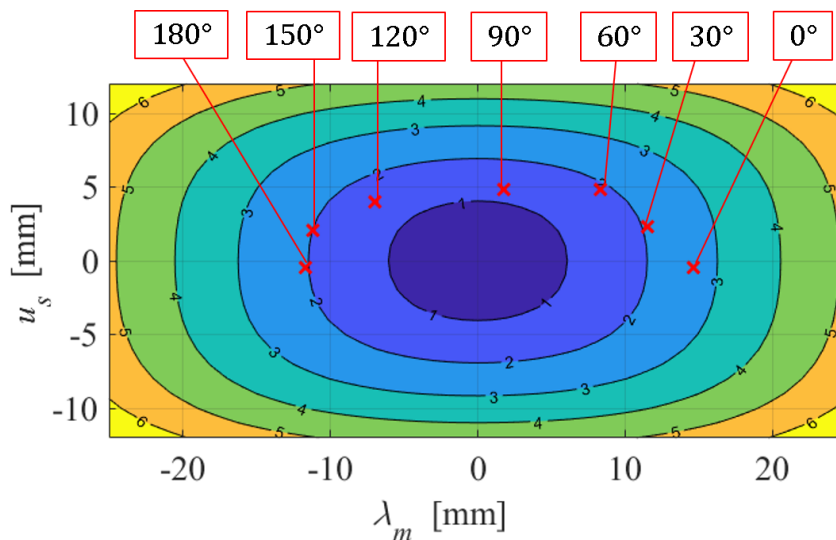
Fig.4.27   Distribution of the measured center position of the sphere on the theoretical contour map

the friction between the links. The positions of from 60° to 120° less displaced in the u_s-direction than the theory. This reason is considered that the tensile force of the cable did not ideally apply to the sphere because the cable attachment point on the sphere did not locate between the center of the sphere and the force gauge.

The result of the above experiment indicates that the design method of the flexible translation constraint is valid.

4.5   Application

The FCRP has zero stiffness in the main-rotation direction and non-zero stiffness in the other sub-directions. Therefore, the FCRP behaves like a revolute pair with 1 DOF under small external loads, while the links can displace in the other relative directions under large external loads. Therefore, a flexible underactuated mechanism can easily be synthesized if ordinary passive revolute pairs in fully-actuated linkage are replaced by the FCRPs. In this section, a flexible robotic mechanism with the FCRPs is designed and fabricated as an application, and its flexibility and kinematic performance are investigated through analysis and experiments.

A flexible mechanism with the FCRP is shown in Fig.4.28. Fig.4.28 (a) shows the photograph of the fabricated mechanism and (b) shows dimensions of the mechanism. This mechanism is a planar closed-loop five-bar mechanism composed of two active revolute pairs (DC motors), two FCRPs and one ordinary passive revolute pair. The output point is located at the passive revolute pair. The FCRPs were designed with parameters shown in Table 4.2 and fabricated by a 3D-printer with the FDM. The specified force-displacement characteristics were based on the contact point between the links so that the size of the FCRP becomes compact.

4.5.1   Kintostatic analysis of the tested mechanism

A method to analyze the kinetostatic motion of the fabricated mechanism on the x-z plane is described. The posture of the fabricated mechanism should be determined so

(a) Photograph of the mechanism   (b) Dimensions of the mechanism
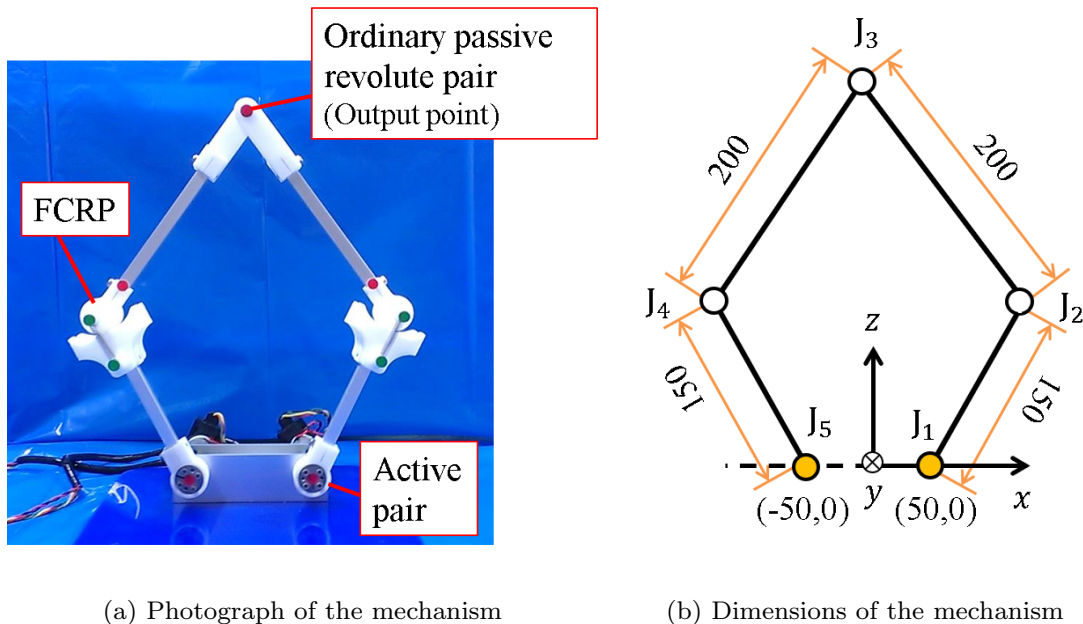
Fig.4.28   The fabricated planar closed-loop five-bar mechanism with the FCRPs

Table 4.2 Design parameters of the FCRP in the fabricated mechanism

Reference position [mm]	$^1\boldsymbol{p} = [0\ 0\ 25]^T$		
Range of the main-DOF [rad]	$-\frac{\pi}{2} \leqq \theta_{r,m} \leqq \frac{\pi}{2}$		
Endpoints of springs [mm]	$^2\boldsymbol{c}_{1,1} = [45\ 0\ 0]^T,\ ^2\boldsymbol{c}_{1,2} = [-45\ 0\ 0]^T$ $^2\boldsymbol{c}_{2,1} = [45\ 0\ 0]^T,\ ^2\boldsymbol{c}_{2,2} = [-45\ 0\ 0]^T$		
Stiffness characteristics [N]	$^s\boldsymbol{f}_d = \begin{bmatrix} \mathrm{sgn}(t_s)(e^{0.1|t_s|} - 1) \\ \mathrm{sgn}(u_s)(e^{0.1|u_s|} - 1) \\ 0 \end{bmatrix}$		
Range of the sub-translations [mm]	$-15 \leqq t_s \leqq 15$		
	$-25 \leqq u_s \leqq 25$		
Characteristics of springs	$k_1 = k_2 = 0.110$ N/mm		
	$l_{0,1} = l_{0,2} = 19.4$ mm		
	$f_{s,0,1} = f_{s,0,2} = 0.686$ N		
Radius of the sphere [mm]	$r_s = 14$		
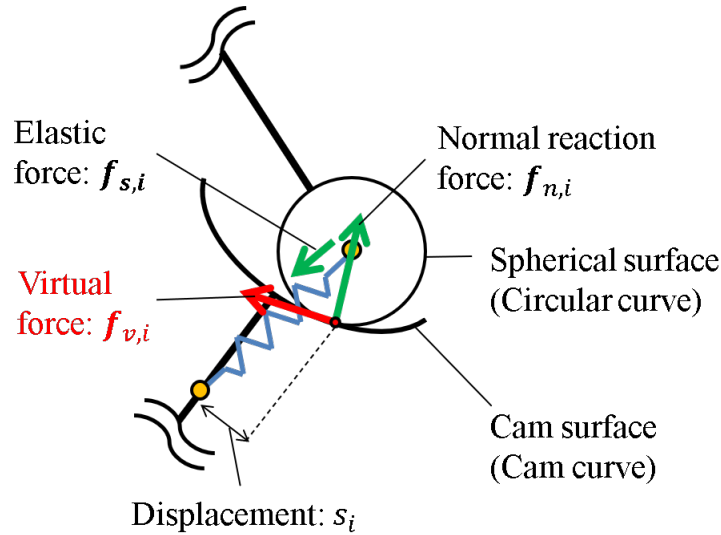
Fig.4.29 Forces acting between pairing elements of each FCRP in the tested mechanism

as to satisfy static balance because the output point J_3 shown in Fig.4.28 (b) displaces when an external force acts on it. The motion of the elastically constrained underactuated mechanism like this mechanism can be analyzed with the method of Iwatsuki et al. [124]. This mechanism was analyzed by the following process.

(1) The external force $\boldsymbol{f}_e$ acting on the output point and the initial posture of the mechanism are assumed.

(2) It is assumed that virtual forces $\boldsymbol{f}_{v,i}$ ($i = 2, 4$) are acted in the tangential direction between pairing elements of J_2 and J_4 as shown in Fig.4.29. Then, statics equations are solved and virtual forces are obtained. The solution of this calculation is uniquely
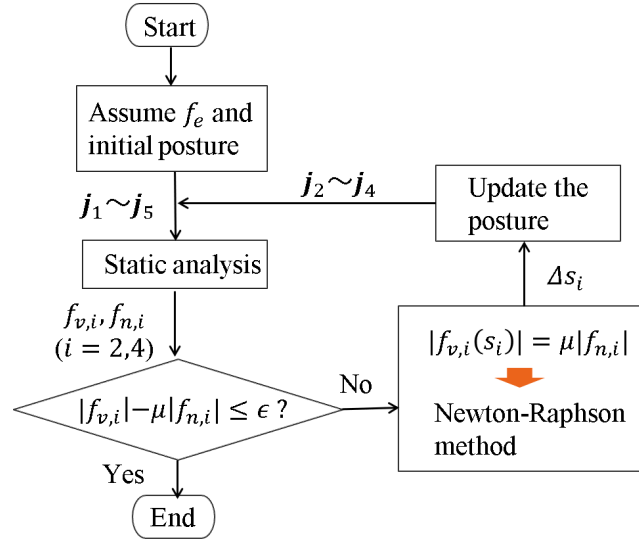
Fig.4.30   Flowchart of the analysis of the elastically constrained underactuated mechanism

determined because the number of the statics equations is 12 and the number of the unknown values is 12.

(3) Relative displacements s_2 and s_4 are updated with update formula of Newton-Raphson method so as to satisfy $\boldsymbol{f}_{v,i} = \boldsymbol{0}$ because virtual forces (frictional force) $\boldsymbol{f}_{v,i}$ should be zero.

(4) Positions of J$_2$, J$_3$, J$_4$ are updated by kinematic analysis

The processes (2)-(4) described above are repeated until virtual forces $\boldsymbol{f}_{v,i}$ are converged in the vicinity of zero. The flowchart shown in Fig.4.30 represents these processes, where $\boldsymbol{j}_1 \sim \boldsymbol{j}_5$ are position vectors of J$_1 \sim$J$_5$.

Note that active pairs J$_1$ and J$_5$ cannot be assumed to be rigid in the actual mechanism due to servo stiffness. In that case, each passive angular displacement of J$_1$ and J$_5$ also can be calculated by solving the following equation in the process (3).

$$\tau_j - k_m(\theta_{j,0} - \theta_j) = 0 \ (j = 1, 5), \tag{4.44}$$

where τ_j is the torque of J$_1$ and J$_5$ calculated in the process (2), k_m is torsional stiffness (servo stiffness) of active revolute pairs, $\theta_{j,0}$ is the initial angle of J$_1$ and J$_5$, and θ_j is the angle of J$_1$ and J$_5$ in each step.

4.5.2   Flexibility of the output point

In order to investigate flexibility at the output point of the fabricated mechanism, the force-displacement characteristics in the y- and z-directions shown in Fig.4.28 (b) were measured. Fig.4.31 shows the experimental setup. Force-displacement characteristics of the output point were measured by pushing the output point in the $y < 0$ and $z < 0$ directions with a force gauge attached to the end effector of a serial robot manipulator. The rotation angles of the DC motors were controlled with the PID control so that the output point under no-load was located at $(x, y, z) = (0, 0, 280)$ [mm].

(a) z-direction   (b) y-direction
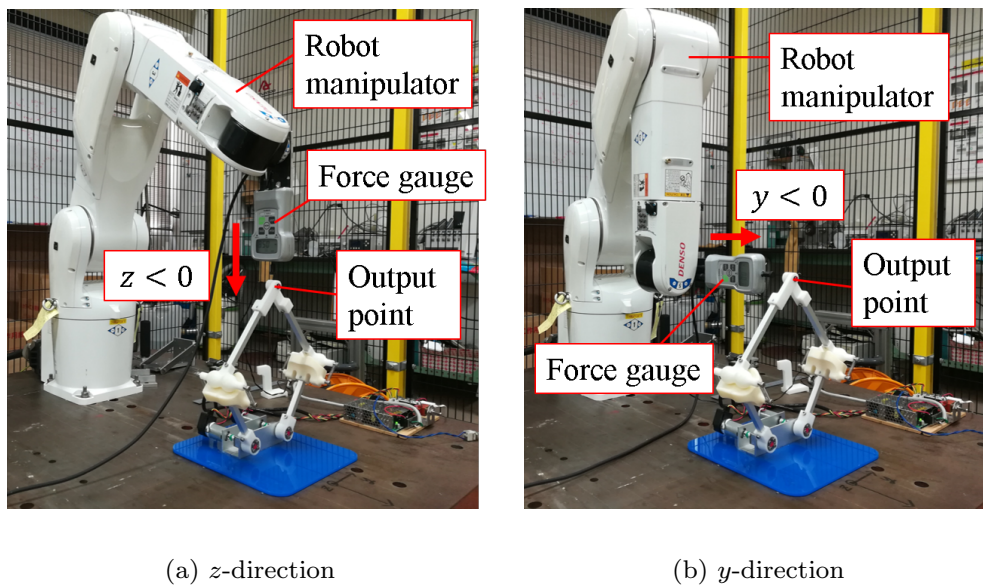
Fig.4.31   Measurement of the force-displacement characteristics at the output point of the fabricated FCP-link mechanism in the multiple directions

(a) z-direction   (b) y-direction
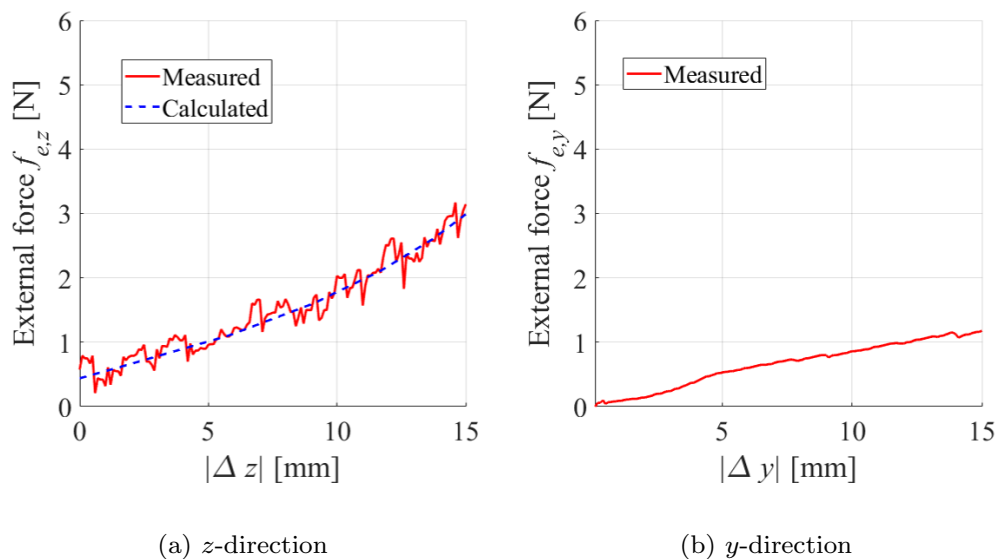
Fig.4.32   Force-displacement characteristics at the output point of the fabricated mechanism

Fig.4.32 shows the result of the measurement, where the red solid line in figure (a) is the measured force-displacement characteristics in the z-direction and the red solid line in figure (b) is the measured characteristics in the y-direction. The broken blue line in Fig.4.32 (a) is the theoretical characteristics calculated with the method described in section 4.5.1. Note that the coefficient of static friction between the two links of the FCRP was assumed to be 0.05, and the stiffness characteristics of the DC motors were

assumed as linear characteristics with the rotational servo stiffness of 1.8×10^4 Nmm/rad. The output point had the hardening stiffness characteristics in the z-direction and the measured characteristics agreed very well with the calculated characteristics. In addition, since the mechanism had the flexibility not only in the z- direction but also in the y-direction, the flexibility in the out of the motion plane was able to be achieved with the FCRPs. Note that the cause of the ripples in the measured characteristics is considered to be due to fabrication accuracy of the FDM.

4.5.3 Kinematic performance

In order to investigate kinematic performances of the flexible mechanism, the output trajectories of the mechanism were measured by a motion capture system. The target trajectory was a rectangular trajectory whose vertexes are at $(x, y, z) = (50, 0, 280)$, $(50, 0, 330)$, $(-50, 0, 330)$, $(-50, 0, 280)$ [mm]. The adjacent two points were interpolated with a dwell-rise-dwell function for time. The output point generated the clockwise (CW) and the counterclockwise (CCW) trajectories starting from $(x, y, z) = (50, 0, 280)$. Input angles were calculated by the inverse kinematics of the planar five-bar closed-loop linkage where all kinematic pairs were assumed as ordinary revolute pairs. The output trajectories were measured with a motion capture system (OptiTrack V120:Duo).

Fig.4.33 shows the measured and target trajectories, where figure (a) shows the trajectories shown in the $x - z$ plane and (b) shows the trajectories shown in the $y - z$ plane. The green dotted line is the target trajectory, the blue solid line is the measured CCW trajectory and the red solid line is the measured CW trajectory. The measured trajectories agreed well with the specified one although motion accuracy was low. Thus,

(a) $x - z$ plane　　　　　(b) $y - z$ plane
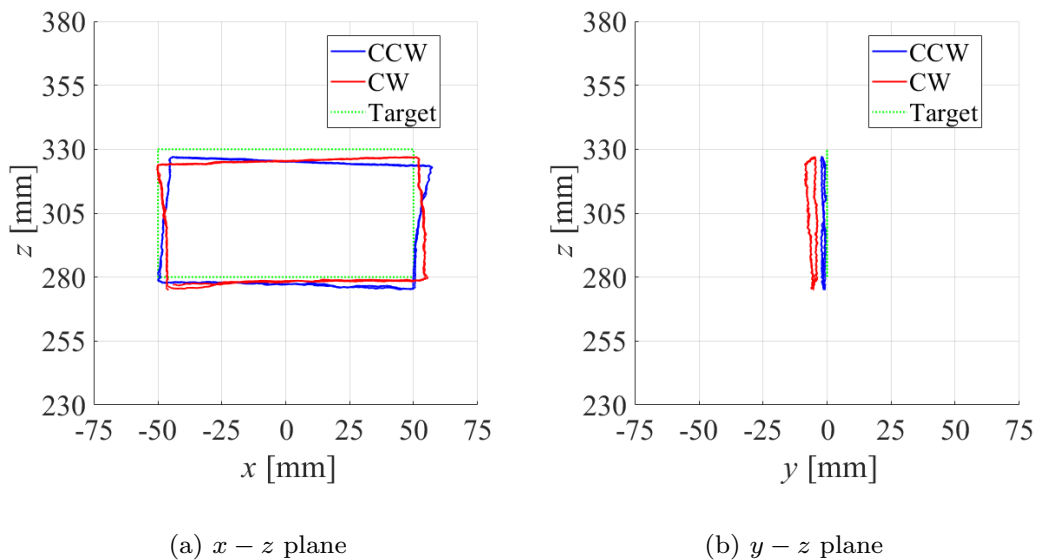
Fig.4.33　The measured and specified trajectories without external load at the output point
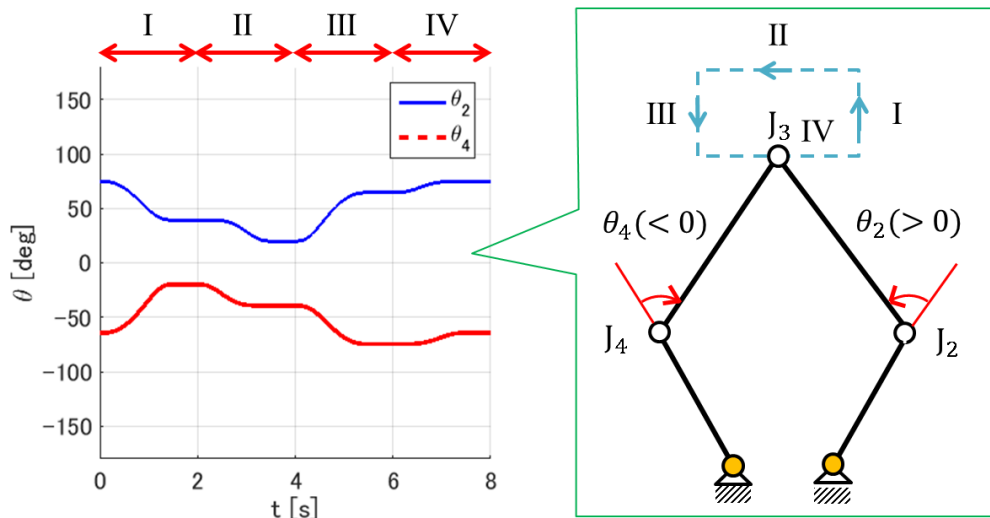
Fig.4.34 Relationship between time shift of relative rotation angles of the FCRPs and the output trajectory of the fabricated mechanism

it is considered that the FCRPs in the mechanism behaved like ordinary revolute pairs. Note that the measured CW trajectory was a little different from the CCW trajectory. If the error between the measured and specified trajectory was caused by the structural error of the mechanism, the two trajectories should be the same trajectories. Thus, it is considered that the error was caused by not the structural error but the displacement between the two links in each of the FCRPs.

In Fig.4.33, the measured rectangular trajectories look being below the specified one. It is considered that this was because the two links in each of the FCRPs displaced relatively due to the effect of the gravity. In addition, Fig.4.33 (a) shows that the output point displaced in the opposite direction of the motion when the top or bottom parts of the rectangular trajectory was generated. The reason is thought to be that rolling motion between the two links in each of the FCRPs occurred because of the friction at the contact points. Fig.4.34 shows the relationship between the position of the output point and time sequence of the relative angle between the two links in each of the FCRPs when the output point generates the CCW trajectory, where the angle θ_2 and θ_4 are relative angle between two links of the FCRPs, J_2 and J_4, respectively. When the output point generates the top part of the rectangular (in the area II in Fig.4.34), the rotational direction of θ_2 is same as θ_4. Then, the link J_2-J_3 and the link J_3-J_4 can displace in the opposite direction of the motion due to the rolling motion between the two links in each of the FCRPs. This idea also can be applied to the case in the bottom part of the rectangular (in the area IV in Fig.4.34).

Next, output trajectories when an impact force applied to the output point of the fabricated mechanism were measured. The specified trajectory was the CCW trajectory with the same rectangular shape starting from $(x, y, z) = (50, 0, 280)$ [mm]. This experiment was performed in the following step.

(1)   The one cycle of the rectangular trajectory was measured under no external load.
(2)   The outpoint was tapped by a human hand in the $z < 0$ or $y < 0$ directions.

(a) $x - z$ plane   (b) $y - z$ plane
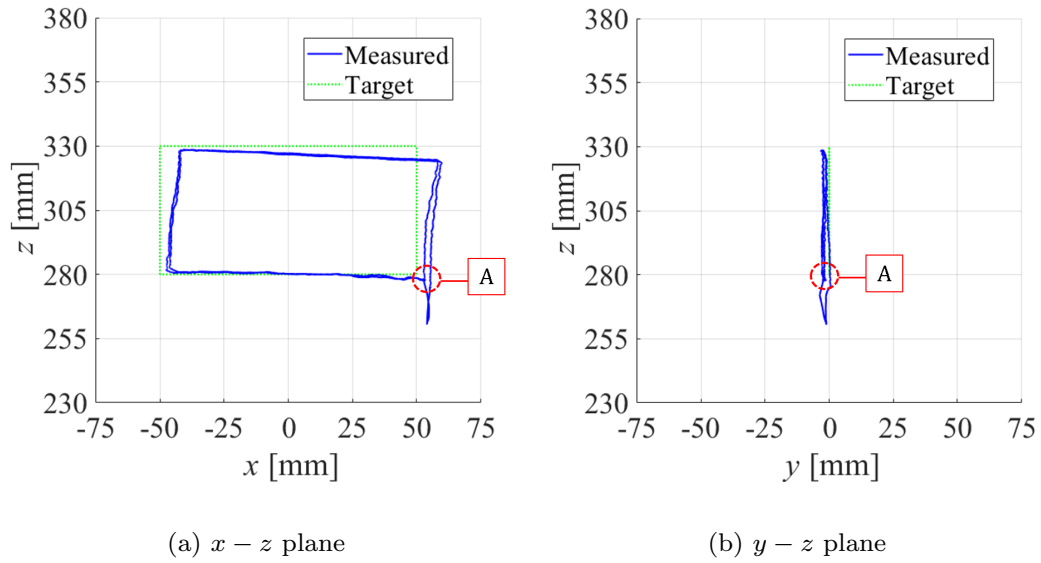
Fig.4.35   The measured trajectory before and after the fabricated FCP-link mechanism subjected to impact force in the $z < 0$ direction

(a) $x - z$ plane   (b) $y - z$ plane
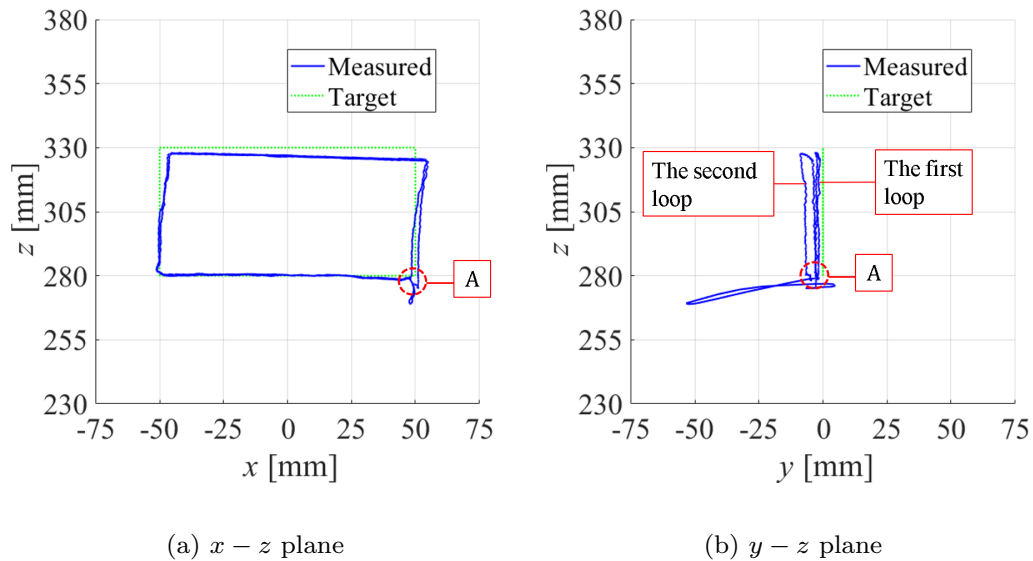
Fig.4.36   The measured trajectory before and after the fabricated mechanism subjected to impact force in the $y < 0$ direction

(3)   The one cycle of the rectangular trajectory after the tapping was measured under no external load.

Fig.4.35 shows the result when the output point was tapped in the z-direction, where figure (a) shows the trajectories shown in the $x - z$ plane and (b) shows the trajectories

shown in the $y - z$ plane. The point A shown in Fig.4.35 is the position where the output point was tapped. These figures show that there were small errors between the trajectory before and after the tapping. Fig.4.36 shows the result when the output point was tapped in the y-direction, where figure (a) shows the trajectories shown in the $x - z$ plane and (b) shows the trajectories shown in the $y - z$ plane. The point A shown in Fig.4.36 is the position where the output point was tapped. The trajectory after the tapping was slightly displaced to the y-direction. The reason is considered that the contact point between the two links in each of the FCRPs was not able to return to the initial position completely due to the static friction. However, the effect of the friction can be reduced with enough lubrication between the two links in each of the FCRPs. Therefore, the motion of the FCP-link mechanism is robust against an external load under the efficient lubrication between two links of the FCRP.

4.6   Discussion

The scope of application of the FCP designed with the proposed method is discussed for future developments of its applications. Although non-linear stiffness characteristics can be specified in the relative sub-direction between the links of the FCP, the characteristics which can be specified are limited. If a complex force-displacement curve whose curvature changes frequently is specified as non-linear stiffness characteristics, the designed profile of the cam surface may be complicated. In this case, the FCP cannot generate the specified force-displacement characteristics in its sub-direction because structural interference (unintended contact state) between the cam surface and the spherical surface may occur. Therefore, a force-displacement curve whose curvature does not change frequently, such as a curve with linear, hardening and softening stiffness characteristics, is preferable to be specified. Actually, softening or hardening stiffness characteristics have been used for many cases such as force limiting of a robotic arm [58], flexible support with robotic legs [65] and grasping objects with a robotic hand [66]. In many cases, the use of hardening and softening stiffness characteristics is considered to be sufficient.

Since the FCP has passive compliance, it is not preferable to be used for applications which require accurate motion. Therefore, the FCP is preferable to be used for applications which allow rough motion and which require adaptability to its environment. Actually, tasks in human daily life, such as grasping something, carrying something and so on, allows rough motion and require adaptability for uncertain environments. Therefore, the FCP is expected to be used to robots which perform such tasks in place of people.

4.7   Chapter summary

The flexibly constrained pair (FCP), which has both motion guidance and the specified multi-directional flexibility, was developed. It has a simple structure composed of several cam surfaces and several spherical surfaces kept in contact at a point with each other by some linear springs. The kinematic constraint with multi-directional flexibility is achieved by a difference of stiffness in the main-directions and sub-directions. By using the FCP, a flexible robotic mechanism with a simple structure can be easily synthesized. In this chapter, a design method of the FCP was proposed, and some examples were designed

and examined by experiments. In addition, a simple robotic mechanism with the FCP was fabricated and examined. The achievements of this chapter are as follows.

(1) A design method for the FCP to have the specified relative motion and flexibility was proposed. Firstly, multiple-DOF between the links are divided into the main-DOF and sub-DOF, and the relative motion of main-DOF is specified. Next, linear springs are optimally arranged between the links to reduce their elastic forces in main-DOF. Then, the cam profile is designed for the FCP to have the force-displacement characteristics which are specified to make a difference of stiffness in the sub-translation directions. Finally, relative sub-rotations are flexibly constrained by arranging several sets of the designed cam surfaces and the spherical surfaces.

(2) As examples, the flexibly constrained revolute pair (FCRP), which allows 1-axial rotation in main-DOF, and a path-generating FCP, which allows 3-axial rotations and the translation along the specified trajectory in main-DOF, were designed by using the proposed design method.

(3) Force-displacement characteristics of the fabricated FCRPs were measured by a tensile testing machine. Besides, the behavior of the fabricated path-generating FCP when external forces were applied was investigated by a motion capture system. As the results, the measured performances agreed well with the specified performances in their design. Therefore, the validity of the design method was confirmed.

(4) A planar closed-loop mechanism with the FCRPs was designed and fabricated as an application, and its performances were investigated with analysis and experiments. As a result, it was confirmed that the mechanism had multi-directional flexibility and was able to generate the specified motion with an adequate position accuracy under small external loads, and that it was able to absorb large external force by passive relative motions of the FCPs.

Chapter 5

The Active Flexibly Constrained Pair

5.1   Chapter introduction

The flexibly constrained pair (FCP) proposed in chapter 4, which has "flexible kinematic constraints" between the links, can introduce multi-directional flexibility into robots with a simple structure. However, since the FCP is a passive kinematic pair, it must be used only in a closed-loop mechanism. In this case, a part of the mechanism with FCPs cannot be flexible because non-flexible active pairs must be used to drive the mechanism. Therefore, the structure of the mechanism with FCPs is limited to a closed-loop mechanism. In order to solve these problems, it is necessary to make the FCP an active kinematic pair. As in the case of the active spatial rolling contact pair proposed in chapter 3, if the linear springs of the FCP are replaced by "active" elastic elements, the FCP can be driven actively with them and it can be regarded as an active kinematic pair. Therefore, the active flexibly constrained pair (AFCP), which is antagonistically driven with several active elastic elements, is developed in this chapter.

Fig.5.1 shows the proposed structure of the AFCP. It is composed of a link with several
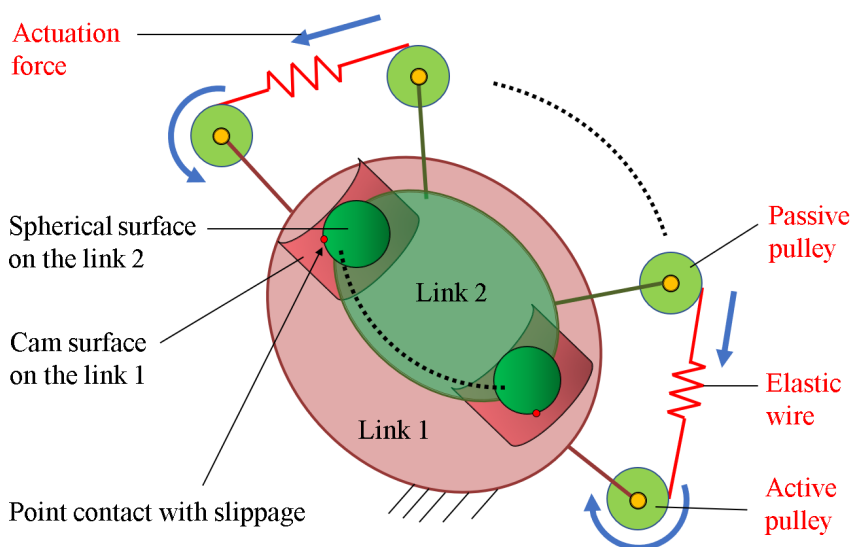
Fig.5.1   Structure of the active flexibly constrained pair (AFCP)

cam surfaces and a link with several spherical surfaces. The two links are driven actively by several active elastic elements while each cam surface and spherical surface are kept in contact at a point. As the active elastic elements, reeled elastic wires are used because their linear stiffness characteristics simplify the design and control of the AFCP. As described in chapter 3, the least number of wires required to drive a kinematic pair is one more number than its DOF. Thus, the required wires to drive the FCP is at most six wires because DOF of the FCP is at most five. However, the structure of the FCP becomes complicated and heavyweight in this case. Therefore, the FCP is regarded to be a kinematic pair with its main-DOF, and only one more wires than the number of its main-DOF are arranged between the links. In this case, motion accuracy of the AFCP decreases because it is an underactuated active kinematic pair. Thus, flexibility and motion accuracy are balanced by designing the stiffness in the sub-DOF with the design method described in chapter 4.

   This chapter describes the following three contributions to achieve AFCP.

(1) Proposal and validation of a method to optimally arrange active elastic elements between the links so as to maximize actuation force transmission in main-direction of an underactuated joint
(2) Proposal and validation of a design method to achieve not only the specified stiffness characteristics in sub-directions between the links of the AFCP but also the required stiffness to do the desired task in main-directions
(3) Prototyping and examination of AFCP with multi-axial flexibility

   In section 5.2, a design method of the AFCP is proposed. In section 5.3, the method to analyze kinetostatic motion between the links is proposed to evaluate motion accuracy between the links. In section 5.4, several examples are designed with the proposed design method. In section 5.5, the designed examples are prototyped, and their performances are examined by motion capture experiments.

5.2   Design method

   A design method of the AFCP is proposed. Firstly, multiple-DOF between the links are divided into main-DOF and sub-DOF, and the relative motion in main-DOF is specified. Next, reeled elastic wires are optimally arranged between the links to maximize the force transmission to main-DOF. Then, the required stiffness of elastic wires is calculated so that the AFCP has sufficient stiffness to perform the desired task. Finally, the cam profile is designed, and several sets of the cam surface and the spherical surface are then arranged between the links to achieve the specified flexible constraints.

5.2.1   Motion specification

   The relative motion between the links of the FCP is specified in the same way described in section 4.2.1. In this section, this method is reviewed briefly.

   Since the FCP allows at most 5 DOF, the motion can be specified with two parameters on translations, t, u, and three parameters on rotations, θ_r, θ_p and θ_y, which are the roll, pitch and yaw angles, respectively. Then, parameters in main-DOF are represented as t_m, u_m, $\theta_{r,m}$, $\theta_{p,m}$ and $\theta_{y,m}$, and parameters in sub-DOF are represented as t_s, u_s, $\theta_{r,s}$, $\theta_{p,s}$ and $\theta_{y,s}$. Firstly, several main-parameters are chosen from the five parameters, and the

other main-parameters are then specified as zero. Then, sub-parameters reciprocating to the chosen main-parameters are chosen, and the other sub-parameters are then specified as zero. Besides, the relative main-motion of the reference position (output position) $^1\boldsymbol{p}$ is specified as a point, a curve (line) or a surface (plane) as follows.

$$^1\boldsymbol{p}(t_m, u_m) = [x_1(t_m, u_m) \; y_1(t_m, u_m) \; z_1(t_m, u_m)]^T, \tag{5.1}$$

where $x_1(t_m, u_m)$, $y_1(t_m, u_m)$ and $z_1(t_m, u_m)$ are arbitrary functions. If $^1\boldsymbol{p}$ is a curve (line), only t_m is used and u_m is specified as zero. In addition, ranges of main-parameters are specified as follows.

$$A_m = \{(t_m, ...)| \; t_{m,0} \leqq t_m \leqq t_{m,1}, ...\} \tag{5.2}$$

5.2.2 Optimal arrangement of reeled elastic wires

Reeled elastic wires are optimally arranged between the links of the FCP to maximize force transmission in main-DOF. As the evaluation criterion of the force transmission, the transmission index for parallel wire-driven mechanisms [98], $\mathrm{TI_w}$, is used in the same way as the design of the active spatial rolling contact pair (ASRCP) in section 3.2. In this section, the method to calculate $\mathrm{TI_w}$ of the AFCP, which is an underactuated joint driven by wires of which number is smaller than its DOF, and the optimization problem to maximize it are proposed.

Fig.5.2 shows the schematic diagram for the design. Σ_1 is the reference coordinate system on the link 1, which has cam surfaces. Σ_2 is the reference coordinate system of the link 2, which has spherical surfaces. In addition to Σ_1 and Σ_2, the reference coordinate system Σ_s is defined. The origin locates at $^1\boldsymbol{p}$, and its bases $^1\boldsymbol{e}_{s,x}$, $^1\boldsymbol{e}_{s,y}$, $^1\boldsymbol{e}_{s,z}$ are specified based on geometry of $^1\boldsymbol{p}$ as follows.
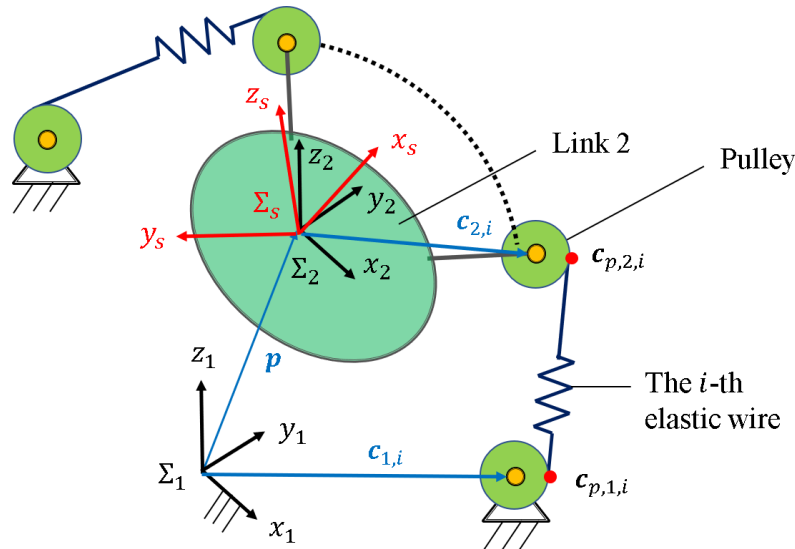
Fig.5.2 Kinetostatic model of the AFCP for the design method

- If $^1\boldsymbol{p}$ is a point, arbitrary independent directions are specified as $^1\boldsymbol{e}_{s,x}$, $^1\boldsymbol{e}_{s,y}$ and $^1\boldsymbol{e}_{s,z}$.
- If $^1\boldsymbol{p}$ is a line, $^1\boldsymbol{e}_{s,x}$ is its tangent vector, and the other independent two directions are specified as $^1\boldsymbol{e}_{s,y}$ and $^1\boldsymbol{e}_{s,z}$.
- If $^1\boldsymbol{p}$ is a curve, $^1\boldsymbol{e}_{s,x}$ is its tangent vector, $^1\boldsymbol{e}_{s,y}$ is its principal normal vector and $^1\boldsymbol{e}_{s,z}$ is its bi-normal vector.
- If $^1\boldsymbol{p}$ is a surface, $^1\boldsymbol{e}_{s,z}$ is its normal vector, and the other two independent directions are specified as $^1\boldsymbol{e}_{s,x}$ and $^1\boldsymbol{e}_{s,y}$.

In order to calculate $\mathrm{TI_w}$ in main-DOF, the FCP is regarded as a kinematic pair with only its main-DOF, and it is assumed that virtual constraint forces are applied at the origin of Σ_s in the sub-directions when external forces are applied between the links. In this case, the direction of the normal reaction force can be represented as the following wrench screw.

$$^1\mathbb{S}_n^r = \begin{bmatrix} ^1\boldsymbol{e}_{s,z} \\ ^1\boldsymbol{p} \times {^1}\boldsymbol{e}_{s,z} \end{bmatrix} \tag{5.3}$$

In the same way, the other independent directions of the constraint forces can be represented virtually as follows.

$$^1\mathbb{S}_{c,1}^r = \begin{bmatrix} ^1\boldsymbol{e}_{s,x} \\ ^1\boldsymbol{p} \times {^1}\boldsymbol{e}_{s,x} \end{bmatrix}, \ \ ^1\mathbb{S}_{c,2}^r = \begin{bmatrix} ^1\boldsymbol{e}_{s,y} \\ ^1\boldsymbol{p} \times {^1}\boldsymbol{e}_{s,y} \end{bmatrix},$$
$$^1\mathbb{S}_{c,3}^r = \begin{bmatrix} \boldsymbol{0} \\ ^1\boldsymbol{e}_{1,x} \end{bmatrix}, \ \ ^1\mathbb{S}_{c,4}^r = \begin{bmatrix} \boldsymbol{0} \\ ^1\boldsymbol{e}_{1,y} \end{bmatrix}, \ \ ^1\mathbb{S}_{c,5}^r = \begin{bmatrix} \boldsymbol{0} \\ ^1\boldsymbol{e}_{1,z} \end{bmatrix}, \tag{5.4}$$

where $^1\boldsymbol{e}_{1,x}$, $^1\boldsymbol{e}_{1,y}$, $^1\boldsymbol{e}_{1,z}$ are bases of Σ_1. $^1\mathbb{S}_{c,1}^r$ and $^1\mathbb{S}_{c,2}^r$ represent the t- and u- directions of translation forces, respectively. $^1\mathbb{S}_{c,3}^r$, $^1\mathbb{S}_{c,4}^r$ and $^1\mathbb{S}_{c,5}^r$ represent the θ_r-, θ_p- and θ_y- directions of rotation torques, respectively. From these five wrench screws of the virtual contact forces, ones corresponding to the chosen sub-parameters are selected. Then, $^1\mathbb{S}_n^r$ and the chosen wrench screws are put together into a matrix as $\boldsymbol{G}_c = [^1\mathbb{S}_n^r ... ^1\mathbb{S}_{c,i}^r ...]$.

Next, actuation forces of the elastic wires are considered. As shown in Fig.5.2, center positions of pulleys for the i-th elastic wire are defined as $^1\boldsymbol{c}_{1,i}$ on Σ_1 and $^2\boldsymbol{c}_{2,i}$ on Σ_2. The position of $^1\boldsymbol{c}_{2,i}$ on Σ_1 is calculated with the following equation.

$$^1\boldsymbol{c}_{2,i} = \boldsymbol{R}_{1,2}(\theta_{r,m}, \theta_{p,m}, \theta_{y,m})^2\boldsymbol{c}_{2,i} + {^1}\boldsymbol{p}(t_m, u_m) \tag{5.5}$$

In order to derive the direction of the i-th wire tension, application points of the tension on the pulleys, $^1\boldsymbol{c}_{p,1,i}$ and $^1\boldsymbol{c}_{p,2,i}$, which are shown in Fig.5.2, have to be derived. The kinematic model of the i-th reeled wire is assumed as shown in Fig.5.3. The pulley attached to the link 1 (pulley 1) allows 2-axial rotation at the center of the pulley, while the pulley attached to the link 2 (pulley 2) allows 3-axial rotations at the center of the pulley. The wire is a common tangent to the two pulleys. Since the length of the wire can extend, it is represented as the kinematic model where the two application points are connected via a prismatic pair. If the center points of the pulleys are assumed to be stationary points, this spatial mechanism is considered to have four links, a spherical pair, a prismatic pair and two revolute pair. By substituting this condition into Gruebler's equation, DOF of the model becomes zero. Thus, the posture of the mechanism is uniquely determined with

$^1c_{1,i}$ and $^1c_{2,i}$. Therefore, the kinematics of this model is solved. Let radii of the pulley 1 and the pulley 2 be $r_{p,1,i}$ and $r_{p,2,i}$, respectively. Then, the condition of the size of the pulley 1 is represented as follows.

$$(^1c_{p,1,i} - {}^1c_{1,i})^T(^1c_{p,1,i} - {}^1c_{1,i}) = r_{p,1,i}^2 \tag{5.6}$$

Since $(^1c_{p,1,i} - {}^1c_{1,i})$ and $(^1c_{p,2,i} - {}^1c_{2,i})$ are parallel, the following equation holds.

$$^1c_{p,2,i} - {}^1c_{2,i} = \frac{r_{p,2,i}}{r_{p,1,i}}(^1c_{p,1,i} - {}^1c_{1,i}) \tag{5.7}$$

Besides, the following equations hold because of orthogonal relationships of vectors.

$$(^1c_{p,2,i} - {}^1c_{p,1,i})^T(^1c_{p,1,i} - {}^1c_{1,i}) = 0, \tag{5.8}$$

$$[(^1c_{p,1,i} - {}^1c_{1,i}) \times (^1c_{p,2,i} - {}^1c_{p,1,i})]^{T\,1}\hat{d}_{p,i} = 0, \tag{5.9}$$

where $^1\hat{d}_{p,i}$ is the direction of a rotation axis of the pulley 1, which is shown in Fig.5.3. By substituting Eq.(5.7) into Eq.(5.8), the following equation holds.

$$[r_{p,2,i}(^1c_{p,1,i} - {}^1c_{1,i}) - r_{p,1,i}(^1c_{p,1,i} - {}^1c_{2,i})]^T(^1c_{p,1,i} - {}^1c_{1,i}) = 0, \tag{5.10}$$

By substituting Eq.(5.7) into Eq.(5.9), the following equation holds.

$$[^1\hat{d}_{p,i} \times (^1c_{p,1,i} - {}^1c_{1,i})]^T[r_{p,2,i}(^1c_{p,1,i} - {}^1c_{1,i}) - r_{p,1,i}(^1c_{p,1,i} - {}^1c_{2,i})] = 0 \tag{5.11}$$

The non-linear simultaneous equations composed of Eqs.(5.6), (5.10) and (5.11) have three unknown variables in $^1c_{p,1,i}$. Thus, these can be solved numerically for $^1c_{p,1,i}$. Then, $^1c_{p,2,i}$ is calculated by substituting $^1c_{p,1,i}$ into Eq.(5.7). Therefore, the direction of the
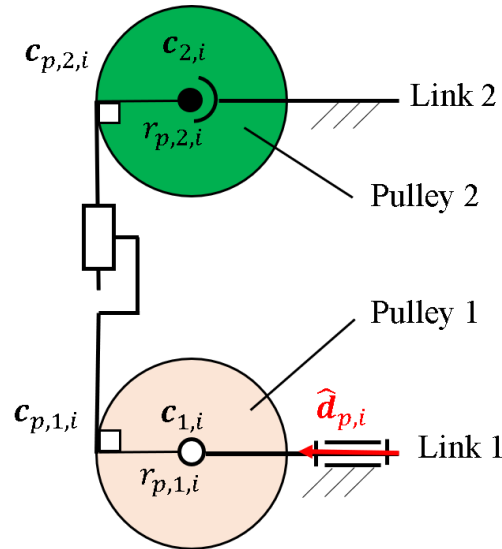
Fig.5.3   An assumed kinematic model of the reeled wire mechanism

i-th wire tension applying to the link 2 can be derived as follows.

$$^1\hat{\boldsymbol{d}}_{a,i} = \frac{^1\boldsymbol{c}_{p,1,i} - {}^1\boldsymbol{c}_{p,2,i}}{|{}^1\boldsymbol{c}_{p,1,i} - {}^1\boldsymbol{c}_{p,2,i}|} \tag{5.12}$$

$$^1\mathbb{S}^r_{a,i} = \begin{bmatrix} {}^1\hat{\boldsymbol{d}}_{a,i} \\ {}^1\boldsymbol{c}_{p,2,i} \times {}^1\hat{\boldsymbol{d}}_{a,i} \end{bmatrix} \tag{5.13}$$

Then, all wrench screws of wire tensions are put together into a matrix as $\boldsymbol{G}_a = [{}^1\mathbb{S}^r_{a,1}...{}^1\mathbb{S}^r_{a,N_a}]$, where N_a is the number of elastic wires.

Let the numerical vector composed of magnitudes of wire-tensions be $\boldsymbol{f}_a = [f_{a,1}...f_{a,N_a}]^T$, and let the numerical vector composed of magnitudes of the normal reaction force and the constraint forces in the sub-directions be $\boldsymbol{f}_c = [f_n...f_{c,i}...]^T$. Then, the following statics equation holds.

$$[\boldsymbol{G}_a \ \boldsymbol{G}_c] \begin{bmatrix} \boldsymbol{f}_a \\ \boldsymbol{f}_c \end{bmatrix} = \boldsymbol{0} \tag{5.14}$$

Let the number of main-DOF be $N_{f,m}$. Then, the number of sub-parameters is $N_{f,s} = 5 - N_{f,m}$, and the number of wires is $N_a = N_{f,m} + 1$. Thus, the number of forces applying to the link 2 is $N_a + 1 + N_s = 7$. Therefore, the FCP can satisfy the force-closure state. In order to calculate TI_w, the statics equation is transformed with focusing on the i-th wire as follows as described in section 3.2.1.

$$\begin{bmatrix} \boldsymbol{f}_{a,-i} \\ \boldsymbol{f}_c \end{bmatrix} = -[\boldsymbol{G}_{a,-i} \ \boldsymbol{G}_c]^{-1}(f_{a,i}{}^1\mathbb{S}^r_{a,i}) = f_{a,i} \begin{bmatrix} \boldsymbol{a}^T_{i,1} \\ \vdots \\ \boldsymbol{a}^T_{i,6} \end{bmatrix} {}^1\hat{\boldsymbol{d}}_{a,i}, \tag{5.15}$$

where $\boldsymbol{f}_{a,-i} = [f_{a,1}...f_{a,i-1} \ f_{a,i+1}...f_{a,N_a}]^T$ and $\boldsymbol{G}_{a,-i} = [\mathbb{S}_{a,1}...\mathbb{S}_{a,i-1} \ \mathbb{S}_{a,i+1}...\mathbb{S}_{a,N_a}]$. The angle between the direction of the i-th wire tension ${}^1\hat{\boldsymbol{d}}_{a,i}$ and the plane $\boldsymbol{a}^T_{i,j}{}^1\hat{\boldsymbol{d}}_{a,i} = 0$ is defined as $\gamma_{i,j}$, and $\sin\gamma_{i,j}$ is calculated as an evaluation criterion. When $\sin\gamma_{i,j}$ is a positive value, $\boldsymbol{a}^T_{i,j}{}^1\hat{\boldsymbol{d}}_{a,i} > 0$ ($j = 1,2,...,6$) holds. In the AFCP, wire-tensions and the normal reaction forces are uni-directional forces. Thus, $f_{a,1},...,f_{a,N_a}$, f_n must be positive values. Therefore, $\sin\gamma_{i,j}$ is considered just in terms of $j = 1,...,N_a$. Then, the transmission index is calculated as follows.

$$\mathrm{TI}_\mathrm{w} = \min_{i=1,...,N_a}[\rho_i \min_{j=1,...,N_a}(\sin\gamma_{i,j})] \tag{5.16}$$

$$\rho_i = \begin{cases} 1 \ (\sin\gamma_{i,j} > 0) \\ 0 \ (\sin\gamma_{i,j} \leqq 0) \end{cases} \tag{5.17}$$

In order to arrange elastic wires to maximize TI_w, the mean value of $\sin\gamma_{i,j}$ is used for the objective function in the same way as described in section 3.2.3. Let design parameters be $\boldsymbol{c} = [{}^1\boldsymbol{c}^T_{1,1},...,{}^1\boldsymbol{c}^T_{1,N_a}, \ {}^2\boldsymbol{c}^T_{2,1},...,{}^2\boldsymbol{c}^T_{2,N_a}]^T$. Then, the optimization problem is as follows.

$$\text{maximize} \qquad\qquad F_a(\boldsymbol{c}) = \underset{A_m}{\mathrm{mean}}[\underset{i,j=1,...,N_a}{\mathrm{mean}}(\sin\gamma_{i,j})], \tag{5.18}$$

$$\text{subject to} \qquad\qquad \boldsymbol{c}_{min} \leqq \boldsymbol{c} \leqq \boldsymbol{c}_{max}, \tag{5.19}$$

where $\underset{A_m}{\mathrm{mean}}(x)$ is the mean value of x in A_m.

5.2.3 Stiffness design in main-DOF

In order to make a robot with the AFCP perform a task, the AFCP must have stiffness in main-DOF enough to perform the task. The stiffness in the main-DOF depends on the stiffness of elastic wires. Therefore, a method to calculate wire-stiffness required for the AFCP to have the specified stiffness in main-DOF is proposed.

In the main-directions of the AFCP, virtual external forces are applied. Anything from $^1\mathbb{S}^r_{c,1}$ to $^1\mathbb{S}^r_{c,5}$ that is not included in $\boldsymbol{G}_c$ is included in $\boldsymbol{G}_v$. In the same way, anything from $f_{c,1}$ to $f_{c,5}$ that is not included in $\boldsymbol{f}_c$ is included in $\boldsymbol{f}_v$. Then, $\boldsymbol{G}_v\boldsymbol{f}_v$ represents the sum of virtual external forces in the main-directions. Thus, the statics equation is represented as follows.

$$[\boldsymbol{G}_a\ \boldsymbol{G}_v\ \boldsymbol{G}_c]\begin{bmatrix}\boldsymbol{f}_a\\\boldsymbol{f}_v\\\boldsymbol{f}_c\end{bmatrix}=\boldsymbol{0} \tag{5.20}$$

Since $[\boldsymbol{G}_v\ \boldsymbol{G}_c]$ is a regular matrix, this equation can be transformed as follows.

$$\begin{bmatrix}\boldsymbol{f}_v\\\boldsymbol{f}_c\end{bmatrix}=-[\boldsymbol{G}_v\ \boldsymbol{G}_c]^{-1}\boldsymbol{G}_a\boldsymbol{f}_a \tag{5.21}$$

From this equation, the relationship between $\boldsymbol{f}_v$ and $\boldsymbol{f}_a$ can be obtained as the following form.

$$\boldsymbol{f}_v=\boldsymbol{D}_v\boldsymbol{f}_a \tag{5.22}$$

Besides, the following equation holds from the principle of virtual work.

$$\boldsymbol{f}_a^T\Delta\boldsymbol{l}_a=\boldsymbol{f}_v^T\Delta\boldsymbol{q}_m, \tag{5.23}$$

where $\boldsymbol{l}_a$ is the numerical vector composed of length of wires, and $\boldsymbol{q}_m$ is the numerical vector composed of main-parameters. In addition, the following equations hold from Hooke's law.

$$\boldsymbol{f}_a=\boldsymbol{K}_a\Delta\boldsymbol{l}_a, \tag{5.24}$$
$$\boldsymbol{f}_v=\boldsymbol{K}_m\Delta\boldsymbol{q}_m, \tag{5.25}$$

where $\boldsymbol{K}_a$ is the stiffness matrix of wires represented as $\boldsymbol{K}_a=\mathrm{diag}(k_{a,1},...,k_{a,N_a})$, and $\boldsymbol{K}_m$ is the stiffness matrix in the main-directions represented as $\boldsymbol{K}_m=\mathrm{diag}(k_{m,1},...,k_{m,N_{f,m}})$. From Eqs.(5.22)-(5.25), the relationship between $\boldsymbol{K}_a$ and $\boldsymbol{K}_m$ is represented as follows.

$$\boldsymbol{K}_m=\boldsymbol{D}_v\boldsymbol{K}_a\boldsymbol{D}_v^T \tag{5.26}$$

In order to make stiffness in the main-directions satisfy the required values, the minimum value of the stiffness in A_m must be larger than the required value. Thus, the

required wire-stiffness is calculated with an optimization problem. Let design parameters be $\boldsymbol{q}_m$ and $\boldsymbol{k}_a = [k_{a,1}...k_{a,N_a}]^T$. Then, the optimization problem is proposed as follows.

$$\text{minimize} \quad F_{s,m}(\boldsymbol{q}_m, \boldsymbol{k}_a) = \boldsymbol{K}_m^T \boldsymbol{K}_m, \quad (5.27)$$

$$\text{subject to} \quad \boldsymbol{q}_m \in A_m, \quad (5.28)$$

$$\boldsymbol{k}_a \geqq \boldsymbol{k}_{a,req}, \quad (5.29)$$

where $\boldsymbol{k}_{a,req}$ is the numerical vector composed of the required stiffness in the main-directions to perform the desired task.

5.2.4 Stiffness design in sub-DOF

As well as the design of the passive FCP, the specified force-displacement characteristics can be implemented in the sub-translation directions of the AFCP by designing the cam profile. Thus, the method to calculate the cam profile of the AFCP is described.

Firstly, the actuation forces of the elastic wires are calculated approximately. Since the cam profile has not been derived in this process, the AFCP is assumed as a kinematic pair only with main-DOF. In this case, the statics equation is as follows.

$$[\boldsymbol{G}_a \ \boldsymbol{G}_c] \begin{bmatrix} \boldsymbol{f}_a \\ \boldsymbol{f}_c \end{bmatrix} = -{}^1\mathbb{W}_e, \quad (5.30)$$

where ${}^1\mathbb{W}_e$ is an external force which applied to perform the desired task. If one of wire tensions, $f_{a,i}$, is assumed as a bias tension, the statics equation can be solved as follows.

$$\begin{bmatrix} \boldsymbol{f}_{a,-i} \\ \boldsymbol{f}_c \end{bmatrix} = -[\boldsymbol{G}_{a,-i} \ \boldsymbol{G}_c]^{-1}(f_{a,i}{}^1\mathbb{S}_{a,i}^r + {}^1\mathbb{W}_e) \quad (5.31)$$
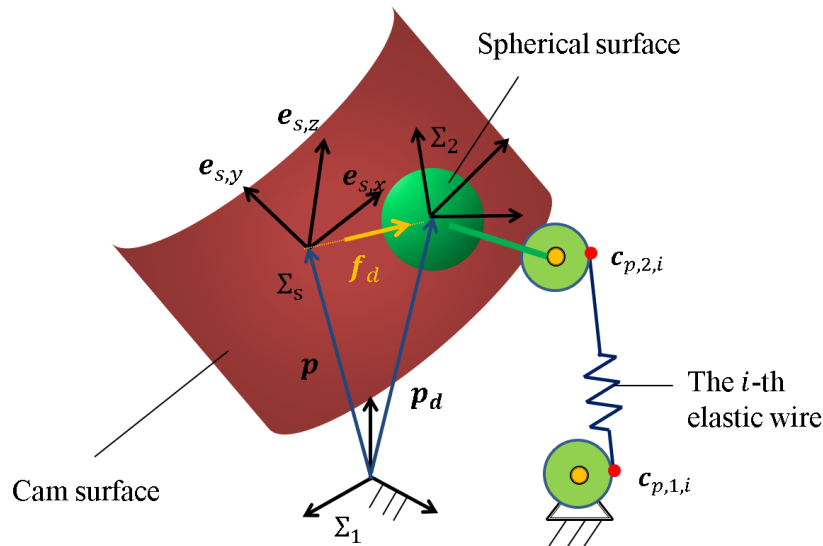
Fig.5.4   Schematic diagram for the cam profile design of the AFCP

Next, the force-displacement characteristics are specified, and the cam profile is calculated. In the design of the AFCP, a relationship between external force and displacement of the center of the spherical surface is used as the specified force-displacement characteristics because it is convenient to know the motion between the links intuitively. Fig.5.4 shows the schematic diagram for the cam profile design, where the center of a single spherical surface is assumed to locate at the origin of Σ_2. When an external force ${}^s\boldsymbol{f}_d(t_s, u_s) = [f_{d,t}(t_s)\ f_{d,u}(u_s)\ 0]^T$, which contains the specified force displacement characteristics defined on Σ_s, is applied between the links, the center point of the spherical surface displaces relatively in the sub-translation direction from ${}^1\boldsymbol{p}(t_m, u_m)$. Then, the displaced position ${}^1\boldsymbol{p}_d$ is represented as following equation.

$$ {}^1\boldsymbol{p}_d = {}^1\boldsymbol{p}(t_m, u_m) + \boldsymbol{R}_{1,s}[t_s\ u_s\ g_d]^T, \tag{5.32} $$

where $\boldsymbol{R}_{1,s}$ is the rotation matrix from Σ_1 to Σ_s. Then, application points of wire tensions ${}^1\boldsymbol{c}_{p,1,i}$ and ${}^1\boldsymbol{c}_{p,2,i}$ ($i = 1, ..., N_a$) are updated through the procedure described in section 5.2.2. In this case, the relationship between the work of ${}^s\boldsymbol{f}_d$ and the potential energy of linear springs are as follows.

$$ \sum_{i=1}^{N_a}[\frac{k_i}{2}\Delta l_{a,i}^2 + f_{a,i}\Delta l_{a,i}] - \int_{u_{s,0}}^{u_s} f_{d,u}(u)du - \int_{t_{s,0}}^{t_s} f_{d,t}(t)dt = 0, \tag{5.33} $$

$$ \Delta l_{a,i} = |{}^1\boldsymbol{d}_{a,i}| - |{}^1\boldsymbol{d}_{a,i,0}|, \tag{5.34} $$

$$ {}^1\boldsymbol{d}_{a,i}(t_m, u_m, \theta_{r,m}, \theta_{p,m}, \theta_{y,m}) = {}^1\boldsymbol{c}_{p,1,i} - {}^1\boldsymbol{c}_{p,2,i}, \tag{5.35} $$

where $|{}^1\boldsymbol{d}_{a,i,0}|$ is $|{}^1\boldsymbol{d}_{a,i}|$ when $t_s = u_s = 0$. Arbitrary posture angles $\theta_{r,m}$, $\theta_{p,m}$ and $\theta_{y,m}$ are assumed. Then, each set of (t_m, u_m, t_s, u_s) is substituted into these non-linear simultaneous equations, and they are solved for g_d numerically. By substituting the calculated value of g_d into Eq.(5.32), the surface which the center of the sphere path through is derived. Since the cam surface of an envelope surface of this surface, the cam profile can be calculated with the following equation.

$$ {}^1\boldsymbol{s}_c = {}^1\boldsymbol{p}_d + \frac{r_s}{\sqrt{1 + (\frac{\partial g_d}{\partial t})^2 + (\frac{\partial g_d}{\partial u})^2}}\boldsymbol{R}_{1,s}\begin{bmatrix}\frac{\partial g_d}{\partial t}\\ \frac{\partial g_d}{\partial u}\\ -1\end{bmatrix}, \tag{5.36} $$

where r_s is the radius of the sphere, t is t_s or t_m, and u is u_s or u_m. Finally, several sets of the designed cam and the spherical surfaces are arranged between the links in the same way as in section 4.2.4.

Note that the stiffness design in sub-DOF is very important to balance between the required motion accuracy and the required stiffness. In order to evaluate motion accuracy between the links before fabrication, kinetostatic analysis described in the next section is performed. If the analyzed motion accuracy is not sufficient, the force-displacement characteristics are adjusted, and the cam profile is derived again.

5.3 Kinetostatic analysis

In order to evaluate motion accuracy between the links of the designed AFCP, a method of kinetostatic analysis is proposed. Fig.5.5 shows the schematic diagram of the analysis.
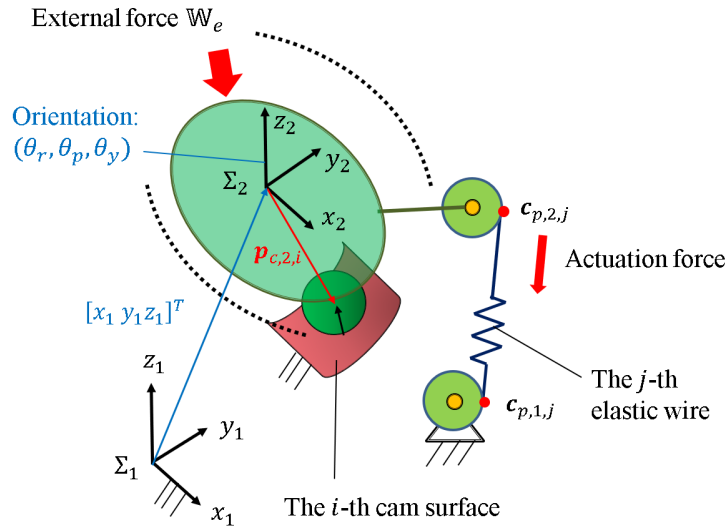
Fig.5.5   Schematic diagram of the kinetostatic analysis of the AFCP

In this analysis, the actuation force which is calculated in Eq.(5.31), and an external force $^1\mathbb{W}_e$ which is required to do a task are applied. Then, it is assumed that the origin of Σ_2 is displaced to $[x_1 \; y_1 \; z_1]^T$ on Σ_1 and the posture angles of Σ_2 on Σ_1 become θ_r, θ_p, θ_y. When the center position of the i-th spherical surface is defined on Σ_2 in $^2\boldsymbol{p}_{c,i}$, it is represented on Σ_1 as follows.

$$^1\boldsymbol{p}_{c,i} = [x_1 \; y_1 \; z_1]^T + \boldsymbol{R}_{1,2}(\theta_r, \theta_p, \theta_y)^2\boldsymbol{p}_{c,i} \tag{5.37}$$

When each cam and spherical surface are assumed to be kept in contact at a point, the following kinematic equation holds.

$$^1\boldsymbol{p}_{c,i} = (^1\boldsymbol{s}_c + r_s\hat{\boldsymbol{n}}_c) + \boldsymbol{R}_{1,2}(0,0,0)^2\boldsymbol{p}_{c,i} = {}^1\boldsymbol{p}_d(t_i, u_i) + {}^2\boldsymbol{p}_{c,i}, \tag{5.38}$$

where $\hat{\boldsymbol{n}}_c$ is the unit normal vector of the cam surface and (t_i, u_i) represents the position of the i-th spherical surface on the i-th cam surface. Besides, the following statics equation holds.

$$\sum_{i=1}^{N_c} f_{n,i} \begin{bmatrix} {}^1\hat{\boldsymbol{n}}_c \\ {}^1\boldsymbol{p}_{c,i} \times {}^1\hat{\boldsymbol{n}}_c \end{bmatrix} + \sum_{j=1}^{N_a} [k_{a,j}(|{}^1\boldsymbol{d}_{a,j}| - |{}^1\boldsymbol{d}_{a,j,0}|) + f_{a,j}] \begin{bmatrix} {}^1\hat{\boldsymbol{d}}_{a,j} \\ {}^1\boldsymbol{c}_{p,2,i} \times \boldsymbol{d}_{a,j} \end{bmatrix}$$
$$+ {}^1\mathbb{W}_e = \boldsymbol{0} \quad (5.39)$$

Simultaneous equations composed of Eqs.(5.38) and (5.39) are $(3N_c + 6)$ nonlinear equations. Since unknown variables are x_1, y_1, z_1, θ_r, θ_p, θ_y, $f_{n,i}$, t_i and u_i $(i = 1, ..., N_c)$, the number of them is also $(3N_c + 6)$. Thus, these equations can be solved numerically. Therefore, the kinetostatic motion between the links can be calculated.

5.4   Design and analysis

By using the proposed design method, several examples of the AFCP were designed and analyzed. In this section, the procedure and the results are described.

5.4.1 Active flexibly constrained revolute pair

As a simple example, the active flexibly constrained revolute pair (AFCRP), which allows only 1-axial main-rotation, was designed. Fig.5.6 shows the schematic diagram of the motion specification. The reference point is at $^1\boldsymbol{p} = \boldsymbol{0}$, and the rotation axis is corresponding to the x_1-axis of Σ_1. Since only the rotation about the x_1-axis was allowed, the roll angle $\theta_{r,m}$ was chosen as the main-parameter and the other parameters were specified to be zero. In contrast, t_s, u_s, $\theta_{p,s}$, $\theta_{y,s}$ were chosen as the sub-parameters, and $\theta_{r,s}$ was specified as zero. The motion range in main-DOF was also specified as $A_m = \{\theta_{r,m}| - \frac{\pi}{4} \leqq \theta_{r,m} \leqq \frac{\pi}{4}\}$, where the unit of the angle was rad.

Next, elastic wires were optimally arranged to maximize force transmission. Since main-DOF of the AFCRP was one, two elastic wires were arranged between the links. In this case, the optimal solution is obvious. As shown in Fig.5.7, the driving force is transmitted from the active pulley on the link 1 to the pulley fixed on the link 2 of which rotation axis is on the main-rotation axis. In this case, force transmission is maximum. Therefore, pulleys with $r_p = 20$ mm were arranged at $[x_1\ y_1\ z_1]^T = [0\ 0\ -100]^T$ [mm] and $[x_1\ y_1\ z_1]^T = [0\ 0\ 0]^T$ [mm] without calculation of the optimization. In the proposed model, one pulley with a wrapping wire shown in Fig.5.7 can be expressed by stacking two pulleys with symmetrical wire arrangements as shown in Fig.5.8. Therefore, $^1\boldsymbol{c}_{1,1} = {}^1\boldsymbol{c}_{1,2} = [0\ 0\ -100]^T$ [mm], $^2\boldsymbol{c}_{2,1} = {}^2\boldsymbol{c}_{2,2} = [0\ 0\ 0]^T$ [mm], $^1\hat{\boldsymbol{d}}_{p,1} = [0\ -1\ 0]^T$ and $\hat{\boldsymbol{d}}_{p,2} = [0\ 1\ 0]^T$ were specified. $\mathrm{TI_w}$ of this arrangement is shown in Fig.5.9, which was calculated by assuming the direction of the normal reaction force as the z_1-direction. As expected, the $\mathrm{TI_w}$ is always one (the maximum value) for $\theta_{r,m}$.

Stiffness of the elastic wires was calculated to achieve the specified rotational stiffness about the main-rotation axis. The required rotational stiffness in the main-direction was
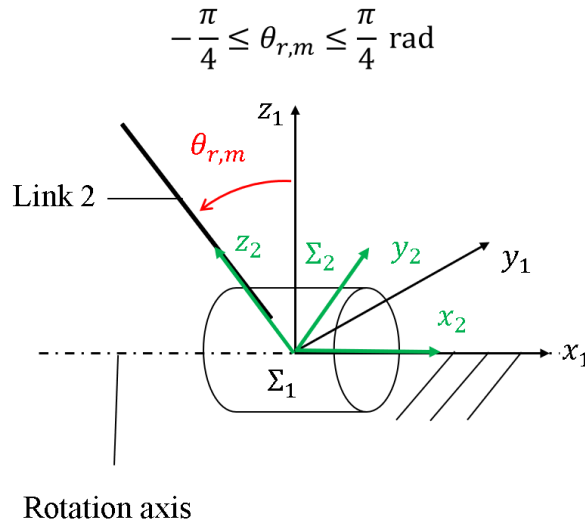
Fig.5.6 Schematic diagram of the motion specification for the active flexibly constrained revolute pair (AFCRP)
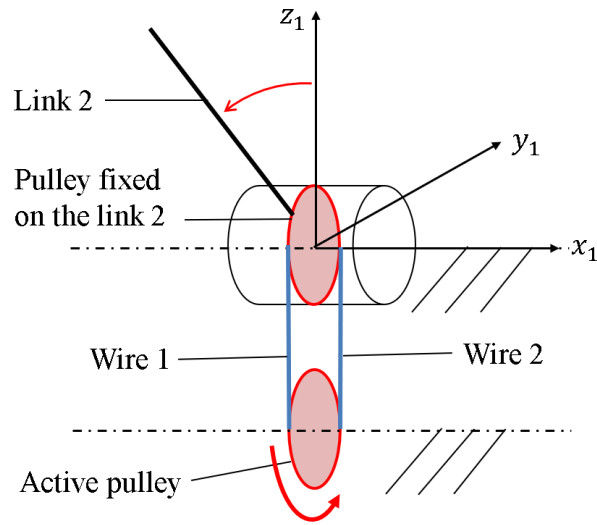
Fig.5.7   Optimal arrangement of reeled elastic wires in the AFCRP
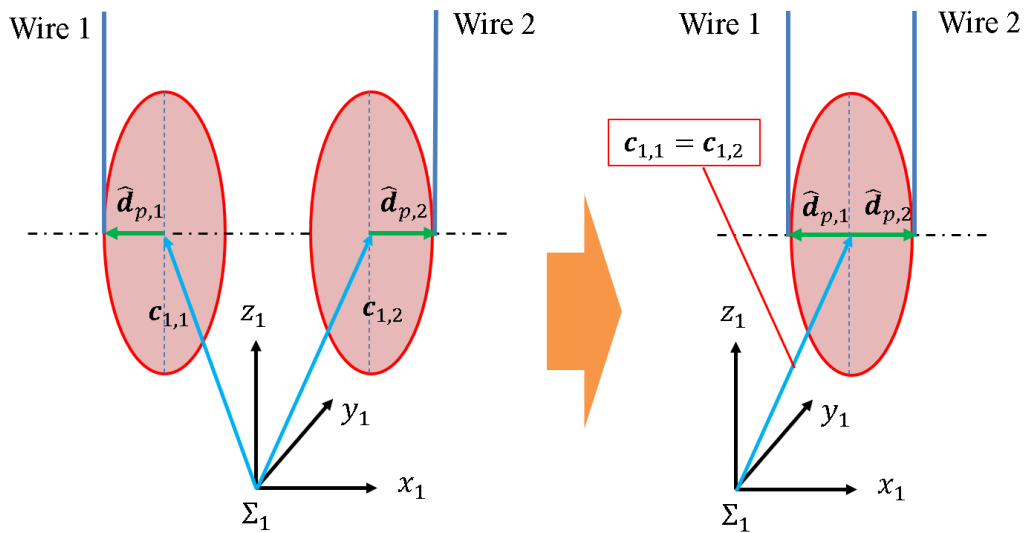
Fig.5.8   Expression of wrapped-wire transmission in the proposed model of the AFCP

specified as $k_{\theta_r,req} = 300$ Nmm/rad. The stiffness of the wire 2, $k_{a,2}$, was assumed to be zero because the tension of the wire 2 is assumed to be controlled constantly. Then, the stiffness of the wire 1 was calculated with the proposed method and became $k_{a,1} = 0.75$ N/mm. Note that the wire stiffness can be calculated easily without the proposed method in this case. Since the statics equation is represented as $k_{\theta_r,req}\theta_{r,m} = k_{a,1}r_p^2\theta_{r,m}$, the wire stiffness can be calculated as $k_{a,1}/(r_p^2) = 300/(20^2) = 0.75$ N/mm. Since the results of the two methods are the same, the proposed method is considered to be valid. The elastic wire with the calculated stiffness can be achieved approximately if a linear spring with the calculated stiffness (spring constant) is connected serially to a rigid wire as described in section 3.5.1. However, it is a rare case to find a commercial linear spring with a
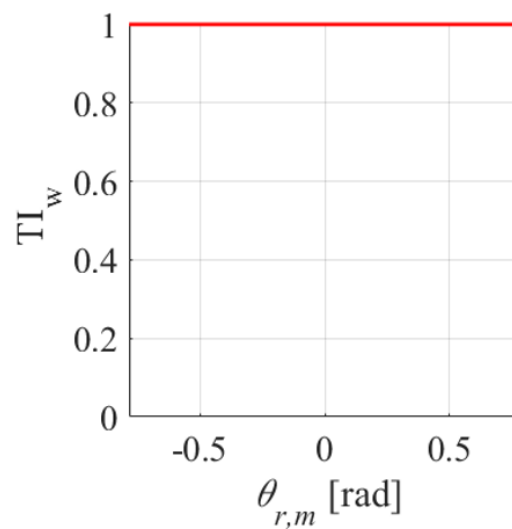
Fig.5.9   Transmission index of the designed AFCRP
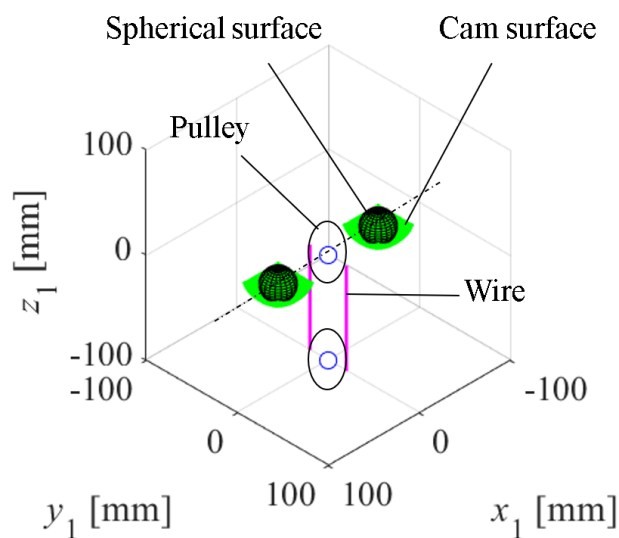
Fig.5.10   Designed structure of the AFCRP

spring constant matching the calculated value. Therefore, a linear spring with the spring constant of 0.772 N/mm was selected and used in the elastic wire.

The cam profile to achieve the specified force-displacement characteristics in the sub-translation directions was designed. External forces applied between the links were assumed to be zero, and the bias actuation force of the wire 2 was assumed to be $f_{a,2} = 2.0$ N. Then, the actuation forces of the elastic wires were calculated. Next, force-displacement

characteristics in the sub-translation directions were specified as follows.

$$
{}^{s}\boldsymbol{f}_d(t_s, u_s) = \begin{bmatrix} 2.0\mathrm{sgn}(t_s)(e^{0.2|t_s|} - 1) \\ 2.0\mathrm{sgn}(u_s)(e^{0.2|u_s|} - 1) \\ 0 \end{bmatrix} \ [\mathrm{N}] \ \ (-10 \leqq t_s, u_s \leqq 10), \qquad (5.40)
$$

where the t_s-direction is the x_1-direction on Σ_1, and the u_s-direction is the y_1-direction on Σ_1. These characteristics are non-linear hardening stiffness characteristics. The radius of the spherical surface was specified as $r_s = 15$ mm. The posture angle was assumed as $\theta_{r,m} = 0$ rad. Then, the cam profile was calculated. Since the FCP allowed 1-axial main rotation, two sets of the designed cam surface and the spherical surface were arranged so that the centers of spheres locate at ${}^{1}\boldsymbol{p}_{c,1} = [55\ 0\ 0]^T$ [mm] and ${}^{1}\boldsymbol{p}_{c,2} = [-55\ 0\ 0]^T$ [mm] on Σ_1. The result is shown in Fig.5.10, where wires, pulleys, cam surfaces and spherical surfaces are shown.

In this example, forces applying in the sub-directions are theoretically zero. Therefore, evaluation of motion accuracy with the kinetostatic analysis is not required.

5.4.2 Path-generating active flexibly constrained pair

The AFCPs which allow the 1-axial main-translation along the specified trajectory were designed. Fig.5.11 shows the schematic diagram of the motion specification. In this examples, t_m was chosen as the main-parameter, and the other main-parameters were specified to be zero. In contrast, u_s, $\theta_{r,s}$, $\theta_{p,s}$ and $\theta_{y,s}$ were chosen as the sub-parameters, and t_s was specified to be zero. As the main-motion, the translation along the following ordinary helix was specified.

$$
{}^{1}\boldsymbol{p}(t_m) = \begin{bmatrix} 60\cos(\frac{\pi t_m}{2}) \\ 60\sin(\frac{\pi t_m}{2}) \\ 30t_m \end{bmatrix} \ [\mathrm{mm}] \qquad (5.41)
$$
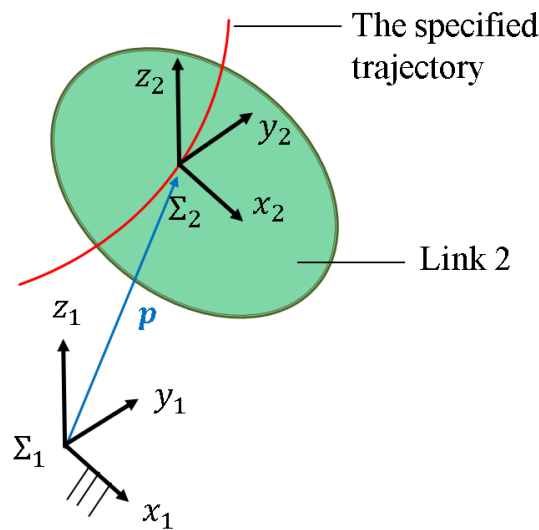
Fig.5.11   Schematic diagram of the motion specification for the path-generating AFCP
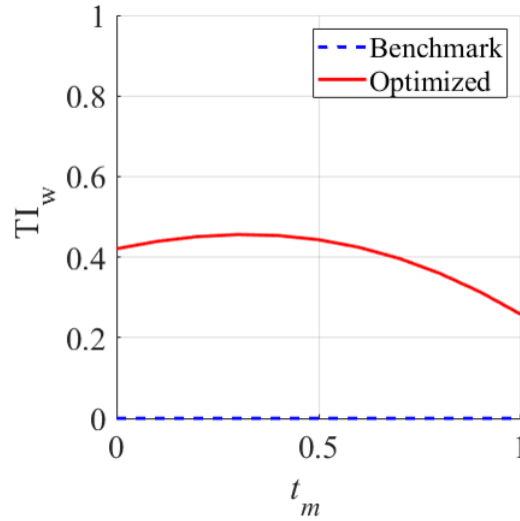
Fig.5.12   Transmission index of the designed path-generating AFCP

The range of the relative main-motion was also specified to $A_m = \{t_m | \ 0 \leqq t_m \leqq 1\}$.

Next, elastic wires were optimally arranged to maximize force transmission. Since main-DOF of this FCP was one, two elastic wires were arranged between the links. The design spaces of center positions of pulleys were specified as follows.

$$[0 \ -150 \ -80]^T \leqq \ ^1\boldsymbol{c}_{1,1} \leqq [120 \ -50 \ -30]^T, \tag{5.42}$$

$$[-100 \ 50 \ -80]^T \leqq \ ^1\boldsymbol{c}_{1,2} \leqq [20 \ 150 \ -30]^T, \tag{5.43}$$

$$[-60 \ -100 \ 50]^T \leqq \ ^2\boldsymbol{c}_{2,1} \leqq [60 \ -30 \ 100]^T, \tag{5.44}$$

$$[-150 \ 30 \ 50]^T \leqq \ ^2\boldsymbol{c}_{2,2} \leqq [-30 \ 100 \ 100]^T, \tag{5.45}$$

where the unit was mm. The radii of pulleys were specified to be zero. This means that pulleys were not used. In this case, attachment directions of pulleys, $^1\boldsymbol{d}_{a,1}$ and $^1\boldsymbol{d}_{a,1}$, do not have to be specified. The direction of the normal reaction force was assumed to be the direction of the bi-normal vector of $^1\boldsymbol{p}(t_m)$ because it was a curve. Many candidates of the initial points for the optimization were randomly generated, and the point to maximize $\mathrm{TI_w}$ was selected as the initial position. Then, the optimization was performed with the interior-point method [118]. The result of the optimization became $^1\boldsymbol{c}_{1,1} = [90.1 \ -139.7 \ -41.3]^T$ [mm], $^1\boldsymbol{c}_{1,2} = [-75.7 \ 150.0 \ -30.0]^T$ [mm], $^2\boldsymbol{c}_{2,1} = [-19.9 \ -53.3 \ 66.5]^T$ [mm] and $^2\boldsymbol{c}_{2,2} = [-35.8 \ 30.0 \ 50.0]^T$ [mm]. In this case, $\mathrm{TI_w}$ for each value of t_m became as shown in Fig.5.12, where the benchmark was also calculated with the center position in the specified design space. Since the optimized $\mathrm{TI_w}$ was larger than the benchmark, it was confirmed that $\mathrm{TI_w}$ was able to become better by the proposed optimization method. In addition, $\mathrm{TI_w}$ was always non-zero value, it is considered that the designed FCP can move overall area in A_m when its two links are assumed not to move relatively in the sub-directions.

Stiffness of the elastic wires was calculated to achieve the specified stiffness in the t_m-direction. The required stiffness in the t_m direction was specified to $k_{t,req} = 1.0$ N/mm. Stiffness of the wire 2, $k_{a,2}$, was assumed to be zero because tension of the wire 2 is
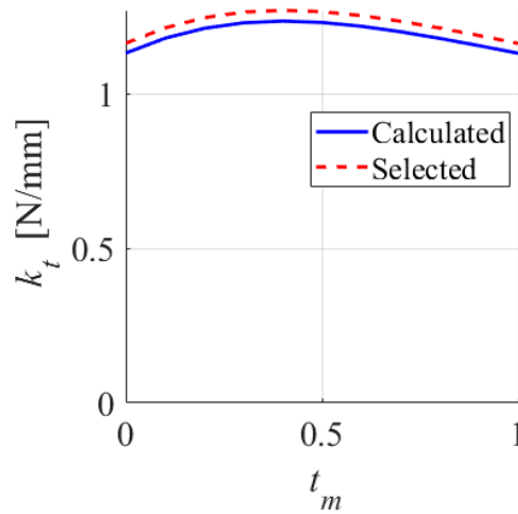
Fig.5.13 Stiffness in the main-translation direction of the designed path-generating AFCP
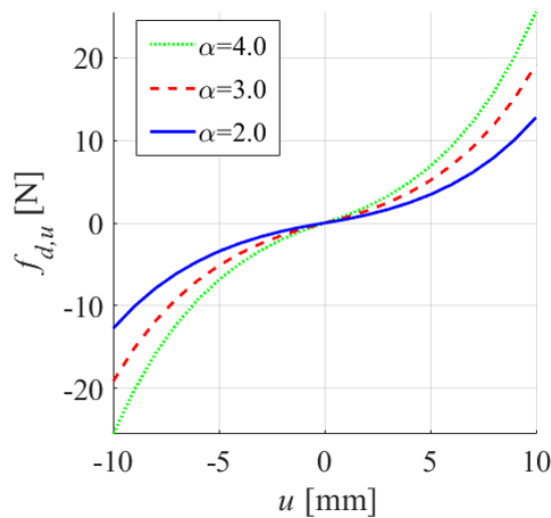
Fig.5.14 The specified force-displacement characteristics in the sub-translation direction of the path-generating AFCP

assumed to be controlled constantly. Then, the stiffness of the wire 1 was calculated with the proposed method and became $k_{a,1} = 1.42$ N/mm. Thus, a commercial linear spring with the spring constant of 1.46 N/mm was selected for the elastic wire. Fig.5.13 shows the stiffness in the t_m-direction, k_t, in each value of t_m. Since k_t was always $k_{t,req}$, it was confirmed that the specified stiffness was able to be implemented by the proposed method.

The cam profile to achieve the specified force-displacement characteristics in the sub-translation directions was designed. In order to investigate the effect of the specified force-displacement characteristics for the motion accuracy in the later analysis, several

examples with different force-displacement characteristics were designed. External forces applied between the links were assumed to be zero, and the bias actuation force of the wire 2 was assumed to be $f_{a,2} = 3.92$ N. Then, the actuation forces of elastic wires were calculated. Next, force-displacement characteristics were specified. The characteristics were as follows.

$${}^{s}\boldsymbol{f}_{d}(t_s, u_s) = \begin{bmatrix} 0 \\ \alpha \operatorname{sgn}(u_s)(e^{0.2|u_s|} - 1) \\ 0 \end{bmatrix} \quad [\text{N}] \quad (-10 \leqq u_s \leqq 10), \qquad (5.46)$$

where $\alpha = 2.0,\ 3.0,\ 4.0$. The specified characteristic are shown in Fig.5.14. These characteristics have different stiffness. The radius of the spherical surface was specified as $r_s = 10$ mm, and the cam profile was then calculated for each specified characteristics. Since the FCP allowed no rotations, three sets of the designed cam surface and the spherical surface were arranged so that the centers of spheres locate at ${}^{1}\boldsymbol{p}_{c,1} = [20\ -10\ 0]^T$ [mm], ${}^{1}\boldsymbol{p}_{c,2} = [-80\ -10\ 0]^T$ [mm] and ${}^{1}\boldsymbol{p}_{c,3} = [-30\ 70\ 0]^T$ [mm] on Σ_1 when $t_m = 0$. The result when $\alpha = 2.0$ is shown in Fig.5.15, where wires, cam surfaces and spherical surfaces are shown.

Finally, motion accuracy of the designed FCPs were evaluated by the kinetostatic analysis. The calculated trajectories of the origin of Σ_2 are shown in Fig.5.16, where figure (a) shows top view of the trajectories and figure (b) shows side view of the trajectories. Mean errors between the specified and the calculated trajectories were 9.67 mm when $\alpha = 2.0$, 7.85 mm when $\alpha = 3.0$, and 6.67 mm when $\alpha = 4.0$. These result shows that the larger the stiffness was, the smaller than the position error was. Therefore, it was confirmed that balance between motion accuracy and flexibility can be controlled by adjusting the stiffness of the force-displacement characteristics.
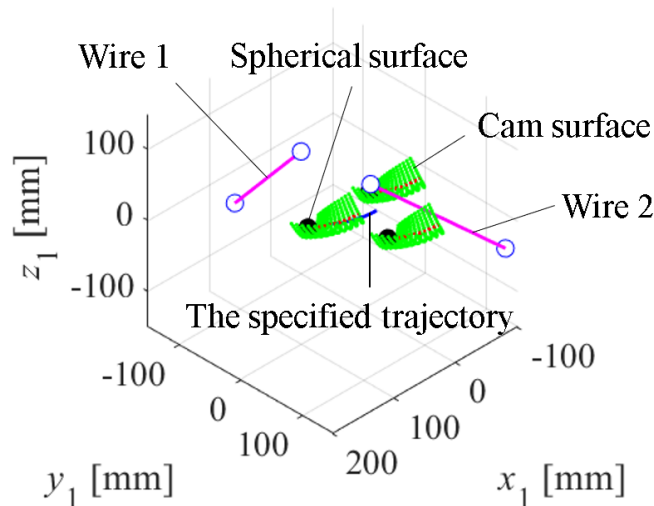
Fig.5.15   Designed structure of the path-generating AFCP

(a) Top view   (b) Side view
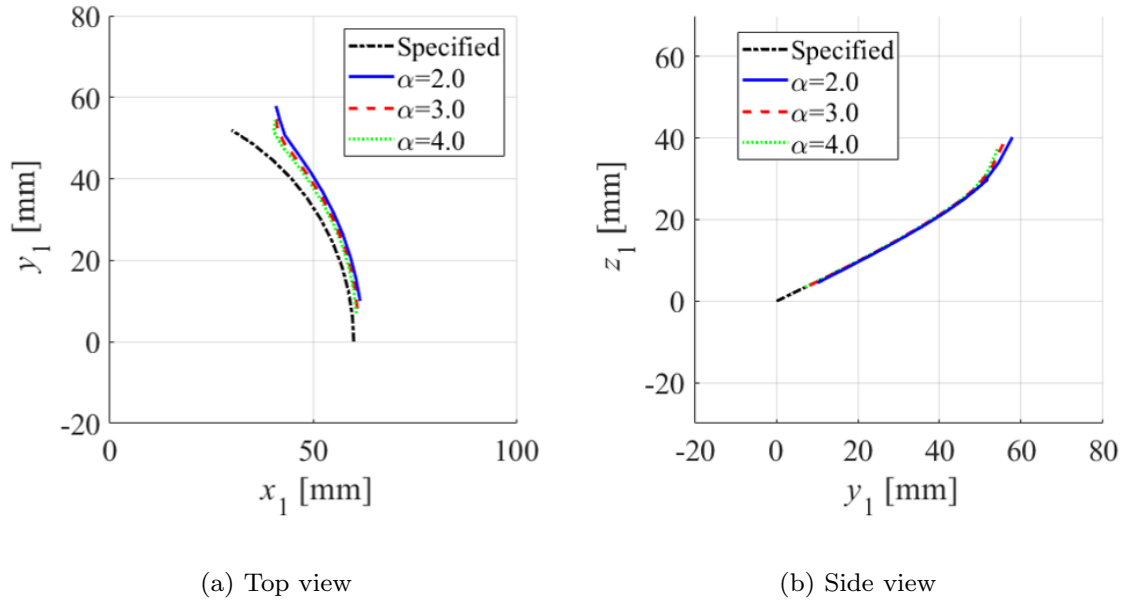
Fig.5.16   Trajectories of the origin of Σ_2 calculated by the method of kinetostaic analysis between the links of the AFCP

5.5   Prototyping and evaluation

The AFCPs designed in section 5.4 were prototyped, and their performances were examined by motion capture experiments.

5.5.1   Active flexibly constrained revolute pair

The prototype of the AFCRP, which was designed in section 5.4.1, was fabricated as shown in Fig.5.17. The two links were fabricated by the selective deposition lamination (SDL) with a 3D-printer. The driving pulley attached to the link 1 is driven with a DC motor. The rotation angle of the DC motor was controlled with the PID control. Fig.5.18 shows the wire routing in detail. One side of the stainless wire is pulled by a constant-force spring unit, and it is routed to the pulley 2 via the pulley 1. The wire is wound to the pulley 2 many times so as to increase friction between the wire and the pulley 2, and it is further routed to the pulley 1 via the linear spring. The driving force is applied when another end of the wire is reeled by the pulley 1.

In order to investigate the kinematic performance of the fabricated AFCRP, the output trajectories were measured by a motion capture system. The output point was on the link 2 and located 150 mm away from the main-rotation axis as shown in Fig.5.17. The rotation angle was controlled to reciprocate three times in the motion range $-\frac{\pi}{4} \leqq \theta_{r,m} \leqq \frac{\pi}{4}$ [rad], and the generated output trajectories were then measured with OptiTrack V120:Duo. The measured trajectories were shown in Fig.5.19. This figure shows that the measured
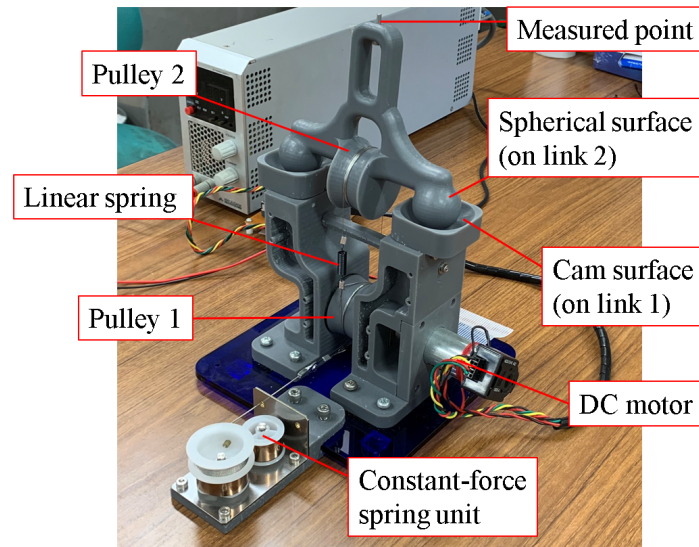
Fig.5.17   The prototype of the designed AFCRP
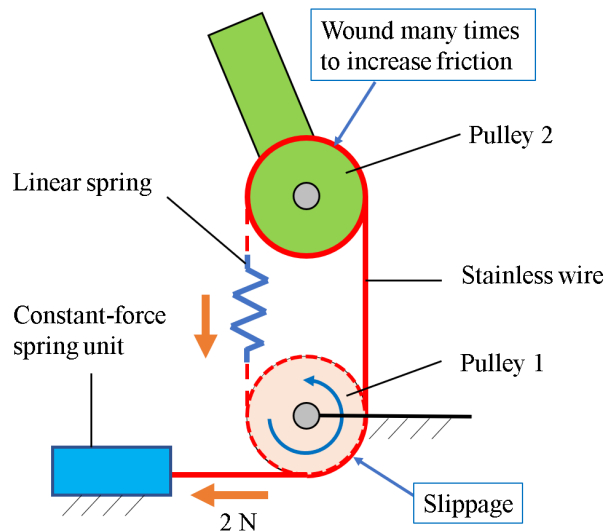
Fig.5.18   Wire routing of the fabricated AFCRP

trajectories were agreed very well with the theoretical one. The mean error between the measured trajectories and the theoretical trajectory was 0.560 mm. Thus, it was very accurate. Note that the position errors are theoretically zero because no-internal forces are applied in the sub-directions. However, since friction between the links are not zero actually, it is possible that small rolling motions occurred between the links. This is thought to be the cause of the position error.

Next, the behavior of the AFCRP when an impact force was applied was measured by the motion capture system. While the output point was reciprocating as in the above motion capture experiment, the link 2 was tapped by hand as shown in Fig.5.20. This series of actions was measured by the motion capture system. The result is shown in
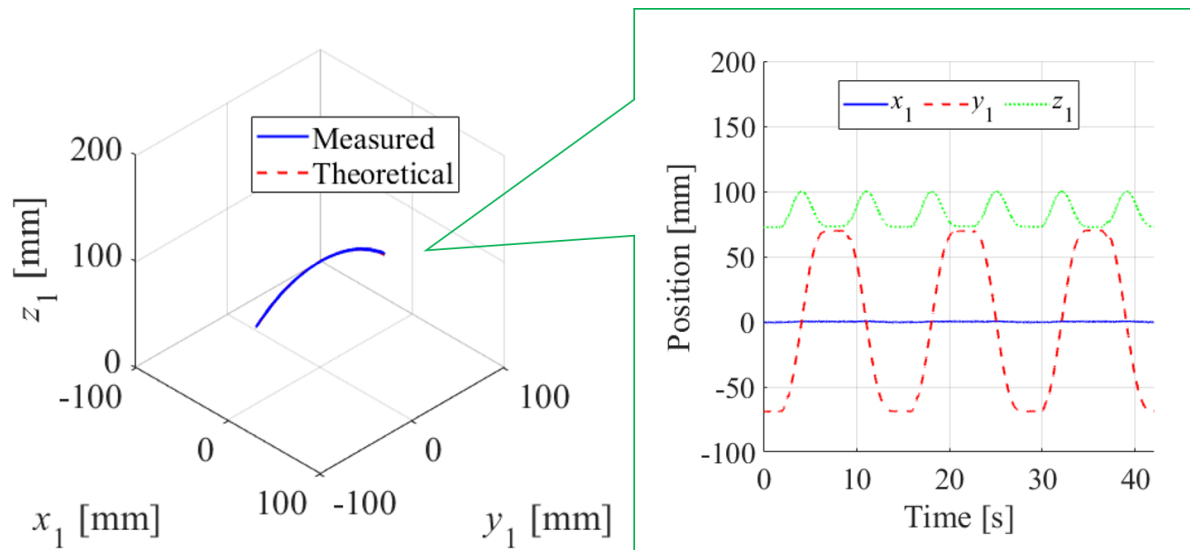
Fig.5.19   The measured output trajectories generated by the fabricated AFCRP
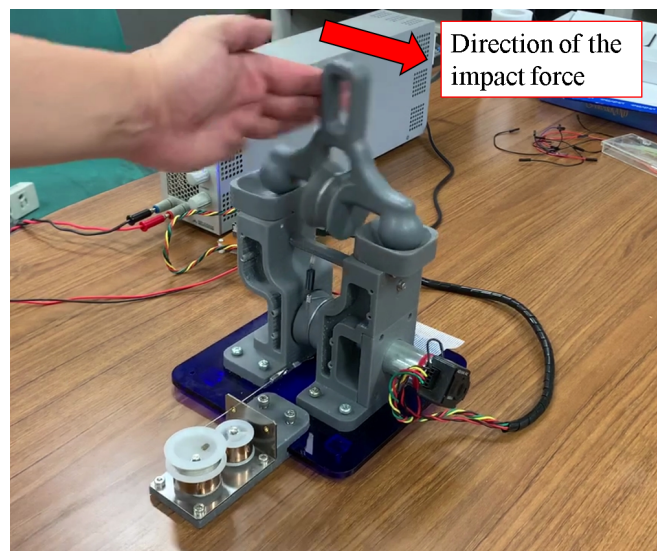
Fig.5.20   An experiment applying an impact force to the fabricated AFCRP

Fig.5.21. When the impact force applied, the two links deformed largely and absorbed the impact force. Then, the two links returned to the normal position very quickly, and the output trajectory generated accurately. In this experiment, the mean error between the measured and the theoretical trajectories was 0.590 mm before the impact force applied, while 0.526 mm after the impact force applied. Although the links largely deformed in the point where the impact force applied, the motion was very accurate before and after the impact force applied. These results indicate that the fabricated AFCRP had both motion accuracy and flexibility and was robust against external forces.
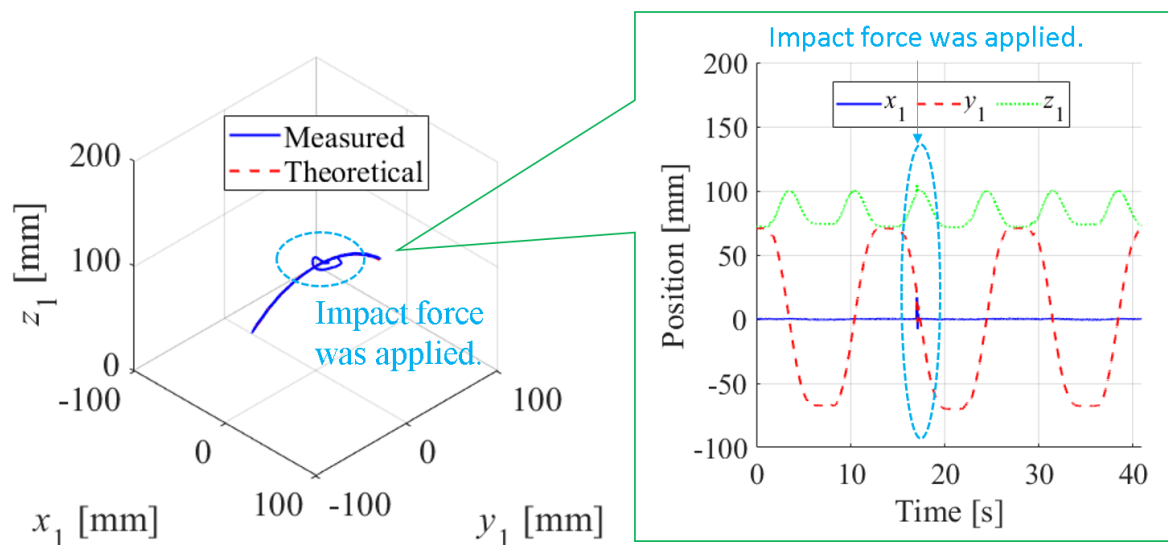
Fig.5.21   The measured output trajectories before and after an impact force was applied to the fabricated AFCRP
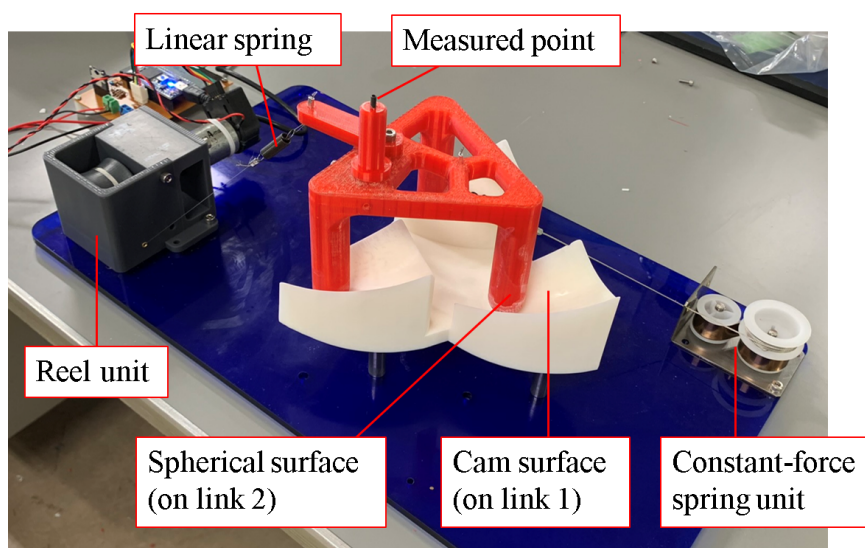
Fig.5.22   The prototype of the designed path-generating AFCP

5.5.2   Path-generating active flexibly constrained pair

A prototype of the path-generating AFCP, which was designed in section 5.4.2, was fabricated as shown in Fig.5.22. The fabricated AFCP has cam surfaces which were designed with $\alpha = 4.0$ in section 5.4.2. The link with cam surfaces (link 1) was fabricated by the SDL, and the link with spherical surfaces (link 2) was fabricated by the FDM. The bias tension of one of two wires was applied with a constant-force spring unit. The reel unit has a pulley driven with a DC motor of which angle is controlled with the PID

(a) 3D view

(b) Top view

(c) Side view
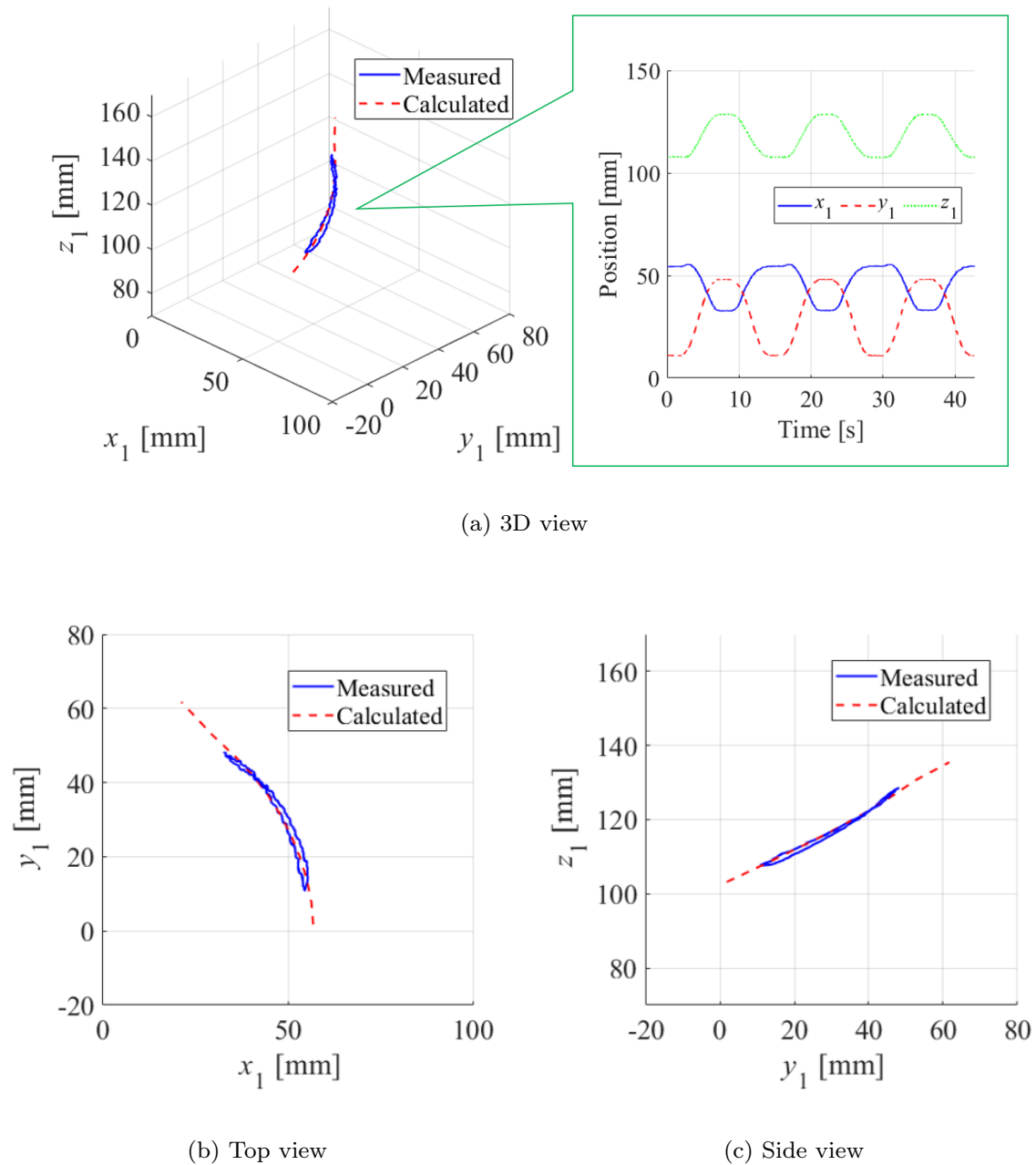
Fig.5.23   The measured output trajectories generated by the fabricated path-generating AFCP

control. The output point locates at $^2\boldsymbol{p}_{out} = [0\ 0\ 100]^T$ [mm] on Σ_2 and a marker can be attached for motion capture experiments.

   The output trajectories were measured by the same motion capture system as used in section 5.5.1. The output motion was controlled to reciprocate three times in the motion range during the motion capture experiment. The motion range was limited to be smaller than its whole motion range. Fig.5.23 shows the results, where figure (a) shows the 3D
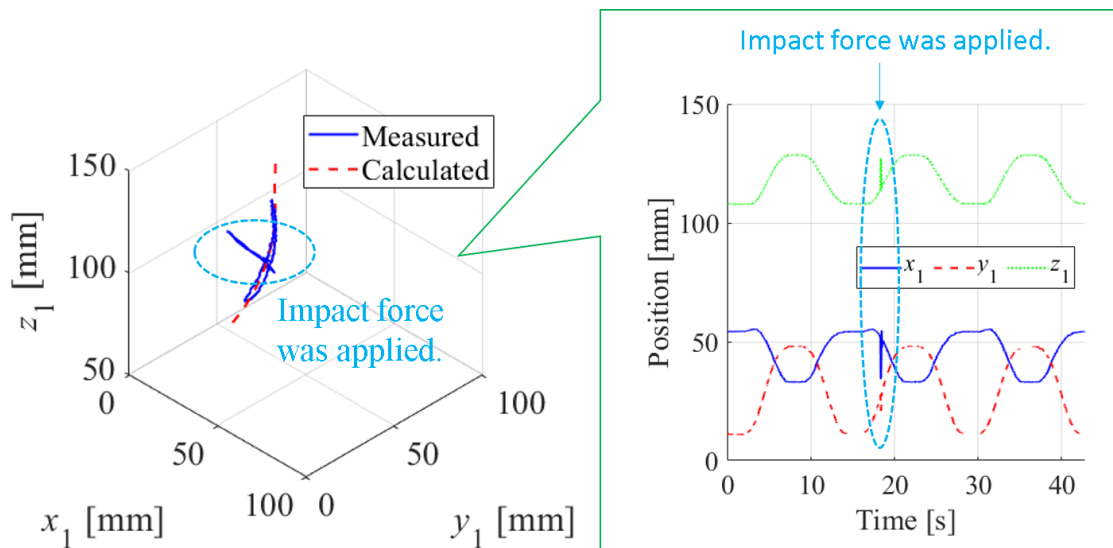
Fig.5.24   The measured output trajectories before and after an impact force was applied to the fabricated path-generating AFCP

view of the trajectories and time series of the output position, figure (b) shows the top view of the trajectories, and figure (c) shows the side view of the trajectories. The "calculated trajectory" shown in the figures was calculated by the proposed method of the kinetostatic analysis described in section 5.3 in the whole motion range. The measured trajectories agreed very well with the calculated trajectories although the mean error between the measured and calculated trajectories was 1.06 mm. This means that the proposed design method and the proposed analysis method are valid, and that the errors between the specified and actual trajectories were almost comparable to those calculated in section 5.4.2. Since hysteresis was shown in the measured trajectory, the cause of the errors is considered to be the friction between the links.

Next, the behavior of the path-generating AFCP when an impact force was applied was measured by the motion capture system. As in the experiment described in section 5.5.1, the link 2 was tapped by hand while the link 2 was reciprocating in the motion range. This series of actions was measured by the motion capture system. The result is shown in Fig.5.24. When the impact force applied, the two links deformed largely and absorbed the impact force. Then, the two links returned to the normal position very quickly. The mean error between the measured and calculated trajectories was 1.19 mm before the impact force applied, while 1.13 mm after the impact force applied. Although the links largely deformed in the point where the impact force applied, motion accuracy did not change before and after the impact force applied. These results indicate that the fabricated path-generating AFCP was also robust against external forces.

5.6   Chapter summary

The active flexibly constrained pair (AFCP), which is an active kinematic pair with multi-directional flexibility, was developed. In the AFCP, the FCP is constrained by reeled

elastic wires to be kept in contact between the links and to be driven actively. Besides, the AFCP has an underactuated structure where the FCP is driven by one more wire than the number of its main-DOF to simplify the structure. In this chapter, A design method of the AFCP was proposed, and some examples were designed and examined by experiments. The achievements are as follows.

(1) A design method for the AFCP to have high actuation force transmission and the specified stiffness between the links was proposed. Firstly, elastic wires are optimally arranged between the links so as to maximize the transmission index (TI_w) used in chapter 3. TI_w for the AFCP is calculated with virtual constraint forces which are assumed in sub-directions between the links and with actuation forces which are derived by solving the kinematics of wire-pulley system. Next, wire stiffness for the AFCP to have required stiffness to do the desired task in main-directions between the links is calculated by solving an optimization problem. Finally, the cam profile for the AFCP is calculated to have the specified force-displacement characteristics in sub-DOF.

(2) The method to analyze the kinetostatics of the AFCP, which is an underactuated active kinematic pair with multiple DOF, was proposed to evaluate motion accuracy between the links.

(3) As a example, the active flexibly constrained revolute pair (AFCRP), which allows 1-axial rotation in main-DOF, was designed by using the proposed design method. Besides, the path-generating FCPs, which allows 1-axial translation along the specified trajectory in main-DOF, were also designed with various stiffness of sub-DOF, and motion accuracy of them was compared on simulations. As a result, it was confirmed that balance between the motion accuracy and flexibility can be controlled by adjusting the stiffness of the force-displacement characteristics.

(4) The designed examples were fabricated, and their output trajectory was measured by motion capture experiments. As a result, it was confirmed that the prototypes had both flexibility and adequate positioning accuracy under small external loads, and that they were robust against external forces because they were able to absorb large external force by passive relative motions of the AFCPs. In addition, the validity of the proposed design method and the analysis method was able to be confirmed because the measured motion of the prototypes agreed well with the simulation.

Chapter 6

Conclusion

6.1   Achievements

Linkage mechanisms are generally synthesized with closed lower pairs. However, relative motion between two links of a lower pair is limited to be simple because of severe geometrical limitations on its contact surfaces between the links. Therefore, a linkage with 1 DOF is difficult to completely generate the specified motion, and a linkage with multiple DOF becomes a complex mechanism with many kinematic pairs. Although the geometrical limitation between the links can be overcome by using unclosed higher pairs such as cams, unclosed higher pairs which can generate complex relative spatial motions have not been developed because of not only difficult theory to generate the specified spatial motion but also the difficulty to manufacture their pairing elements. However, since multi-spindle CNC machining technology and additive manufacturing technology have been developed recently, the difficulty can be overcome. Developing such mechanical elements to generate the specified complex spatial motion is very important to extend the synthesis of spatial mechanisms and their applications. Therefore, novel kinematic pairs composed of elastically constrained two curved surfaces were developed in this dissertation. They are geometrically unclosed pairs, which allow complex relative spatial motion and multiple DOF between the links, constrained with elastic elements for their practical uses. Although they are kinds of mechanisms, they can be regarded as kinematic pairs and be treated in the same way as geometrically closed pairs in mechanism synthesis because they can keep the connection between the links by themselves. Therefore, the joint mechanisms with this structure were named "elastically closed pairs". This idea means that only relative motion between its main two links can be focused on in mechanism synthesis without considering its detailed structure. This idea is important for efficient mechanism synthesis because the number of available kinematic pairs can be increased and important parts of the mechanism only have to be focused on in mechanism synthesis. In this dissertation, several practical kinematic pairs were proposed based on the features of elastically closed pairs, and their design methods were also proposed and validated by experiments with their prototype fabricated with additive manufacturing. In addition, spatial mechanisms with them, which were called "ECP-linkages", were synthesized and prototyped, and their performances were examined.

Taking advantage of the characteristic that elastically closed pairs can generate complex relative motions between the links, the "Spatial Rolling Contact Pair" (SRCP) was developed, and its design method was proposed and validated. The SRCP is a kinematic

pair with 1-DOF of which two links roll relatively while generating the specified trajectory. By using this kinematic pair, a spatial ECP-linkage with 1-DOF which can completely generate the specified trajectory can be synthesized easily. Besides, by replacing some parts of elastic elements of the SRCP with active elastic elements, the "Active Spatial Rolling Contact Pair" (ASRCP) was developed as an "elastically closed active pair", and its design and control methods were proposed and validate. When the passive SRCP is used to generate the specified trajectory, it must be driven in a closed-loop ECP-linkage with many machine elements. However, the ASRCP can generate the specified trajectory as it is.

Taking advantage of the characteristic that elastically closed pairs have flexibility between the links by their elastic elements, the "Flexibly Constrained Pair" (FCP) was developed, and its design method was proposed and validated. The FCP is a kinematic pair with multiple-DOF which has a "flexible kinematic constraint" generated by stiffness difference in directions of the relative motion. Since the FCP has both a simple structure and multi-directional flexibility, the structure of a flexible robotic mechanism, which needs redundant passive DOF, can be simplified with it. Besides, the "Active Flexibly Constrained Pair" (AFCP) was also developed as an "elastically closed active pair" by replacing some parts of elastic elements of the FCP to active elastic elements, and its design method was proposed and validated. The AFCP is expected to further simplify the structure of a flexible robotic mechanism.

The main achievements of this research are summarized as follows.

(1) For the SRCP, a method to specify the relative rolling motion between two links to satisfy the kinematic condition of the rolling contact and the method to derive rolling contact surfaces which can generate the specified trajectory between the links were proposed. In order to suppress slippage and separation between the links, a hybrid elastic constraint composed of both flexible bands and linear springs was proposed. To make the SRCP generate the ideal rolling motion, a method to optimally arrange linear springs between the links was proposed. Some examples of the SRCP were designed and prototyped, and their performances were theoretically and experimentally examined. As a result, it was confirmed that the proposed design methods of rolling contact surfaces and elastic constraints are valid and that exact-path generation is possible with the SRCP. Moreover, it was confirmed that the synthesis of a path-generating spatial mechanism with SRCP can be achieved more easily than the conventional mechanism synthesis with only lower pairs.

(2) For the ASRCP, a design method where several active elastic elements are optimally arranged between the links was proposed. As the evaluation criterion for the optimization, a transmission index for parallel wire-driven mechanisms was introduced. In order to obtain a large workspace in the ASRCP, the redundant number of active elastic elements were used, and the transmission index was modified to achieve evaluation in that case. In addition, a method to control the ASRCP, where driving forces of active elastic elements are optimally calculated with the use of its actuation redundancy to generate the ideal rolling motion, was proposed. An example of the ASRCP was designed, and its simulation of control was performed. Then, it was confirmed

that the ASRCP can generate the ideal rolling motion more efficiently than the passive SRCP because of its actuation redundancy. The ASRCP driven by reeled elastic wires was prototyped and examined. As a result, it was confirmed that the prototype was able to generate the specified trajectory accurately. This result indicates that the proposed design and control methods are valid. In addition, the ASRCP with a compact structure was achieved by using fluid-driven artificial muscles.

(3) For the FCP, a design method of the structure with the specified relative main motions and the specified multi-directional flexibility was proposed. Especially, the specified force-displacement characteristics (non-linear stiffness characteristics) can be implemented in detail as the flexible translation constraints between the links by designing the contact surface between the links. Some examples of the FCPs were designed and prototyped, and their performances were examined by experiments. Then, it was confirmed that the proposed design method is valid. Moreover, a flexible robotic mechanism with a simple structure was synthesized and fabricated by using the FCPs. This mechanism was synthesized easily by replacing several revolute pairs of a planar closed-loop five-bar mechanism with the FCPs which allow 1-axial rotation in main-DOF. Then, its performances were theoretically and experimentally examined. As a result, it was confirmed that the mechanism had multi-directional flexibility and was able to generate the specified motion with an adequate position accuracy under small external loads and that it was able to absorb large external force by passive relative motions in sub-DOF of the FCPs.

(4) For the AFCP, a design method to have high-force transmission, an adequate stiffness to perform the task and the specified multi-directional flexibility was proposed. This method has three steps composed of optimal arrangement of reeled elastic wires so as to maximize the transmission index, wire stiffness design to achieve an adequate stiffness to perform the desired task, and design of contact surfaces to achieve the specified multi-axial flexibility to have both flexibility and motion accuracy. Some examples of the AFCP were designed and simulated. As a result, it was confirmed that the positioning accuracy of the AFCP can be adjusted depending on the specified stiffness for sub-DOF. In addition, they were prototyped, and their performances were examined by experiments. As a result, it was confirmed that they had both multi-directional flexibility and adequate positioning accuracy under small external loads, and that they were able to absorb large external forces by passive relative motions in sub-DOF. In addition, it was confirmed that the proposed design method is valid because the measured motion was well agreed with the simulated motion.

6.2 Future challenges

In this dissertation, concepts of several kinds of elastically closed pairs were developed, and some ECP-linkages were synthesized with them as examples. However, in order to use the proposed kinematic pairs in more practical applications, further improvements of their performances are required. In particular, higher durability, lower costs, higher accuracy, and higher efficiency have to be pursued in the future. In order to improve

these characteristics, their materials, processing methods, lubrication methods between the links, and their detailed structure have to be further considered.

Besides, it is also important to develop specific applications of the proposed kinematic pairs. For example, since the SRCP can generate the specified trajectory with the simple structure, an automatic transfer machine in a factory or a simple leg mechanism of a walking robot can be designed with simple structures. Since the SRCP can generate the complex relative motion like a human knee joint, it is possible that an exoskeleton for human knee joints can be designed with a simple structure. Although the SRCP has a disadvantage that constraints between the links are weaker than closed pairs, this feature may become an advantage in this application because this feature works as safety for unintentional external loads for the knee joint. The FCP is possible to be used for human friendly robots, such as a nursing care robot, a households robot, and so on because their flexible mechanisms can be designed with simple and safe structures. Since the FCP can have the specified non-linear stiffness characteristics in the relative translation direction between the links, a suspension mechanism for a wheeled robot or a flexible leg mechanism for a walking robot can be designed. As described in section 1.2.2, hardening spring characteristics are useful for the mechanisms to have both flexibility to absorb shock and rigidity to support the body of the robot. In addition, although friction between the links is considered to be disadvantage that it reduce mechanical efficiency, this feature may become advantage in such applications because friction between the links works as damping of vibration. To reveal this dynamic effect of the FCP is also a future challenge of this research.

This research can open the door for some future fields of study. Mechanical elements proposed in this dissertation were mainly fabricated by 3D-printers because mechanical parts with complex shapes can be manufactured easily by using them. By using additive manufacturing as shown in this research, mechanical elements with higher performance than conventional ones are possible to be developed because geometrical limitations of mechanical elements can be relaxed. The basic idea of this research to design complex curved surface between the links to generate the specified kinematic function is different from the general mechanical design. Therefore, this research may open the door for establishing a methodology to design novel mechanical elements with the use of large design space expanded by relaxing the geometrical limitation. Although the additive manufacturing technology currently has some problems of the strength of materials, high cost, and so on, if it develops in the future, demand for novel design methodology of mechanical elements with the use of additive manufacturing will increase. Besides, the idea of designing kinematic pair to generate the specified relative motion and the idea to arrange actuators between the links according to their relative motion enable to design an original musculoskeletal robotic system suitable for performing the specified task. This idea will spur to built "task-based design" methods of robotic mechanisms.

As you can see, various applications of the proposed kinematic pairs and future fields of study based on the proposed design methods can be considered. The author hopes that the proposed ideas of elastically closed pairs will extend mechanism synthesis and they will be applied to a wide variety of future machines.

References

[1] Freudenstein, F., Approximate Synthesis of Four-Bar Linkages, Transactions of the ASME, Vol.77, (1955), pp.853-861.

[2] Wamper, C. W., Morgan, A. P. and Sommese, A. J., Complete Solution of the Nine-Point Path Synthesis Problem for Four-Bar Linkages, Transactions of the ASME, Journal of Mechanical Design, Vol.114, No.1 (1992), pp.153-159.

[3] McLARNAN, C. W., Synthesis of Six-Link Plane Mechanisms by Numerical Analysis, Transactions of the ASME, Journal of Engineering for Industry, Vol.85, No.1 (1963), pp.5-10.

[4] Roth, B. and Freudenstein, F., Synthesis of Path-Generating Mechanisms by Numerical Methods, Transactions of the ASME, Journal of Engineering for Industry, Vol.85, No.3 (1963), pp.298-304.

[5] Denavit, J. and Hartenberg, R. S., Approximate Synthesis of Spatial Linkages, Transactions of the ASME, Journal of applied mechanics, Vol.27, No.1 (1960), pp.201-206.

[6] Ogawa, K., Funabashi, H. and Takanashi, A., Synthesis of spatial four-bar mechanisms : 1st report, classification of mechanisms and synthesis of a linkage with two revolute pairs, one cylindrical pair and one spherical pair, Transactions of the JSME, Vol.33, No.247 (1967), pp.443-450 (in Japanese).

[7] Ogawa, K. and Funabashi, H., Synthesis of spatial four-bar mechanisms : 2nd report, synthesis of linkages with two spherical pairs, Transactions of the JSME, Vol.33, No.247 (1967), pp.451-457 (in Japanese).

[8] Willson, J. T., Analytical Kinematic Synthesis by Finite Displacements, Transactions of the ASME, Journal of Engineering for Industry, Vol.87, No.2 (1965), pp.161-169.

[9] Suh, C. H. and Radcliffe, C. W., Synthesis of Plane Linkages With Use of the Displacement Matrix, Transactions of the ASME, Journal of Engineering for Industry, Vol.89, No.2 (1967), pp.206-214.

[10] Suh, C. H. and Radcliffe, C. W., Synthesis of Spherical Linkages With Use of the Displacement Matrix, Transactions of the ASME, Journal of Engineering for Industry, Vol.89, No.2 (1967), pp.215-221.

[11] Suh, C. H., Design of Space Mechanisms for Rigid Body Guidance, Transactions of the ASME, Journal of Engineering for Industry, Vol.90, No.3 (1968), pp.499-506.

[12] Kim, H. S. and Hamid, S., Synthesis of Six-Link Mechanisms for Point Path Generation, Journal of Mechanisms, Vol.6, No.4 (1971), pp.447-461.

[13] Sandor, G. N., Principles of a General Quaternion-Operator Method of Spatial Kinematic Synthesis, Transactions of the ASME, Journal of Applied Mechanics, Vol.35, No.1 (1968), pp.40-46.

[14] Tsai, L. W. and Roth, B., Design of Dyads with helical, cylindrical, spherical, revolute and prismatic joints, Mechanism and Machine Theory, Vol.7, (1972), pp.85-102.

[15] Sandor, G. N., Weng, T. C. and Xu, Y., The synthesis of spatial motion generators with prismatic, revolute and cylindric pairs without branching defect, Mechanism and Machine Theory, Vol.23, No.4 (1988), pp.269-274.

[16] Perez, A., Synthesis of Spatial RPRP Closed Linkages for a Given Screw System, Journal of Mechanism and Robotics, Vol.3, No.2 (2011), 021009 (8 pages).

[17] Han, C. H., A GENERAL METHOD FOR THE OPTIMUM DESIGN OF MECHANISMS, Journal of Mechanisms, Vol.1, No.3-4 (1966), pp.301-313.

[18] Lewis, D. W. and Gyory, C. K., Kinematic Synthesis of Plane Curves, Journal of Engineering for Industry, Vol.89, No.1 (1967), pp.173-175.

[19] Fox, R. L. and Willmert, K. D., Optimum Design of Curve-Generating Linkages with Inequality Constraints, Transactions of the ASME, Journal of Engineering for Industry, Vol.89, No.1 (1967), pp.144-151.

[20] Nechi, A. J., A Relaxation and Gradient Combination Applied to the Computer Simulation of a Plane Four-Bar Chain, Transactions of the ASME, Journal of Engineering for Industry, Vol.93, No.1 (1971), pp.113-119.

[21] Paradis, M. J., and Willmert, K. D., Optimal Mechanism Design Using the Gauss Constrained Method, Journal of Mechanisms, Transmissions, and Automation in Design, Vol.105, (1983), pp.187-196.

[22] Ananthasuresh, G. A. and Kramar, S. N., Analysis and Optimal Synthesis of the RSCR Spatial Mechanism, Journal of Mechanical Design, Vol.116, (1994), pp.174-181.

[23] Zhang, X., Zhou, J., and Ye, Y., Optimal mechanism design using interior-point methods, Mechanism and Machine Theory, Vol.35, (2000), pp.83-98.

[24] Sancibrian, R., Viadero, F., Garcia, P and Fernandez, A., Gradient-based optimization of path synthesis problems in planar mechanisms, Mechanism and Machine Theory, Vol.39, (2004), pp.839-856.

[25] Krishnamurty, S. and Turcic, D. A., OPTIMAL SYNTHESIS OF MECHANISMS USING NONLINEAR GOAL PROGRAMMING TECHNIQUES, Mechanism and Machine Theory, Vol.27, No.5 (1992), pp.599-612.

[26] Cabrera, J.A., Simon, A. and Prado, M., Optimal synthesis of mechanisms with genetic algorithms, Mechanism and Machine Theory, Vol.37, (2002), pp.1165-1177.

[27] Shiacolas, P. S., Koladiya, D. and Kebrle, J., On the optimum synthesis of six-bar linkages using differential evolution and the geometric centroid of precision positions technique, Mechanism and Machine Theory, Vol.40, (2005), pp.319-335.

[28] Lin, W.-Y., A GA-DE hybrid evolutionary algorithm for path synthesis of four-bar linkage, Mechanism and Machine Theory, Vol.45, No.8 (2010), pp.1096-1107.

[29] Laribi, M. A. , Romdhane, L. and Zeghloul, S., Analysis and optimal synthesis of single loop spatial mechanisms, ournal of Zhejiang University-SCIENCE A, Vol.12, No.9 (2011), pp.665-679.

[30] Sarkisyan, Y. L., Gupta, K. C. and Roth, B., Kinematic Geometry Associated With the Least-Square Approximation of a Given Motion, Transactions of the ASME, Journal of Engineering for Industry, Vol.95, No.2 (1973), pp.503-510.

[31] Zhou, H. and Cheung, E. H. M., Optimal synthesis of crank-rocker linkages for path generation using the orientation structural error of the fixed link, Mechanism and Machine Theory, Vol.36, (2001), pp.973-982.

[32] Ullah, I. and Kota, S., F., Optimal Synthesis of Mechanisms for Path Generation Using Fourier Descriptors and Global Search Methods, Transactions of the ASME, Journal of Mechanical Design, Vol.119, (1997), pp.504-510.

[33] Kim, J., Seo, T. and Kim, J., A new design methodology for four-bar linkage mechanisms based on derivations of coupler curve, Mechanism and Machine Theory, Vol.100, (2016), pp.138-154.

[34] Hyodo, K. and Kobayashi, H., A Study on Tendon Controlled Wrist Mechanism with Nonlinear Spring Tensioner, Journal of the Robotics Society of Japan, Vol.11, No.8 (1993), pp.1244-1251 (in Japanese).

[35] Tonietti, G., Schiavi, R. and Bicchi, A., Design and Control of a Variable Stiffness Actuator for Safe and Fast Physical Human/Robot Interaction, Proceedings of the 2005 IEEE

International Conference on Robotics and Automation, (2005), pp.526-531.

[36] Migliore, S. A., Brown, E. A. and DeWeerth, S. P., Biologically Inspired Joint Stiffness Control, Proceedings of the 2005 IEEE International Conference on Robotics and Automation, (2005), pp.4508-4513.

[37] Friedl, W., Hoepner, H., Petit, F. and Hirzinger, G., Wrist and Forearm Rotation of the DLR Hand Arm System: Mechanical Design, Shape Analysis and Experimental Validation, Proc. of the 2011 IEEE International Conference on Intelligent Robots and Systems, (2011), pp.1836-1842.

[38] Matsuda, T. and Murata, S., Variable Stiffness Hinge Using Non-circular Gears, Journal of the Robotics Society of Japan, Vol.25, No.3 (2007), pp.105-115 (in Japanese).

[39] WANG, Y., YANG, G., YAN, K., Zhang, C. and Zheng, T., Design Optimization for a 2-DOF Cable-driven Joint with Large Stiffness Range, Proc. of the 2017 IEEE Conference on Industrial Electronics and Applications, (2017), pp.264-269.

[40] Schiavi, R., Grioli, G., Sen, S. and Bicchi, A., VSA-II: a Novel Prototype of Variable Stiffness Actuator for Safe and Performing Robots Interacting with Humans, Proc. of the 2008 IEEE International Conference on Robotics and Automation, (2008), pp.2171-2176.

[41] Palli, G., Berselli, G., Melchiorri, C. and Vassura, G., Design of a Variable Stiffness Actuator Based on Flexures, Journal of Mechanisms and Robotics, Vol.3, No.3, (2011), 034501 (5 pages).

[42] Koganezawa, K., Mechanical stiffness control for antagonistically driven joints, Proc. of the 2005 IEEE/RSJ International Conference on Intelligent Robots and Systems, (2005), pp.2512-2519.

[43] English, C. and Russell, D., Implementation of variable joint stiffness through antagonistic actuation using rolamite springs, Mechanism and Machine Theory, Vol.34 (1999), pp.27-40.

[44] Nakamura, T., Variable Stiffness Mechanism using Pnumatic Artificial Muscle Actuator, Journal of the Robotics Society of Japan, Vol.31, No.6 (2013), pp.572-576 (in Japanese).

[45] Morita, T. and Sugano, S., New Control Method for Robot Joint by Mechanical Impedance Adjuster -Proposition of Mechanisms and Application to Robot Finger-, Journal of the Robotics Society of Japan, Vol.14, No.1 (1996), pp.131-136 (in Japanese).

[46] Kim, B.-S. and Song, J.-B., Hybrid Dual Actuator Unit: A Design of a Variable Stiffness Actuator based on an Adjustable Moment Arm Mechanism, Proc. of the 2010 IEEE International Conference on Robotics and Automation, (2010), pp.1655-1660.

[47] Groothuis, S., Carloni, R. and Stramigioli, S., A Novel Variable Stiffness Mechanism Capable of an Infinite Stiffness Range and Unlimited Decoupled Output Motion, Actuators, Vol.3, No.2 (2014), pp.107-123.

[48] Wolf, S. and Hirzinger, G., A New Variable Stiffness Design: Matching Requirements of the Next Robot Generation, Proc. of the 2008 IEEE International Conference on Robotics and Automation, (2008), pp.1741-1746.

[49] Wolf, S., Eiberger, O. and Hirzinger, G., The DLR FSJ: Energy based design of a variable stiffness joint, Proc. of the 2011 IEEE International Conference on Robotics and Automation, (2011), pp.5082-5089.

[50] Ahmed, M. R. and Kalaykov, I., Semi-Active Compliant Robot Enabling Collision Safety for Human Robot Interaction, Proc. of the 2010 IEEE International Conference on Mechatronics and Automation, (2010), pp.1932-1937.

[51] Kajikawa, S. and Abe, K., Robot Finger Module With Multidirectional Adjustable Joint Stiffness, IEEE/ASME Transaction on Mechatronics, Vol.17, No.1 (2012), pp.128-135.

[52] Pratt, G. A. and Williamson, M. M, Series Elastic Actuators, Proc. of the IEEE International Conference on Intelligent Robots and Systems, (1995), pp.399-406.

[53] Lee, Y. F., Chu, C. Y., Xu, J. Y., and Lan, C. C., A humanoid robotic wrist with two-dimensional series elastic actuation for accurate force/torque interaction, IEEE/ASME

Transactions on Mechatronics, Vol.21, No.3 (2016), pp.1315-1325.

[54] Okada, M. and Nakamura, Y., Development of a cybernetic shoulder-a 3-dof mechanism that imitates biological shoulder motion, IEEE Transactions on Robotics, Vol. 21, No. 3 (2005), pp.438-444.

[55] Grebenstein, M., Chalon, M., Hirzinger, G. and Siegwart, R., Antagonistically Driven Finger Design for the Anthropomorphic DLR Hand Arm System, Proc. of the 2010 IEEE-RAS International Conference on Humanoid Robots, (2010), pp.609-616.

[56] Lessard, S., Castro, D., Asper, W., Chopra, S. D., Baltaxe-Admony, L. B., Teodorescu, M., SunSpiral, V. Agogino, A., A bio-inspired tensegrity manipulator with multi-DOF, structurally compliant joints, Proc. of the 2016 IEEE/RSJ International Conference on Intelligent Robots and Systems, (2016), pp. 5515-5520.

[57] Jung, E., Ly, V., Cessna, N., Ngo, M. L., Castro, D., SunSpiral, V., and Teodorescu, M., Bio-inspired tensegrity flexural joints, Proc. of the 2018 IEEE International Conference on Robotics and Automation, (2018), pp.5561-5566.

[58] Park, J.-J. and Song, J.-B., A Nonlinear Stiffness Safe Joint Mechanism Design for Human Robot Interaction, Journal of Mechanical Design, Vol.132, No.6, (2010), 061005 (8 pages).

[59] Ogawa, T., Nagatani, K. and Tanaka, Y., Development of Dislocation Joint to Perform Mechanical Softness, Transactions of the JSME), Vol.71, No.705 (2005), pp.226-233 (in Japanese).

[60] Lauzier, N. and Gosselin, C., 3-DOF Cartesian Force Limiting Device Based on the Delta Architecture for Safe Physical Human-Robot Interaction, Proc. of the 2010 IEEE International Conference on Robotics and Automation, (2010), pp.3420-3425.

[61] Lauzier, N. and Gosselin, C., Series Clutch Actuators for Safe Physical Human-Robot Interaction, Proc. of the 2011 IEEE International Conference on Robotics and Automation, (2011), pp.5401-5406.

[62] Matsumoto, K., Yanagawa, H., Takanishi, A. and Lim, H., Development of human-friendly robot's waist and passive collision force suppression mechanism, Transactions of the JSME, (2016), 15-0033 (9 pages) (in Japanese).

[63] Lim, H., Maenisi, K. and Sunagawa, M., Development of Collision Force Suppression Mechanism, Proc. of the International Conference on Control, Automation and Systems, (2008), pp.2032-2037.

[64] Okada, M. and Kino, S., Torque Transmission Mechanism with Nonlinear Passive Stiffness using Mechanical Singularity, Proc. of the 2008 IEEE International Conference on Robotics and Automation, (2008), pp.1735-1740.

[65] Okada, M. and Takeishi, J., Kineto-static Mechanical Synthesis for Nonlinear Profile Design of Passive Stiffness Using Closed Kinematic Chain and Its Application to Landing Mechanism for Impact Absorption, Journal of the Robotics Society of Japan, Vol.29, No.3 (2011), pp291-297 (in Japanese).

[66] Kuo, P.-H. and Deshpande, A. D., A Novel Joint Design for Robotic Hands with Humanlike Nonlinear Compliance, Journal of Mechanisms and Robotics, Vol.8, No.2 (2015), 10 pages.

[67] Brar, J. S. and Bansal, R. K., A TEXT BOOK OF THEORY OF MACHINES, LAXMI publications, (2004), pp.2-3.

[68] Singh, S., Hand Book of Mechanical Engineering 2nd Edition, S. Chand, (2011), p.320.

[69] Singh, Y. P. and Kohli, D., Synthesis of Cam-Link Mechanisms for Exact Path Generation, Mechanism and Machine Theory, Vol.16, No.4 (1981), pp.447-457.

[70] Ye, Z. and Smith, M. R., Design of a combined cam-linkage mechanism with an oscillating roller follower by an analytical method, Proceedings of the Institution of Mechanical Engineers, Part C: Journal of Mechanical Engineering Science, Vol.219, No.4 (2005), pp.419-427.

[71] Mundo, D., Liu, J. Y. and Yan, H. S., Optimal Synthesis of Cam Linkage Mechanisms for Precise Path Generation, Transactions of the ASME, Journal of Mechanical Design, Vol.128,

No.6 (2006), pp.1253-1260.

[72] Gatti, G. and Mundo, D., Optimal synthesis of six-bar cammed-linkages for exact rigid-body guidance, Mechanism and Machine Theory, Vol.42, No.9 (2007), pp.1069-1081.

[73] Soong, R.-C. and Chang, S.-B., Synthesis of function-generation mechanisms using variable length driving links, Mechanism and Machine Theory, Vol.46, No.11 (2011), pp.1696-1706.

[74] Shao, Y., Xiang, Z., Liu, H. and Li, L., Conceptual design and dimensional synthesis of cam-linkage mechanisms for gait rehabilitation, Mechanism and Machine Theory, Vol.104, (2016), pp.31-42.

[75] Soong, R.-C., A new cam-geared mechanism for exact path generation, Journal of Advanced Mechanical Design, Systems, and Manufacturing, Vol.11, No.4 (2019), 041006 (8pages).

[76] Zhao, P., Zhu, L., Zi, B. and Li, X., Design of Planar 1-DOF Cam-Linkages for Lower-Limb Rehabilitation Via Kinematic Mapping Motion Synthesis, Journal of Mechanisms and Robotics, Vol.11, No.4 (2019), 041006 (8pages).

[77] Zhang, C., Zhang, X., Ye, H., Wei, M. and Ning, X., An Efficient Parking Solution: A Cam-Linkage Double-Parallelogram Mechanism Based 1-Degrees of Freedom Stack Parking System, Journal of Mechanisms and Robotics, Vol.11, No.4 (2019), 045001 (8pages).

[78] Mckinley, J. R., Dooner, D. B., Crane III, C. and Kammath, J.-F., Planar Motion Generation Incorporating a 6-Link Mechanism and Non-Circular Elements, Proc. of the ASME 2005 International Design Engineering Technical Conferences & Computers and Information in Engineering Conference, (2005), 11pages.

[79] Mundo, D., Gatti, G. and Dooner, D., Optimized five-bar linkages with non-circular gears for exact path generation, Mechanism and Machine Theory, Vol.44, No.4 (2009), pp.751-760.

[80] Mallik, A. K., Ghosh, A. and Dittrich, G., Kinematic Analysis and Synthesis of Mechanisms, CRC Press (1994), pp.506-513.

[81] Japan manufactures association for cam, Cam Mechanism Handbook, Nikkan Kogyo Shimbun, Ltd. (2001), pp.158-175 (in Japanese).

[82] Huesing, M., Riedel, M., Corves, B. and Nefzi, M., Development of Tailor-Made Robots -From Concept to Realization for Small and Medium-Sized Enterprises, Proc. of the 13th World Congress in Mechanism and Machine Science, (2011), pp.19-25.

[83] Salisbury, J. K., ACTIVE STIFFNESS CONTROL OF A MANIPULATOR IN CARTESIAN COORDINATES, Proc. of the 19th IEEE conference on decision and control including the symposium on adaptive processes, (1980), pp.95-100.

[84] Hogan, N., Impedance Control: An Approach to Manipulation: Part I-III, Journal of Dynamic Systems, Measurement, and Control, Vol.107, (1985), pp.1-24.

[85] Tsuji, T., Takahashi, T. and Ito, K., Joint Compliance Regulation for Manipulators Utilizing Redundant Degrees of Freedom, Transactions of the Society of Instrument and Control Engineers, Vol.26, No.5 (1990), pp.557-563 (in Japanese).

[86] Hirose, H. and Ma, S., Development of Tendon Driven Multi-Joint Manipulator Based on Coupled Drive, Transactions of the Society of Instrument and Control Engineers, Vol.26, No.11 (1990), pp.1291-1298 (in Japanese).

[87] Kim, Y.-J., Anthropomorphic Low-Inertia High-Stiffness Manipulator for High-Speed Safe Interaction, IEEE Transactions on Robotics, Vol.33, No.6 (2017), pp.1358-1374.

[88] Hirose, S. and Umetani, Y., The Development of Soft Gripper for the Versatile Robot Hand, Mechanism and Machine Theory, Vol.13, No.3 (1978), pp.351-359.

[89] Ozawa, R. Kobayashi, H. and Hashiri, K., Analysis, Classification, and Design of Tendon Driven Mechanisms, IEEE Transactions on Robotics, Vol.30, No.2 (2014), pp.396-410.

[90] Zhang, Z., Yang, G., Yeo, S. H., Lim, W. B., and Mustafa, S. K., Design optimization of a cable-driven two-DOF joint module with a flexible backbone, Proc. of the 2010 IEEE/ASME International Conference on Advanced Intelligent Mechatronics, (2010), pp. 385-390.

[91] Dong, X., Raffles, M., Guzman, S. C., Axinte, D., and Kell, J., Design and analysis of a

family of snake arm robots connected by compliant joints, Mechanism and Machine Theory, Vol.77, (2014), pp.73-91.

[92] Li, Z., Ren, H., Chiu, P. W. Y., Du, R., and Yu, H., A novel constrained wire-driven flexible mechanism and its kinematic analysis. Mechanism and Machine Theory, Vol.95, (2016), pp.59-75.

[93] Ji, D., Kang, T. H., Shim, S., Lee, S., and Hong, J., Wire-driven flexible manipulator with constrained spherical joints for minimally invasive surgery, International journal of computer assisted radiology and surgery, Vol.14, No.8 (2019), pp.1365-1377.

[94] Nai, T. Y., and Herder, J. L., Steerable Mechanical Joint for High Load Transmission in Minimally Invasive Instruments, Journal of Medical Devices, Vol.5 (2011), 6 pages.

[95] Suh, J. W., Kim, K. Y., Jeong, J. W., and Lee, J. J., Design considerations for a hyper-redundant pulleyless rolling joint with elastic fixtures, IEEE/ASME Transactions on Mechatronics, Vol.20, No.6, pp.2841-2852.

[96] Suh, J. W. and Kim, K. Y., Harmonious Cable Actuation Mechanism for Soft Robot Joints Using a Pair of Noncircular Pulleys, Journal of Mechanisms and Robotics, Vol.10, No.6 (2018), 11 pages.

[97] Jelinek, F., Pessers, R., and Breedveld, P., DragonFlex smart steerable laparoscopic instrument, Journal of medical devices,Vol.8 (2014), 015001 (9 pages).

[98] Takeda, Y., Funabashi, H., A Transmission Index for In-Parallel Wire-Driven Mechanisms, JSME International Journal, Vol. 44, No. 1(2001), pp.180-186.

[99] Takeda, Y., Funabashi, H., Niwa, Y. and Higuchi, M., Motion Control of In-Parallel Actuated Mechanisms Driven by Pneumatic Rubber Muscles, Transactions of the JSME, Vol.67, No.662 (2001), pp.3271-3276.

[100] Lim, W. B., Yeo, S. H., Yang, G. and Mustafa, S. K., Kinematic Analysis and Design Optimization of a Cable-Driven Universal Joint Module, Proc. of 2009 IEEE/ASME International Conference on Advanced Intelligent Mechatronics (2009), pp.1933-1938.

[101] Agrawal, S. K., Dubey, V. N., Gangloff, J. J., Brackbill, E., Mao, Y., and Sangwan, V., Design and optimization of a cable driven upper arm exoskeleton, Journal of Medical Devices, Vol.3, No.3 (2009), 031004 (8 pages).

[102] Bryson, J. T., Jin, X., and Agrawal, S. K., Optimal Design of Cable Driven Manipulators Using Particle Swarm Optimization, Journal of Mechanisms and Robotics, Vol.8, No.4 (2016), 041003 (8 pages).

[103] Asano, Y., Mizoguchi, H., Osada, M., Kozuki, T., Urata, J., Izawa, T., Nakanishi, Y., Okada, K. and Inaba, M., Biomimetic design of musculoskeletal humanoid knee joint with patella and screw-home mechanism, Proc. of the 2011 IEEE International Conference on Robotics and Biomimetics, (2011), pp. 1813-1818.

[104] Asano, Y., Mizoguchi, H., Kozuki, T., Motegi, Y., Osada, M., Urata, J., Nakanishi, Y., Okada, K. and Inaba, M., Lower thigh design of detailed musculoskeletal humanoid "Kenshiro", Proc. of the 2012 IEEE/RSJ International Conference on Intelligent Robots and Systems, (2012), pp. 4367-4372.

[105] Kurumaya, S., Suzumori, K., Nabae, H. and Wakimoto, S., Musculoskeletal lower-limb robot driven by multifilament muscles, Robomech Journal, Vol.3, No.13 (2016), 15 pages.

[106] Russel, F.,Zhu, Y., Hey, W., Vaidyanathan, R. and Ellison, P., A biomimicking design for mechanical knee joints, Bioinspiration & Biomimetics, Vol.13, (2018), 056012 (12 pages).

[107] Kuntz, J.P., Rolling Link Mechanisms, PhD thesis, Delft University of Technology, (1995).

[108] Jeanneau, A., Herder, J., Laliberte, T. and Gosselin, C., A compliant rolling contact joint and its application in a 3-dof planar parallel mechanism with kinematic analysis, Proc. of ASME 2004 Design Engineering Technical Conferences and Computers and Information in Engineering Conference, (2004), DETC2004-57264 (10 pages).

[109] Halverson, P.A., Howell, L.L. and Magleby, P.S., Tension-based multi-stable compliant

rolling-contact elements, Mechanism and Machine Theory, Vol.45, (2010), pp.147-156.

[110] Halverson, P.A., Bowden, A.E. and Howell, L.L., A compliant-mechanism approach to achieving specific quality of motion in a lumbar total disc replacement, International Journal of Spine Surgery, Vol.6, (2012), pp.78-86.

[111] Nelson, T.G., Lang, R.J., Magleby, S.P. and Howell, L.L., Curved-folding-inspired deployable compliant rolling-contact element (D-CORE), Mechanism and Machine Theory, Vol. 96, (2016), pp.225-238.

[112] Nelson, T.G. and Herder, J.L., Developable compliant-aided rolling-contact mechanisms, Mechanism and Machine Theory, Vol.126, (2018), pp.225-242.

[113] Raussen, M., Elementary Differential Geometry: Curves and Surfaces, Aalborg University, Denmark (2008).

[114] Vukobratovic, M., and Stepanenko, J. On the stability of anthropomorphic systems, Mathematical biosciences, Vol.15 (1972), pp.1-37.

[115] Sardain, P. and Bessonnet, G., Forces acting on a biped robot. Center of pressure-zero moment point., IEEE Transactions on Systems, Man, and Cybernetics-Part A: Systems and Humans, Vol.34, No.5 (2004), pp.630-637.

[116] Kino, H. and Kawamura, S., Mechanism and Control of Parallel-Wire Driven System, Journal of Robotics and Mechatronics, Vol.27, No.6 (2015), pp.599-607.

[117] Press, W. H., Teukolsky, S. A., Vetterling, W. T. and Flannery, B. P., Numerical Recipes: The Art of Scientific Computing with IBM PC or Macintosh, Cambridge University Press (1996).

[118] Waltz, R.A., Morales, J.L., Nocedal, J. and Orban, D., An interior algorithm for nonlinear optimization that combines line search and trust region steps, Mathematical programming, Vol.107, No.3 (2006), pp.391-408.

[119] Andrikopoulos, G., Nikolakopoulos, G. and Manesis, S., A Survey on Applications of Pneumatic Artificial Muscles, Proc. of the 19th Mediterranean Conference on Control and Automation, (2011), pp.1439-1446.

[120] Derby, S., Sreekumar, M., Nagarajan, T., Singaperumal, M., Zoppi, M. and Molfino, R., Critical review of current trends in shape memory alloy actuators for intelligent robots, Industrial Robot, Vol.34, No.4 (2007), pp.285-294.

[121] Kheirikhah, M.M., Rabiee, S. and Edalat, M. E., A Review of Shape Memory Alloy Actuators in Robotics, RoboCup 2010: Robot Soccer World Cup XIV, (2010), pp.206-217.

[122] Gu, G. Y., Zhu, J., Zhu, L. M. and Zhu, X., A survey on dielectric elastomer actuators for soft robots, Bioinspiration and Biomimetics, Vol.12, (2017), 011003 (22 pages).

[123] Li, S., Vogt, D. M., Rus, D., and Wood, R. J., Fluid-driven origami-inspired artificial muscles, Proc. of the National academy of Sciences, Vol.114, No.50 (2017), pp.13132-13137.

[124] Iwatsuki, N. and Terashima, N., Flexibility Control of Redundant Closed-loop Mechanisms with Elastic Elements, Proc. of The 1st IFToMM Asian Conference on Mechanism and Machine Science, (2010), pp.210-215.

[125] Morishita, M., Strength of Materials II, Morikita Pub. Co., (2018), p.28, (in Japanese).

Appendix A

Fabrication accuracy required to the spatial rolling contact pair

A.1 Chapter introduction

The spatial rolling contact pair (SRCP) proposed in chapter 2 can completely generate the specified trajectory, theoretically. However, exact path generation is actually impossible because the actual machine elements have dimension errors. In the SRCP, the output position error is possible to be large because of processing errors of the rolling contact surfaces and assembly errors between the links and flexible bands. On the other hand, although the conventional spatial-path generators with 1 DOF composed of only lower pairs can generate the specified trajectory only in an approximate manner, they can be fabricated accurately because of simple structures of joints. Thus, in order to use SRCP in conventional mechanisms, the SRCP must be fabricated so as to generate the specified trajectory more accurately than they do.

In this chapter, output position errors of several spatial-path generators with only closed lower pairs are investigated, and fabrication errors of the SRCP to achieve more accurate path generation than they do are revealed.

A.2 Calculation of benchmark

Several spatial-path generators with only lower pairs were synthesized and their output position errors were calculated as benchmarks. In the calculation of the position errors, the clearance at each joint of the linkages was neglected to evaluate fabrication errors of the SRCP in a strict condition.

At first, structural synthesis of the linkages was performed. In order to simplify the mechanism and synthesis procedure, the following conditions were specified.

(1) The topology is a single closed-loop composed of four links.
(2) The input joint is a revolute pair.
(3) The passive joints are selected from a revolute pair (R), a prismatic pair (P), a cylindrical pair (C), and a spherical pair (S).
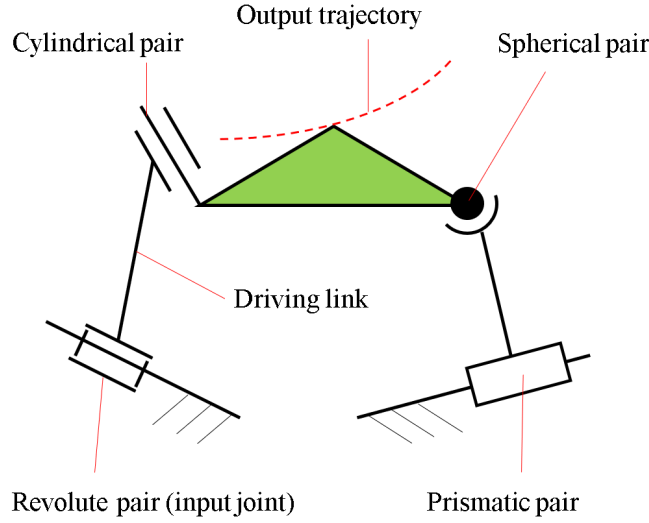(4) The analytical kinematic solution can be derived easily.

Fig.A.1   An RCSP spatial 4-bar linkage to generate the specified trajectory

By substituting the conditions (1) and (2) into Gruebler's equation, the sum of DOF of all joints in the linkage except the input joint was six. In this case, many combinations of kinematic pairs were able to be considered. From the condition (4), the RCSP structure as shown in Fig.A.1 was selected. The forward kinematics of this linkage can be solved analytically as follows.

Fig.A.2 shows the driving link. The initial positions of the revolute pair and the cylindrical pair are ${}^1\boldsymbol{j}_{1,0}$ and ${}^1\boldsymbol{j}_{2,0}$ on Σ_1, respectively. The initial directions of the rotation axis of the revolute pair and the cylindrical pair are ${}^1\hat{\boldsymbol{\omega}}_{1,0}$ and ${}^1\hat{\boldsymbol{\omega}}_{2,0}$, respectively. When the input angle of the revolute pair is θ, position and orientation of the cylindrical pair, ${}^1\boldsymbol{j}_2$, ${}^1\hat{\boldsymbol{\omega}}_2$, can be calculated with Rodriguez's theorem as follows.

$$
{}^1\boldsymbol{d}_{1,2} = {}^1\boldsymbol{j}_{2,0} - {}^1\boldsymbol{j}_{1,0} \tag{A.1}
$$

$$
{}^1\boldsymbol{j}_2 = {}^1\boldsymbol{j}_{1,0} + {}^1\boldsymbol{d}_{1,2}\cos\theta + ({}^1\boldsymbol{d}_{1,2}^T\,{}^1\hat{\boldsymbol{\omega}}_{1,0})^1\hat{\boldsymbol{\omega}}_{1,0}(1-\cos\theta) + ({}^1\hat{\boldsymbol{\omega}}_{1,0} \times {}^1\boldsymbol{d}_{1,2})\sin\theta \tag{A.2}
$$

$$
{}^1\hat{\boldsymbol{\omega}}_2 = {}^1\hat{\boldsymbol{\omega}}_{2,0}\cos\theta + ({}^1\hat{\boldsymbol{\omega}}_{2,0}^T\,{}^1\hat{\boldsymbol{\omega}}_{1,0})^1\hat{\boldsymbol{\omega}}_{1,0}(1-\cos\theta) + ({}^1\hat{\boldsymbol{\omega}}_{1,0} \times {}^1\hat{\boldsymbol{\omega}}_{2,0})\sin\theta \tag{A.3}
$$

Since the prismatic pair is on the stationary link, the position and orientation of the prismatic pair are known. Therefore, the position of the spherical pair can be calculated as an intersection of the cylinder and the line as shown in Fig.A.3. Let the position of the foot of the perpendicular line from the spherical pair to the rotation axis of the cylindrical pair be ${}^1\boldsymbol{a}$. Then, the equations of the cylinder are as follows.

$$
{}^1\boldsymbol{a} = {}^1\boldsymbol{j}_2 + u_c\,{}^1\boldsymbol{\omega}_2, \tag{A.4}
$$

$$
|{}^1\boldsymbol{j}_3 - {}^1\boldsymbol{a}|^2 = r^2, \tag{A.5}
$$

$$
({}^1\boldsymbol{j}_3 - {}^1\boldsymbol{a})^T\,{}^1\hat{\boldsymbol{\omega}}_2 = 0, \tag{A.6}
$$

where u_c is an arbitrary value and ${}^1\boldsymbol{j}_3$ is position of the spherical pair, and r is the radius of the cylinder. r can be calculated with the initial values of ${}^1\boldsymbol{j}_3$ and ${}^1\boldsymbol{a}$ as follows.
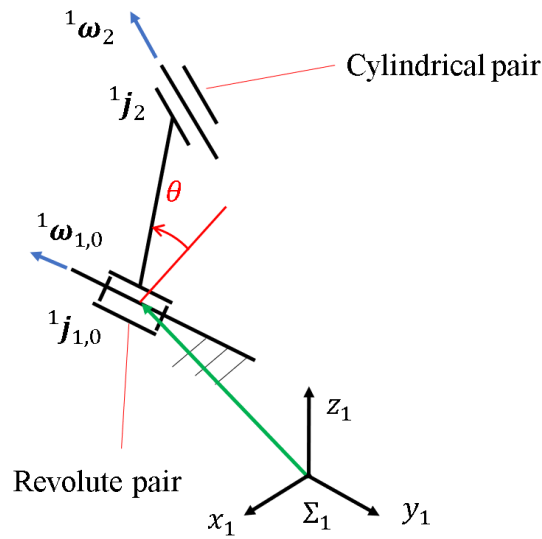
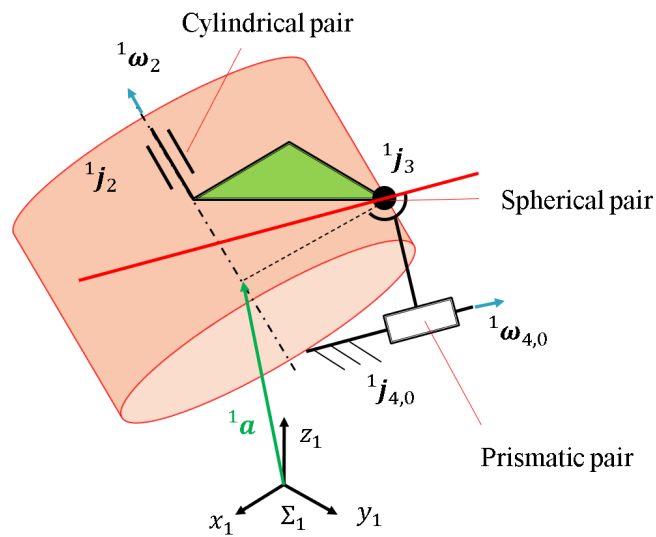Fig.A.2   Kinematics of the driving link of an RCSP linkage

Fig.A.3   Kinematics of the CSP kinematic chain

$$r = |{}^1\boldsymbol{j}_{3,0} - {}^1\boldsymbol{a}_0| \tag{A.7}$$

Besides, the equation of the line is as follows.

$${}^1\boldsymbol{j}_3 = {}^1\boldsymbol{j}_{3,0} + u_p\,{}^1\hat{\boldsymbol{\omega}}_{4,0}, \tag{A.8}$$
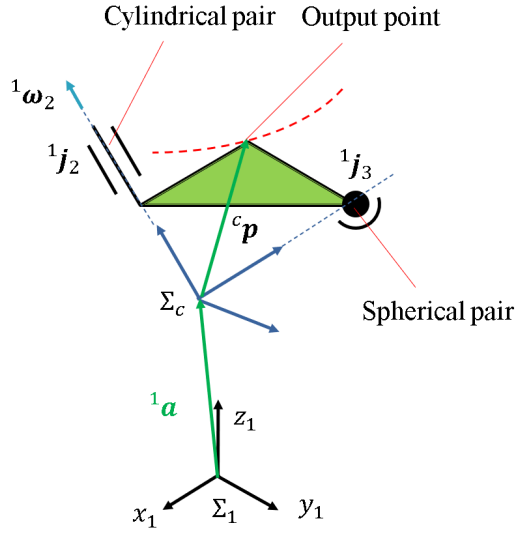
Fig.A.4   The output link of the synthesized linkage

where $^1\hat{\boldsymbol{\omega}}_{4,0}$ is the direction of the translation axis of the prismatic pair. From Eqs.(A.4)-(A.8), u_p can be calculated as follows.

$$
\begin{cases}
u_p = \dfrac{-\boldsymbol{q}_1^T \boldsymbol{q}_2 - \sqrt{D}}{|\boldsymbol{q}_1|^2} \\
D = (\boldsymbol{q}_1^T \boldsymbol{q}_2)^2 - |\boldsymbol{q}_1|^2 (|\boldsymbol{q}_2|^2 - r^2) \\
\boldsymbol{q}_1 = {}^1\hat{\boldsymbol{\omega}}_4 - ({}^1\hat{\boldsymbol{\omega}}_2^{T\,1}\hat{\boldsymbol{\omega}}_4)^1\hat{\boldsymbol{\omega}}_2 \\
\boldsymbol{q}_2 = {}^1\boldsymbol{j}_{3,0} - {}^1\boldsymbol{j}_2 - [({}^1\boldsymbol{j}_{3,0} - {}^1\boldsymbol{j}_2)^{T\,1}\hat{\boldsymbol{\omega}}_2]^1\hat{\boldsymbol{\omega}}_2
\end{cases}
\tag{A.9}
$$

Therefore, the positions $^1\boldsymbol{p}_2$, $^1\boldsymbol{p}_3$, and orientation $^1\hat{\boldsymbol{\omega}}_2$ are derived.

In order to use the RCSP linkage as a spatial-path generator, the output point was defined on the coupler link. As shown in Fig.A.4, a reference frame Σ_c was defined on the coupler link, and its bases were defined as follows.

$$
^1\boldsymbol{e}_{c,x} = \frac{1}{r}({}^1\boldsymbol{j}_3 - {}^1\boldsymbol{a})
\tag{A.10}
$$

$$
^1\boldsymbol{e}_{c,y} = {}^1\hat{\boldsymbol{\omega}}_2
\tag{A.11}
$$

$$
^1\boldsymbol{e}_{c,z} = {}^1\boldsymbol{e}_1 \times {}^1\boldsymbol{e}_2
\tag{A.12}
$$

The output point was represented on Σ_c as $^c\boldsymbol{p}$. Thus, the output point on Σ_1 was calculated as follows.

$$
^1\boldsymbol{p} = [{}^1\boldsymbol{e}_{c,x}\ {}^1\boldsymbol{e}_{c,y}\ {}^1\boldsymbol{e}_{c,z}]^c\boldsymbol{p} + {}^1\boldsymbol{a}
\tag{A.13}
$$

By using this kinematic model, dimensional synthesis was performed with a numerical optimization. Design parameters were $^c\boldsymbol{p}$, $^1\boldsymbol{p}_{i,0}$ and $^1\hat{\boldsymbol{\omega}}_{i,0}$ ($i = 1, 2, 3, 4$). Here, $^1\hat{\boldsymbol{\omega}}_{i,0}$ was represented as the angle $\phi_{y_1,i}$ about the y_1-axis and the angle $\phi_{z_1,i}$ about the z_1-axis.
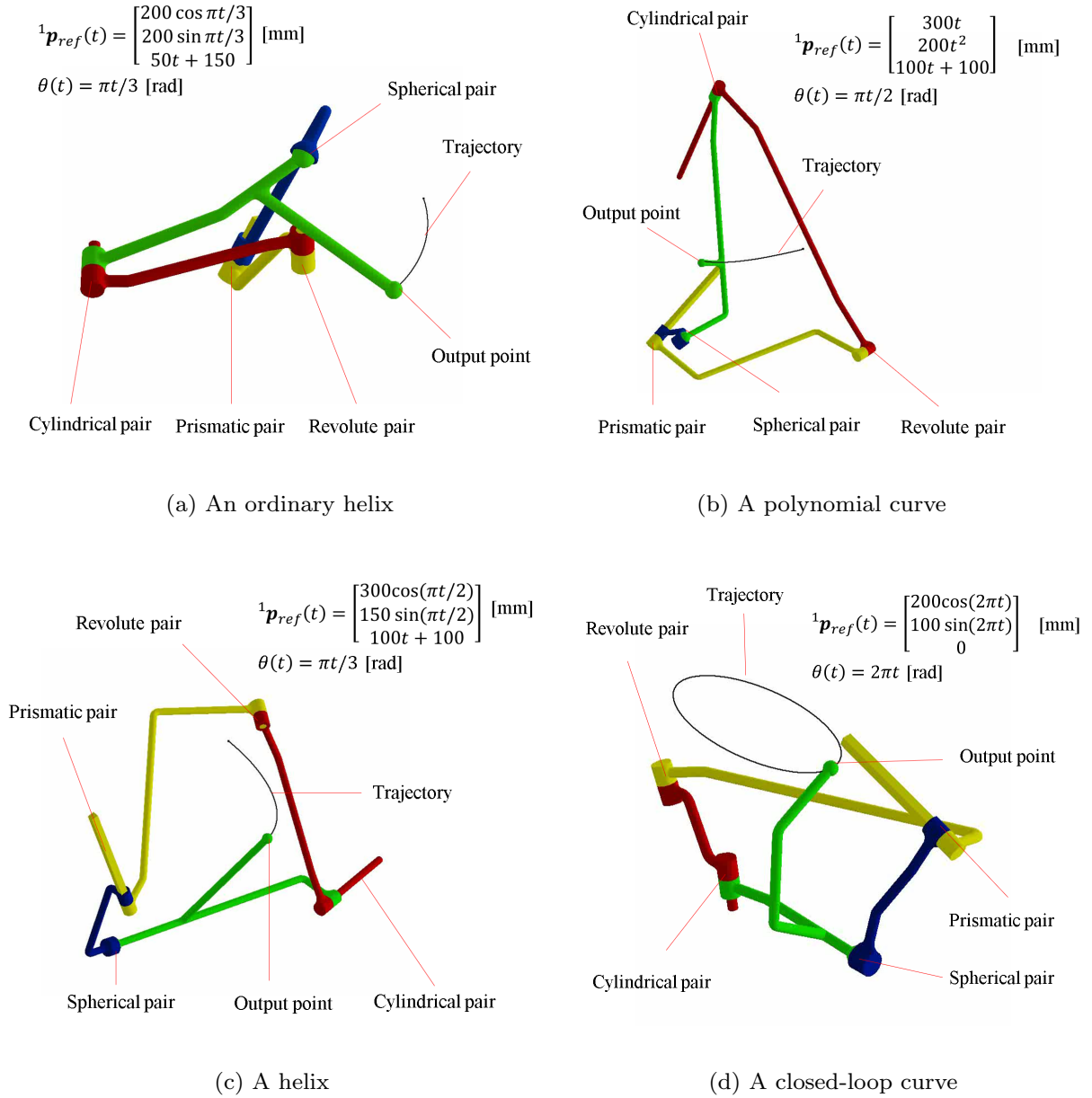
$$^{1}\boldsymbol{p}_{ref}(t) = \begin{bmatrix} 200\cos\pi t/3 \\ 200\sin\pi t/3 \\ 50t + 150 \end{bmatrix} \text{[mm]}$$

$$\theta(t) = \pi t/3 \text{ [rad]}$$

Spherical pair

Trajectory

Output point

Cylindrical pair   Prismatic pair   Revolute pair

(a) An ordinary helix

Cylindrical pair

$$^{1}\boldsymbol{p}_{ref}(t) = \begin{bmatrix} 300t \\ 200t^2 \\ 100t + 100 \end{bmatrix} \text{[mm]}$$

$$\theta(t) = \pi t/2 \text{ [rad]}$$

Trajectory

Output point

Prismatic pair   Spherical pair   Revolute pair

(b) A polynomial curve

Revolute pair

Prismatic pair

$$^{1}\boldsymbol{p}_{ref}(t) = \begin{bmatrix} 300\cos(\pi t/2) \\ 150\sin(\pi t/2) \\ 100t + 100 \end{bmatrix} \text{[mm]}$$

$$\theta(t) = \pi t/3 \text{ [rad]}$$

Trajectory

Spherical pair   Output point   Cylindrical pair

(c) A helix

Trajectory

Revolute pair

$$^{1}\boldsymbol{p}_{ref}(t) = \begin{bmatrix} 200\cos(2\pi t) \\ 100\sin(2\pi t) \\ 0 \end{bmatrix} \text{[mm]}$$

$$\theta(t) = 2\pi t \text{ [rad]}$$

Output point

Prismatic pair

Cylindrical pair   Spherical pair

(d) A closed-loop curve

Fig.A.5   The measured output trajectories generated by the fabricated ASRCP with the FOAMs

Then, the objective function was as follows.

$$F_l = \sum_{j=1}^{N_d} |^{1}\boldsymbol{p}(\theta_j) - {}^{1}\boldsymbol{p}_{ref}(\theta_j)|^2, \tag{A.14}$$

where $^{1}\boldsymbol{p}_{ref}(\theta_j)$ is the j-th designated point and N_d is the number of the designated points. This objective function was minimized subject to the size limitation which is shown in Table A.1 and $D \geqq 0$, which is shown in Eq.(A.9), with the interior-point method [118] for

Table A.1   Size limitation of the synthesized RCSP linkages

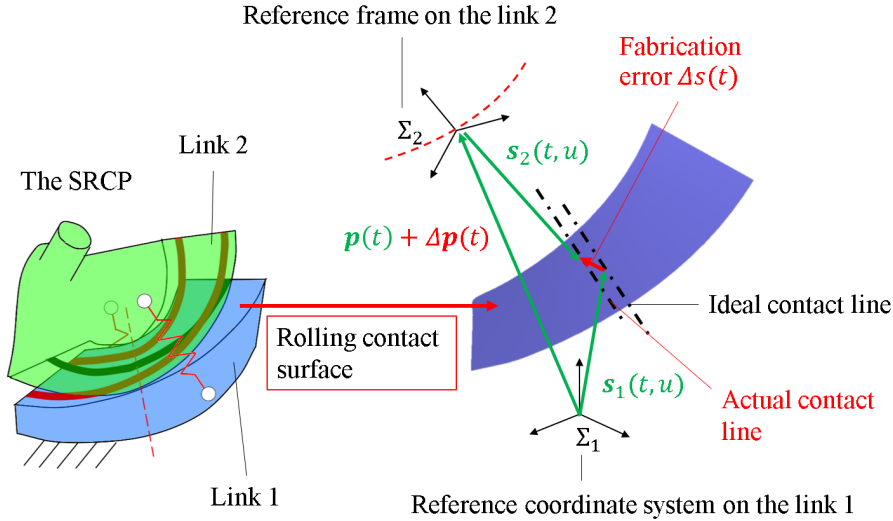|	$^c\boldsymbol{p}^T$ [mm]	$^1\boldsymbol{p}_{i,0}^T$ [mm]	$(\phi_{y_1,i},\ \phi_{z_1,i})$ [rad]
minimum values	$[-400\ -400\ -400]$	$[-400\ -400\ -400]$	$(-\pi,\ -\pi)$
maximum values	$[400\ 400\ 400]$	$[400\ 400\ 400]$	$(\pi,\ \pi)$

Fig.A.6   The kinematic model of the SRCP including the fabrication errors

many initial points generated randomly. Then, the minimum value among the calculated candidates was selected as the solution.

By using the described methods, four samples were synthesized. The specified motions and pictures of the synthesized linkages are shown in Fig.A.5. Mean values of the output position errors of the samples (a), (b), (c) and (d) were 0.0041 mm, 1.065 mm, 0.9483 mm, and 0.1205 mm, respectively. The sample (a) was the most accurate among the four samples. This reason is considered that the specified trajectory (an ordinary helix) was close to one of motions of lower pairs. The specified trajectory of the samples from (b) to (d) is a little complicated to be made with only lower pairs. These position errors were used for benchmarks.

A.3   Allowable fabrication error of the SRCP

In order to reveal the fabrication error required to generate the specified trajectory more accurately than the linkage with lower pairs do, the relationship between the fabrication error and the output position error of the SRCP was derived. As shown in Fig.A.6, the rolling contact surface on the link 1 is represented as $^1\boldsymbol{s}_1(t,u)$ on Σ_1 and the surface on the link 2 is represented as $^2\boldsymbol{s}_2(t,u)$ on Σ_2. As described in section 2.2.2, $^1\boldsymbol{s}_2(t,u)$ corresponds to $^1\boldsymbol{s}_1(t,u)$ for each value of t. Therefore, the following relationship holds.

$$^1\boldsymbol{p}(t) = {}^1\boldsymbol{s}_1(t,u) - \boldsymbol{R}_{1,2}(t)\,^2\boldsymbol{s}_2(t,u), \tag{A.15}$$

where $\boldsymbol{R}_{1,2}(t)$ is the rotation matrix from Σ_1 to Σ_2. By the way, the fabrication error of the SRCP were represented as follows.

(1) Processing errors of the rolling contact surfaces were represented as infinitesimal displacement of ${}^1\boldsymbol{s}_2(t, u)$ in the normal direction of ${}^1\boldsymbol{s}_1(t, u)$.
(2) Assembly errors of the flexible bands between the links were represented infinitesimal displacement of ${}^1\boldsymbol{s}_2(t, u)$ in the two independent tangent directions of ${}^1\boldsymbol{s}_1(t, u)$.

Since these three directions are independent, the fabrication error can be represented as an infinitesimal position displacement $\Delta^1\boldsymbol{s}$. Thus, when the output error $\Delta^1\boldsymbol{p}$ is generated by the fabrication error $\Delta^1\boldsymbol{s}$, Eq.(A.15) is rewritten as follows.

$$ {}^1\boldsymbol{p}(t) + \Delta^1\boldsymbol{p} = {}^1\boldsymbol{s}_1(t, u) - \boldsymbol{R}_{1,2}(t)^2\boldsymbol{s}_2(t, u) + \Delta^1\boldsymbol{s} \tag{A.16} $$

Therefore, $\Delta^1\boldsymbol{p} = \Delta^1\boldsymbol{s}$. This means that the fabrication error effects the output error directly.

In order to generate the specified trajectory with the SRCP more accurately than the synthesized samples generate, the fabrication error must be smaller than their output position errors. However, it is difficult to achieve a smaller error than the smallest value of them, 0.0041 mm, if not impossible. Nevertheless, the fabrication error about 100 μm, which is required to generate the trajectory with the SRCP more accurately than the samples (b)-(c) generate, is possible to be achieved even if the SRCP is fabricated by an additive manufacturing method. Therefore, the SRCP is useful especially when the specified output trajectory is complicated.

A.4   Chapter summary

In this chapter, output position errors of several spatial-path generators with only closed lower pairs were calculated, and fabrication errors of the SRCP to achieve more accurate path generation than they do were revealed. The results are summarized as follows.

(1) Several spatial-path generators with 1-DOF were optimally synthesized, and their output position errors were calculated by assuming their fabrication errors and backlash at their joints to be zero. As a result, it was confirmed that the error was larger than 100 μm when the specified trajectories were not so simple.

(2) In the SRCP, the fabrication error can be assumed to be corresponding to the output position errors. Therefore, the allowable fabrication errors were considered to be about 100 μm. It can be considered that this error value is possible to be achieved easily even if the SRCP is fabricated by an additive manufacturing method.

Appendix B

Design of the fluid-driven origami-inspired artificial muscle

B.1   Chapter introduction

In section 3.5.2, the fluid-driven origami-inspired artificial muscle (FOAM) [123] was used as a fluid-driven pneumatic artificial muscle. In the previous research on the FOAM by Li et al. [123], design methods for the FOAM to have the specified size and contraction ratio had not been proposed. Therefore, a design method of the pneumatic FOAM was proposed, and the FOAM used in section 3.5.2 was designed with the proposed method. In this chapter, the proposed design method is described. In addition, the design procedure of the FOAM used in section 3.5.2 is described.

B.2   Design method

B.2.1   Structural design

The pneumatic FOAM is composed of an elastic skeleton with zigzag shape, thin skin, and internal fluid as shown in Fig.B.1. When internal fluid is vacuumed from the skin,
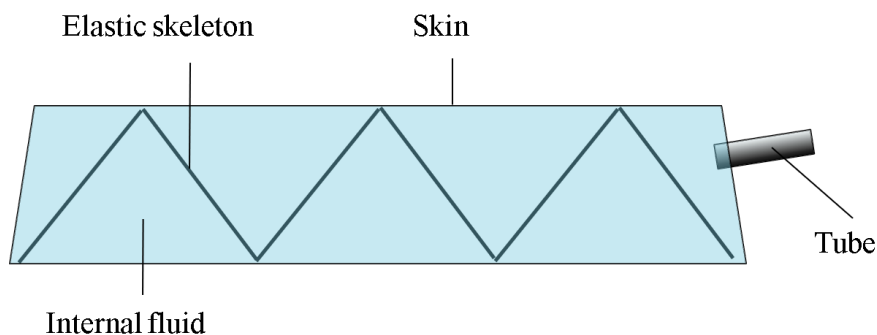
Fig.B.1   Schematic diagram of the pneumatic FOAM
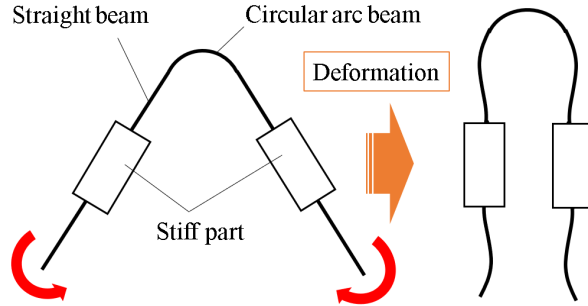
Fig.B.2   Elastic hinge at the vertex of the skeleton of the FOAM

the FOAM contracts. In this case, each vertex of the zigzag skeleton ideally has to move like a revolute pair, and the other parts of the skeleton have not to move. In addition, the skeleton must not deform plastically in its workspace. In order to satisfy such conditions, a suitable structure of the skeleton is proposed as shown Fig.B.2. Each vertex of the skeleton has an elastic hinge which is composed of a cylindrical beam and flat beams, and its thickness is smaller than the thickness of other parts. Since the elastic hinge can deform locally, the skeleton can generate the ideal motion. Besides, when the elastic hinge deforms, the stress in the circular arc beam can distribute into the flat beams. Thus, it is difficult to deform plastically.

B.2.2   Dimensional design

In order to get the FOAM with the specified size and contraction ratio, dimensions of the skeleton are designed. Fig.B.3 shows design variables of the skeleton. As required parameters, the maximum and minimum length of the skeleton L_{max}, L_{min}, maximum width of the skeleton $b_{1,max}$ and width of another side b_2 are given. In addition, radius and thickness of the elastic hinge r, h and a ratio between flexible part and stiff part of the flat beam, q, are given. Then, the number of the mountains in the zigzag skeleton N_z, length of the flat part D and the length of the thin flat part a are calculated by the following equations.

$$N_z = \text{floor}(\frac{L_{min}}{4}), \tag{B.1}$$

$$D = b_{1,max} - 2(r + \frac{h}{2}), \tag{B.2}$$
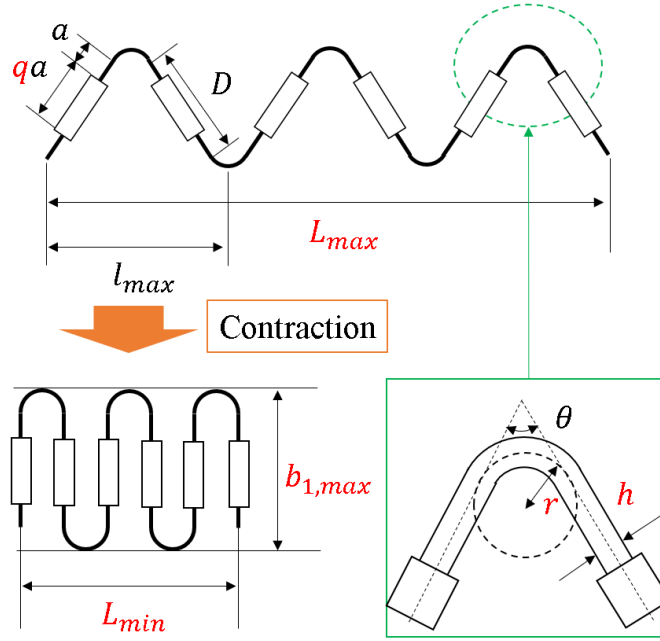
$$a = \frac{D}{2+q} \tag{B.3}$$

Fig.B.3 Dimensions of the skeleton

where $\text{floor}(x) = \{n \in \mathbb{N} | n \leqq x\}$. These equations are geometrical relationship in the skeleton. Besides, the following equation holds.

$$D \sin \frac{\theta}{2} + 2r \cos \frac{\theta}{2} - \frac{L_{max}}{2N_z} = 0 \qquad (B.4)$$

The angle at the vertex of the skeleton θ is calculated by solving Eq.B.4 with a numerical method such as bi-section method in $0 \leqq \theta \leqq \pi$ [rad].

In order to generate the ideal motion, r and a have to be small. However, they have to be increased to reduce maximum stress in the elastic hinge. Thus, those values have to be determined so that the maximum stress is less than the allowable stress. Thus, after the calculation of the design variables, stress analysis of the elastic hinge in the maximally deformed state has to be performed and it is confirmed whether the maximum stress is less than the allowable stress or not. If not, h, r and q are modified and the above calculation is performed again.

B.2.3 Stress analysis

In order to perform the above procedure effectively, a method to calculate the maximum stress in the elastic hinge is proposed. This method is the combination of the deformation analysis with an elastically constrained closed-loop linkage model and stress analysis of a curved beam.

Firstly, the deformation of the elastic hinge is calculated. In this calculation, the neutral surface of the elastic hinge is modeled as an elastically constrained closed-loop linkage with $3N$ links and $3N + 1$ revolute pairs as shown in Fig.B.4. The kinematic state of each joint is represented as curvature of beam κ_i $(i = 1, 2, ..., 3N + 1)$ instead of the
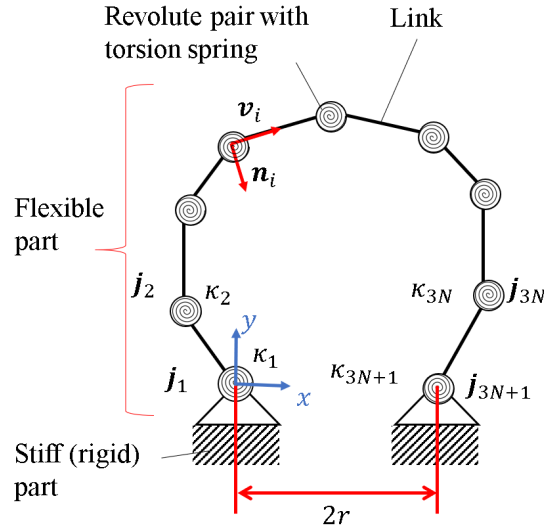
Fig.B.4   Kinetostatic model of the flexible part in the elastic hinge

link angle and position of each joint is represented as $\boldsymbol{j}_i$. The part in $1 \leqq i \leqq N+1$ and $2N+1 \leqq i \leqq 3N+1$ is the flat beam so the initial curvature is $\kappa_{i,0} = 0$. The part in $N+2 \leqq i \leqq 2N$ is cylindrical beam so the initial curvature is $\kappa_{i,0} = 1/r$. The tangent and normal direction of the beam at $\boldsymbol{j}_i$ are represented as $\boldsymbol{v}_i$ and $\boldsymbol{n}_i$. When boundary conditions at $\boldsymbol{j}_1$ are $\boldsymbol{v}_1 = [0 \ 1]^T$ and $\boldsymbol{n}_1 = [1 \ 0]^T$, $\boldsymbol{v}_i$ and $\boldsymbol{n}_i$ $(i = 2, \cdots, 3N+1)$ can be calculated with the Frenet-Serret equation. The Frenet-Serret equation is represented as the following equation with arc-length parameter λ.

$$\frac{d}{d\lambda}\begin{bmatrix} \boldsymbol{v}^T \\ \boldsymbol{n}^T \end{bmatrix} = \begin{bmatrix} 0 & \kappa \\ -\kappa & 0 \end{bmatrix}\begin{bmatrix} \boldsymbol{v}^T \\ \boldsymbol{n}^T \end{bmatrix} \quad \Leftrightarrow \quad \frac{d}{d\lambda}\boldsymbol{V} = \boldsymbol{\Gamma}\boldsymbol{V} \tag{B.5}$$

Thus, the Frenet-Serret equation can be discretized based on the trapezoidal integration as the following equation.

$$\boldsymbol{V}_i = (2\boldsymbol{I} - \Delta\lambda\boldsymbol{\Gamma}_i)^{-1}(2\boldsymbol{I} + \Delta\lambda\boldsymbol{\Gamma}_{i-1})\boldsymbol{V}_{i-1} \tag{B.6}$$

where $\boldsymbol{I}$ is identity matrix, $\Delta\lambda_i$ is a/N in the flat beam and $r(\pi-\theta)/N$ in the cylindrical beam. Then, each position of the joint can be calculated with the following update function.

$$\boldsymbol{j}_i = \boldsymbol{j}_{i-1} + \frac{\boldsymbol{v}_i - \boldsymbol{v}_{i-1}}{2}\Delta\lambda_i \tag{B.7}$$

Note that another edge of the elastic hinge must be satisfied boundary conditions $\boldsymbol{j}_{3N+1} = [2r \ 0]^T$, $\boldsymbol{v}_{3N+1} = [0 \ -1]^T$. Therefore, curvatures are updated to minimize the potential energy of the elastic hinge with subject to the boundary conditions by using a numerical optimization method. The objective function (the approximated potential energy U_p) is
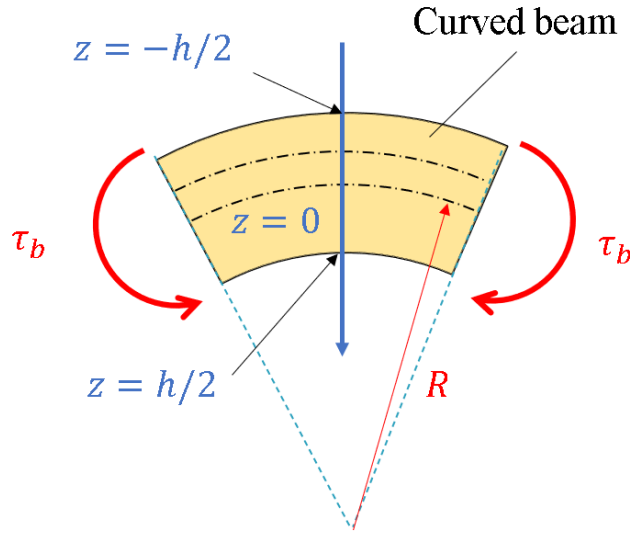

Fig.B.5   A segment of the curved beam

represented as the following equation.

$$U_p = \frac{E}{2}(\frac{b_2 h^3}{12}) \sum_{i=2}^{3N+1} [\frac{1}{2} \sum_{j=i-1}^{i} (\kappa_j - \kappa_{j,0})^2] \Delta \lambda_i \tag{B.8}$$

where E is Young's modulus.

Next, the maximum stress of the elastic hinge is calculated. Fig.B.5 shows a segment of the curved beam. $R = 1/\kappa$ is the radius of curvature and τ_b is the bending moment. The relationship between R and τ_b is represented as the following equation [125].

$$\frac{1}{R} = \frac{1}{R_0}[1 + \frac{\tau_b}{\chi(ESR_0 + \tau_b)}], \tag{B.9}$$

where R_0 is the initial radius of curvature, S is the cross-sectional area which is calculated by $S = hb_2$ and χ is the section modulus of the curved beam. Note that it is considered that the maximum stress is generated on the outer circumference, i.e. the area of $z = -h/2$. Thus, χ at $z = -h/2$ is calculated by the following equation [125].

$$\chi = \frac{1}{S} \int_S \frac{z}{R+z} dS = \frac{R_0}{h} \ln(\frac{R_0 + h/2}{R_0 - h/2}) - 1 \tag{B.10}$$

Thus, the bending moment at each joint is calculated with the following equation.

$$\tau_{b,i} = ES(R_i + R_{0,i})[1 - \frac{R_i}{R_{0,i}}(1 - \frac{1}{\chi})]^{-1} \tag{B.11}$$

By using calculated $\tau_{b,i}$, the stress at $z = -h/2$ is calculated with the following equation [125].

$$\sigma_i = \frac{\tau_{b,i}}{SR_{0,i}}[1 - \frac{h/2}{\chi(R_{0,i} - h/2)}] \tag{B.12}$$

Therefore, the maximum stress can be derived and the following condition must be satisfied.

$$\sigma_{max} = \max_{i=1,...,3N+1}(\sigma_i) \leqq \sigma_{yield},\tag{B.13}$$

where σ_{yield} is the yield stress of the skeleton. It is thought that this method can achieve lower cost calculation than FEM of commercial software because the division number of this calculation can be small.

B.3   Evaluation

In order to confirm the validity of the proposed method to calculate the stress of the elastic hinge, the maximum stresses of some examples were calculated with the proposed method and they were compared with results calculated with the finite element method (FEM) by commercial software under the same conditions. In this investigation, three examples of the elastic hinge were used. All examples had $E = 1.6$ GPa, $b_2 = 20$ mm, $h = 1$ mm, $r = 2$ mm, $\theta = 45$ deg but they had different values of a with each other: $a = 5$ mm, 10 mm, 15 mm. As the commercial software, ANSYS was used, and maximum principal stresses of the examples were calculated by the large deformation analysis.

Errors between the maximum stress calculated by the proposed method and FEM were 1.33 % in a=5 mm, 2.36 % in a=10 mm and 4.33 % in a=15 mm. Fig.B.6 shows the stress distribution along the outer circumference of the cylindrical beam when the elastic hinge has $a = 15$ mm, where λ is the arc length parameter from end to end of the circumference. These results show that maximum stress calculated by the proposed method agrees very well with maximum principal stress calculated by ANSYS. Note that the reason why the stress calculated with FEM is zero at both ends of λ is that ANSYS calculated triaxial
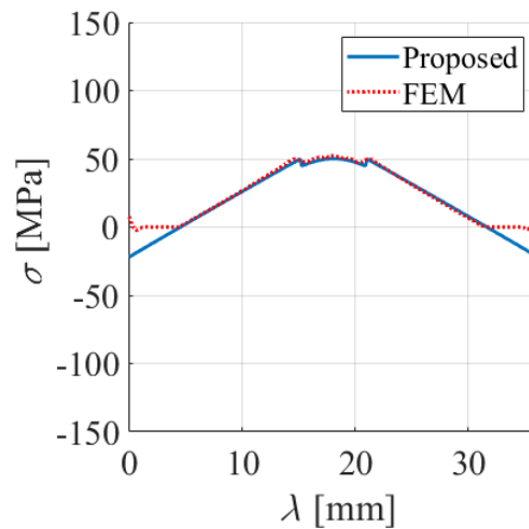
Fig.B.6   Comparison between the stress calculated by the proposed method and by the FEM

stress and its component had both zero and negative values. Therefore, it can be thought that the proposed method is valid.

In this calculation, the number of the links in the closed-linkage model was 120 ($N = 40$). Although the division number was small and calculation time is low, the maximum stress was able to be calculated accurately. Therefore, this method is useful for the proposed design procedure.

B.4   Design for the example of the ASRCP

In section 3.5.2, the FOAM of which minimum length is smaller than 87 mm, stroke is larger than 89 mm and the contraction ratio is larger than 44 %, was required to drive the SRCP. In order to design such FOAM, $L_{min} = 25$ mm, $L_{max} = 125$ mm, $r = 1.5$ mm, $h = 0.8$ mm, $w_{1,max} = 30$ mm and $q = 5$ were specified. Then, the other parameters were calculated with the method described in section B.2.2, and $D = 26.2$ mm, $\theta = 59.6$ deg, $N_z = 4$ and $a = 3.74$ mm were obtained. When copolyester is used as the material of the skeleton, Young's modulus of the skeleton is $E = 150$ MPa. Then, the maximum stress of the skeleton with this material was $\sigma_{max} = 10.36$ MPa. This value is less than the tensile strength of this material: 14 MPa. Therefore, this skeleton does not plastically deform in the motion range.

B.5   Chapter summary

In this chapter, a design method of the FOAM was described. Besides, the design procedure of the FOAM used in section 3.5.2 was described. The summary is as follows.

(1) A design method of the FOAM with the specified size and contraction ratio and without plastic deformation of its skeleton was described.

(2) The validity of the proposed method to analyze maximum stress in the skeleton was confirmed by comparing results calculated with the proposed method and results calculated with commercial software.

(3) The FOAM to drive the example in section 3.5.2 was able to be designed to satisfy its requirements and to be without plastic deformation in the skeleton.

Publications

Journal papers

(1) Naoto KIMURA, Nobuyuki IWATSUKI and Ikuma IKEDA, Design of a flexibly-constrained revolute pair with non-linear stiffness in multiple directions, Mechanical Engineering Journal, Vol.7, No.4 (2020), pp.1-15.

(2) Naoto KIMURA, Nobuyuki IWATSUKI and Ikuma IKEDA, Spatial rolling contact pair with a hybrid elastic constraint composed of flexible bands and linear springs, Mechanical Engineering Journal, Vol. 6, No. 6 (2019), pp. 1-15.

(3) Naoto Kimura, Nobuyuki Iwatsuki and Ikuma Ikeda, Design of a Flexibly-Constrained Revolute Pair with Non-Linear Stiffness for Safe Robot Mechanisms, Journal of Robotics and Mechatronics, Vol. 31, No. 1 (2019), pp. 156-165.

(4) Naoto KIMURA, Nobuyuki IWATSUKI and Ikuma IKEDA, Development of kinematic pair consisting of elastically constrained two curved surfaces which can generate the specified rolling motion, Transactions of the JSME, Vol. 84, No. 863 (2018), pp.1-15 (in Japanese).

Proceedings of international conferences

(5) Naoto KIMURA, Nobuyuki IWATSUKI and Ikuma IKEDA, Design and Control of the Fluid-driven Origami-inspired Artificial Muscle to Drive the Spatial Rolling Contact Pair, Proc. of the 5th International Conference on Design Engineering and Science, No.49 (2020), pp.1-10 (accepted).

(6) Naoto Kimura, Nobuyuki Iwatsuki and Ikuma Ikeda, Design and Control Methodology of a Cable Driven Active Spatial Rolling Contact Pair, Proc. of the 15th IFToMM World Congress on Mechanism and Machine Science, (2019), pp. 1305-1314.

(7) Naoto Kimura, Nobuyuki Iwatsuki and Ikuma Ikeda, Design of the Elastic Constraints

with Flexures and Linear Springs for the Spatial Rolling Contact Pair, Proc. of the 22nd International Conference on Mechatronics Technology (ICMT2018), No.49 (2018),pp.1-2.

(8) Naoto Kimura, Nobuyuki Iwatsuki and Ikuma Ikeda, Flexibly Constrained Revolute Pair for Safe Robot Mechanisms, Proc. of the 21st International Conference on Mechatronics Technology (ICMT2017), (2017), pp. 119-124.

(9) Naoto Kimura and Nobuyuki Iwatsuki, Stability Analysis for Designing Elastic Constraint for the Spatial Rolling Contact Pair, The 7th International Conference on Manufacturing, Machine Design and Tribology, Proc. of the 7th International Conference on Manufacturing, Machine Design and Tribology (ICMDT2017), p. 12, Apr. 2017.

(10) Naoto Kimura and Nobuyuki Iwatsuki, Spatial Rolling Contact Pair Generating the Specied Relative Motion between Links, Proc. of the 4th IFToMM Asian Conference on Mechanisms and Machine Science (IFToMM Asian MMS 2016), (2016), pp. 307-316.

Proceedings of domestic conferences

(11) Naoto KIMURA, Nobuyuki IWATSUKI and Ikuma IKEDA, Design and Analysis of the Multi-Directionaly Flexibly Constrained Revolute Pair Driven by Elastic Wires, Proc. of the 2020 JSME Conference on Robotics and Mechatronics, (2020), 1P2-K04 (4 pages) (in Japanese).

(12) Naoto KIMURA, Nobuyuki IWATSUKI and lkurna IKEDA, Design of the Flexible Kinematic Pair with multiple DOF Consisting of Curved Surface Contact and Elastic Constraints, Proc. of the 18th Machine Design and Tribology Division meeting in JSME, (2018), pp.139-142 (in Japanese).

(13) Naoto KIMURA, Nobuyuki IWATSUKI and Ikuma IKEDA, Revolute Pair with In-plane Flexible Constraint, Proc. of JSME annual Conference on Robotics and Mechatronics 2017, (2017), 2P1-B06 (4 pages) (in Japanese).

(14) Naoto Kimura and Nobuyuki Iwatsuki, Design of Kinematic Pair Composed of Elastically Constrained Two Curved Surfaces Which Can Generate the Specified Rolling Motion, Proc. of the JSME Student Members' Presentation on Graduate Thesis, No.620 (2016), pp.1-2 (in Japanese).

Acknowledgements

謝 辞

　本研究を遂行するにあたり，東京工業大学工学院機械系の岩附信行教授には，研究の進め方，論文の書き方，研究発表の仕方など，研究における様々な事柄について懇切丁寧なご指導，ご助言を頂きました．また，学部4年生の頃からの長きにわたり，自由に楽しく研究を行うことができたのも，私の自主性を重んじて寛大なご指導をくださった岩附教授のおかげだと考えます．心より感謝申し上げます．また，同大学工学院機械系の池田生馬助教は，異なる専門的視点から多くのご助言をくださっただけでなく，研究室の環境も整えてくださいました．おかげさまで，研究室生活を快適に過ごすことができました．深く感謝申し上げます．

　同大学工学院機械系の鈴森康一教授，武田行生教授，岡田昌史教授，菅原雄介准教授には，修士論文審査の際に，非常に的確で有益なご助言を頂きました．また，鈴森教授，武田教授，岡田教授，に加え，同大学未来産業技術研究所の進士忠彦教授には，博士課程中間発表会，博士論文公聴会において，非常に有益なご助言を頂きました．そして，同大学名誉教授の広瀬茂男先生には博士論文公聴会にて，本研究の展望に関する有益なご助言を頂きました．さらに，同大学大岡山設計工作センターの技官の皆様には，実験装置を製作するにあたって多くのご助言を頂きました．皆様のご助言により，研究をより良い方向に進められ，さらに本論文の内容に磨きをかけることができましたことを，心より感謝申し上げます．

　本研究は2018年よりJSPS特別研究員奨励費18J21095による経済的ご支援のもと行われました．おかげさまで，実験・工作に必要な設備を拡充することができました．また，株式会社デンソー様は，第4章の実験で用いたロボットマニピュレータを無償貸与してくださいました．株式会社ストラタシス・ジャパン様は，ご厚意で，第4章の試作品の一部を3Dプリンタで無償で製作してくださいました．皆様の経済的，物的ご支援により，研究をスムーズに行うことができましたことを，心より感謝申し上げます．

　同大学岩附研究室のメンバーは，進捗報告会等において積極的に議論に参加してくださいました．皆様の多様な視点のおかげで，本研究をより良い方向に導くことができたと思います．また，皆線のおかげで研究室生活を楽しく過ごすことができましたことを深く感謝申し上げます．また，博士課程で研究を行うにあたり，私の心の支えになった同じ博士課程の友人たち，私の生活を支えてくださった私の家族にも心より感謝申し上げます．

　以上，皆様の暖かいご指導，ご協力のもと，本論文を書き上げることができました．今一度，皆様に心から感謝を申し上げます．

<div style="text-align: right">2020年8月13日　木村 直人</div>